

Abstract

Title of Dissertation: PROBING THE MULTIPHASE
INTERSTELLAR MEDIUM AND
STAR FORMATION IN
NEARBY GALAXIES
THROUGH FAR-INFRARED
SPECTROSCOPY

Rodrigo Herrera Camus, Doctor of Philosophy, 2015

Dissertation directed by: Professor Alberto Bolatto
Department of Astronomy

We present a study of different aspects of the multi-phase interstellar medium (ISM) of nearby galaxies, including detailed analysis of the low-excitation ionized gas, the thermal pressure (P_{th}) of the neutral gas, the dust-to-gas mass ratio (DGR) in low-metallicity environments, and the use of far-infrared transitions as tracers of the star formation rate (SFR). We based our work on the largest sample to date of spatially-resolved, infrared observations of nearby galaxies drawn from the KINGFISH and “Beyond the Peak” surveys.

We use deep infrared observations to study the DGR of the extremely metal-poor galaxy I Zw 18. We measure a DGR upper-limit of 8.1×10^{-5} . This value is a factor of ~ 8 lower than the expected DGR if a linear correlation between DGR and metallicity, as observed in spirals, were to hold.

Based on the line ratio between the [N II] 122 and 205 μm transitions, for 140 regions selected from 21 galaxies we measure electron densities of the singly-ionized gas in the $n_e \sim 1 - 230 \text{ cm}^{-3}$ range, with a median value of $n_e = 30 \text{ cm}^{-3}$. We find that n_e increases as a function of SFR and radiation field strength.

We study the reliability of the [C II] and [N II] 122 and 205 μm transitions as SFR tracers. In general, we find good correlations between the emission from

these fine-structure lines and star formation activity. However, a decrease in the photoelectric heating efficiency in the case of the [C II] line, or collisional quenching of the [N II] lines, can cause calibrations based on these transitions to underestimate the SFR.

Finally, for a sample of atomic-dominated regions selected from 31 galaxies, we use the [C II] and HI lines to measure the cooling rate per H atom and P_{th} of the cold, neutral gas. We find a P_{th} distribution that can be well described by a log-normal distribution with median $P_{\text{th}}/k \approx 5,500 \text{ K cm}^{-3}$. We find correlations of increasing P_{th} with radiation field intensity and SFR, which is consistent with the results from a two-phase ISM model in pressure equilibrium (Wolfire et al. 2003).

PROBING THE MULTIPHASE
INTERSTELLAR MEDIUM AND
STAR FORMATION IN
NEARBY GALAXIES
THROUGH FAR-INFRARED
SPECTROSCOPY

by

Rodrigo Herrera Camus

Dissertation submitted to the Faculty of the Graduate School of the
University of Maryland at College Park in partial fulfillment
of the requirements for the degree of
Doctor of Philosophy
2015

Advisory Committee:

Professor Alberto Bolatto, Chair
Professor Daniela Calzetti
Professor Stuart Vogel
Professor Sylvain Veilleux
Dr. Mark Wolfire
Professor Kara Hoffman, Dean's representative

© Copyright by
Rodrigo Herrera Camus
2015

Preface

Part of the work presented in this thesis dissertation has been published, and the rest is in preparation for submission. Chapter 2 has been published in *The Astrophysical Journal* as “*Dust-to-Gas Ratio in the Extremely Metal-Poor Galaxy I Zw 18*” (Herrera-Camus, Fisher, Bolatto, et al. 2012, ApJ, 752, 112). A follow-up paper on I Zw 18, of which I was a co-author, was published in *Nature* by Fisher et al. 2014. Chapter 3 and the Appendix were published together in *The Astrophysical Journal* as “[*C II*] 158 μm Emission as a Star Formation Tracer” (Herrera-Camus, Bolatto, Wolfire, et al. 2015, ApJ, 800, 1). Chapter 4 is submitted to the *The Astrophysical Journal*. Chapter 5 is currently in preparation for submission to the *The Astrophysical Journal*.

Al Creador.



A Fares, mi arbol favorito.



A Margarita, la mujer que
me presentó las Nubes de Magallanes.

Acknowledgements

I would like to start by expressing my deepest gratitude to my advisor Prof. Alberto Bolatto. Without your support, encouragement, and dedication to assist me, this dissertation would have not been possible. I look back when we first started working together and I can see how much you helped me to grow in many areas that are required to be a good scientist.

Besides my advisor, I would like to thank the rest of my thesis committee: Prof. Daniela Calzetti, Prof. Stuart Vogel, Prof. Sylvain Veilleux, Dr. Mark Wolfire, and Prof. Kara Hoffman, for your insightful comments and encouragement.

My sincere thanks also goes to the members of the KINGFISH and “Beyond the Peak” teams, in special to the PIs Rob Kennicutt and J. D. Smith. Thank you very much for giving me the opportunity to be part of these monumental projects and write my thesis based on these unprecedented set of observations of nearby galaxies. I would also like to

thank Mark Wolfire and Bruce Draine for your valuable scientific insight and careful reading of my papers.

Thank you to the members of the Laboratory for Millimeter-wave Astronomy at UMD. I feel privileged to have had the opportunity to participate in the CARMA summer school, and then return to the array every year of my PhD to work as a service observer. Peter Teuben, thank you very much for your help using MIRIAD, pictures of memorable moments, and daily visits to my office.

I thank my fellow graduate students for six years full of good memories. Special thanks to my officemates and dearest friends Shaye and Megan. To my classmates Katie, Jonathan, Anne, Jessica and Mark. To my friend, housemate and soccer team captain Alex. To the old and wise grads Hao, Kwang Ho, Edmund, Ashley and Kari. I really missed you these last couple of years. Thank you very much to the professional staff working at the UMD astronomy department –Eric, Mary Ann, Susan, Adrienne– for taking care of all my administrative needs.

I also thank the Fulbright Commission and CONICYT for fully funding my first four years of grad school and helping me during the graduate school application process. I also thank support from National Science Foundation grants AST0955836 and AST1412419.

Last but not least, I would like to thank God, my wife Fares and my family. For you, a few words in Spanish: *Fares, no podría pensar en otra persona que me pueda amar, apoyar e inspirar más que tú. Todos los créditos de mi doctorado son compartidos contigo y te agradezco profundamente tu paciencia y compañía en este maratónico proceso. Siempre*

serás mi arrebol favorito. Papás, habría sido imposible llegar a esta instancia sin su incondicional amor y apoyo. Es sobre sus hombros que hoy me puedo presentar ante mi comisión de tesis a defender mi doctorado. Les agradezco haber siempre depositado su confianza en mi. Hermano, tu compañía, a pesar de la distancia, siempre ha significado una extraordinaria fuerza adicional para seguir adelante. Gracias por tu cariño y apoyo constantes. A mis abuelos (Margarita, Gilberto, Gilda y Julio), tías, tíos, primos, primas, familia de mi esposa Fares, cada uno ha contribuido de gran forma a que yo pueda perseguir mis sueños, y por eso, estoy profundamente agradecido. Gracias a Dios por ustedes y por la oportunidad de estudiar su maravilloso universo. Muchas gracias Dios por tu compañía constante en mi vida.

Contents

List of Tables	x
List of Figures	xi
1 Introduction	1
1.1 The Multiphase Interstellar Medium	1
1.2 Heating and Cooling of the Interstellar Gas	5
1.3 The Two-phase Interstellar Medium Model	10
1.4 The Herschel Space Observatory	12
1.5 The KINGFISH Sample	13
1.6 Outline of the Thesis	15
2 Dust-to-Gas Ratio in the Extremely Metal-Poor Galaxy I Zw 18	17
2.1 Introduction	17
2.2 Methods	19
2.2.1 Observations	19
2.2.2 Photometry	23
2.3 Results	26
2.3.1 Dust Mass	26
2.3.2 Comparison of Dust Masses	30
2.3.3 Gas Mass	32
2.3.4 Dust-to-Gas Mass Ratio and Metallicity	34
2.4 Conclusions	36
3 [C II] 158 μm Emission as a Star Formation Tracer	38
3.1 Introduction	38
3.2 Main Sample Description	43
3.2.1 Methods	45
3.3 Results	47
3.3.1 [C II] – 24 μm Correlation	47
3.3.2 AGN Contribution	48
3.3.3 24 μm “Cirrus” Emission	49

3.3.4	[C II] compared to other SFR tracers	52
3.4	Analysis	56
3.4.1	Local Variations	57
3.4.2	IR Color Adjustment	61
3.4.3	Galaxy-to-Galaxy Variations	62
3.4.4	Low Metallicity Galaxies	65
3.4.5	Dependence with inclination	70
3.4.6	The effect of the IR color adjustment	70
3.5	Comparison with Models and Observations	73
3.5.1	Comparison to other extragalactic [C II] samples	73
3.5.2	Comparison with Models: Starburst99	79
3.6	Summary and Conclusions	83
4	The Ionized Gas in Nearby Galaxies as traced by the [N II] lines	88
4.1	Introduction	88
4.2	Main Sample Description	91
4.2.1	Spectroscopic Data	91
4.2.2	Supplementary Data	93
4.2.3	Models	95
4.2.4	Methods	96
4.3	Results and Discussion	97
4.3.1	Estimating ionized gas densities from the [N II] lines	97
4.3.2	Observed distribution of [N II] 122/205 line ratios and n_e	99
4.3.3	Electron density variations within individual galaxies	103
4.3.4	Relationship between n_e and the ISM environment	105
4.3.5	Estimating SFRs from the [N II] lines	109
4.3.6	Correlations between the [N II] lines and SFR	116
4.3.7	Comparison with models and other extragalactic samples	120
4.4	Summary and Conclusions	123
5	Thermal Pressure in the Diffuse Gas of Nearby Galaxies	128
5.1	Introduction	128
5.2	Main Sample Description	131
5.2.1	KINGFISH [C II]	131
5.2.2	THINGS HI	132
5.2.3	HERACLES CO	132
5.2.4	Additional Data	133
5.2.5	Methods	133
5.3	[C II] emission and the thermal pressure in the diffuse ISM	134
5.4	Results and Discussion	136
5.4.1	Criteria for selection of atomic dominated regions	136

5.4.2	Thermal pressure and star formation activity	142
5.5	Summary and Conclusions	147
6	Summary and Future Work	149
6.1	Summary and Conclusions	149
6.2	Future Work	154
A	Appendix	157
A.1	KINGFISH galaxies not included in Chapter 3 analysis	157
A.2	Supplementary data in Chapter 3	158
A.3	Cirrus emission	160
A.4	Dust attenuation	162
A.5	Additional samples of galaxies included in Chapter 3	162
A.6	$\Sigma_{[\text{CII}]} - \Sigma_{24 \mu\text{m}}$ Correlation for the KINGFISH Galaxies	165
	Bibliography	165

List of Tables

2.1	Derived dust properties based on the DL07 model	30
3.1	Effect of 24 μm cirrus correction	51
3.2	IR color adjustment coefficients	62
3.3	[C II]-SFR calibration coefficients and uncertainties	72

List of Figures

1.1	The multiphase interstellar medium	2
1.2	Heating and cooling in the ISM	7
1.3	[C II] 158 μm emission in star-forming galaxies.	9
1.4	ISM Two-phase model	11
1.5	The Herschel Space Observatory	13
1.6	KINGFISH tuning fork	14
2.1	I Zw 18 70 μm and 160 μm maps.	20
2.2	I Zw 18 160 μm , 250 μm maps and foreground HI emission	23
2.3	Infrared SED of I Zw 18	27
2.4	Dust-to-gas mass ratio versus metallicity	32
3.1	PACS [C II] 158 μm images of four KINGFISH galaxies	46
3.2	$\Sigma_{[\text{CII}]}$ versus $\Sigma_{24\mu\text{m}}$ correlation	50
3.3	$\Sigma_{[\text{CII}]}$ versus Σ_{SFR} correlation	54
3.4	Scatter of the $\Sigma_{[\text{CII}]} - \Sigma_{\text{SFR}}$ correlation	59
3.5	Galaxy-to-galaxy variations	64
3.6	[O I] 63 μm to [C II] 158 μm ratio as a function of Σ_{SFR}	66
3.7	$\Sigma_{[\text{CII}]} - \Sigma_{\text{SFR}}$ before and after the IR color adjustment	71
3.8	ALMA’s ability to detect [C II] emission at high redshift	73
3.9	Comparison between the KINGFISH galaxies and other samples I	74
3.10	Comparison between the KINGFISH galaxies and other samples II	77
3.11	The [C II]-based SFR calibration and comparison to <i>Starburst99</i>	81
4.1	PACS [N II] 122 μm image of NGC 4254	94
4.2	n_e as a function of the [N II] 122/205 μm ratio	99
4.3	Histogram of [N II] line ratios in the “Beyond the Peak” sample	101
4.4	Distribution of n_e in the “Beyond the Peak” sample	102
4.5	Distribution of n_e for individual galaxies	104
4.6	n_e as a function of ISM properties	108
4.7	Calibration coefficient C as a function of [N II] 122/205 line ratio	114
4.8	[N II]-SFR correlations	119

4.9	[N II]-SFR correlations compared to models and other samples	122
5.1	[C II] cooling rate per H atom as a function of temperature	135
5.2	[C II] cooling rate per H atom as a function of $\Sigma_{\text{HI}}/\Sigma_{\text{H}_2}$	138
5.3	Correlations between P_{th} and ISM properties	140
5.4	Comparison to the P_{th} distribution of the Galactic plane	142
5.5	P_{th} versus Σ_{SFR} and comparison to models	144
6.1	Multi-phase ISM of Haro 11	156
A.1	Fit residual of the $\Sigma_{[\text{CII}]} - \Sigma_{\text{SFR}}$ correlation vs absorbed FUV	163
A.2	[C II]- $\Sigma_{24 \mu\text{m}}$ correlation for individual galaxies (panel 1)	166
A.3	[C II]- $\Sigma_{24 \mu\text{m}}$ correlation for individual galaxies (panel 2)	167

Chapter 1

Introduction

1.1 The Multiphase Interstellar Medium

The interstellar medium (ISM) is the gas and dust distributed between the stars. The ISM constitute only a small fraction of the total mass of a galaxy ($\sim 10\%$), however, it plays a crucial role in galaxy evolution by providing the environment where new stars are born. Stars heat and ionize the surrounding gas, and by the end of their lives the most massive ones explode as supernova, reheating the gas and enriching it with metals. All these interactions between gas, dust and stars shape the ISM into a collection of multiple thermal phases that coexist in pressure equilibrium (Cox 2005; Field et al. 1969; McKee & Ostriker 1977).

In order to better understand the complex structure of the multiphase ISM in galaxies, it is perhaps useful to start by showing a multiwavelength view of one of our closest galaxy neighbors, the Small Magellanic Cloud (SMC). In the image of the SMC in Figure 1.1a, each color represents a different gas component. The atomic hydrogen gas traced by the 21 cm line emission is shown in red. This gas is diffuse and widespread across the galaxy. The more clumpy gas shown in green corresponds to hot, ionized gas powered by young, massive stars and visible in $H\alpha$ line emission.

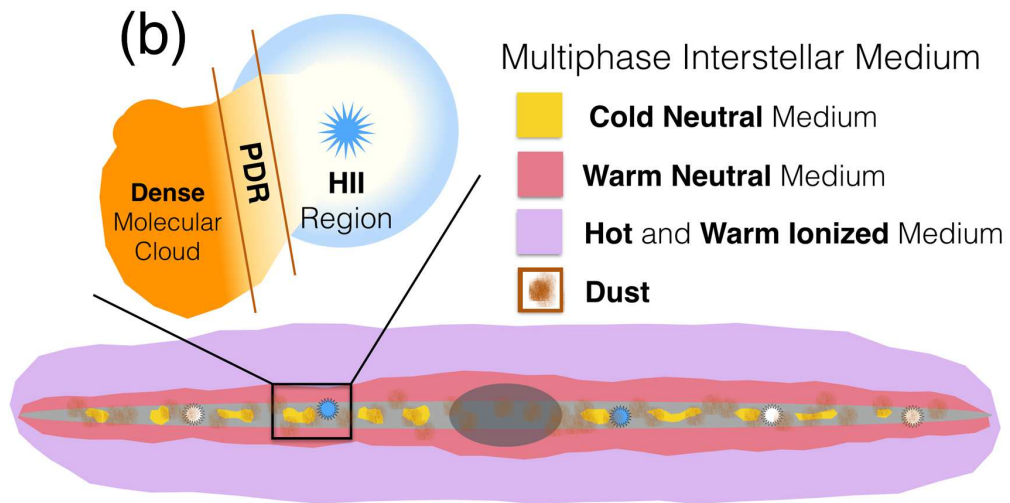
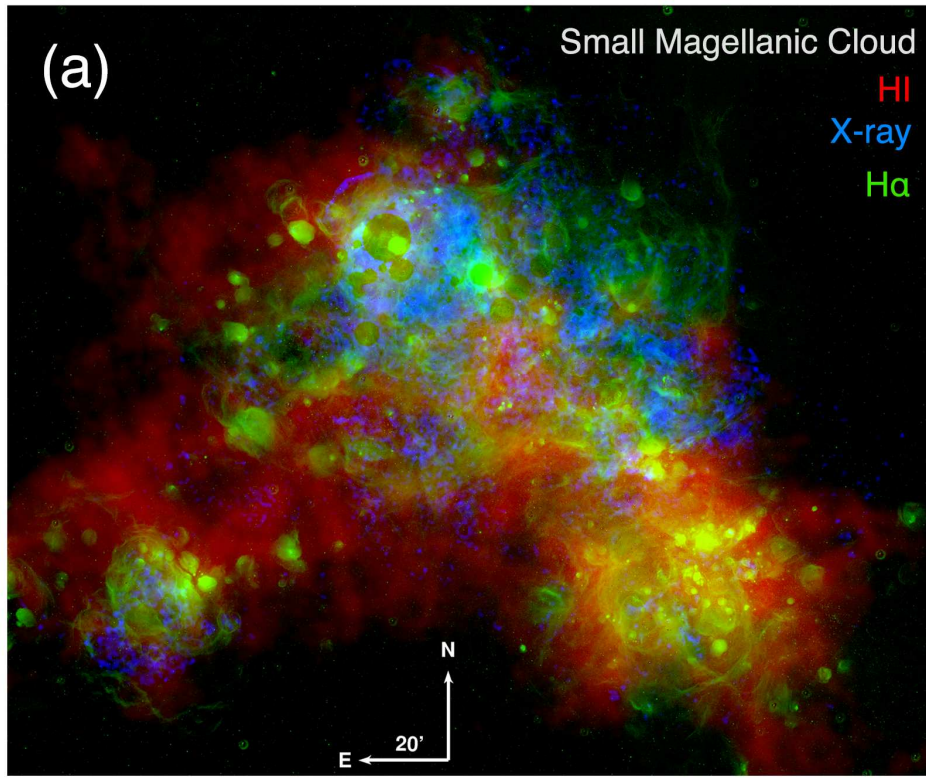


Figure 1.1: (a) Multi-wavelength view of the Small Magellanic Cloud. Red: cold HI gas traced by the 21 cm emission. Green: H α emission arising from hot, ionized gas. Blue: hot gas (~ 0.2 keV) seen in X-ray emission (Credits: Max Planck Institute for extraterrestrial Physics). (b) Schematic illustrating the multiple thermal phases and components of the interstellar medium.

Finally, very hot ($T \sim 10^6$ K), diffuse gas that has been shock-heated by supernovae and observed in X-ray emission is shown in blue. These three gas components – cold, hot and very hot gas – are only one part of a more complex multi-phase ISM structure. Overall, the main thermal phases of the ISM are:

Hot Ionized Medium (HIM): gas that has been heated by supernovae to temperatures $T \gtrsim 10^6$ K. Its density is very low ($n_e \approx 0.004 \text{ cm}^{-3}$), and occupies about $\sim 50\%$ of the volume of the galactic disk.

Warm Ionized Medium (WIM)/H II Regions: gas with temperature around $T \approx 10^4$ K that has been primarily photoionized by UV photons from hot stars. About 90% of the gas in the WIM is diffuse ($n_e \sim 0.1 - 10 \text{ cm}^{-3}$). The remaining 10% resides in H II regions, which are dense ($n_e \sim 10^2 - 10^4 \text{ cm}^{-3}$) clouds of photoionized gas formed around young, massive stars.

Warm Neutral Medium (WNM): neutral atomic gas at heated to temperatures in the $T \sim 600 - 10^4$ K range, with a peak temperature in our Galaxy of $T \approx 8,000$ K (Heiles & Troland 2003). It is low-density and fills around $\sim 40\%$ of the volume of the ISM.

Cold Neutral Medium (CNM): cold ($T \approx 100$ K), neutral atomic gas that is distributed in sheets and filaments with densities $n_H \approx 30 \text{ cm}^{-3}$, and that occupies about $\sim 1\%$ of the volume of the ISM.

Molecular Clouds: H_2 gas that is gravitationally bound and have densities $n_H \gtrsim 10^3 \text{ cm}^{-3}$ and temperatures around $T \sim 10 - 20$ K. Even though they only occupy less than $\sim 1\%$ of the volume of the galactic disk, they constitute $\sim 30\%$ of the mass of the ISM. Molecular clouds are the place in the ISM where stars are born.

Photodissociation Regions (PDR): Dense gas interface between molecular clouds and H II regions where FUV photons play a significant role in the chemistry and/or the heating of the gas.

Together with the gas thermal phases, one additional and key component of the ISM is dust. We consider as dust small solid particles with less than $\sim 1 \mu\text{m}$ in size. Gas and dust are strongly related in a cycle where dust grains form from the available metals in the gas (Savage & Sembach 1996), and then metals return to the gas when dust is destroyed. The dust-to-gas ratio (DGR) is then the quantity that links the amount of metals locked up in dust with that still present in the gas phase. If we assume that the fraction of metals incorporated in the dust is constant (James et al. 2002), then we expect a linear relation between DGR and metallicity. This prediction is consistent with the trends of DGR and metallicity observed in normal, star-forming galaxies (Draine et al. 2007; Magrini et al. 2011). In low metallicity environments, however, the situation seems to be different, as studies suggest that low metallicity galaxies do not follow a linear relationship between DGR and metallicity (see Chapter 2; Fisher et al. 2014; Galametz et al. 2011; Lisensfeld & Ferrara 1998; Rémy-Ruyer et al. 2014).

To summarize, Figure 1.1b shows a schematic illustration of some of the principal components of the ISM previously reviewed. During their lifetime, baryons will reside in one or multiple of these ISM phases. The reason is that the ISM is a place in constant evolution, where multiple cooling and heating mechanisms drive the gas and dust to transition from one phase to the other.

1.2 Heating and Cooling of the Interstellar Gas

The temperature of the gas in the ISM is determined by the balance between the physical processes that add to the kinetic energy of the particles in the gas (i.e., heating), and those that remove thermal energy from the gas (i.e., cooling). There are multiple heating and cooling mechanisms, and their relative importance depend on the thermal phase of the ISM involved.

In H II regions, the main source of heating are photoelectrons resulting from the photoionization of H and He atoms. These photoelectrons can then recombine with hydrogen nuclei, or they can collisionally excite other ions, which for both cases result in a decrease of the kinetic energy of the gas. A third source of cooling for the H II gas is free-free emission. Figure 1.2a shows the heating (Γ_{pe}) and cooling ($\Lambda = \Lambda_{ce} + \Lambda_{rr} + \Lambda_{ff}$) curves as a function of temperature T for a gas with solar composition and heated by a $T_{eff} = 3.5 \times 10^4$ K central source. The gas stabilize at the temperature where the net cooling and heating curves intersect, which in this case is at $T \approx 8,050$ K.

Due to importance of collisional excitation and radiative recombination in the cooling of the ionized gas, the emerging spectra will be dominated by recombination lines of H and He, and by forbidden lines of heavy elements. The latter can be used as tracers of the electron density of the ionized gas within a limited range defined by the critical densities of the two transitions involved. In the optical, doublets of lines such as the [SII] 6716, 6731 Å or [OII] 3726, 3729 Å have been commonly used to study the density of H II regions in the Galaxy and other extragalactic systems (Ho et al. 1997; Kennicutt 1984).

The limitation of gas diagnostics based on optical lines is that they are not sensitive to electron densities below $n_e \lesssim 100 \text{ cm}^{-3}$ – therefore excluding from

the analysis the diffuse gas that fills the space between dense H II regions. One alternative to characterize the gas in the $n_e \sim 10 - 300 \text{ cm}^{-3}$ range is to use the pair of [N II] fine-structure lines at $122 \text{ }\mu\text{m}$ ($n_{\text{crit}} \approx 300 \text{ cm}^{-3}$) and $205 \text{ }\mu\text{m}$ ($n_{\text{crit}} \approx 40 \text{ cm}^{-3}$). Due to Earth’s atmosphere, these lines are very difficult to observe from the ground, and the number of observations using space observatories before *Herschel* Space Observatory was available was scarce. This is the reason why there were only a handful of ionized gas density measurements that rely on the [N II] far-infrared lines at the time of launch (e.g., Carina nebula (Oberst et al. 2011, 2006), M 82 (Petuchowski et al. 1994), Milky Way (Bennett et al. 1994)). The advent of *Herschel* changed this scenario dramatically, and now we have access to a rich sample of [N II] far-infrared observations that allow for the characterization of the properties of the ionized gas in a variety of ISM environments (See Chapter 4).

Another interesting application of the [N II] far-infrared lines is to use them as tracers of star formation activity. This is important because the rate at which galaxies form stars is one of the most relevant properties of galaxies in the local and high redshift (z) universe (Kennicutt & Evans 2012; Madau & Dickinson 2014). As we mentioned before, the observed [N II] 122 and 205 μm transitions are the result of collisional excitations by photoelectrons, therefore, they can be used to count the number of ionizing photons produced by young, massive stars. This application can be useful to study the star forming properties of high-redshift galaxies, as ground based observatories like the Atacama Large Millimeter/submillimeter Array (ALMA) can detect the [N II] far-infrared transitions at redshift greater than $z \gtrsim 1$. We explore the reliability of the [N II] lines as star formation tracers in Chapter 4.

Turning now to the neutral phases of the ISM, Figure 1.2b shows the heating and cooling curves as a function of the neutral gas density (n) for conditions that resemble the Galactic ISM at a distance of 8.5 kpc from the center (Wolfire et al.

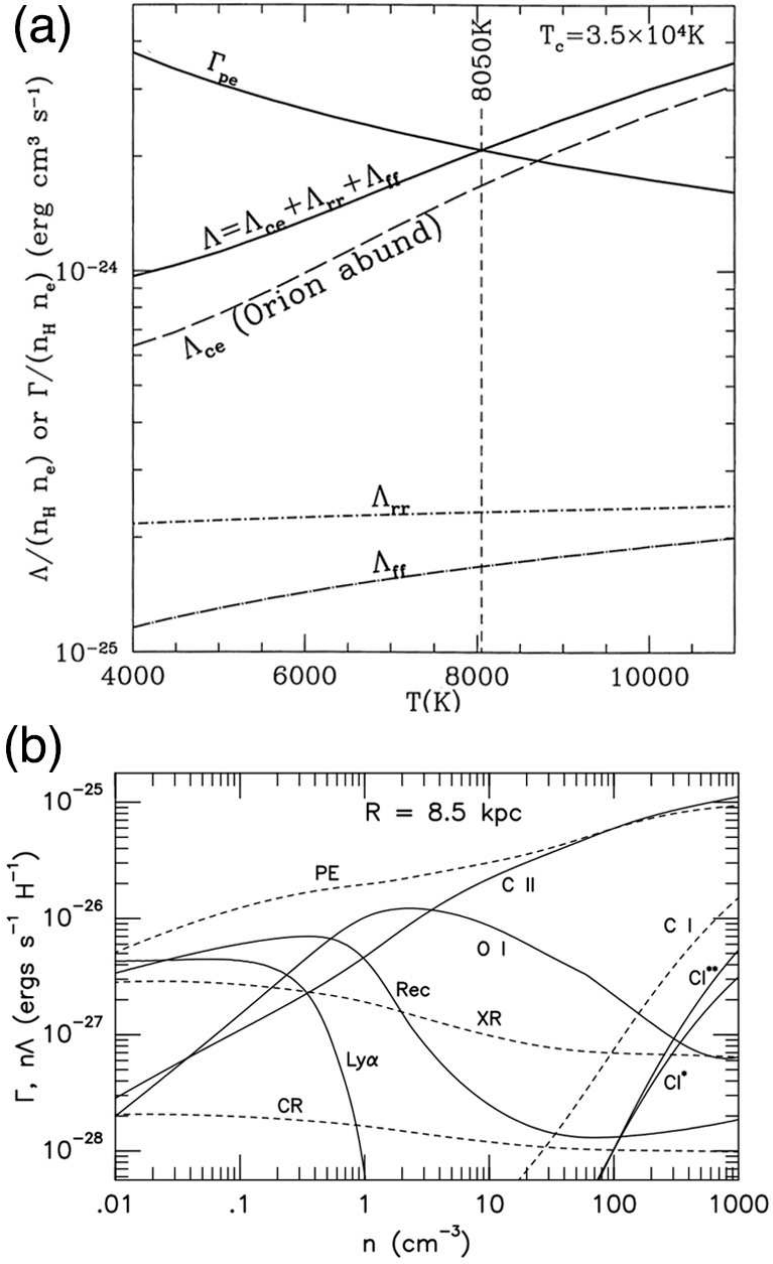


Figure 1.2: (a) Photoelectric heating (Γ_{pe}) and radiative cooling (Λ) functions as a function of temperature T in a H II region with a central source with $T_{\text{eff}} = 3.5 \times 10^4$ K, Orion-like abundance, and density $n_H = 4,000$ cm⁻³. Heating and cooling balances at $T \approx 8,050$ K (Reproduced from Draine 2011b). (b) Heating and cooling curves versus hydrogen nucleus density in a diffuse gas at a Galactic distance of $R = 8.5$ kpc. Overall, the main heating source is photoelectric heating (PE), and the [CII] emission dominates the cooling in the CNM. (Reproduced from Wolfire et al. 2003)

2003). We see that for both WNM and CNM phases the heating of the gas is dominated by the photoelectric effect on small dust grains and polycyclic aromatic hydrocarbons (PAHs) (Draine 1978; Watson 1972; Wolfire et al. 1995). For the WNM there are also minor contributions to the heating by X-rays and cosmic rays. Regarding the cooling, in the WNM the main sources are Lyman- α line emission (Ly- α) and recombination of the electrons onto small dust grains and PAHs. While in the CNM, the dominant cooling channel is the [C II] 158 μm transition, followed by the [O I] 63 μm line.

As the major coolant for the neutral atomic gas, the [C II] 158 μm transition represents a powerful tool to investigate the thermodynamics of the ISM in galaxies across redshift. Consider that if the gas is in thermal balance, then the [C II] line measures the total energy that is put into the gas by star formation activity, i.e., has great potential to be used as a star formation tracer (De Looze et al. 2014; Herrera-Camus et al. 2015; Pineda et al. 2014). To illustrate this point, Figure A.3 shows the correlation between the [C II] line luminosity and the far-infrared luminosity (arising from dust heated by the interstellar radiation field and proportional to the star formation activity) for normal star-forming galaxies, luminous infrared galaxies ($L_{\text{FIR}} > 10^{11} L_{\odot}$; LIRGs) and high redshift systems (Magdis et al. 2014, and references therein). The majority of star forming galaxies follow the linear relation within the ~ 0.3 dex scatter over nearly six orders of magnitude in luminosity. The galaxies that show higher deviations from the relation –AGN/QSOs, local ultra-LIRGs, some high redshift star-forming galaxies – tend to show lower [C II] to far-infrared luminosity ratios, which is commonly known as the “[C II]-deficit” (Díaz-Santos et al. 2013; Graciá-Carpio et al. 2011; Malhotra et al. 2001); but for most of the normal, star-forming galaxies, observations suggest that [C II] emission can trace the FIR emission.

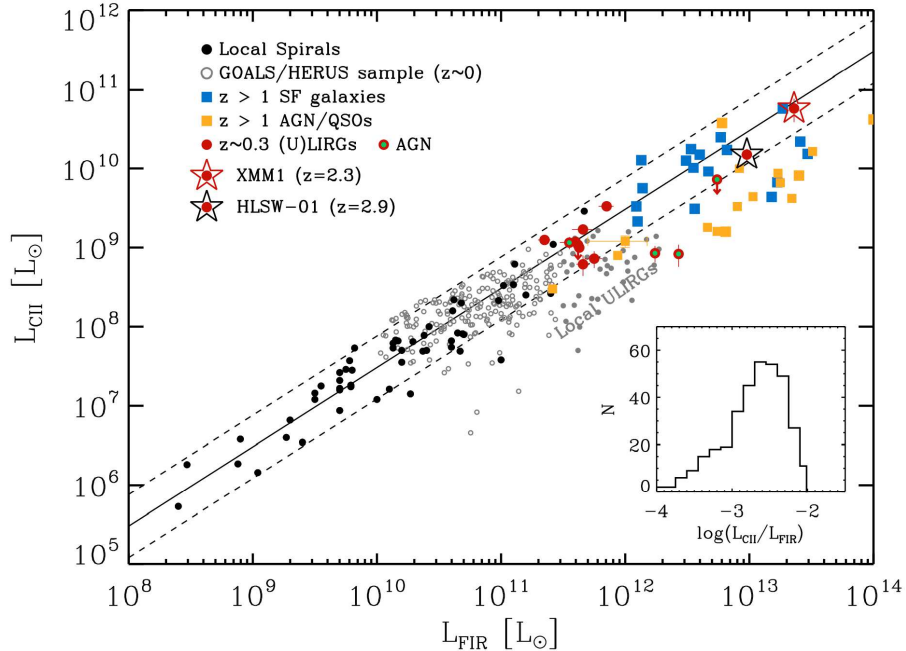


Figure 1.3: [CII] 158 μm line luminosity ($L_{\text{[CII]}}$) versus far-infrared luminosity (L_{FIR}) for a sample of local normal galaxies (filled black circles), local luminous infrared galaxies (empty grey circles), high redshift star-forming galaxies (blue squares) and high redshift AGN dominated sources and QSOs (filled orange squares). The solid black lines correspond to the best linear fit to the local normal galaxies of Malhotra et al. (2001) with a scatter of 0.3 dex (dashed lines) and a slope of unity (Magdis et al. 2014, and references therein).

In order to assess how reliable is a [C II]-based star formation rate calibration, it is key to understand how well the [C II] emission trace the star formation activity in different ISM environments. So far there have been studies that focused on luminous infrared galaxies (De Looze et al. 2011; Sargsyan et al. 2012), low metallicity galaxies (De Looze et al. 2014), and the Galactic plane (Pineda et al. 2014), but there is still no comprehensive study on a large sample of regions selected from normal, star forming galaxies. Thanks to *Herschel* and the KINGFISH sample of nearby galaxies (Kennicutt et al. 2011) this is now possible, and in Chapter 3 we address this challenge.

1.3 The Two-phase Interstellar Medium Model

One of the first attempts to explain the absorption and emission characteristics observed in the neutral ISM (e.g., Clark 1965; Hagen et al. 1955) was by Field et al. (1969), in what is commonly known as the Two-Phase Model of the ISM. In this model, thermal balance between the heating and cooling of the ISM –reviewed in the previous section– define a thermal pressure curve that is a function of the neutral gas density. This pressure curve is characterized by a sinuous shape, and defines the range of thermal pressures where the CNM and the WNM can coexist.

The thermal pressure curve in the Two-Phase Model is not universal, it changes as the heating and cooling sources of the gas vary with metallicity, FUV radiation field, gas column density, among other ISM properties (e.g., Wolfire et al. 1995, 2003). As an example, Figure 1.4 shows a set of thermal pressure curves calculated for different values of FUV radiation field intensity (Wolfire et al. 1995). As the FUV radiation field increases, so does the photoelectric heating of the gas, causing the thermal pressure curve to shift upwards.

For the particular case of the solar neighborhood ($\text{ISRF} \times 1$), the model predicts a thermal stable phase for gas with $n \lesssim 1 \text{ cm}^{-3}$ (WNM), and $n \gtrsim 6 \text{ cm}^{-3}$ (CNM), and a thermal unstable phase in between these density values. The median two-phase thermal pressure derived in the Wolfire et al. (1995) model is consistent with the observed value of the thermal pressure in the Galactic Plane (Gerin et al. 2015; Jenkins & Tripp 2011).

Pressure plays a crucial role in the process of star formation: it controls the balance between the different phases through the cooling curve and determines the conditions for the formation of giant molecular clouds (Blitz & Rosolowsky 2006). Thus, in a multi-phase ISM that evolves towards a simultaneous dynamical, thermal

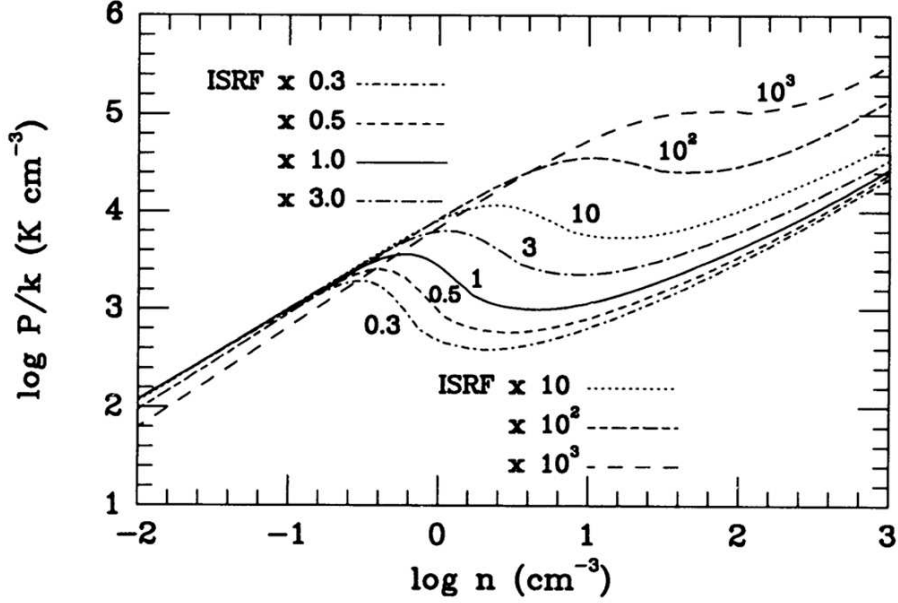


Figure 1.4: (a) Thermal pressure P/k versus hydrogen nucleus density, n , for various values of the interstellar FUV radiation field normalized to the one measured in the solar neighborhood (ISRF). The thermal pressure curve shift upwards as the radiation field intensity, and consequently the heating rate, increases. (Reproduced from Wolfire et al. 1995)

and star formation equilibrium (Ostriker et al. 2010), it is of great interest to measure the pressure directly. Apart from the thermal pressure measurements in the Galactic plane (Gerin et al. 2015; Jenkins & Tripp 2011), there are only a few direct measurements of thermal pressures in extragalactic objects (e.g., Madden et al. 1993).

One robust method to measure the thermal pressure in the neutral gas involves using the the [C II] $158 \mu\text{m}$ emission to derive the volume density of the atomic gas, and then, the thermal pressure $P \approx nkT$ (Kulkarni & Heiles 1987). This technique requires [C II] observations from regions where the collisional excitations of C^+ ions are dominated by hydrogen atoms, which were very limited before the *Herschel* era. Nowadays, thanks to the rich multiwavelength coverage of nearby galaxies that include *Herschel* [C II], HI (atomic gas tracer) and CO (molecular gas tracer)

observations, we can use the [C II] line to study for the first time the distribution of thermal pressures in a large and diverse sample of extragalactic regions (See Chapter 5).

1.4 The Herschel Space Observatory

The work in this thesis is mainly based on far-infrared spectroscopic observations of nearby galaxies, one of the least explored spectral regions of the electromagnetic spectrum. The first observations of this type started in the 1980s with balloon experiments, the Kuiper Airborne Observatory (KAO) and the Cosmic Background Explorer (COBE), and then greatly improved in the 1990s thanks to the advent of the Infrared Space Observatory (ISO). ISO made possible, for the first time, to study of the infrared spectroscopic properties of large samples of galaxies (e.g., Luhman et al. 2003; Malhotra et al. 2001).

The latest and major step forward in the field of far-infrared observations was the launch of the *Herschel* Space Observatory on 2009 (Pilbratt et al. 2010). Figure 1.5 shows a model of *Herschel*, a telescope with a 3.5 m diameter mirror and equipped with three instruments: (1) PACS (Photodetector Array Camera and Spectrometer; Poglitsch et al. 2010), a camera and low resolution spectrometer for wavelengths in the 55 – 210 μm range, (2) SPIRE (Spectral and Photometric Imaging Receiver; Griffin et al. 2010), a camera and low resolution spectrometer for wavelengths in the 194 – 672 μm range, and (3) HIFI (Herschel-Heterodyne Instrument for the Far-Infrared de Graauw et al. 2009), a high-resolution heterodyne spectrometer covering the 490 – 1250 GHz and 1410 – 1910 GHz frequency bands. As can be seen from the galaxy model spectral energy distribution in Figure 1.5, the *Herschel* PACS and SPIRE instruments cover the principal far-infrared fine-structure cooling lines:

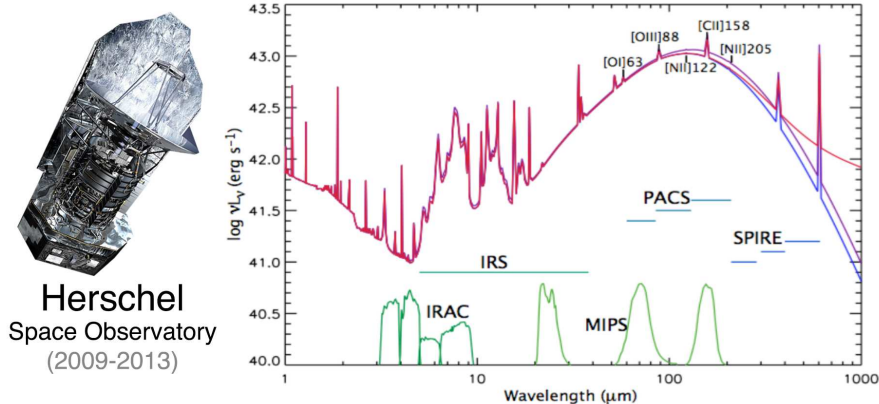


Figure 1.5: *Herschel* Space Observatory (2009–2013) and a series of model spectral energy distributions (SED) for a star-forming galaxy. The image shows the coverage of the SED by *Spitzer* instruments IRAC, IRS and MIPS, and the coverage by *Herschel* instruments PACS and SPIRE. *Herschel* was capable of observing the principal far-infrared fine-structure cooling lines of the ISM: [OI] 63 μm , [OIII] 88 μm , [NII] 122 μm , [CII] 158 μm and [NII] 205 μm .

[OI] 63 μm , [OIII] 88 μm , [N II] 122 μm , [C II] 158 μm and [N II] 205 μm .

In summary, *Herschel*’s key capabilities – good spatial resolution, extended far-infrared wavelength coverage, and spectroscopic power– provide an unprecedented opportunity to study the multi-phase ISM in nearby galaxies.

1.5 The KINGFISH Sample

With the exception of Chapter 2 that focus on the low metallicity galaxy I Zw 18, the rest of my thesis is based on the KINGFISH (“The Key Insights on Nearby Galaxies: a Far-Infrared Survey with *Herschel*”; Kennicutt et al. 2011) sample of galaxies. KINGFISH is a imaging and spectroscopic survey of 61 nearby ($d < 30$ Mpc) galaxies, chosen to cover a wide range of galaxy properties and ISM environments.

Figure 1.6 shows the KINGFISH galaxies arranged by morphological type. Most of the galaxies are spiral of all types, but the sample also includes irregulars and early-type systems. The sample covers a wide range in metallicity ($7.7 \lesssim 12 +$

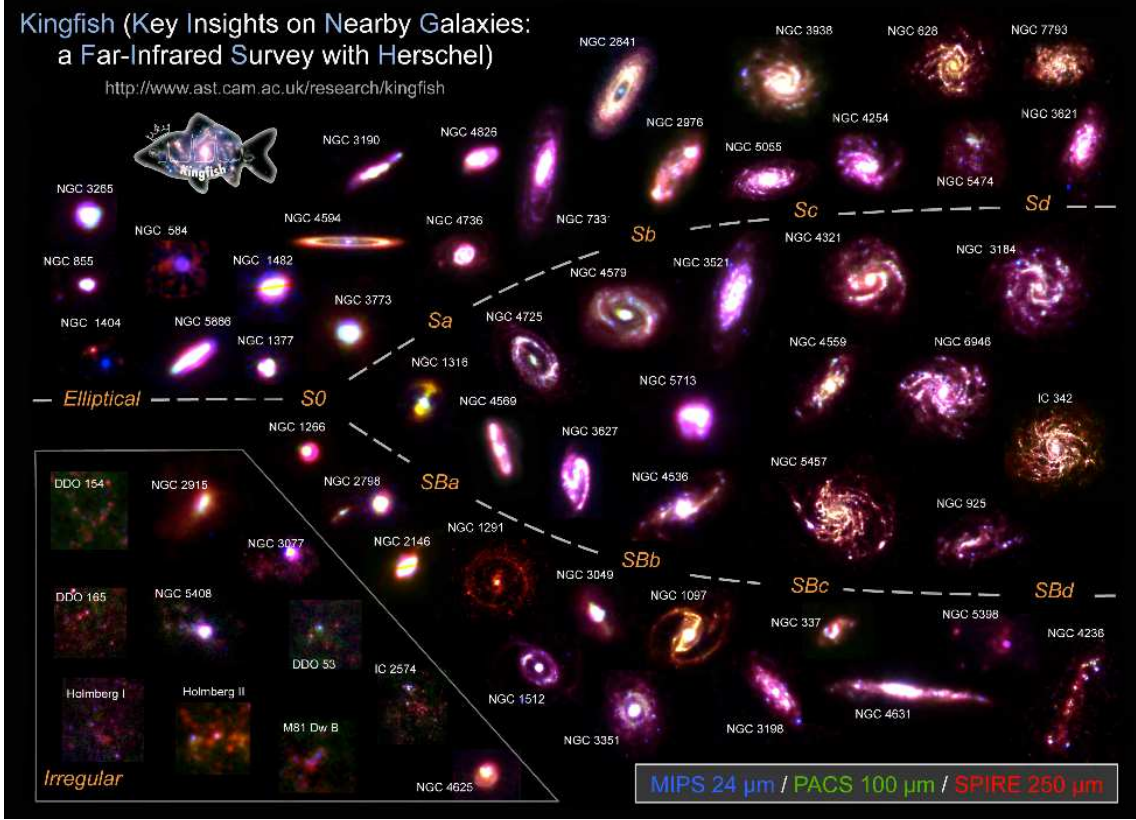


Figure 1.6: 61 KINGFISH galaxies arranged in a tuning fork based on their optical morphology. The composite images were created using *Spitzer*/MIPS 24 μm (blue), *Herschel*/PACS 100 μm (green) and *Herschel*/PACS 250 μm (red) images.

$\log_{10}(\text{O}/\text{H}) \lesssim 9$), total infrared luminosity ($10^7 \lesssim L_{\text{TIR}}/L_{\odot} \lesssim 10^{11}$), and specific star formation rate ($10^{-8.5} \lesssim \text{SSFR}/\text{yr}^{-1} \lesssim 10^{-11.5}$).

One of the major strengths of the KINGFISH sample is the wealth of ancillary data available. On the infrared side, it includes *Spitzer* and *Herschel* infrared photometry that combined cover the 3.6 – 500 μm range of the spectrum; dust maps derived from the infrared spectral energy distribution using the Draine & Li (2007) model; *Spitzer* and *Herschel* mid- and far-infrared spectroscopy, including SPIRE/FTS observations from the “*Beyond the Peak*” sample (PI J.D. Smith). Ancillary data available also include atomic and molecular gas information based on 21 cm and CO line observations as part of the HERACLES (Leroy et al. 2009) and THINGS (Walter et al. 2008) surveys, and ground-based $\text{H}\alpha$ and GALEX FUV ob-

servations that trace recent star formation activity. All these tracers combined offer a unique and complete view of the multi-phase ISM, providing the resources needed to address the scientific questions that motivate my thesis work.

1.6 Outline of the Thesis

This thesis is organized as follows:

In Chapter 2 we study the dust and gas properties of the extremely low-metallicity galaxy I Zw 18. We measure its dust-to-gas ratio and we discuss our findings in the context of the dust-to-gas ratio-metallicity relation observed in normal galaxies. This chapter was published as “*Dust-to-Gas Ratio in the Extremely Metal-Poor Galaxy I Zw 18*” (Herrera-Camus, Fisher, Bolatto, et al. 2012, ApJ, 752, 112).

In Chapter 3 we study the reliability of the [C II] 158 μm transition as a star formation tracer. We analyze the correlation of the [C II] emission with different tracers of star formation activity ($\text{H}\alpha$, FUV, infrared emission) on \sim kiloparsec scales. We study the scatter of the correlation as a function of ISM environment variables, identifying the limits of applicability of a [C II]-based star formation rate calibration. We finally compare our results to other sample of galaxies and predictions from the *Starburst99* model. This chapter was published as “[C II] 158 μm Emission as a Star Formation Tracer” (Herrera-Camus, Bolatto, Wolfire, et al. 2015, ApJ, 800, 1).

In Chapter 4 we explore the properties of the ionized gas in nearby galaxies based on the [N II] 122 μm and 205 μm transitions. We measure the electron density of the ionized gas on \sim kiloparsec scales, and we study its dependence with various ISM properties. We then explore the reliability of the [N II] lines emission as a star formation tracer, and we compare our results to predictions from the MAPPINGS-

III photoionization code. This chapter is submitted to *The Astrophysical Journal*.

Finally, in Chapter 5 we use [C II] emission arising from atomic-dominated regions to measure the thermal pressure of the neutral gas. We compare the distribution of thermal pressures to those observed in the Galactic plane, and we study the connection between the thermal pressure and the radiation field strength and the star formation activity. We compare our results with the predictions from the models by Wolfire et al. (2003) and Ostriker et al. (2010). This chapter is in preparation to be submitted to *The Astrophysical Journal*.

Chapter 2

Dust-to-Gas Ratio in the Extremely Metal-Poor Galaxy I Zw 18

2.1 Introduction

The link between dust-to-gas mass ratio (DGR) and heavy element abundance (metallicity) in galaxies remains an open issue (e.g, Edmunds 2001; Hunt et al. 2005; Lisenfeld & Ferrara 1998). Specifically, in very low metallicity systems ($12 + \log(\text{O}/\text{H}) \lesssim 8$) it is unclear how the DGR scales with metallicity. Models considering dust destruction by supernovae (Hirashita et al. 2002) or mass outflows from the galaxy (Lisenfeld & Ferrara 1998) predict a nonlinear relation. On the other hand, if the fraction of metals incorporated in the dust is constant (James et al. 2002), we expect a linear relation between DGR and metallicity, in a sense that the ratio decreases as metallicity decreases. Measurements of DGRs over a range of metallicity are necessary to better constrain this relationship.

The blue compact dwarf galaxy I Zw 18 has one of the lowest nebular metallicities measured to date. Skillman & Kennicutt (1993) measure an oxygen abundance of $12+\log(\text{O}/\text{H}) = 7.17$. This is 3.2% of the solar abundance (using the scale of Asplund et al. 2009). Most local universe galaxies have $12+\log(\text{O}/\text{H}) \sim 8.5$ (e.g., Moustakas et al. 2010, for SINGS), and the Milky Way has $12+\log(\text{O}/\text{H}) \sim 8.7$ (Baumgartner & Mushotzky 2006). I Zw 18 therefore represents the extreme low end of the metallicity range in the local universe and is thus a key datum for understanding the relationship between DGR and metallicity.

The dust mass of I Zw 18 is poorly known. Typical galaxies of similar morphology (blue compact dwarfs) have dust masses that range between $10^3 - 10^5 M_{\odot}$, with DGR ranging between $10^{-3} - 10^{-5}$ (Lisenfeld & Ferrara 1998). Using $\text{H}\alpha/\text{H}\beta$ flux ratios as a dust tracer, Cannon et al. (2002) find a total dust mass for I Zw 18 of $\sim 7 - 10 \times 10^3 M_{\odot}$ ¹ by assuming a linear scaling between DGR and metallicity (as measured by O/H). Engelbracht et al. (2008), using *Spitzer* data limited by a non-detection at $160 \mu\text{m}$, measure an upper limit for the dust mass of $4.2 \times 10^4 M_{\odot}$. A more recent study of a large sample by Galametz et al. (2011) uses previously published *Spitzer* and SCUBA data to constrain the dust mass of I Zw 18 to be $\lesssim 1.1 \times 10^5 M_{\odot}$ and the DGR to $\lesssim 4.5 \times 10^{-4}$.

I Zw 18 contains intense radiation fields stemming from active star formation. It therefore provides a nearby testing ground to probe the physics of distant primeval sources. Previous studies using *Spitzer* (Engelbracht et al. 2008; Wu et al. 2007) show that its continuum emission from 15 to $70 \mu\text{m}$ has a slope characteristic of a starburst galaxy of solar abundance. Moreover, its mid-infrared spectrum from

¹We scale Cannon et al. (2002) and Engelbracht et al. (2008) result by a factor of $(18.2/12.6)^2$ and Galametz et al. (2011) result by a factor of $(18.2/13)^2$ to account for the differences in assumed distances. We note that our final result, the DGR, is distance independent.

5 to 36 μm shows no detectable emission from polycyclic aromatic hydrocarbons (PAHs). Such low abundance of PAHs is likely the consequence of a high radiation field in combination with the low metallicity of the source.

In this paper we estimate the DGR for I Zw 18. We use previously unpublished *Spitzer Space Telescope* and archival *Herschel Space Observatory*² continuum observations, combined with dust emission models and a gas mass (van Zee et al. 1998) to constrain the radiation field intensity, temperature, dust mass and DGR in I Zw 18. Throughout this paper we assume a distance of 18.2 Mpc (Aloisi et al. 2007). Revisions to this distance will affect our dust and gas masses, but not the DGR.

2.2 Methods

2.2.1 Observations

We use a variety of data from several different facilities to map the far infrared, sub millimeter, millimeter and radio wave emission of I Zw 18. Therefore our data set uses the following observatories and instruments: *Spitzer* Multiband Imaging Spectrometer (MIPS, Rieke et al. 2004); *Herschel* Photodetector Array Camera and Spectrometer (PACS, Poglitsch et al. 2010); *Herschel* Spectral and Photometric Imaging Receiver (SPIRE, Griffin et al. 2010); IRAM Plateau de Bure Interferometer (PdBI) and Very Large Array (VLA). In this section we will briefly describe new observations.

Spitzer: We observed I Zw 18 at 70 and 160 μm using MIPS in photometry mode as part of a cycle 5 proposal (P.I. A. Bolatto, AOR: 22369536). The total

²Herschel is an ESA space observatory with science instruments provided by European-led Principal Investigator consortia and with important participation from NASA.

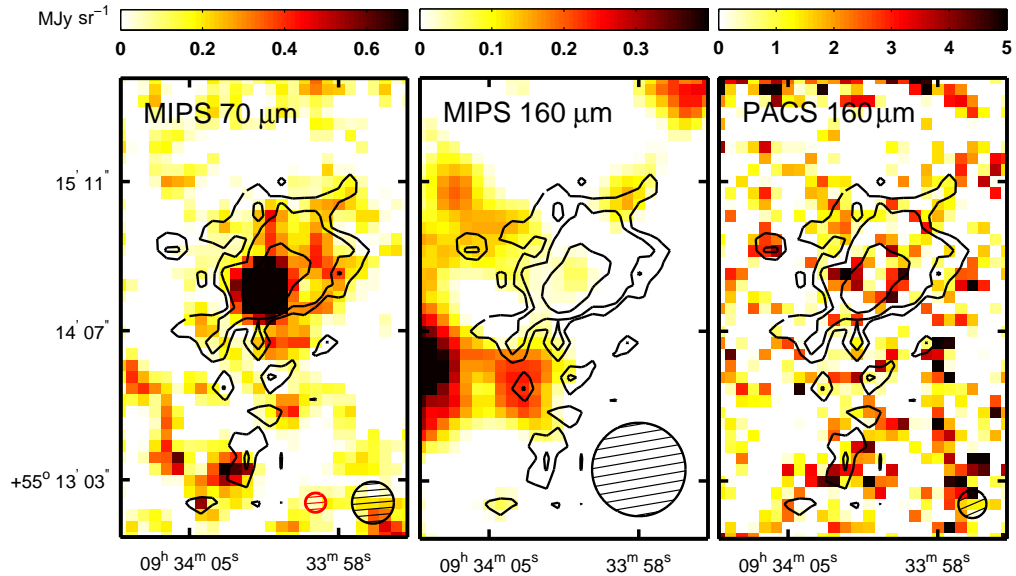


Figure 2.1: The left two panels show the *Spitzer* images of I Zw 18 at 70 and 160 μm . The right panel shows the *Herschel* PACS image at 160 μm . Overlaid as black contours is the HI column density distribution from van Zee et al. (1998) using the VLA. The contours are 0.7, 1.4 and $5 \times 10^{20} \text{ cm}^{-2}$. The black circle in the bottom right corner of each panel corresponds to the respective beam size of the FIR observations. The smaller circle in the first panel corresponds to the beam size of the HI observations. At 70 μm , the bulk of the emission coincides with the HI contours and the diffuse emission extends preferentially towards the NW. I Zw 18 is undetected in both 160 μm maps.

observation time was 8 hours. The reduction of these images very closely follows the procedure described in Gordon et al. (2007) and Stansberry et al. (2007) for the 70 and 160 μm map respectively.

***Herschel*/PACS:** We use archival 70 and 160 μm observations from *Herschel*. The observations were taken with PACS using the Large Scan Map mode as part of the *Herschel* Guaranteed Time Key Program, Dwarf Galaxy Survey (P.I. S. Madden, obs. ID: 1342187135/36). The scan maps were taken at 90° angles from one another at the medium scan speed ($20'' \text{ s}^{-1}$) and then combined together in order to reduce the noise caused by streaking along the scan direction. The scan leg length is 4.0' and the total on source time for the combined images was 192 s.

Unlike *Spitzer* data, the methods to reduce PACS data are still evolving significantly. Therefore, we reduce the data in two separate ways. We first use Herschel Interactive Processing Environment (HIPE) v4.2 with the standard pipeline scripts. We also process the data up to level 1 in HIPE v7. We use the standard pipeline, which includes pixel flagging, flux density conversion, and sky coordinate association for each pixel of the detector. At this stage, the PACS timelines are still affected by $1/f$ noise and baseline drifts. In order to subtract the baseline, remove glitches, and project the timelines on the final map, we applied the scanamorphos algorithm (Roussel 2012) to the level-1 PACS timelines.

Herschel/SPIRE: We use archival *Herschel* Spectral and Photometric Imaging Receiver (SPIRE; Griffin et al. 2010) photometric observations at 250, 350, and 500 μm . Observations were made in the large map mode with the nominal scan speed of 30 arcsec s^{-1} and the cross-scanning method as part of *Herschel* Science Demonstration Phase (PI: S. Madden; obs. ID 1342188663). Data reprocessing was carried out in HIPE using the standard large map pipeline with the latest SPIRE calibration tree available³ which includes deglitching the timeline data, flux calibration and various corrections. After removal of a linear baseline, images were made using the standard naive mapper. The final maps are in units Jy beam^{-1} with pixel scales of 6, 10 and 14 arcsec at 250, 350 and 500 μm , respectively as described in the SPIRE Data Reduction Guide.

PdBI: We present new observations of the CO $J = 1 \rightarrow 0$ transition in I Zw 18 using the IRAM Plateau de Bure Interferometer as project t027 (P.I. A. Leroy). The data were observed on 24, 27, and 28 September 2009 using the "5Dq" configuration, meaning that 5 telescopes were operational and that the array was in a compact configuration. They data is calibrated in the standard way in December 2009 using

³We used HIPE 8.1 and the SPIRE calibration tree v. 8.1.

the PdBI pipeline implemented in the CLIC and MAPPING packages of GILDAS. The effective time on source was 12.5 hours after flagging during the pipeline run. The effective bandwidth was ~ 850 MHz, or about 2200 km s^{-1} with native resolution ~ 2.5 MHz (6.5 km s^{-1}). We do not detect CO emission. At 26 km s^{-1} velocity resolution we achieved an RMS noise of $1.26 \text{ mJy beam}^{-1}$, implying a 4σ flux upper limit for a point source of $0.131 \text{ Jy km s}^{-1}$.

VLA: The observations used to construct the HI map are described in van Zee et al. (1998). We obtained two hours of Rapid Response 21 cm VLA observations (project 08B-246; P.I. A. Bolatto) to evaluate the Galactic foreground contribution. This contribution can be estimated by measuring the HI column density toward I Zw 18 and convert it to dust emission using typical high-latitude Galactic ratios (e.g, Boulanger et al. 1996). The observations were obtained during the move between CnD and D configuration with a synthesized beam size of $67'' \times 41''$, and a native resolution of 6.1 kHz (1.3 km s^{-1}). Data was reduced in AIPS using the standard procedure and calibrations, and care was taken to remove the baselines affected by the frequency aliasing problems due to the VLA-JVLA transition. At 10.3 km s^{-1} velocity resolution we achieved an RMS noise of $1.1 \text{ mJy beam}^{-1}$, implying an HI column density of $N_{\text{HI}} = 2.4 \times 10^{18} \text{ cm}^{-2}$. Galactic neutral hydrogen emission was observed in the central 30 km s^{-1} of the passband. Nonetheless, even after spatially filtering the $160 \mu\text{m}$ MIPS map to approximately match the uv coverage of the VLA the correlation between the high resolution HI column density and the $160 \mu\text{m}$ surface brightness remained extremely low (Fig. 2.2) , showing that most of the emission present in the 160 and $250 \mu\text{m}$ images is not due to the high-latitude Galactic foreground.

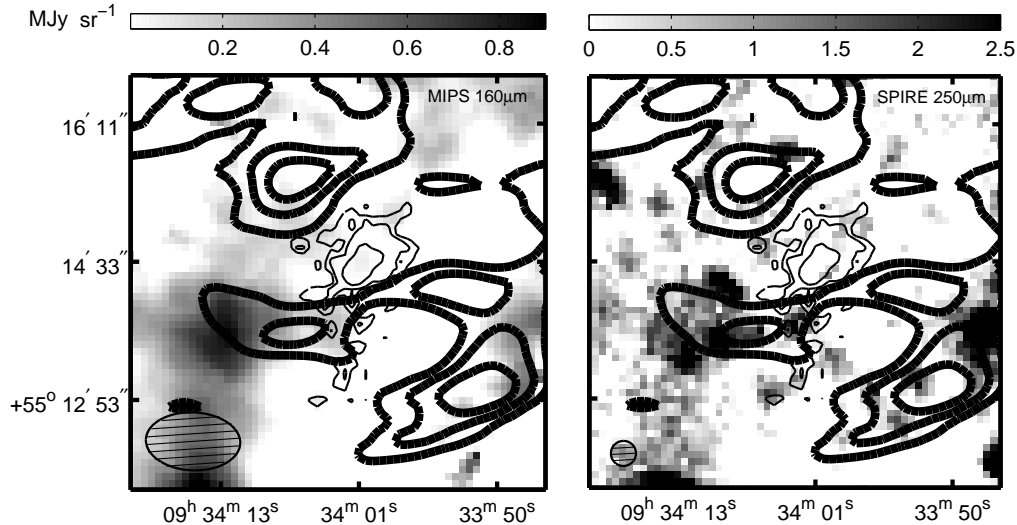


Figure 2.2: *Spitzer* 160 μm (left) and *Herschel* 250 μm (right) maps of a $\sim 5 \times 5$ arcmin field around I Zw 18. The thick black contours show the VLA observations of the Galactic HI foreground emission at 2, 4 and 6σ significance level. The thin black contours are the same as shown in Fig. 2.1. The VLA beam size is $\theta = 67.3'' \times 41.3''$ and is shown in the corner of the left panel. The SPIRE 250 μm beam is shown in the right panel. The bulk of the 160 μm emission, located south-east of our object, fragments into at least three point sources in the 250 μm map, which has better spatial resolution. There is no correlation between the far infrared and the Galactic HI foreground emission, suggesting that the confusion is dominated by background galaxies.

2.2.2 Photometry

In Fig. 2.1 we present the *Spitzer* MIPS 70 and 160 μm maps and the *Herschel* PACS 160 μm image for I Zw 18. Overlaid on each image is the HI column density distribution observed by van Zee et al. (1998). The HI contours correspond to 0.7, 1.4 and $5 \times 10^{20} \text{ cm}^{-2}$ enclosing 98, 96 and 78% of the total flux at 70 μm . We use the MIPS 70 μm map over the PACS 70 μm because it has a much better surface brightness sensitivity (0.17 versus 2.87 MJy sr^{-1}), yielding a better signal to noise. The bulk of the 70 μm emission coincides with the HI column density maximum. This peak also coincides with the location of active star forming regions observed by Cannon et al. (2002) using the *Hubble Space Telescope* (HST). The

diffuse component at $70\ \mu\text{m}$ extends preferentially ~ 3 kpc north-west from the peak. We subtract the background emission measured in a region free of sources. We integrate the flux using a circular aperture with radius of $45''$ centered at the peak of the $70\ \mu\text{m}$ emission and applying an aperture correction factor of 1.13 (determined by integrating over the point spread function and compatible with those in the MIPS Instrument Handbook). The calibration error on *Spitzer* is about 5% at $70\ \mu\text{m}$. We estimate a photometry error of 1.7 mJy by adding in quadrature the calibration uncertainty and the background noise. We measure a total flux density of 33.6 ± 1.7 mJy at $70\ \mu\text{m}$. Our flux value is consistent with the $70\ \mu\text{m}$ flux measured by Engelbracht et al. (2008) of 34.9 ± 4.79 mJy.

The *Spitzer* $160\ \mu\text{m}$ map is confusion-limited. The bulk of the emission is associated with sources outside the HI emitting region of I Zw 18. Although the Galactic latitude of I Zw 18 is $\sim 44^\circ$, it could be possible that a significant source of confusion were Galactic cirrus. We use the VLA HI observations to explore this possibility. Fig. 2.2 shows the MIPS $160\ \mu\text{m}$ and the SPIRE $250\ \mu\text{m}$ map of a $\sim 5 \times 5$ arcmin field around I Zw 18. The thick lines represent the HI foreground emission from VLA. The thin lines represent the HI emission of I Zw 18. It is clear from visual inspection that the maxima of the HI foreground and the $160\ \mu\text{m}$ and $250\ \mu\text{m}$ emission are not coincident. We find a Pearson correlation coefficient close to zero. In most of the *Spitzer* confusion-limited images at $160\ \mu\text{m}$ the confusion is mainly due to faint unresolved background sources (Dole et al. 2004). The bulk of the $160\ \mu\text{m}$ emission, located south-east of our object, fragments into at least three point sources in the $250\ \mu\text{m}$ map, which has finer spatial resolution. The $160\ \mu\text{m}$ peak also coincides with several background galaxies in deep *B* and *R*-band images (S. Janowiecki, private communication). The difference between the 160 and $250\ \mu\text{m}$ maps is consistent with what one would observe if the peak of the emission at $160\ \mu\text{m}$ is associated

with background galaxies.

The background contamination and the absence of correlation between the 160/250 μm emission and the HI foreground emission makes it impossible to recover the flux associated with I Zw 18. Thus, we use an annular sector around the galaxy to measure a one-sigma surface brightness sensitivity of 0.18 mJy sr^{-1} that includes the effects of confusion. We estimate the flux upper limit multiplying this value by the area associated with the 1.4×10^{20} atoms cm^{-2} HI contour that encloses 96% of the 70 μm flux and 62% of the HI mass. To find the aperture correction factor associated to this area, we can approximate the contour using a circular aperture of 48'' radius. This corresponds to an aperture correction factor of 1.6 at 160 μm . After applying the aperture correction factor, we obtain a corresponding 3σ flux upper limit of 40.5 mJy. This new upper limit is a factor of ~ 2 lower than the previous upper limit published by Engelbracht et al. (2008).

The *Herschel* PACS image at 160 μm also fails to detect I Zw 18. In this case, however, the image is not confusion-limited. The 1σ surface brightness sensitivity is 1.8 MJy sr^{-1} . If we assume that the emission from I Zw 18 is compact on 12'' scales, the corresponding 3σ flux upper limit integrating over the 12'' beam and applying an aperture correction factor of 1.32 is 27.2 mJy.

We will work with the PACS 160 μm flux upper limit of 27.2 mJy for the rest of the paper. However, the upper limit measured from the PACS data relies upon the assumption that the source is compact. If the 160 μm emission is significantly extended over scales larger than 12'' (~ 1 kpc), it may be more appropriate to use the MIPS 160 μm upper limit of 40.5 mJy.

Finally, the SPIRE maps at 250, 350 and 500 μm show no detection of I Zw 18. From these images we measure a surface brightness sensitivity using an annular sector around the source. We then apply aperture corrections and point source color

corrections assuming $\beta = 1.5$ (β in $f_\nu \propto \nu^\beta$) described in the SPIRE Photometry Cookbook (Bendo, G. J. and the SPIRE-ICC, 2011) We measure 3σ flux upper limits of 22.2, 23.9 and 25.4 mJy at 250, 350 and 500 μm , respectively.

2.3 Results

2.3.1 Dust Mass

We use two methods to estimate the dust mass of I Zw 18. In the first, we follow the procedure outlined by Hildebrand (1983), assuming an idealized graybody source with a single temperature. In the second one we use the Draine & Li (2007) (DL07) model. The main difference between the DL07 model and the idealized graybody is that DL07 assumes a grain size distribution that reproduces the observed wavelength-dependence extinction in the Milky Way, and consequently a distribution of temperatures. Given the extreme nature of I Zw 18, it is not clear that either model is exactly applicable. Nonetheless, we used them so we can make a consistent comparison to larger samples of galaxies.

Modified Blackbody Model

For an idealized cloud, the dust mass is estimated by fitting its far infrared spectrum as the product of a blackbody spectrum ($B_{\lambda,T}$) and a mass absorption coefficient (κ_λ). The absorption coefficient varies with wavelength as the negative power of the grain emissivity index ($\kappa_\lambda \propto \lambda^{-\beta}$, where β represents the emissivity index). Then, for a cloud that is optically thick to starlight and optically thin to far infrared emission, the dust mass M_{Dust} is given by the following expression:

$$M_{Dust} = \frac{F_\lambda D^2}{\kappa_\lambda B_{\lambda,T}} \quad , \quad (2.1)$$

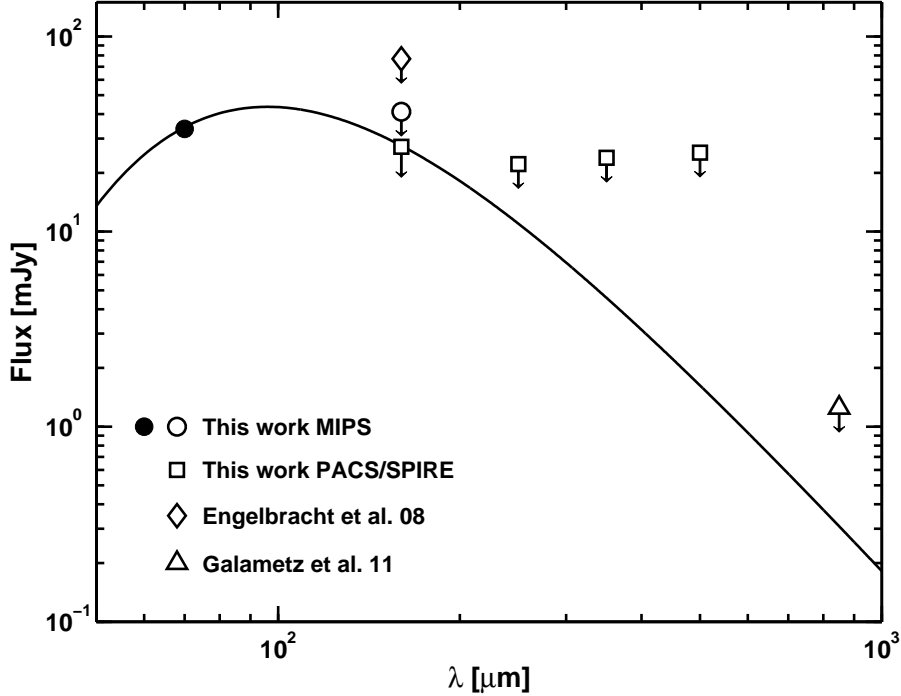


Figure 2.3: A Infrared SED of I Zw 18. Open symbols represent 3σ upper limits. The circles show the new MIPS data. The squares show the PACS and SPIRE data. The open diamond and triangle at 160 and 850 μm corresponds to upper limits estimated by Engelbracht et al. (2008) and Galamez et al. (2011) respectively. The solid line corresponds to the modified blackbody fit to the MIPS 70 μm detection and the PACS 160 μm upper limit.

where D is the distance to the galaxy, F_λ is the observed flux and $B_{\lambda,T}$ is the blackbody intensity. The flux at any point on a graybody spectrum is $F_\lambda \propto B_{\lambda,T} \lambda^{-\beta}$, with β independent of wavelength. Therefore, we can solve for the color temperature ($T_{70/160}$) using the ratio F_{70} / F_{160} .

Measured values for κ_λ at 250 μm (κ_{250}) span the range $\approx 5-15 \text{ cm}^2 \text{ g}^{-1}$ (Alton et al. 2004), and commonly used values for β are 1 – 2 depending on the environment. For this work we adopt $\kappa_{250} = 9.5 \text{ cm}^2 \text{ g}^{-1}$ and $\beta = 1.5$; these are commonly used values for low metallicity galaxies (e.g. Leroy et al. 2007a). Using $\beta = 1$ or 2 changes our dust mass limits by $\sim 10\%$.

Fig. 2.3 shows the spectral energy distribution (SED) of I Zw 18. The source

is only detected at 70 μm . At longer wavelengths each point corresponds to a 3σ flux upper limits. Among these limits, the 160 μm upper limit represents the strongest constraint on the I Zw 18 SED. Thus, based on the 70 and 160 μm emission, the modified blackbody spectrum model constrains the dust temperature to be $T_{70/160} > 33.7$ K. This translates into a predicted 850 μm flux of 0.28 mJy, compatible with the observed upper limit of 1.25 mJy (Galametz et al. 2011). Combining our temperature lower limit with the 70 μm flux, Eq. 2.1 yields a dust mass of $M_{Dust} < 3.2 \times 10^3 M_{\odot}$. If we use the MIPS 160 μm upper limit instead of the PACS upper limit, we measure a temperature limit $T_{70/160} > 29.8$ K and a dust mass a factor of ~ 2 higher, i.e., $M_{Dust} < 6.9 \times 10^3 M_{\odot}$.

Draine & Li Model

For a detailed description we refer to DL07 and Draine et al. (2007). Essentially, DL07 models characterize the dust as a mixture of carbonaceous and amorphous silicate grains with size distributions chosen to match the observed extinction in the Milky Way. To characterize the intensity of the radiation that is heating the dust, the model adopts the spectrum of the local interstellar radiation field (this may not be a good approximation for I Zw 18, a starburst system characterized by high intensity radiation fields and low metallicity). In DL07, most dust is heated by the interstellar radiation field, and a small fraction is heated by stronger radiation fields associated with star formation.

We caution the reader that estimating dust masses based on broadband infrared fluxes, as we do here, is a poorly constrained technique; there are very few data points compared to the number of parameters in the model. The DL07 model uses five parameters to characterize the emission from dust in galaxies: M_{Dust} , U_{min} , U_{max} , γ , and α . The dust mass is represented by M_{Dust} . U_{min} represents the

interstellar radiation field heating the diffuse ISM, and U_{max} represents the upper limit on the interstellar radiation field. The starlight heating the dust is described using the dimensionless parameter U , that by definition is always between U_{min} and U_{max} . The value $U = 1$ is the local interstellar radiation in the Milky Way. The parameter γ represents the fraction of gas that is exposed to strong radiation fields with intensities in the range $U_{min} < U < U_{max}$. Finally, α characterizes the distribution of starlight intensities. In practice we fix two of these parameters, α and U_{max} . We adopt the values set by Draine & Li (2007) of $U_{max} = 10^6$ and $\alpha = 2$. Therefore three parameters are free in the model (M_{Dust} , U_{min} , and γ). We remind the reader that we constrain this model with only four broadband fluxes, at 8, 24, 70 and 160 μm . We can also use the returned values of these parameters to calculate a temperature for the majority of the dust grains (T_{Umin}), the fraction of dust luminosity that originates in photon dominated regions (f_{PDR}), and the dust-weighted mean starlight intensity ($\langle U \rangle$).

Muñoz-Mateos et al. (2009a) derived empirical fits relating a grid of DL07 emission model outputs to the *Spitzer* fluxes. In particular, the DL07 parameters M_{Dust} , γ , $\langle U \rangle$, and f_{PDR} can all be derived using measurements at 8, 24, 70 and 160 μm . We can calculate U_{min} using $\langle U \rangle$ and γ according to Eq. (33) in DL07. For the I Zw 18 fluxes at 8 and 24 μm we used the values measured by Engelbracht et al. (2008) of 0.47 and 6.28 mJy respectively. The agreement between the dust mass derived using the empirical fits and DL07 models is very good, with a scatter of about 9% and an offset of +5%. The DL07 dust masses are strongly dependent on $R_{70} \equiv \langle \nu F_\nu \rangle_{70} / \langle \nu F_\nu \rangle_{160}$, with $M_{Dust} \propto R_{70}^{-1.8}$. R_{70} is sensitive to the temperature of the largest grains dominating the FIR emission, and any new constraint or detection at 160 μm will strongly affect the resulting dust mass. Essentially, the smaller the 160 μm flux, the hotter the temperature and thus the less dust is needed to produce

Table 2.1: Derived dust properties based on the DL07 model

Object	M_{Dust} (M_{\odot})	U_{min}	$\langle U \rangle$	γ (%)	f_{PDR} (%)	$T_{U_{min}}$ (K)
I Zw 18	$< 1.1 \times 10^4$	> 8.8	> 21.1	> 13.1	> 48.9	> 24.4
Mrk 33	2.9×10^6	4.0	14.3	11.8	47.6	21.4
Tol 89	2.8×10^6	2.0	3.6	6.4	33.2	19.1
NGC 3049	5.5×10^6	3.0	5.1	6.1	32.6	20.4
SINGS ^a	1.5×10^7	1.5	1.7	0.9	7.8	18.2

^a

Median values for 48 SINGS galaxies (Table 5, Draine et al. 2007)

the observed 70 μm emission.

The derived dust properties for I Zw 18 are summarized in Table 2.1. Median values for 48 SINGS galaxies analyzed by Draine et al. (2007) and three starburst system out of the same sample are included for comparison. The lower limits obtained for U_{min} , $\langle U \rangle$, γ and f_{PDR} in I Zw 18 are high compared to the mean values in the SINGS sample (Draine et al. 2007). The high radiation intensity environment of I Zw 18 is comparable to starbursting systems like Mrk 33, Tol 89 and NGC 3049, as also found by Wu et al. (2007). We find that the DL07 model yields a mass upper limit of $M_{Dust} < 1.1 \times 10^4 M_{\odot}$. Just like the modified blackbody case, if we use the MIPS 160 μm upper limit instead of the PACS upper limit, we measure a dust mass a factor of ~ 2 higher, i.e., $M_{Dust} < 2.6 \times 10^4 M_{\odot}$.

2.3.2 Comparison of Dust Masses

The DL07 dust mass upper limit is a factor ~ 3.5 larger than the dust mass estimated using the modified blackbody model. DL07 model treats dust emission as an ensemble of dust grains at different temperatures that includes larger masses of dust at colder temperatures than what is predicted by the single temperature fit. Therefore, it is not surprising that this model generates a higher dust mass than

the modified blackbody model. However, the fact that these two measurements are not extremely different increases our confidence in the dust mass limit, which we conservatively take to be that resulting from the DL07 model.

It is interesting to compare this result to other modeling efforts for I Zw 18 and low metallicity galaxies. In particular, Galametz et al. (2011) determine dust masses in a large sample of galaxies with literature data, using full spectral energy distribution modelling based on the Zubko et al. (2004) grain model. They find that the inclusion of submm-wave data tends to drive dusty galaxies toward lower dust masses, while for low metallicity galaxies the inclusion of submm-wave constraints yields higher dust mass predictions than those from far-infrared alone. By contrast Draine et al. (2007) found their masses to be robust to the inclusion of submm-wave data. This is in part driven by modeling choices, in particular the inclusion of a minimum radiation field or the interpretation of submm-wave excess (Bot et al. 2010; Israel et al. 2010) as caused by cold dust. The latter appears to be associated with low metallicities, and although recent studies suggest that it is not caused by cold dust (Galliano et al. 2011), it remains a large systematic uncertainty in dust mass determinations. Also note that for dwarf galaxies the SCUBA data included by Galametz et al. 2011 is much deeper than the data used by Draine et al. 2007. Observational biases and limitations have a non negligible impact on the interpretation of the observed trends in dust-to-gas ratio versus metallicity.

Galametz et al. (2011) use a $160 \mu\text{m}$ flux upper limit of 76.8 mJy (Engelbracht et al. 2008). For submm-wave data they use a $850 \mu\text{m}$ flux upper limit of 1.25 mJy (Galliano et al. 2008). They measure an upper limit to the dust mass of $1.1 \times 10^5 M_{\odot}$ scaled to our adopted distance. Our dust mass upper limit is an order of magnitude smaller than that of Galametz et al. (2011). Using the DL07 model and the data in Galametz et al. (2011) we would obtain an upper limit of $1.0 \times 10^5 M_{\odot}$. This is

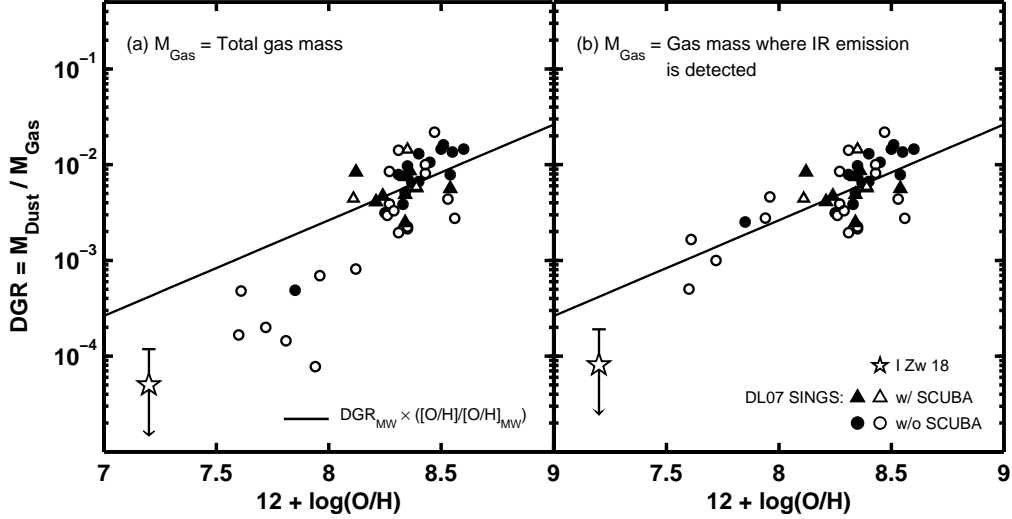


Figure 2.4: Dust-to-gas mass ratio is shown as a function of oxygen abundance. Open symbols correspond to upper limits (3σ). I Zw 18 DGR is measured based on the PACS $160\ \mu\text{m}$ flux upper-limit and is shown as an open star. The upper error bar corresponds to the value of the DGR if estimated based on the MIPS $160\ \mu\text{m}$ flux (3σ) upper-limit. Circles and triangles correspond to SINGS galaxies with and without SCUBA fluxes, respectively. The dust and gas mass values are from Tables 4 and 5 in Draine et al. (2007). The values in the left panel represent the global DGR when estimated using the total gas mass of the galaxy. The right panel shows the DGR values when they are estimated “locally”, using only the gas mass in the region where the IR emission is detected. The solid line shows a linear scaling between DGR and metallicity normalized to match the Milky Way values (eq. 13, Draine et al. 2007).

nearly equivalent to the dust mass Galametz et al. (2011) finds, highlighting the fact that the mass limits are likely reasonably robust to the choice of models. Therefore, our lower dust mass limit is due to the tighter flux limits at $160\ \mu\text{m}$.

2.3.3 Gas Mass

The total HI mass of I Zw 18 is $M_{\text{HI}} = 2.3 \times 10^8 M_{\odot}$ (van Zee et al. 1998). The molecular content of I Zw 18, however, remains unknown since no CO emission has been detected. Our new upper limit on the CO $J = 1 \rightarrow 0$ luminosity of I Zw 18 is $L_{\text{CO}} \leq 10^5 \text{ K km s}^{-1} \text{ pc}^2$ (4σ), which corresponds to $M_{\text{H}_2} \leq 450,000 M_{\odot}$ for

a standard conversion factor ($\alpha_{CO} = 4.5 M_{\odot} (\text{K km s}^{-1} \text{ pc}^2)^{-1}$). Note that our luminosity is similar to that quoted by Leroy et al. (2007b) because we adopt here a larger distance (for matched smoothing and assumptions we improve the sensitivity of that study by a factor of 2). Using this Milky Way based conversion factor, M_{H_2} is at most 0.2% of the total gas mass.

There is no reason to expect that the Milky Way based conversion factor between CO luminosity and H_2 mass applies to low metallicity galaxies like I Zw 18. In the Local Group, α_{CO} is a strong function of metallicity (Leroy et al. 2011). Genzel et al. (2012) derive a correlation between oxygen abundance and conversion factor, α_{CO} . Applying their formula to a galaxy with the metallicity of I Zw 18, we find a conversion factor $\alpha_{CO} \approx 477.5 M_{\odot} (\text{K km s}^{-1} \text{ pc}^2)^{-1}$. This factor is ~ 100 times larger than α_{CO} in a typical spiral galaxy. Using this conversion factor we calculate a molecular gas mass upper limit of $M_{\text{H}_2} \leq 4.8 \times 10^7 M_{\odot}$. This M_{H_2} is $\sim 20\%$ of the total gas mass.

There is some evidence that, at low metallicities, the star formation activity may be a better indicator of the molecular mass than the CO emission (Bolatto et al. 2011; Krumholz et al. 2011; Schruba et al. 2011). The $\text{H}\alpha$ flux of I Zw 18 suggests a recent star formation rate (SFR) of $\sim 0.1 M_{\odot} \text{ yr}^{-1}$. In large star-forming galaxies, a typical H_2 -to-SFR ratio (H_2 depletion time) is $\sim 1 - 2$ Gyr (Bigiel et al. 2011). The H_2 mass corresponding to this amount of star formation in such a galaxy would thus be $\sim 10^8 M_{\odot}$. Given the level at which star formation obviously dominates the morphology and ISM conditions in I Zw 18 we strongly suspect that this kind of equilibrium assumption very much overestimates the H_2 , which will have been dissociated or otherwise destroyed by the recent burst. Nonetheless, even in this limit the H_2 only makes up $\sim 30\%$ of the integrated gas mass. The similarity with the results obtained from applying the Genzel et al. (2012) correlation is not

surprising, since the underlying assumption is the same. Because of its uncertainty, we do not include the H_2 correction in the following calculations.

2.3.4 Dust-to-Gas Mass Ratio and Metallicity

Draine et al. (2007) finds that the DGR changes significantly depending on whether the dust mass is compared to the total gas mass or only the gas mass enclosed in the aperture where the infrared emission is measured. For example, IC 2574 (a dwarf galaxy in the SINGS sample), only 19% of the HI gas mass is enclosed in the area where the infrared emission is detected (Walter et al. 2007). We take the point of view that these are two valid definitions of the DGR: global, or local where the dust emission is detected. Using the total HI mass from van Zee et al. (1998), we measure an upper limit for the global DGR $\lesssim 5 \times 10^{-5}$. Using instead the HI mass enclosed in the area where we measure the $160 \mu\text{m}$ flux upper limit (62% of the total HI mass), yields a local DGR $\lesssim 8.1 \times 10^{-5}$.

Figure 2.4 shows the DGR as a function of oxygen abundance for I Zw 18 and a subsample of SINGS galaxies. Open symbols indicate 3σ upper limits. The solid line represents a linear scaling of the DGR with metallicity. This linear relation assumes that the abundances of all heavy elements are proportional to the oxygen abundance and that the same fraction of all heavy elements are in solid form as in the Milky Way (Draine et al. 2007). The I Zw 18 DGR upper limit is primarily driven by the upper limit in the dust mass, while in the SINGS galaxies the upper limits are due to lower limits in the gas mass (due to the non inclusion of H_2). As we discussed in Section 3.1, we obtain different dust masses for I Zw 18 depending on the assumption we make about the distribution of the $160 \mu\text{m}$ emission (point-like with PACS and extended with MIPS). The open star shows the DGR of I Zw 18 when we assume point-like emission, while the upper limit of the bar shows the DGR

when we assume extended emission. For the SINGS galaxies, the dust and gas masses are from Draine et al. (2007) and the metallicities are from Moustakas et al. (2010). Note that Draine et al. (2007) computes molecular gas masses assuming a fixed X_{CO} factor of $4 \times 10^{20} \text{ cm}^{-2} (\text{K km s}^{-1})^{-1}$ following (Blitz et al. 2007). We show SINGS galaxies with and without measured SCUBA fluxes as triangles and circles respectively, as Draine et al. (2007) find that the dust mass estimates with and without SCUBA data can differ by a factor of ~ 2 .

The left panel of Figure 2.4 shows the global DGR, estimated using the total gas masses. The right panel shows how the DGR changes when estimating it locally in low metallicity systems, including I Zw 18, by using the gas mass enclosed in the region where the infrared emission is detected. For SINGS galaxies with metallicities $12 + \log(\text{O}/\text{H}) \gtrsim 8.1$, the total DGR seems to agree within a factor of ~ 2 with a linear relationship between DGR and metallicity. Low metallicity galaxies do not seem to follow the same linear correlation that includes the Milky Way DGR. The I Zw 18 global DGR falls below the linear scaling by a factor of ~ 8 . The right panel of Figure 2.4 shows the local DGR. The DGRs of the SINGS low metallicity systems scale up and appear consistent with the linear relationship within a factor of ~ 2 , although most of the low metallicity points are only upper limits. For I Zw 18, however, the local DGR falls below the linear scaling by a factor of ~ 5 . Therefore, our dust mass limits for I Zw 18 suggest a breakdown of the linear relationship between DGR and metallicity at very low metallicities. Note further that, at least in terms of the global DGR, I Zw 18 seems to continue the trend found for other low metallicity galaxies.

We show in Fig. 2.4 that only one of the seven SINGS galaxies with $12 + \log(\text{O}/\text{H}) \lesssim 8.1$ has a DGR that is not an upper limit. It may be possible that the local DGR of this system is higher than other low metallicity galaxies and the trend is really steeper

than linear, as our result for I Zw 18 and other studies suggest (Lisenfeld & Ferrara 1998; Muñoz-Mateos et al. 2009a). Clearly more work is needed to determine, robustly, whether low metallicity galaxies do or do not follow the linear scaling shown in Fig. 2.4.

Note that the abundance of oxygen may not be the correct abundance to refer to. Indeed, the abundances of refractory elements that constitute the bulk of the dust such as carbon or silicon are likely more relevant to establishing the DGR. Garnett et al. (1999), for example, find a trend of increasing C/O with O/H for a sample of irregular and spiral galaxies observed with HST. This could suggest that the nonlinear trend of DGR with metallicity is really an artifact of using O/H as a proxy for metallicity, and the relation could become more nearly linear when plotted against C/H. Garnett et al. (1999) find a gas-phase abundance of C in I Zw 18 that is significantly higher than that predicted by the extrapolation of the observed C/O vs. O/H trend in low metallicity irregular galaxies. In fact, C/O in I Zw 18 is only 0.3 dex lower than Solar. This is barely enough to reconcile our limits on the local DGR with a linear trend with C/H, and probably not enough to explain our low global DGR, but it certainly goes in the right direction.

2.4 Conclusions

In this work we study I Zw 18 using data from *Spitzer*, *Herschel Space Telescope* and IRAM Plateau de Bure Interferometer. We reduce the flux upper limit at 160 μm by a factor of ~ 3 and the CO $J = 1 \rightarrow 0$ flux upper limit by a factor of ~ 2 compared to previous measurements. Combining these observations with the dust emission model from Draine & Li (2007), we constrain the dust mass to be $M_{dust} < 1.1 \times 10^4 M_{\odot}$. We note that any dust mass measurement relies on

assumptions about the mass emissivity of dust grains in the interstellar medium, with the important associated systematic uncertainties. We find a global dust-to-gas mass ratio of $M_{dust}/M_{gas} < 5.0 \times 10^{-5}$, while the ratio measured in regions where the 70 μm emission peaks is $M_{dust}/M_{gas} < 8.1 \times 10^{-5}$.

These measurements are suggestive that low metallicity galaxies do not follow the same linear relationship between metallicity and DGR as typical local spirals. At face value our DGR upper limit is inconsistent with the hypothesis that the fraction of heavy elements incorporated into dust is the same in high metallicity galaxies (such as the Milky Way) and in extremely low metallicity galaxies (such as I Zw 18). There are other scenarios, however, that can produce a break or non-linear power-law relationship between DGR and metallicity. For instance, models that include more detailed physical processes such as the production and destruction of dust by supernovae, removal of dust through outflows from galaxies, and dust production in the envelopes of stars (e.g, Edmunds 2001; Hirashita et al. 2002; Lisensfeld & Ferrara 1998) may yield non-linear relations. Much more work is needed with sensitive maps of low metallicity galaxies, like I Zw 18, to better understand the relationship between DGR and metallicity.

Chapter 3

[CII] 158 μm Emission as a Star

Formation Tracer

3.1 Introduction

The [C II] 157.74 μm fine-structure transition ($^2P_{3/2} - ^2P_{1/2}$) is one of the brightest emission lines in star-forming galaxies (Stacey et al. 1991, 2010) and a major coolant for the neutral atomic gas (Wolfire et al. 2003). In this phase of the interstellar medium (ISM), far-ultraviolet (FUV) photons produced by O and B stars heat the gas via the photoelectric effect on small dust grains and polycyclic aromatic hydrocarbons (PAHs; Helou et al. 2001). The ejected photoelectrons are thermalized and heat the gas. Neutral collisions marginally dominate the excitation of the fine-structure level of singly ionized carbon atoms and the gas cools by emission of [C II] 158 μm photons. This chain of events provides a link between the star formation activity and the [C II] emission: if the gas is in thermal balance, and it is cooled mainly by 158 μm emission, the [C II] line measures the total energy that is put into the gas by star formation activity.

The ionization potential of neutral carbon is 11.3 eV, so ionized carbon (C^+) can be found in phases of the ISM where hydrogen is in molecular, neutral atomic or ionized form. C^+ can be excited by collisions with electrons (e^-), hydrogen atoms (H) and molecules (H_2). Assuming collisional excitation, the [C II] integrated line intensity ($I_{[C II]}$) in the optically thin limit is (Crawford et al. 1985)

$$I_{[C II]} = 2.3 \times 10^{-24} \left[\frac{2e^{-91.2/T}}{1 + 2e^{-91.2/T} + n_{\text{crit}}/n} \right] N_{C^+}, \quad (3.1)$$

where $I_{[C II]}$ is in units of $W m^{-2} sr^{-1}$, T is the kinetic temperature in K, n is the volume density of the collisional partner (H, H_2 or e^-) in cm^{-3} , N_{C^+} is the column density of C^+ in cm^{-2} and n_{crit} is the critical density for collisions with a given partner in cm^{-3} . The latter is a function of temperature. For a typical cold neutral medium (CNM) temperature of $T \approx 100$ K (Heiles & Troland 2003; Wolfire et al. 2003), the critical density for collisions with e^- and H is $9 cm^{-3}$ and $3,000 cm^{-3}$ respectively (Goldsmith et al. 2012). Typical volume densities of H atoms in the CNM are $n_H \approx 50 cm^{-3}$ ($\ll n_{\text{crit}}(H)$) and the fractional ionization $n_{e^-}/n_H \lesssim 10^{-3}$, so in this phase collisions with H atoms dominate the C^+ excitation. In the dense gas interface between molecular clouds and HII regions – also known as photodissociation regions (PDRs) – the excitation is dominated by collisions with molecular hydrogen. At a gas temperature of 100 K, the critical density for collisions with H_2 is $6,100 cm^{-3}$ (Goldsmith et al. 2012). In the warm ionized medium (WIM), for a characteristic temperature of $T \approx 8,000$ K (Haffner et al. 1999; McKee & Ostriker 1977), the critical density for collisions with e^- is $44 cm^{-3}$ (Goldsmith et al. 2012). For a range of electron densities in the WIM of $\sim 0.08 - 0.4 cm^{-3}$ (Haffner et al. 2009; Velusamy et al. 2012), collisions with e^- are responsible for the excitation of C^+ .

The multiphase contribution to the [C II] emission includes the CNM, PDRs, HII

regions and the WIM (Bennett et al. 1994; Pineda et al. 2013; Shibai et al. 1991; Stacey et al. 2010, 1985). The individual contribution of each one of these ISM components to the total [C II] luminosity is still a matter of study and depends on the nature of the object, location and resolution of the observations. In the Galactic plane, early observations by the COsmic Background Explorer (COBE) show that the [C II] emission tends to follow the spiral arms and peaks at the molecular ring (Bennett et al. 1994; Wright et al. 1991). More recently, Pineda et al. (2013), based on the *Herschel*/HIFI project “Galactic Observations of Terahertz C+” (GOT C+), also find that in the plane of the galaxy the [C II] emission is mostly associated with the spiral arms, with dense PDRs as the main source of the total [C II] emission ($\sim 47\%$), followed by atomic gas ($\sim 21\%$) and small contributions from the ionized gas ($\sim 4\%$). In low metallicity galaxies, the PDR contribution to the [C II] emission can be dominant (80% in IC 10, Madden et al. 1997) or small (10% in Haro 11, Cormier et al. 2012). Moving to higher redshifts, Stacey et al. (2010) find that for 3 starburst systems in the redshift range $z \sim 1 - 2$ the origin of the [C II] emission is also dominated by the PDR component, with the ratio of the [C II] to the FIR emission similar to what is measured in nearby starburst galaxies.

Previous studies have searched for the connection between [C II] emission and star formation activity. One of the first surveys of nearby, gas rich spirals observed in the [C II] transition was done by Stacey et al. (1991) using the Kuiper Airbone Observatory (KAO). They find that the integrated [C II]/ $^{12}\text{CO}(1 - 0)$ line intensity ratio for starburst nuclei is similar to the ratio measured in Galactic OB star-forming regions. They also measure ratios a factor ~ 3 smaller in non-starburst systems and therefore, proposed to use this ratio as a tool to characterize the star formation activity. With the advent of the *Infrared Space Observatory* (ISO), Boselli et al. (2002) derive one of the first calibrations of the star formation rate (SFR) based on

the [C II] luminosity ($L_{\text{[C II]}}$). For a sample of 22 late-type galaxies including galaxies from the Virgo cluster and M82, they find a nonlinear relationship between $H\alpha$ and [C II] global luminosities ($L_{H\alpha} \propto L_{\text{[C II]}}^{0.79}$) with a dispersion of at least a factor of ~ 3 . Also using ISO [C II] observations, De Looze et al. (2011) find a nearly linear correlation between $\text{SFR}(\text{FUV}+24 \mu\text{m})$ and $L_{\text{[C II]}}$ with a dispersion of ~ 0.3 dex for a sample of 24 local, star-forming galaxies.

More evidence in favor of [C II] emission as a star formation tracer comes from *Herschel* observations. Mookerjee et al. (2011) find that the [C II] emission in the M33 HII region, BCLMP 302, strongly correlates with $H\alpha$ and dust continuum emission on scales of ~ 50 pc. More recently, Sargsyan et al. (2012), De Looze et al. (2014) and Pineda et al. (2014) explore the [C II]–SFR connection in luminous infrared galaxies (LIRGs, $L_{\text{IR}} > 10^{11} L_{\odot}$), dwarf galaxies and the Milky Way, respectively. Sargsyan et al. (2012) find a linear relationship between the $\text{SFR}(\text{FIR})$ and $L_{\text{[C II]}}$ for a sample of 24 LIRGs. De Looze et al. (2014), using the Dwarf Galaxy Survey (Madden et al. 2013), conclude that the [O I] 63 μm line is a better SFR tracer than [C II] in low metallicity galaxies. Pineda et al. (2014) find that [C II] emission emerging from different phases of the ISM in the Milky Way correlates well with SFR at Galactic scales.

The [C II] transition presents many advantages as a SFR indicator. Among these: (1) it is a very bright line, with luminosities typically $\sim 0.1 - 1\%$ of the FIR luminosity; (2) it is practically unaffected by extinction – possible exceptions include edge-on galaxies (Heiles 1994) and extreme starbursts (Luhman et al. 1998); (3) it can be used to study star-forming galaxies at redshifts $z \gtrsim 1$ using ground based-observatories like the Atacama Large Millimeter Array (ALMA) (e.g. see Figure 3.8). For many of these high redshift objects, the [C II] luminosity might be one of the few available tools to measure SFRs.

The so called “[C II] deficit” is the most important potential limitation for using [C II] as a SFR indicator. Observed in luminous and ultraluminous infrared galaxies (Brauhar et al. 2008; Díaz-Santos et al. 2013; Graciá-Carpio et al. 2011; Malhotra et al. 1997, 2001) and nearby galaxies (Beirão et al. 2012; Croxall et al. 2012), the “[C II] deficit” corresponds to lower [C II] to FIR ratios measured as a function of increasingly warm infrared color. Several explanations for the observed low ratio of [C II] to FIR have been proposed over the years. Some of these explanations may account only for a small subset of the low ratios: [C II] self absorption, high dust extinction, softer UV radiation coming from older stellar populations (see Malhotra et al. 2001, for more discussion of these scenarios). Other alternatives seem to be applicable to a larger range of environments: (1) charging of the dust grains: at high radiation fields, the dust grains become positively charged (Croxall et al. 2012; Malhotra et al. 1997). A higher charge implies a higher Coulomb barrier for the photoelectrons to overcome; as a result the photoelectric heating efficiency drops. (2) [O I] as an additional cooling channel: if the FUV radiation field and the density of the atomic gas increases above the critical density for collisional excitation with H atoms ($n_{\text{crit}} \sim 10^3 \text{ cm}^{-3}$), then collisional de-excitations start to suppress the [C II] emission and the contribution to the cooling by the [O I] 63 μm line ($n_{\text{crit}} \sim 10^5 \text{ cm}^{-3}$) becomes dominant. (3) High ionization parameter (Graciá-Carpio et al. 2011): in HII regions with high ionization parameter, a larger fraction of the non-ionizing stellar UV is absorbed by dust in the HII region, and thus a smaller fraction of the UV photons are available to heat the neutral gas.

The goal of this paper is to derive an accurate [C II]–SFR calibration for normal galaxies, obtain a deeper understanding of the origin of the [C II]–SFR correlation, and identify the limits of applicability of the calibration. To do this, we use a

large sample of resolved extragalactic regions – with a median size of ~ 0.5 kpc – selected from 46 nearby galaxies that are part of the KINGFISH sample of galaxies (Kennicutt et al. 2011, Key Insights on Nearby Galaxies: A Far-Infrared Survey with *Herschel*). This, combined with the wealth of ancillary data available – such as IR, $H\alpha$ and FUV observations – allow us to probe different timescales and environments associated with the star formation activity.

This paper is organized as follows. In §2 we describe the KINGFISH sample and the supplementary data. In §3 we present the correlations between [C II] and SFR estimated from 24 μm , total infrared (TIR), $H\alpha$ and FUV data. We also describe how we removed the cirrus and AGN contributions to the 24 μm emission. In §4 we analyze the scatter of the [C II]–SFR correlation in terms of the IR color and other properties of the ISM derived from the Draine & Li (2007) model. We also compare our calibration to previous [C II]–SFR calibrations derived based on ISO and *Herschel* samples. Finally, we use the *Starburst99* code to analyze the scatter in terms of a combination of the duration of the star formation activity and the photoelectric heating efficiency of the dust grains.

3.2 Main Sample Description

We focus our study on 46 galaxies from the KINGFISH sample (Kennicutt et al. 2011). KINGFISH combines deep *Herschel* infrared imaging with spectroscopy of the key interstellar medium diagnostic lines: [C II] 158 μm , [NII] 122 μm & 205 μm , [O I] 63 μm and [OIII] 88 μm . Our spectroscopic sample includes 40 spiral galaxies that encompass the full range of late-type morphologies, as well as 4 irregulars (Holmberg II, NGC 2915, NGC 3077 and NGC 5408), and 2 ellipticals (NGC 855 and NGC 3265).

There are eight other KINGFISH galaxies with spectroscopic data available that we do not include in this study. These are: NGC 1266, NGC 1316, NGC 1097, NGC 1377, NGC 1404, NGC 4594, NGC 4631 and NGC 4559. The reasons why we exclude these galaxies are presented in Appendix A.1.

Our sample spans more than three orders of magnitude in total infrared luminosity ($L_{\text{TIR}} \sim 10^{7.6} - 10^{11} L_{\odot}$) and about one order of magnitude in distance ($D \sim 2.8 - 26.5$ Mpc). The sample also covers a metallicity range of $12 + \log(\text{O}/\text{H}) \sim 7.72 - 8.77$, measured by Moustakas et al. (2010) using the Kobulnicky & Kewley (2004) calibration. The beam size of the [C II] 158 μm data is $\sim 12''$; given the range of distances, our sample covers a range of spatial resolutions that goes from ~ 0.2 kpc for IC 2574 to ~ 1.5 kpc for NGC 5713, with a median value of 0.6 ± 0.3 kpc. In order to allow comparison between regions with different sizes, we report our measurements as luminosities per unit of physical area (surface brightness or luminosity surface density).

The FIR spectroscopic line observations were carried out with the Photodetector Array Camera & Spectrometer (PACS) on board *Herschel* as part of the *Herschel* key program KINGFISH. The spectral observations were reduced using the *Herschel* Interactive Processing Environment (HIPE) version 11.0. The reduced cubes were then processed to obtain zero, first and second moment maps. For a detailed description on the reduction and processing of the KINGFISH FIR spectral maps we refer to Croxall et al. (2013). About half of the images consists of strip maps, in some cases including extranuclear regions; the other half corresponds to rectangular regions centered on the nucleus of the galaxy.

The work in this paper is based on the [C II] line, the brightest emission line in our sample. About 70% of the galaxies in our sample show [C II] line emission above the 3σ level in at least 70% of the map. Figure 3.1 shows [C II] surface brightness

maps and 24 μm continuum contours for four KINGFISH galaxies: NGC 2915, irregular low metallicity galaxy with the lowest total infrared (TIR) luminosity in our sample; NGC 4736, spiral galaxy with a well defined circumnuclear ring visible in both, [C II] and 24 μm emission; NGC 5055 and NGC 7793, two flocculent spiral systems with extended [C II] emission detected across the disk and extranuclear regions. At this spatial scale, there is a very good agreement between the [C II] line and the 24 μm dust continuum emission, a well characterized indicator of SFR.

In order to study the reliability of the [C II] 158 μm line emission as a SFR tracer, it is crucial to combine this FIR line with archival data that provide information about the dust, gas and young stellar population. In Appendix A.2 we describe the supplementary data used in our analysis, which includes ground-based $\text{H}\alpha$, GALEX FUV and *Spitzer* and *Herschel* infrared data. We also use maps of dust properties, like the ones presented in Aniano et al. (2012), based on the Draine & Li dust model (Draine & Li 2007) (DL07).

3.2.1 Methods

The native pixel size of the [C II] maps after the reduction process was 2.7". We regrid the maps in order to define a new pixel size that is roughly the size of the [C II] beam, i.e. 12". Among our data, the [C II] maps have the lowest resolution, so we convolve all the other maps from the supplementary data to the [C II] PSF. For this task, we use a library of convolution kernels for the cameras of the *Spitzer*, *Herschel Space Observatory*, GALEX and ground-based telescopes constructed by Aniano et al. (2011). After this step, we regrid the convolved maps to be aligned with the [C II] maps.

For all the surface brightness and SFR surface density values we correct for inclination by a factor of $\cos i$.

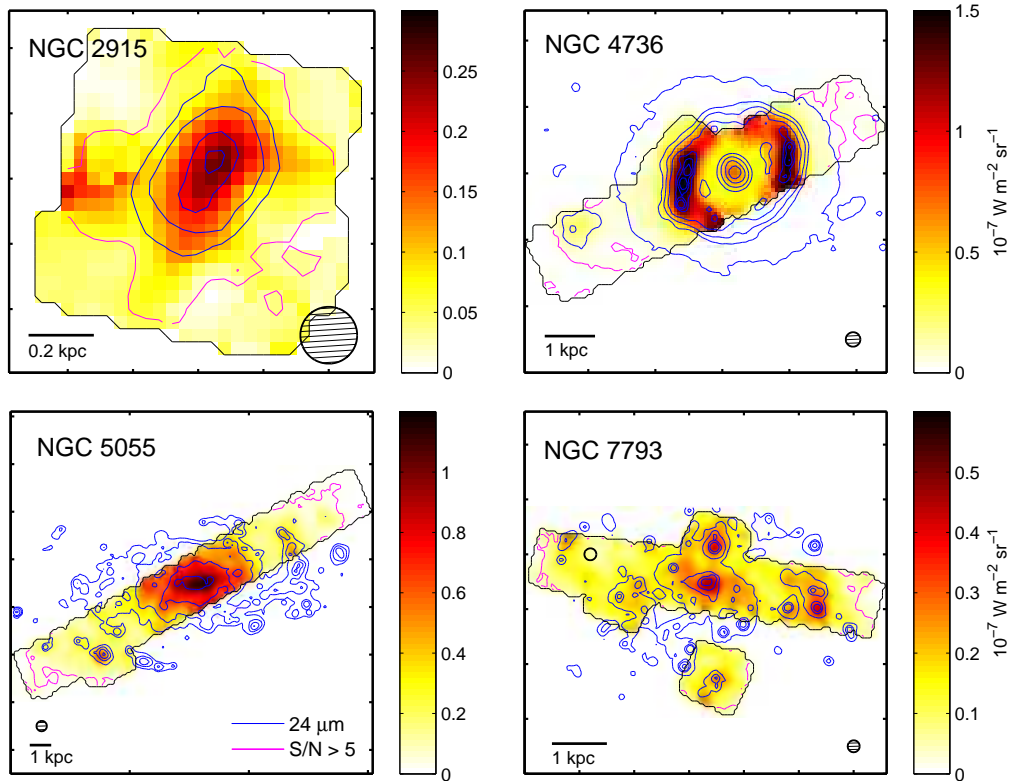


Figure 3.1: PACS [C II] $158 \mu\text{m}$ images for four galaxies selected from the KINGFISH sample. The black contours delineate the areas which have [C II] data. The physical scale and the size of the $\sim 12''$ beam are shown in the corners. The color scale shows the [C II] surface brightness in units of $\text{W m}^{-2} \text{ sr}^{-1}$ and the blue contours show the $24 \mu\text{m}$ dust continuum emission. At this spatial scale, there is a very good agreement between the [C II] line and the $24 \mu\text{m}$ continuum emission. The area enclosed by the magenta contours corresponds to the parts of the galaxy where the S/N of the [C II] emission is greater than 3. The four galaxies in the image are: (*top-left*) NGC 2915, a blue compact dwarf galaxy and one of the four systems in our sample with metallicity $12+\log(\text{O}/\text{H}) < 8.1$. This galaxy also has the lowest TIR luminosity of the sample ($L_{\text{TIR}} = 3.9 \times 10^7 L_{\odot}$). (*top-right*) NGC 4736, an early-type spiral galaxy with a circumnuclear ring traced by both, [C II] and $24 \mu\text{m}$ emission. (*bottom-left*) NGC 5055, a spiral (SAbc) galaxy. The detected [C II] emission along the disk covers more than one order of magnitude in surface brightness. (*bottom-right*) NGC 7703, a flocculent spiral with [C II] emission mapped using a strip section and one extranuclear regions.

3.3 Results

Our goal is to study if the [C II] line can be used as a SFR tracer. To do this we compare the [C II] line emission to four widely used SFR tracers: H α , FUV, 24 μ m and TIR emission. H α and FUV provide measures of star formation through the rate of production of ionizing photons and the photospheric emission from O and B stars, respectively. The 24 μ m and TIR dust emission yields a measure of star formation via the reprocessing of light by dust in star-forming regions. Combination of these tracers is useful to account for the obscured (traced by 24 μ m or TIR) and unobscured (traced by H α or FUV) contributions produced by star-forming regions.

3.3.1 [C II] – 24 μ m Correlation

We start our analysis with the $\Sigma_{[\text{C II}]} - \Sigma_{24 \mu\text{m}}$ correlation because we have 24 μ m images available for all the galaxies in our sample. Figure 3.2 shows this correlation for 4,142 regions selected from KINGFISH galaxies. Three sigma upper limits for [C II] emission are shown as dark red triangles.

The 24 μ m continuum emission is thought to be primarily produced by small hot dust grains in diffuse regions, transiently heated by the interstellar radiation field. One important contributor to the dust heating are young, hot stars (e.g. Law et al. 2011); however, contribution from older stellar populations cannot be ignored. For example, in M 31, old stars contribute to the heating of the dust in star-forming regions in the disk (Draine et al. 2014) and dominate the heating in the bulge (Groves et al. 2012). In addition, non-stellar contribution to the radiation field by active nuclei can also be an important source of heating of dust grains (Dale et al. 2006; Deo et al. 2009). Given that our plan is to use the 24 μ m to trace the young star formation that is reprocessed by dust, in the following section we

describe how we account and correct for the $24\ \mu\text{m}$ component that is not associated with star formation activity.

3.3.2 AGN Contribution

X-ray photons produced by the AGN heat the surrounding dust and gas creating X-ray dominated regions (XDRs), (Maloney et al. 1996); as a result, XDRs can contribute to the total [C II] and $24\ \mu\text{m}$ dust emission. Even though by design of the sample the global luminosity of the KINGFISH galaxies is not dominated by AGN, the effect of the XDRs can be important in the central portions of galaxies. According to the nuclear spectral classification by Moustakas et al. (2010), 19 of the 49 galaxies in our sample are optically classified as AGN and two other as mixed systems (SF/AGN). Another 6 galaxies that show no AGN signature in the optical have nuclear X-ray measured fluxes that may indicate AGN activity (Grier et al. 2011; Tajer et al. 2005). To study the effect of the AGN, we select the central region using circular apertures of ~ 0.5 kpc radius. For galaxies further than ~ 17 Mpc, the central $12''$ region is larger than 1 kpc; thus, for these cases we only mask the central $12''$ region.

The size of this aperture should be enough to enclose the emission arising from the XDRs powered by the AGN. The left panel on Figure 3.2 shows the properties of the AGN-selected regions (color diamonds) and star-forming regions (grey dots) in the [C II] – $24\ \mu\text{m}$ surface brightness plane. The AGN-selected regions are color coded according to the nucleus classification: optically selected AGN (red) and X-ray selected AGN (green). About half of the AGN-selected regions tend to show a $24\ \mu\text{m}$ excess compared to [C II] (or a [C II] deficit compared to $24\ \mu\text{m}$); in the most extreme cases, the excess can be as high as a factor of ~ 6 (e.g. regions from NGC 4736, see Appendix A.6 for individual correlations). It is likely that these

higher $24 \mu\text{m} - [\text{C II}]$ ratios are caused by (1) the AGN contributing more to the dust continuum than to the $[\text{C II}]$ emission; (2) a reduction in the photoelectric heating efficiency due to the destruction of the small dust grains and PAHs by strong AGN radiation fields. Our goal is to use the $24 \mu\text{m}$ emission as a SFR tracer; thus, we remove from our sample the AGN-selected regions in order to avoid non star-forming contributions to the emission.

Figure 3.2, right panel, shows the $\Sigma_{24\mu\text{m}} - \Sigma_{[\text{CII}]}$ correlation after removing the $[\text{C II}]$ 3σ upper limits and the AGN points. The black solid line represents the best linear fit to the remaining 3,486 points and the blue points show the median $\Sigma_{24\mu\text{m}}$ in bins of $\Sigma_{[\text{CII}]}$ with error bars indicating 1σ scatter. The correlation is tight, with a 1σ scatter around the fit of 0.23 dex and a slope of 1.20 ± 0.01 . This value is in excellent agreement with the 1.23 slope found by Calzetti et al. (2007) for the $\Sigma_{24\mu\text{m}} - \Sigma_{\text{SFR}}$ correlation; thus, we expect a nearly linear correlation between $\Sigma_{[\text{CII}]}$ and Σ_{SFR} . We discuss more about the $\Sigma_{[\text{CII}]} - \Sigma_{\text{SFR}}$ relationship in section 4.

3.3.3 $24 \mu\text{m}$ “Cirrus” Emission

Emission at $24 \mu\text{m}$ can be used as a reliable obscured SFR tracer (Calzetti et al. 2007; Rieke et al. 2009); an important consideration, however, is to account for the $24 \mu\text{m}$ emission that is produced by dust heated by non star-forming sources (e.g., old stars). We will refer to this emission as $24 \mu\text{m}$ cirrus.

We estimate the intensity of the $24 \mu\text{m}$ cirrus following a similar procedure to the one described in Leroy et al. (2012). The details of the cirrus calculation are presented in Appendix A.3. The challenge in this method is to quantify the incident radiation field produced by non star-forming sources, i.e., U_{cirrus} . For our estimation of the $24 \mu\text{m}$ cirrus emission, we assume two distinct scenarios: (1) U_{cirrus} is constant across the galaxy, or (2) U_{cirrus} scales with U_{min} (in the DL07 model, U_{min}

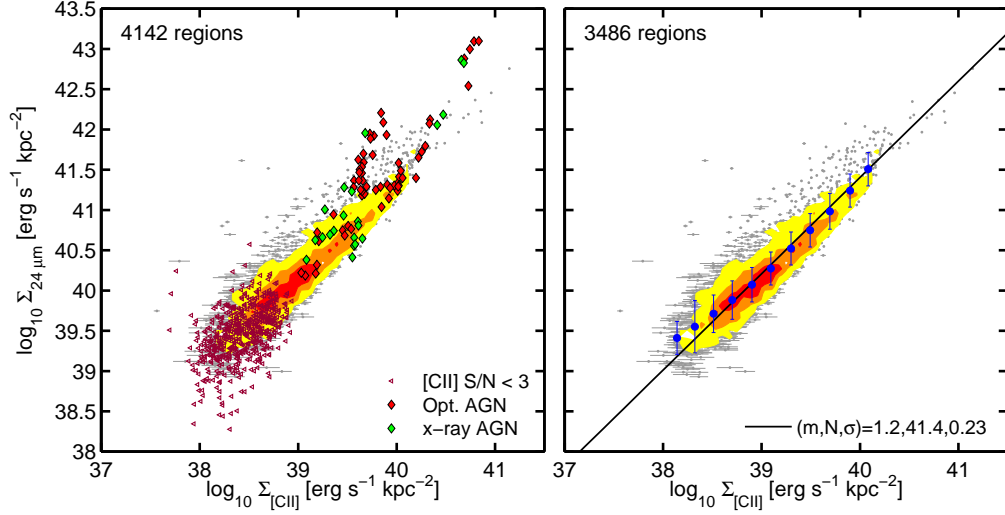


Figure 3.2: $24 \mu\text{m}$ surface brightness ($\Sigma_{24\mu\text{m}}$) versus [C II] $158 \mu\text{m}$ surface brightness ($\Sigma_{[\text{CII}]}$) of $12''$ (1 beam) size regions of 46 galaxies from the KINGFISH sample. Filled contours show the data density (similar to a Hess diagram), and enclose 90, 45 and 25% of the data. (*Left*) Triangles correspond to [C II] 3σ upper limits of regions with $S/N < 3$ ($\sim 11\%$ of the points). The diamonds represent the regions located within the central $\sim 0.5 \text{ kpc}$ radius in 25 galaxies classified as AGN ($\sim 2\%$ of the points). Regions from the 19 galaxies optically classified as AGN are shown as red diamonds. Regions from the 6 galaxies that, based on the nuclear X-ray luminosity may indicate AGN activity, are shown as green diamonds. (*Right*) Same as left panel, but excluding points with [C II] $S/N < 3$, with emission associated with AGN. The black line correspond to the best linear fit to the data (in the log-log space). The slope, the logarithmic value of $\Sigma_{24\mu\text{m}}$ at $\log_{10}(\Sigma_{[\text{CII}]} / [\text{erg s}^{-1} \text{kpc}^{-2}]) = 40$ and the standard deviation dex of the fit are listed as (m, N, σ) on the bottom right corner. The blue dots show the running median and standard deviation in bins of $\Sigma_{[\text{CII}]}$.

corresponds to the lowest interstellar radiation field heating the diffuse ISM). The resulting fraction of the $24 \mu\text{m}$ emission associated with cirrus (f_{cir}) and the effect of the cirrus correction on the $\Sigma_{24\mu\text{m}} - \Sigma_{[\text{CII}]}$ correlation can be found in Table 3.1. In summary, $24 \mu\text{m}$ cirrus corrections based on a scaled version of U_{min} do not produce significant changes on the $\Sigma_{[\text{CII}]} - \Sigma_{24 \mu\text{m}}$ correlation, and the fraction of $24 \mu\text{m}$ cirrus emission is, on average, in the 18 to 39% range (depending on the scaling factor assumed). We conclude that the results are robust to the choice of correction except when the correction is pushed to extreme values (e.g., $U_{\text{cirrus}} = 1.1$). We know

Table 3.1: Effect of cirrus correction on the [C II] – 24 μm correlation

Description	Slope	Normalization ^a	Scatter	r_{corr}	Median $f_{\text{cir}}(-1\sigma, +1\sigma)$
	m	N	[1σ dex]		
No Cirrus	1.20	41.40	0.23	0.92	0 (0,0)
Scaled Cirrus					
$U_{\text{cir}} = 0.5U_{\text{min}}$	1.21	41.32	0.24	0.89	0.18 (0.12,0.24)
..... = $0.75U_{\text{min}}$	1.27	41.32	0.24	0.89	0.29 (0.19,0.39)
..... = U_{min}	1.30	41.26	0.27	0.87	0.39 (0.28,0.51)
Constant Cirrus					
$U_{\text{cir}} = 0.6$	1.30	41.41	0.24	0.90	0.15 (0.06,0.25)
..... = 0.8	1.38	41.43	0.26	0.90	0.26 (0.11,0.42)
..... = 1.1	1.60	41.50	0.33	0.87	0.43 (0.20,0.66)

^a

The normalization N is the value of $\log_{10}(\Sigma_{24\mu\text{m}})$ at $\log_{10}(\Sigma_{[\text{CII}]}) = 40$. Units are [$\text{erg s}^{-1} \text{kpc}^{-2}$].

these extreme and likely fairly drastic cirrus assumptions are not representative of our local, ~ 1 kpc neighborhood. Therefore, for the rest of the paper we choose to work with the 24 μm cirrus subtraction that is based on the same assumption made by Leroy et al. (2012) for their sample of local galaxies, i.e. $U_{\text{cirrus}} = 0.5 U_{\text{min}}$.

3.3.4 [C II] compared to other star formation tracers: H α , FUV and 24 μ m

On average, interstellar dust absorbs roughly half the starlight of typical spiral galaxies and re-emits it in the infrared; therefore, observations in the infrared are essential for deriving a complete inventory of star formation (Kennicutt & Evans 2012). The best way to account for this dust-driven extinction is to combine unobscured star formation tracers, like H α or FUV emission, with the dust-reprocessed infrared continuum. In this section we explore the correlations between [C II] and the SFR estimated from 24 μ m and TIR emission and combinations of 24 μ m and TIR with H α and FUV emission.

We measure the SFR and Σ_{SFR} based on: (1) H α emission using Calzetti et al. (2007) calculation, Equation (6) and applying a typical extinction correction of $A_{\text{H}\alpha} = 1.1$ mag (Kennicutt 1983). Calzetti et al. (2007) adopts the default *Starburst99* IMF, i.e., a truncated Salpeter IMF with slope 1.3 in the range $0.1 - 0.5 M_{\odot}$ and slope 2.3 in the range $0.5 - 120 M_{\odot}$. (2) 24 μ m emission using Equation (8) and (9) in Calzetti et al. (2007). (3) The combination of 24 μ m and H α using Calzetti et al. (2007) calculation, Equation (7). (4) The combination of TIR luminosity and H α using Kennicutt et al. (2009) Equation (16) and a scaling coefficient of 0.0024 (Table 4, Kennicutt et al. 2009). As Calzetti et al. (2007), Kennicutt et al. (2009) also adopts the default *Starburst99* IMF. We measure the TIR emission using 8, 24, 70 and 160 μ m bands following Equation (22) in Draine & Li (2007). (5) The combination of 24 μ m and FUV, using Leroy et al. (2008) Equation (D10) and (D11). These two calibrations were constructed from the FUV-based SFR calibration by Salim et al. (2007). For all galaxies the 24 μ m continuum emission is cirrus subtracted following §3.1.2.

Figure 3.3 shows the correlations we find between $\Sigma_{[\text{CII}]}$ and Σ_{SFR} . The first panel shows the correlation for 46 galaxies for which we measure Σ_{SFR} using only 24 μm emission. The slope of the correlation is nearly linear and the scatter is 0.19 dex. The next panel shows Σ_{SFR} measured using $\text{H}\alpha$ for the 27 galaxies for which we have $\text{H}\alpha$ data available. The correlation is good ($r_{\text{corr}} = 0.83$), with the highest surface brightness points lying below the main trend probably because of increasing extinction in $\text{H}\alpha$. Given that $\text{H}\alpha$ is a tracer of recent star formation, with an age sensitivity of a few Myr (McKee & Williams 1997), the fact that we find a good correlation with $[\text{C II}]$ strengthens the case in favor of using this FIR cooling line as a SFR tracer. For the same 27 galaxies, the third and the fourth panel shows the combination between $\text{H}\alpha$ and 24 μm and TIR emission, respectively. Combining $\text{H}\alpha$ and IR continuum emission significantly reduces the scatter and corrects for the attenuation of $\text{H}\alpha$ emission at high SFR values. The fifth panel shows the $\Sigma_{[\text{CII}]} - \Sigma_{\text{SFR}}$ correlation for 33 galaxies when using a combination of 24 μm and FUV emission to measure Σ_{SFR} . The correlation is tight, with a 1σ scatter around the fit of 0.2 dex. The fit parameters are similar to those measured when the SFR is measured as a combination of $\text{H}\alpha$ and 24 μm emission.

Given that we do not have $\text{H}\alpha$ or FUV maps available for all the galaxies in our sample, unlike 24 μm , we define the Σ_{SFR} we use from now on as “our reference” Σ_{SFR} coming from the combination of: (1) 24 μm + $\text{H}\alpha$ (27 cases); (2) 24 μm + FUV if $\text{H}\alpha$ is not available (8 cases); (3) only 24 μm if neither $\text{H}\alpha$ nor FUV are available (11 cases). The correlation between the $\Sigma_{[\text{CII}]}$ and “our reference” Σ_{SFR} is shown in the last panel of Fig. 3.3. The best linear fit to the data, as estimated by the OLS linear bisector method (Isobe et al. 1990), yields the following relationship:

$$\Sigma_{\text{SFR}} (\text{M}_{\odot} \text{ yr}^{-1} \text{ kpc}^{-2}) = 3.79 \times 10^{-47} \times (\Sigma_{[\text{CII}]} [\text{erg s}^{-1} \text{ kpc}^{-2}])^{1.13}. \quad (3.2)$$

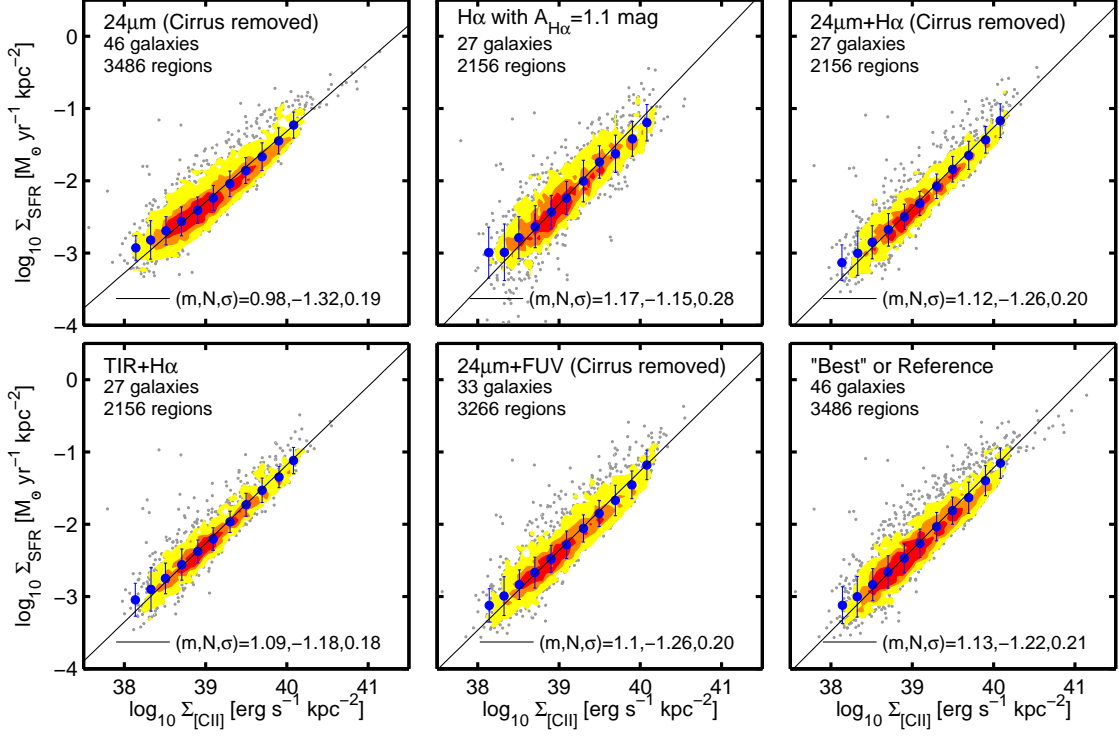


Figure 3.3: Star formation rate surface density, Σ_{SFR} , versus $[\text{C II}]\tilde{158} \mu\text{m}$ surface brightness, $\Sigma_{[\text{CII}]}$, for 46 galaxies from the KINGFISH sample. Gray points correspond to $12''$ (1 beam) size regions and filled contours show data density. The numbers on the bottom-right corner of each panel correspond to the fit parameters: slope (m), y -axis value at $x = 40$ (N) and 1σ standard deviation in dex (σ). Each panel shows the correlation for a different method of measuring Σ_{SFR} . (*Top-left*) We measure Σ_{SFR} from $24 \mu\text{m}$ emission (after cirrus subtraction) following Calzetti et al. (2007) (*Top-middle*) For 27 galaxies with $\text{H}\alpha$ maps available, we measure Σ_{SFR} from $\text{H}\alpha$ emission, corrected for internal extinction (1.1 mag), following Calzetti et al. (2007) calibration. (*Top-right*) We estimate Σ_{SFR} based on the combination of $24 \mu\text{m}$ emission (cirrus subtracted) and $\text{H}\alpha$ emission for the 27 galaxies for which $\text{H}\alpha$ maps are available. We use Calzetti et al. (2007) calibration. (*Bottom-left*) We measure Σ_{SFR} from the combination between TIR and $\text{H}\alpha$ emission following Kennicutt et al. (2009) calibration. (*Bottom-middle*) We measure Σ_{SFR} as the combination of $24 \mu\text{m}$ emission (cirrus subtracted) and FUV emission for 33 galaxies with FUV maps available following Leroy et al. (2008) calibration. (*Bottom-right*) We show the “Best” or Reference Σ_{SFR} , that we measure from $\text{H}\alpha+24 \mu\text{m}$ (when $\text{H}\alpha$ is available), FUV+ $24 \mu\text{m}$ (when $\text{H}\alpha$ is not available) and only $24 \mu\text{m}$ when neither $\text{H}\alpha$ nor FUV maps are available.

The scatter of the correlation is 0.21 dex.

In order to derive a calibration for the SFR based on [C II] luminosities, we convert the [C II] luminosity surface densities into [C II] luminosities, and then we fit the data using the OLS linear bisector method. The resulting [C II]–based SFR calibration is:

$$\text{SFR} (M_{\odot} \text{ yr}^{-1}) = 2.29 \times 10^{-43} \times (L_{[\text{C II}]} [\text{erg s}^{-1}])^{1.03}. \quad (3.3)$$

The scatter of the correlation is 0.21 dex. Due to the distance effect introduced by the conversion to luminosities, the calibration in equation (3.3) has a slope closer to unity, but similar scatter. Recall that “luminosity-luminosity” relations implicitly have distance squared in both axes ($\propto D^2$), while in “surface density-surface density” correlations, the quantities in both axes depend upon the ratio between luminosity ($\propto D^2$) and area ($\propto D^2$), so surface densities are independent of distance.

Before applying these calibrations, it is important to understand their reliability and limits of applicability. For instance, the luminosity calibration is subject to the caveats mentioned in the Introduction regarding the “[C II]-deficit”, which implies that galaxies with similar IR luminosity can show variations of a factor of 10x or more in their [C II] luminosity (Stacey et al. 2010). In order to explore the reliability of the [C II]–SFR calibration, in the next section we study in detail the nature of the scatter in the [C II]–SFR correlation and we also apply these calibrations to other samples of extragalactic objects observed in [C II] emission.

3.4 Analysis

In the previous section we found a tight correlation between $\Sigma_{[\text{C II}]}$ and Σ_{SFR} . In this section we try to understand the origin of this correlation and the reason why some galaxies or regions within galaxies deviate from this quasi-linear relationship.

Variations of the [C II] luminosity compared to the IR continuum were first observed by ISO. Low [C II] to FIR ratios are found for global measurements of normal star-forming galaxies with warm dust temperatures ($F_\nu(60 \mu\text{m})/F_\nu(100 \mu\text{m}) \gtrsim 0.8$) (Brauhar et al. 2008; Malhotra et al. 1997, 2001) and luminous and ultraluminous infrared galaxies (U/LIRGs; $L_{\text{IR}} > 10^{11-12} L_\odot$) (Luhman et al. 1998, 2003). This is important in the context of our study because the FIR luminosity is commonly used a SFR tracer in U/LIRGs. Therefore, any variation in the [C II] to FIR ratio will imply a difference between the SFR measured using [C II] and FIR emission.

With *Herschel*, low [C II] to FIR ratios are observed for U/LIRGS as a function of increasing dust temperature, compactness of the source (Díaz-Santos et al. 2013) and FIR luminosity to molecular gas mass (M_{H_2}) ratio (Graciá-Carpio et al. 2011). In addition, *Herschel* allowed for the first time to resolve the regions that exhibit low [C II] to FIR ratios in nearby galaxies. Croxall et al. (2012) observe in NGC 4559 and NGC 1097 a drop in the [C II] to FIR ratio for regions with warm dust temperatures ($\nu f_\nu(70 \mu\text{m})/\nu f_\nu(100 \mu\text{m}) \gtrsim 0.95$) and intense radiation fields. They conclude that the most plausible scenario to account for the [C II] deficit is the charging of the dust grains caused by the high radiation fields. Beirão et al. (2012) find a similar trend when comparing the circumnuclear ring and extranuclear regions of NGC 1097.

Similar to the observed variations in the [C II] to FIR ratios, De Looze et al. (2014) report variations in the [C II] to SFR correlation observed in galaxies from

the DGS sample. Compared to a standard SFR measured as a combination of FUV and 24 μm emission, they find systematically lower values of [C II]-based SFRs as a function of increasing dust temperature, [O I] 63 μm /[C II]+[O I] 63 μm ratio, and decreasing metallicity. Thus, for warm, low metallicity regions De Looze et al. (2014) conclude that [O I] 63 μm is a more reliable SFR tracer than [C II]. For additional discussion on the connection between metal abundance and the dispersion of the [C II]-SFR correlation, see De Looze et al. (2014) .

In order to evaluate the reliability of a SFR calibration based on the [C II] line, it is key to understand the scatter in the correlation. The goal is to identify the variables that drive the deviations from the fit (equations 4.5 and 3.3), and use this information to reduce the scatter and establish the limits of applicability of the calibration. In the next two sections we discuss how local regions within a galaxy and galaxies as a whole deviate from the fit. We study the deviations as a function of a set of parameters that characterize the ISM properties and can be derived directly from the dust continuum SEDs and spectra. These parameters are: (1) IR color, $\nu f_\nu(70 \mu\text{m})/\nu f_\nu(160 \mu\text{m})$; (2) oxygen abundance ($12 + \log(\text{O}/\text{H})$); (3) fraction of the IR luminosity radiated from regions with high radiation fields, $f(L_{\text{IR}}; U > 100)$; (4) dust-weighted mean starlight intensity, $\langle U \rangle$, and (5) PAH abundance, q_{PAH} . These last three parameters are derived from the DL07 dust model (see Appendix A.2 for details).

3.4.1 Local Variations

The high spatial resolution provided by *Herschel* allow us to study the scatter on \sim kiloparsec scales. The benefit of studying local variations in a large sample of galaxies with varying global properties is that allow us to identify the more likely of the possible scenarios behind the scatter. Figure 3.4 summarizes the results of our

fit residual analysis for all the $\sim 12''$ regions of the 46 galaxies in our sample. The top-left panel shows the fit residual as a function of IR color, which is an observable quantity and can be used as a proxy for the dust temperature. About 20% of the regions have IR colors warmer than $\nu f_\nu(70 \mu\text{m})/\nu f_\nu(160 \mu\text{m}) \gtrsim 1.3$; the fit residual for these regions systematically increases as a function of IR color, with a median deviation from the fit as high as a factor of ~ 3 for the warmest regions (i.e., warm dust regions systematically exhibit higher Σ_{SFR} (or SFR) than expected from their [C II] meaning they are underluminous in [C II]). This corresponds to a particular dust color temperature, T_{dust} . We estimate T_{dust} using a modified blackbody model with emissivity spectral index $\beta = 1.5$ and the 70 to 160 μm flux ratio. Most of the regions have dust color temperatures in the range $T_{\text{dust}} \sim 20 - 32$ K, and we find that regions start to systematically deviate from the fit for dust color temperatures higher than $T_{\text{dust}} \gtrsim 29$ K.

A similar trend is observed as a function of the model-derived variables. The remaining left-panels of Figure 3.4 show that for a dust-weighted mean starlight intensity of $\langle U \rangle \gtrsim 6$, a fraction of the IR luminosity produced in high radiation field regions $f(L_{\text{IR}}; U > 100) \gtrsim 25\%$, or a PAH abundance $q_{\text{PAH}} \lesssim 2\%$, points tend to deviate from the fit in a similar fashion as for IR color. It is important to note that $\sim 99\%$, $\sim 85\%$ and $\sim 73\%$ of the regions with $\langle U \rangle \gtrsim 6$, $f(L_{\text{IR}}; U > 100) \gtrsim 25\%$ and $q_{\text{PAH}} \lesssim 2\%$ have IR colors $\gtrsim 1.3$, respectively; this shows that regions that systematically deviate from the fit in the different panels are essentially the same. We also observed a similar systematic deviation as a function of the $\nu f_\nu(70 \mu\text{m})/\nu f_\nu(100 \mu\text{m})$ IR color, starting at the threshold value of $\nu f_\nu(70 \mu\text{m})/\nu f_\nu(100 \mu\text{m}) \approx 0.8$.

We also analyze the local variations as a function of dust attenuation, which we measure as the fraction of FUV and optical emission absorbed and reprocessed by dust versus the escaping FUV emission as the ratio of the 24 μm to the FUV

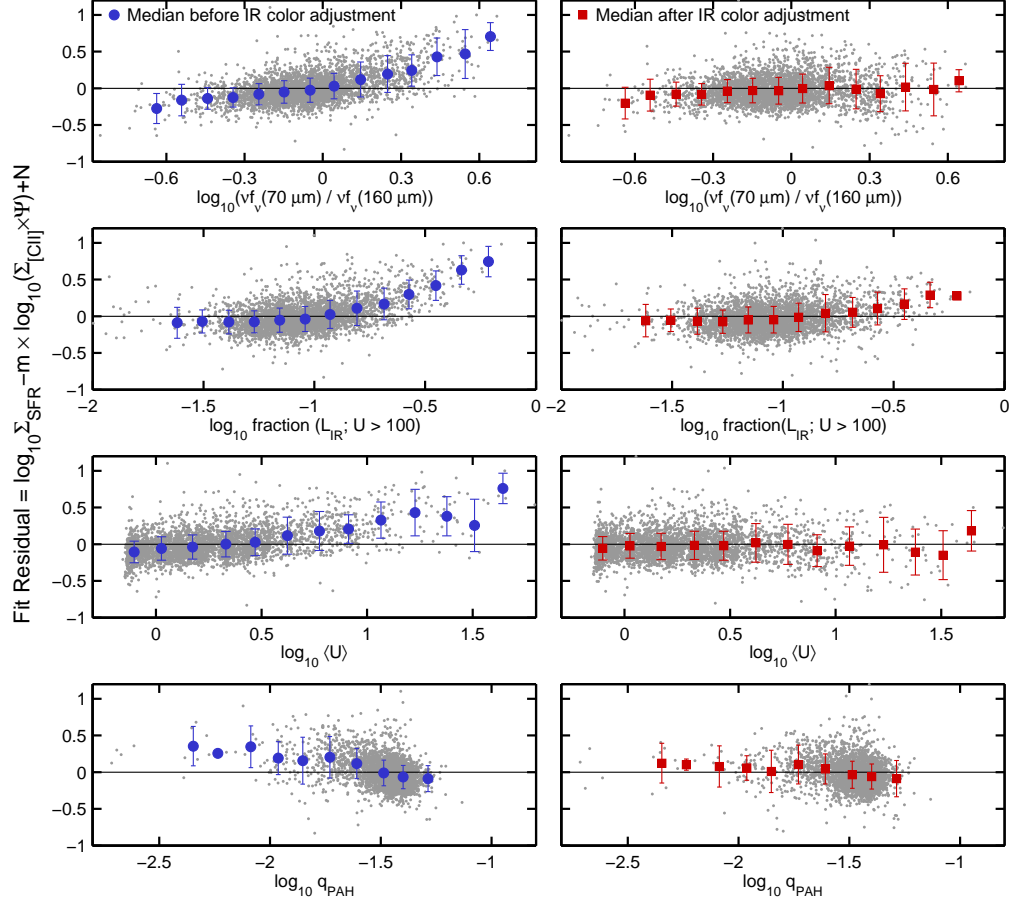


Figure 3.4: Fit residual of the $\Sigma_{[\text{CII}]} - \Sigma_{\text{SFR}}$ correlation as a function of: IR color ($\nu f_{\nu}(70)/\nu f_{\nu}(160)$), fraction of the IR luminosity radiated from regions with high radiation field ($\text{fraction}(L_{\text{IR}}; U > 100)$), median radiation field ($\langle U \rangle$) and PAH abundance (q_{PAH}). The left and the right panel show the fit residual before and after applying the IR color adjustment derived in §4.2.1, respectively. Gray points represent 12'' size regions of the 46 galaxies in the sample. Filled blue dots (left panel), red squares (right panel) and the corresponding vertical bars correspond to the median and the 1σ standard deviation in dex of the binned distribution of points.

intensity, $I_{24\mu\text{m}}/I_{\text{FUV}}$. The details of this analysis can be found in Appendix A.4. Around the $I_{24\mu\text{m}}/I_{\text{FUV}}$ ratio of ~ 10 , we observe a systematic increase of the fit residuals as a function of decreasing dust attenuation. Low metallicity regions from Holmberg II and IC 2574 also show high fit residuals at low $I_{24\mu\text{m}}/I_{\text{FUV}}$ ratios, and we discuss the implications of these results in §4.2.1.

Before analyzing the possible physical reasons behind the fit residual increase described in the previous paragraph, we need to discard that these deviations are not introduced by systematic disagreements between the different SFR tracers combined to produce our reference Σ_{SFR} (§3.2). In order to explore this possibility, we first construct two alternative versions of the reference Σ_{SFR} : one that is solely based on the combination of 24 μm and $\text{H}\alpha$, and one that is based on the combination of 24 μm and FUV only. For both cases, we observe a similar systematic increase of the fit residuals as a function of $\langle U \rangle$ as the one shown in Figure 3.4. Therefore, we discard that the way we construct our reference Σ_{SFR} has any implication on the observed trend of the fit residuals.

Next, we try to identify the physical basis for the systematic increase of the fit residuals. As we mentioned before, at least $\sim 85\%$ of the regions with warm IR colors ($\gtrsim 1.3$) show evidence of high radiation fields. These regions also show lower PAH abundances, which is expected given that it appears that PAHs are destroyed in HII regions (Povich et al. 2007). One of the possible reasons for the systematic increase of the residual towards positive values is the decrease of the photoelectric heating efficiency due to the positive charging of the dust grains and the decrease in the gas heating rates due the lower abundance of PAHs. What this implies for the purpose of measuring the Σ_{SFR} (or SFR) based on $\Sigma_{[\text{CII}]}$ (or $L_{[\text{CII}]}$) alone is that a simple calibration that ignores dust color temperature will underestimate the amount of star formation activity in these regions.

3.4.2 IR Color Adjustment

Motivated by the observed systematic increase of the fit residual after a given IR color threshold, we derived an IR color adjustment that accounts for the underestimation of Σ_{SFR} (or SFR). We choose an adjustment based on an IR color, over a model-dependent variable adjustment (e.g., $\langle U \rangle$), because the IR color is an observable, free of assumptions and easier to measure. For a given IR color $\gamma(\lambda_1, \lambda_2) = \nu f_\nu(\lambda_1 \text{ } \mu\text{m})/\nu f_\nu(\lambda_2 \text{ } \mu\text{m})$, we define the IR color factor Ψ as:

$$\Psi(\gamma) = \begin{cases} 1 & \text{if } \gamma < \gamma_t \\ (\gamma/\gamma_t)^\alpha & \text{if } \gamma \geq \gamma_t. \end{cases} \quad (3.4)$$

The IR color threshold, γ_t , and the power law exponent, α , are derived in order to minimize the logarithmic residuals between the observed and the [C II]-based Σ_{SFR} (or SFR). Values of γ_t and α for the IR colors $\gamma(70, 100)$ and $\gamma(70, 160)$ are listed in Table 3.2. This proposed IR color based adjustment Ψ represents a simple and straightforward attempt to account for the systematic increment of the fit residual of regions that show warm colors/high radiation fields. Based on the IR color factor Ψ , the adjusted [C II] surface brightness (or luminosity) can now be written as $\Sigma_{[\text{CII}]} \times \Psi$ (or $L_{[\text{CII}]} \times \Psi$).

The effects of the IR color adjustment on the correlation residuals are shown in the right panels of Figure 3.4. The red squares show the adjusted median residuals as a function of IR color, $\langle U \rangle$, $f(L_{\text{IR}}; U > 100)$ and q_{PAH} . By design, the IR color adjustment removes the trend of increasing residuals with IR color for warmer regions. This is true even for the last bin in IR color where the difference between the adjusted and the unadjusted data is a factor of ~ 3 . As the second and third left panels show, applying the IR color adjustment also helps to remove the trend

Table 3.2: IR Color Adjustment Coefficients

$\log_{10}(\Sigma_{\text{SFR}}) = m \times \log_{10}(\Sigma_{[\text{CII}]} \times \Psi(\gamma)) + N$		
IR Color (γ)	Threshold (γ_t)	α
$\nu f_\nu(70 \mu\text{m})/\nu f_\nu(160 \mu\text{m})$	1.24	0.94
$\nu f_\nu(70 \mu\text{m})/\nu f_\nu(100 \mu\text{m})$	0.80	1.57

$\log_{10}(\text{SFR}) = m \times \log_{10}(L_{[\text{CII}]} \times \Psi(\gamma)) + N$		
IR Color (γ)	Threshold (γ_t)	α
$\nu f_\nu(70 \mu\text{m})/\nu f_\nu(160 \mu\text{m})$	1.12	1.20
$\nu f_\nu(70 \mu\text{m})/\nu f_\nu(100 \mu\text{m})$	0.80	1.90

Note: Coefficients m and N can be found in Table 3.3

of increasing residuals with $\langle U \rangle$ and $f(L_{\text{IR}}; U > 100)$. This is a consequence of the large overlap between regions with warm colors and high radiation field signatures. In the case of the PAH abundance, the fourth panel show that the IR color adjustment helps to reduce the increasing residuals as a function of q_{PAH} . This is expected given the correlation between IR color, $\langle U \rangle$ and q_{PAH} .

3.4.3 Galaxy-to-Galaxy Variations

In this section we continue the study of the scatter of the correlation, but this time in terms of the galaxy-to-galaxy variations. Treating each galaxy as a single point is an oversimplification of the underlying physics, but it is useful because frequently only a global measurement of the [C II] flux can be obtained.

In order to analyze how much each galaxy deviates from the fit as a whole, we fix the slope to that determined for the $\Sigma_{[\text{CII}]}-\Sigma_{\text{SFR}}$ correlation (i.e. 1.13 ± 0.01 , eq. 4.5) and then we calculate the median residual for each galaxy. Figure 3.5 shows the median fit residual as a function of IR color ($\nu f_\nu(70)/\nu f_\nu(160)$), dust-weighted mean

starlight intensity $\langle U \rangle$, fraction of the IR luminosity radiated from regions with high radiation fields, $f(L_{\text{IR}}; U > 100)$ and the global measurements of oxygen abundance ($12 + \log_{10}(\text{O}/\text{H})$). Each point represents one galaxy. Those with mean IR colors below the IR color adjustment threshold (i.e. $\gamma_t(70, 160) = 1.24$) are shown as filled circles. The rest of the galaxies, for which the IR color adjustment applies, are shown as filled and open squares for unadjusted and adjusted mean residual values, respectively.

The first panel of Figure 3.5 shows the median residuals as a function of IR color. Starting around $\nu f_\nu(70)/\nu f_\nu(160) \sim 1.2$, we observe a trend of increasing residuals with warmer IR color, similar to what we find in the analysis for the resolved regions (§4.1). The effect of the IR color adjustment on the residuals is clearly shown by the growing separation between the unadjusted and adjusted mean residual values as a function of IR color. The second and the third panels show the residual as a function of two radiation field strength related parameters: $\langle U \rangle$ and $f(L_{\text{IR}}; U > 100)$. We find that systems with $\langle U \rangle \gtrsim 3$ or $f(L_{\text{IR}}; U > 100) \gtrsim 20\%$ start to show increasing deviations from the fit. This is similar to what we observe in the IR color panel and expected given the close connection between the radiation field strength and the IR color. As we previously showed in the analysis of the resolved regions, it is clear from these two panels how the IR color adjustment helps to reduce the absolute scatter in the correlation. In terms of the standard deviation of the median residuals, applying the IR color adjustment reduces the galaxy-to-galaxy scatter from 0.22 dex to 0.16 dex.

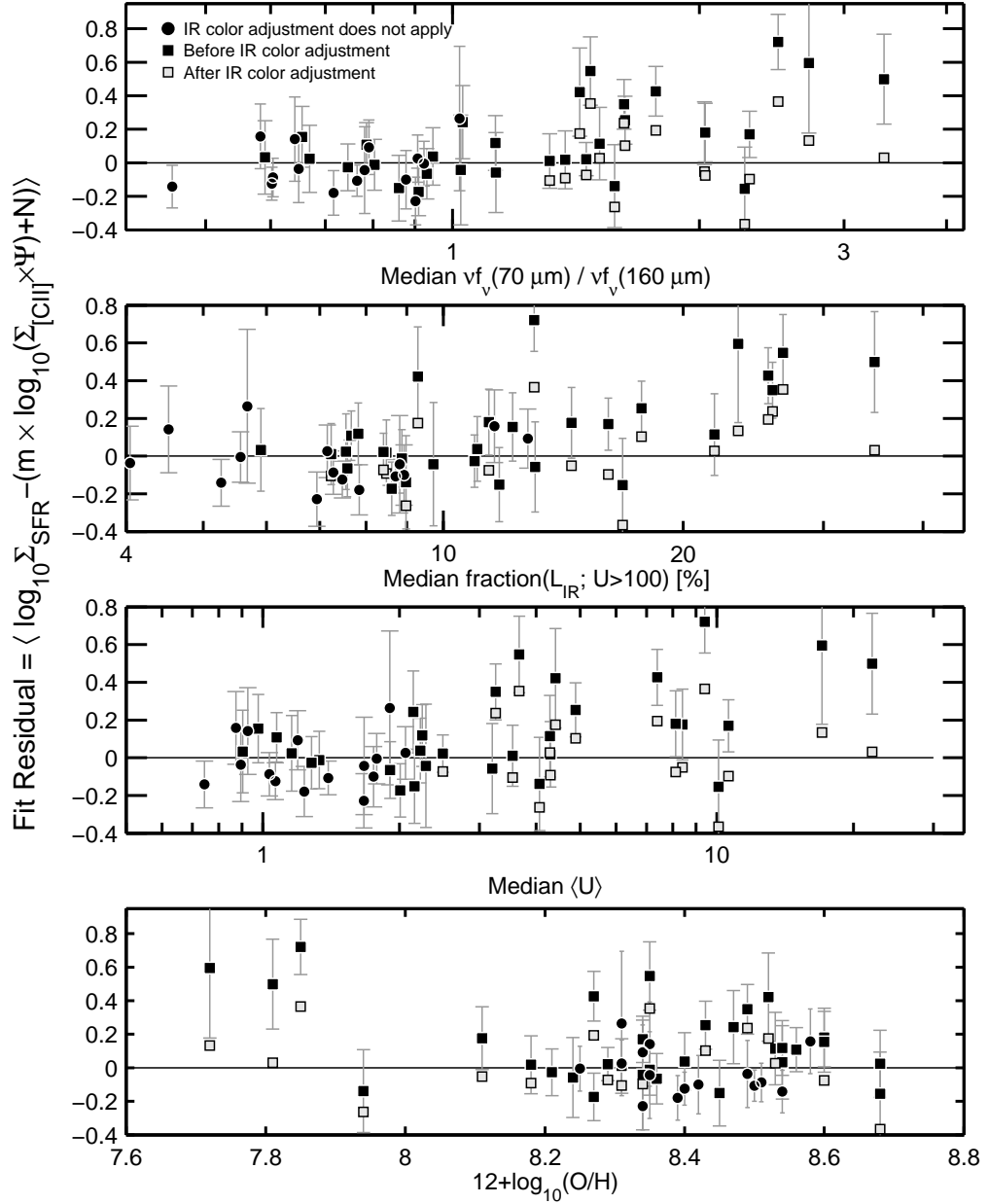


Figure 3.5: Median of the fit residual for each of the 46 galaxies in our sample versus median IR color ($\nu f_{\nu}(70 \mu\text{m})/\nu f_{\nu}(160 \mu\text{m})$), median radiation field ($\langle U \rangle$), median fraction of the luminosity coming from regions with $U > 100$ and oxygen abundance ($12 + \log(\text{O}/\text{H})$). The vertical bars represent $1-\sigma$ standard deviation around the median. Black squares and open squares show the median fit residual before and after applying the IR color adjustment. Black circles show the median fit residual for galaxies that, on average, are not warm enough to apply the IR color adjustment.

3.4.4 Low Metallicity Galaxies

The KINGFISH sample contains only a handful of low metallicity systems, which despite their paucity show some potentially interesting trends. The bottom panel in Figure 3.5 shows that low metallicities galaxies tend to deviate from the fit. What this implies for the three of them – Holmberg II, IC 2574, and NGC 5408 –, is that the [C II]-based calibration yields a SFR that is at least a factor of ~ 4 lower than the SFR measured using the standard tracers available (i.e. FUV+24 μm for Holmberg II and IC 2574, and 24 μm for NGC 5408). These are diffuse galaxies with no well-defined bulge or nucleus, so we discard potential AGN contamination in the SFR measurement (Moustakas et al. 2010). In the case of the irregular dwarf galaxy IC 2574, the [C II] data covers only the HI supergiant shell located in the northeast part of the galaxy discovered by Walter et al. (1998). This region contains a central stellar cluster about 11 Myr old and recent star formation activity located in the rim of the expanding shell (Stewart & Walter 2000). This far-UV intense environment heats the surrounding dust grains, resulting in high dust temperatures. In fact, this region from IC 2574, together with Holmberg II and NGC 5408, correspond to the three warmest systems in our sample as measured by their IR colors: for an emissivity index of $\beta = 1.5$, their dust color temperatures are in the $T_{\text{dust}} = 30\text{--}34$ K range. In addition, these galaxies have [C II] to total infrared (TIR) luminosity ratios in the 0.35 – 0.6% range. This is slightly higher than the 0.3% measured for the Milky Way (Wright et al. 1991). Compared to other low metallicity systems, these ratios are lower than those found for NGC 4214 (0.5 – 0.8%, Cormier et al. 2010) and the Large Magellanic Cloud (0.9%, Rubin et al. 2009), and higher than those measured in 30 Doradus (0.12%, Poglitsch et al. 1995) and Haro 11 (0.1%, Cormier et al. 2012).

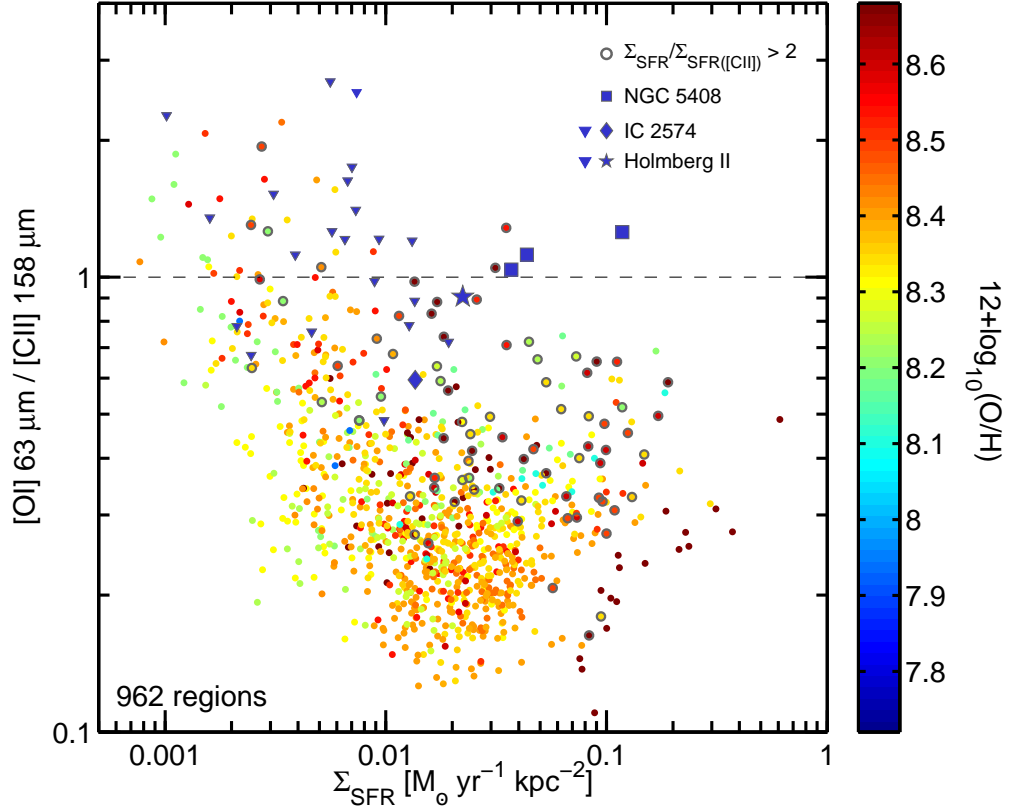


Figure 3.6: Ratio between the [OI] $63 \mu\text{m}$ and [C II] $158 \mu\text{m}$ emission for regions selected from the KINGFISH sample as a function of the SFR surface density (Σ_{SFR}) measured as the combination of $24 \mu\text{m}$, $\text{H}\alpha$ and FUV emission (see §3.2). The color scale shows the global metallicity value of the galaxy from Moustakas et al. (2010). The circles with grey border show regions where this Σ_{SFR} value is greater than the [C II]-based Σ_{SFR} by more than a factor of two. The panel also shows regions selected from three low metallicity systems: Holmberg II (star), IC 2574 (diamond) and NGC 5408 (square). The triangles pointing down correspond to $3\text{-}\sigma$ upper limits due to non-detections in [OI] $63 \mu\text{m}$ emission. These low metallicity regions also tend to show [C II]-based Σ_{SFR} values that are lower than Σ_{SFR} by a factor of two or more (see Figure 3.5, panel 4).

There are multiple factors that can play a role in the high $\Sigma_{\text{SFR}}/\Sigma_{\text{SFR}([\text{C II}]})$ ratios observed in low metallicity regions (e.g., De Looze et al. 2014). If we assume that it is correct to use the same method to measure Σ_{SFR} in both high and low metallicity regions, then the high residuals can only be explained by variations in the heating and [C II]-cooling as a function of metallicity. On one hand, in low-metallicity environments low PAH abundances, low dust-to-gas ratios, and low FUV extinction reduce the gas heating efficiency and heating rate. On the other, FUV photons produced by O and B stars travel farther from their point of origin, thereby producing a low diffuse FUV flux in much of the ISM that may keep dust grains mostly electrically neutral and maintain a high gas heating efficiency (Israel & Maloney 2011). Note, however, that we measure the highest dust temperatures, implying high dust-weighted mean starlight intensities ($\langle U \rangle > 10$), in our low metallicity sample.

A possible explanation of the deviations observed in low metallicity regions is that we are missing a non-negligible fraction of the neutral gas cooling, coming out in FIR lines other than [C II] (e.g., [O I] 63 μm). In order to explore this scenario, we measure the ratio of the [O I] 63 μm to [C II] emission as a function of the SFR surface density. Figure 3.6 shows the line ratio for 962 regions in the KINGFISH sample for which we have [O I] 63 μm and [C II] detections with $S/N > 3$. At low Σ_{SFR} values, regions tend to have higher [O I] 63 μm to [C II] line ratios compared to the rest of the sample. To investigate this, we have done data simulations in which we apply different S/N cuts, and we find that the absence of regions with small line ratios at low Σ_{SFR} is not real, but most likely a bias introduced by the selection of the $S/N = 3$ cut. From Figure 3.6 we conclude that the [O I] 63 μm line emission is not the dominant cooling channel for the KINGFISH metal-rich regions. We also include in the plot the three low metallicity systems in our sample: NGC 5408

(blue) and $3\text{-}\sigma$ upper limits for Holmberg II (red) and IC 2574 (magenta). Together with these low metallicity regions, the other regions in our sample that show Σ_{SFR} to $\Sigma_{\text{SFR}([\text{C II}])}$ ratios greater than two are shown as circles with grey border. It can be seen that these regions tend to show higher $[\text{O I}] 63 \mu\text{m}$ to $[\text{C II}]$ line ratios than the rest of the sample. In the case of NGC 5408, the cooling of the neutral gas is approximately equally split between the $[\text{C II}]$ and $[\text{O I}] 63 \mu\text{m}$ transitions. This result is similar to the $[\text{C II}]$ to $[\text{O I}] 63\mu\text{m}$ ratios of 1.1 and 1.2 measured by Hunter et al. (2001) for the irregular galaxies NGC 1569 and IC 4662, respectively. For Holmberg II and IC 2574, the upper limits do not rule out the possibility of a non-negligible contribution to the cooling of the neutral gas via $[\text{O I}] 63 \mu\text{m}$. What this implies for low metallicity regions, is that a purely $[\text{C II}]$ -based SFR calibration would underestimate the total SFR value; for NGC 5408, this would account for at least half of the factor of ~ 4 deviation.

Can $[\text{O I}] 63 \mu\text{m}$ emission be used to provide a better SFR estimate? De Looze et al. (2014) find that a $[\text{C II}]$ -based SFR calibration systematically underestimates the SFR as a function of increasing $[\text{O I}] 63 \mu\text{m}/([\text{C II}]+[\text{O I}] 63 \mu\text{m})$ ratio. For regions with sub-solar metallicity, they conclude that $[\text{O I}] 63 \mu\text{m}$ is a more reliable SFR tracer than $[\text{C II}]$ emission. Over the same KINGFISH sample we study in $[\text{C II}]$, the $\Sigma_{[\text{O I}]} - \Sigma_{\text{SFR}}$ correlation has a slope of 1.2 and a scatter of 0.25 dex. This is less linear and has higher scatter than what we measure in the $\Sigma_{[\text{C II}]} - \Sigma_{\text{SFR}}$ correlation. It is possible that the sample of dwarf galaxies in De Looze et al. (2014) is biased towards starbursting systems, where stronger radiation fields arising from dense PDRs favor $[\text{O I}]$ as a more reliable star formation tracer than $[\text{C II}]$. If we combine the $[\text{C II}]$ and $[\text{O I}] 63 \mu\text{m}$ emission in our sample, we find that the slope and the scatter of the correlation between $\Sigma_{[\text{C II}]+[\text{O I}]} - \Sigma_{\text{SFR}}$ are similar to that of the $\Sigma_{[\text{C II}]} - \Sigma_{\text{SFR}}$ correlation.

Perhaps more importantly, at lower metallicities we expect lower dust optical depth, resulting in regions that are more transparent to the FUV radiation than their metal-rich counterparts because of low dust-to-gas ratios. Under these conditions, the fraction of FUV photons that escapes the system without interactions with the dust is larger than at normal metallicity. In dense PDRs – the main source of [O I] emission – the FUV leakage would play against the production of both lines, [C II] and [O I], for which interaction of FUV photons with the dust is required for heating. We speculate, however, that the lower density material that emits preferentially in [C II] is more affected by the escape of FUV photons, giving rise to higher [O I] $63\ \mu\text{m}$ /[C II] ratios in these sources. This would help to explain the high [O I] $63\ \mu\text{m}$ /[C II] ratios observed in the low-metallicity regions compared to the rest of the sample.

A higher fraction of escaping FUV photons at low metallicity would also imply that the IR emission would not be able to account for the total value of the SFR. As an example, Calzetti et al. (2007) find that using $24\ \mu\text{m}$ emission can underestimate the SFR of low metallicity systems by a factor of $\sim 2 - 4$. In order to explore this scenario we measure the FUV to [C II] and FUV to TIR ratios, which can be used as a rough measure of the amount of extinction at ultraviolet wavelengths (Dale et al. 2007). We find that the mean FUV to [C II] ratio (and the corresponding 68% range in parenthesis) for the low metallicity regions from Holmberg II and IC 2574 is $281(134 - 588)$, whereas the remaining 31 galaxies with FUV data available have a median FUV to [C II] ratio of $32(13 - 77)$. We observe a similar trend for the FUV to TIR ratios. Thus our results favor the scenario described above, where a larger fraction of escaping FUV photons in low metallicity regions would mostly explain the low SFRs based on [C II] emission.

3.4.5 Dependence of the correlation fit parameters with distance and inclination

The galaxies in our sample span a range in distance (2.8 – 26.5 Mpc) and inclination ($\lesssim 75^\circ$) that might have potential consequences on the individual $\Sigma_{[\text{C II}]} - \Sigma_{\text{SFR}}$ correlation properties. To test this, we look for trends between the correlation fit parameters and the distance or inclination of the source. We fit the $\Sigma_{[\text{C II}]} - \Sigma_{\text{SFR}}$ correlation for each individual galaxy using the OLS bisector method (we leave out of this analysis four galaxies that have fewer than 5 pointings with $S/N > 3$). We do not find any clear trend between the fit parameters (i.e., slope and normalization) with distance or inclination. The Pearson correlation coefficient for the four correlations made as the combination of the slope/normalization versus the distance/inclination is less than ~ 0.2 for all the cases. Therefore we conclude that the calibrations presented here are robust to spatial resolution and inclination.

3.4.6 The [C II] – star formation rate correlation before and after the IR color adjustment

As we show in §4.1 and §4.2, it is possible to use an IR color based adjustment to reduce the scatter of both the $\Sigma_{\text{SFR}} - \Sigma_{[\text{C II}]}$ and $\text{SFR} - L_{[\text{C II}]}$ correlations. The consequences of applying these adjustments are shown in Fig. 3.7. The left panel shows the $\Sigma_{[\text{C II}]} - \Sigma_{\text{SFR}}$ correlation before applying the IR color adjustment. The regions that are warm enough to be modified by the adjustment ($\nu f_\nu(70)/\nu f_\nu(160) \geq 1.25$) are shown as blue dots. The black solid line correspond to the best fit to the data (eq. 4.5). The right panel on Fig. 3.7 shows the correlation after applying the IR color adjustment. The net effect is that the asymmetry of the scatter cloud decreases, reducing the dispersion of the correlation to 0.19 dex. The OLS bisector

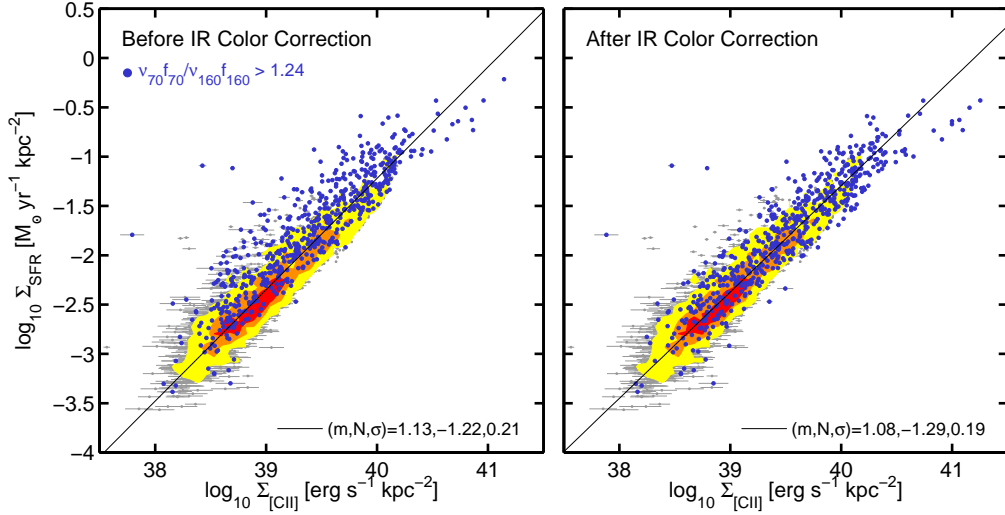


Figure 3.7: (*Left*) Star formation rate surface density, Σ_{SFR} , as a function of [C II] $\tilde{1}58\ \mu\text{m}$ surface brightness, $\Sigma_{[\text{CII}]}$, for 46 galaxies from the KINGFISH sample. Σ_{SFR} is estimated from $\text{H}\alpha+24\ \mu\text{m}$ (when $\text{H}\alpha$ is available), $\text{FUV}+24\ \mu\text{m}$ (when $\text{H}\alpha$ is not available) and only $24\ \mu\text{m}$ when neither $\text{H}\alpha$ nor FUV maps are available. Gray points correspond to $12''$ (1 beam) size regions and contours show data density. The numbers on the bottom-right corner of each panel correspond to the fit parameters: slope (m), y -axis value at $x = 40$ (N) and 1σ standard deviation (σ). (*Right*) Same as left panel, but for this case we adjusted the $\Sigma_{[\text{CII}]}$ using the IR color adjustment described in equation 3.4.

fit to the IR color corrected correlation yields a slope that is slightly closer to linear (1.08).

Table 3.3 summarizes the best-fit parameters we measure for the $\Sigma_{\text{SFR}}-\Sigma_{[\text{CII}]}$ and $\text{SFR}-L_{[\text{CII}]}$ correlations. We also list the $1-\sigma$ dispersion around the fit and the correlation coefficient r_{corr} . We include the calibration coefficients for four different cases: (1) the correlation including the $24\ \mu\text{m}$ normal cirrus subtraction. These correspond to the coefficients in equation (4.5) and equation (3.3); (2) same as (1), but after applying the IR color adjustment from equation (3.4); (3) the correlation after applying the strong $24\ \mu\text{m}$ cirrus subtraction (which assumes $U_{\text{cirrus}} = U_{\text{min}}$); (4) if we fit the correlation using a fixed slope of 1. For regions or galaxies in the surface brightness range of the KINGFISH sample ($10^{39} \lesssim \Sigma_{[\text{CII}]} \lesssim 10^{40.5}$ [$\text{erg s}^{-1} \text{kpc}^{-2}$]),

Table 3.3: [C II]-SFR calibration coefficients and uncertainties

$$\log_{10}(\Sigma_{\text{SFR}}/[M_{\odot} \text{ yr}^{-1} \text{ kpc}^{-2}]) = m \times (\log_{10}(\Sigma_{[\text{CII}]}/[\text{erg s}^{-1} \text{ kpc}^{-2}]) - 40) + N$$

Description	Slope m	Normalization ^a N	Scatter [1 σ dex]	r_{corr}
Normal 24 μm Cirrus (Eq. 4.5)	1.13 ± 0.01	-1.22 ± 0.01	0.21	0.92
IR Color Adjusted	1.08 ± 0.01	-1.29 ± 0.01	0.19	0.93
Strong 24 μm Cirrus	1.18 ± 0.01	-1.25 ± 0.02	0.23	0.90
Fixed Slope	1.00	-1.34 ± 0.01	0.21	0.92

$$\log_{10}(\text{SFR}/[M_{\odot} \text{ yr}^{-1}]) = m \times (\log_{10}(L_{[\text{CII}]}/[\text{erg s}^{-1}]) - 40) + N$$

Description	Slope m	Normalization ^b N	Scatter [1 σ dex]	r_{corr}
Normal 24 μm Cirrus (Eq. 3.3)	1.03 ± 0.01	-1.28 ± 0.01	0.22	0.94
IR Color Adjusted	0.98 ± 0.01	-1.40 ± 0.01	0.20	0.96
Strong 24 μm Cirrus	1.03 ± 0.01	-1.02 ± 0.01	0.24	0.92
Fixed Slope	1.00	-1.32 ± 0.01	0.22	0.94

^a

The normalization N is the value of $\log_{10}(\Sigma_{\text{SFR}}/[M_{\odot} \text{ yr}^{-1} \text{ kpc}^{-2}])$ at $\log_{10}(\Sigma_{[\text{CII}]}/[\text{erg s}^{-1} \text{ kpc}^{-2}]) = 40$.

^b The normalization N is the value of $\log_{10}(\text{SFR}/[M_{\odot} \text{ yr}^{-1}])$ at $\log_{10}(L_{[\text{CII}]}/[\text{erg s}^{-1}]) = 40$.

the resulting SFRs using the calibration parameters from the first two cases are very similar. However, the calibration coefficients from case 1 (Eq. 4.5 and Eq. 3.3) seem better suited to measure SFRs in higher surface brightness objects (e.g., LIRGs) as can be seen in the next section.

As a summary, the [C II]-based calibration can be written as:

$$\log_{10}(\Sigma_{\text{SFR}}) = m \times (\log_{10}(\Sigma_{[\text{CII}]} \times \Psi(\gamma)) - 40) + N \quad (3.5)$$

where the calibration coefficients m and N are listed in Table 3.3. We recommend

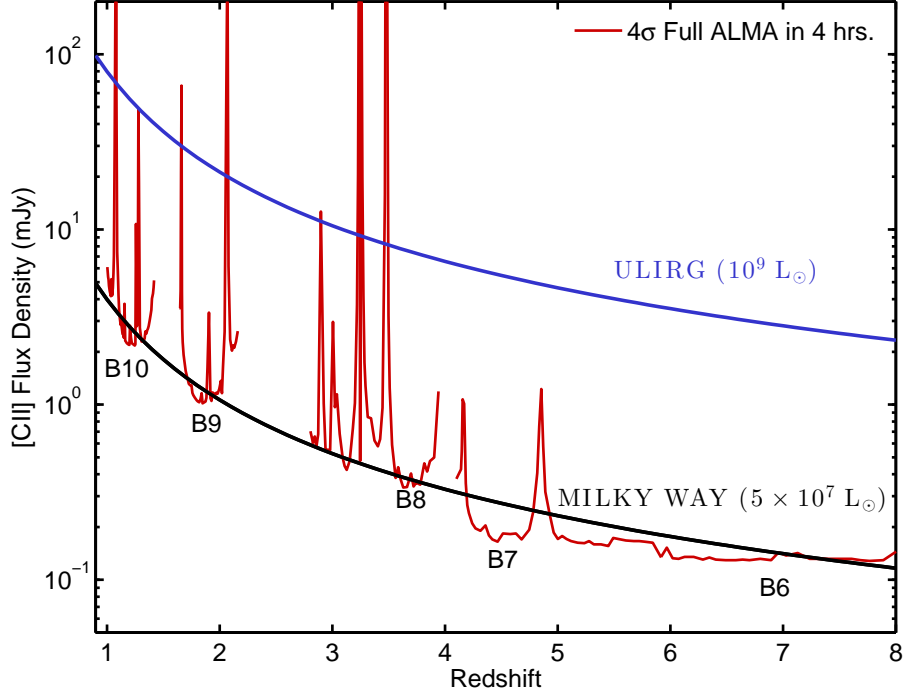


Figure 3.8: ALMA’s ability to detect Milky Way type (black line at $5 \times 10^7 L_{\odot}$; Bennett et al. 1994; Wright et al. 1991) and ultraluminous infrared type galaxies (blue line at $10^9 L_{\odot}$) in the [C II] $\tilde{158} \mu\text{m}$ transition after 4 hours of time integration as a function of redshift. The red line represents ALMA’s sensitivity estimated using the ALMA sensitivity calculator (assuming a linewidth of 300 km/s). From Band 10 (B10) to Band 6 (B6), galaxies can be detected by ALMA in the [C II] transition in the redshift range of $z \sim 1.2 - 7$.

using the calibration coefficients from Equation 4.5. If there is IR color information available, we also recommend to use Table 3.2 to measure the IR color factor Ψ and apply the IR color adjustment to the [C II] emission.

3.5 Comparison with Models and Observations

3.5.1 Comparison to other extragalactic [C II] samples

Comparing our results with previous analyses done for samples of galaxies observed in [C II] by *ISO* and *Herschel* can provide useful information about the reliability

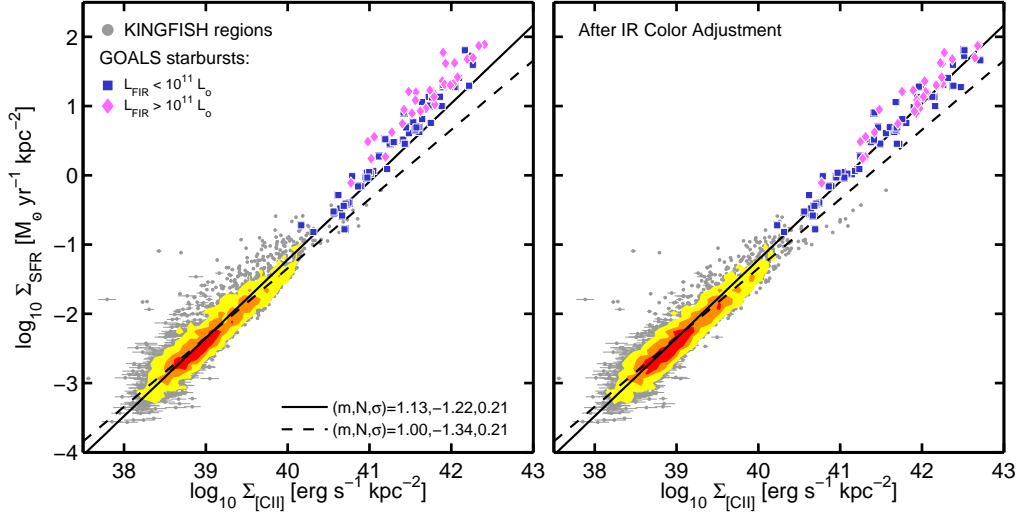


Figure 3.9: (*Left*) Star formation rate surface density versus [C II] surface brightness for resolved regions from the KINGFISH sample (grey points and color density contours) and global measurements from a subset of pure starburst systems from the GOALS sample. These were selected using their $6.2 \mu\text{m}$ PAH EW. The blue squares and the magenta diamonds show the GOALS galaxies that have IR luminosities lower and higher than $10^{11} L_{\odot}$, respectively. The solid and the dashed line correspond to Equation 4.5 and the fit with a fixed slope of 1, respectively. The numbers on the bottom-right corner correspond to the fit parameters: slope (m), y -axis value at $x = 40$ (N) and 1σ standard deviation in dex (σ). These are the same parameters as in equation 4.5. (*Right*) Same as left panel, but for this case we adjusted the $\Sigma_{[\text{C II}]}$ in both samples using the IR color adjustment described in equation 3.4. The solid and dashed line are the same as in the left panel.

and limits of applicability of our [C II]-based SFR calibration. This is particularly true for very luminous galaxies, which are poorly represented in the KINGFISH sample. This comparison can be done in surface density or luminosity space. Surface density comparisons are the most interesting from a physical standpoint, since they are distance independent. Moreover, surface density is more directly related to parameters like radiation field intensity, which are thought to dominate the physical processes in PDRs. Luminosity, on the other hand, is frequently the only measurement directly available for very distant galaxies, and it is thus also interesting to investigate. For instance, Figure 3.8 shows ALMA’s ability to detect, in the [C II]

transition, galaxies like the Milky Way and ULIRGs as a function of redshift. For an integration time of 4 hours, the full ALMA can potentially detect in the [C II] transition Milky Way type galaxies at redshift intervals that span the range from $z \sim 1.2$ to 7.

First, we do the comparison in the surface density space. For this purpose, we use galaxies from the Great Observatories All-sky LIRG Survey (Armus et al. 2009, GOALS). A brief description of the selection criteria and properties of the GOALS systems included in this analysis is available in Appendix A.5. Figure 3.9 shows the $\Sigma_{\text{SFR}} - \Sigma_{[\text{CII}]}$ correlation for the KINGFISH regions and the GOALS galaxies; the latter are divided in pure starburst with $L_{\text{FIR}} < 10^{11} L_{\odot}$ and non-AGN U/LIRGs. The left and right panels show the correlation before and after applying the IR color adjustment, respectively. The solid line in both panels represents equation (4.5). The dashed line correspond to the best linear fit to the KINGFISH regions (Table 3.3). For the data with no IR color adjustment applied, the GOALS pure starburst galaxies with $L_{\text{FIR}} < 10^{11} L_{\odot}$ and $\Sigma_{[\text{CII}]} \lesssim 10^{41.5} [\text{erg s}^{-1} \text{ kpc}^{-2}]$ agree well with equation (4.5). At greater luminosity surface densities, these systems start to systematically deviate from the fit, although they still lie roughly within a factor of two from equation (4.5). On the other hand, all the non-AGN U/LIRGs lie above the fit, following a trend parallel to the KINGFISH data. If we fit the GOALS pure starburst with $L_{\text{FIR}} < 10^{11} L_{\odot}$ and non-AGN U/LIRGs using the slope from equation (4.5), we find that the fit normalization is, on average, a factor 1.5 and 3 higher, respectively. When compared to the linear fit, GOALS starbursts galaxies with $\Sigma_{[\text{CII}]} \gtrsim 10^{41} [\text{erg s}^{-1} \text{ kpc}^{-2}]$ show deviations in the $\sim 5 - 10$ range. As we show in §4.1, part of these deviations are associated to the IR color of the region. Therefore, we apply the IR adjustment derived for the KINGFISH sample to the regions and galaxies in both samples. The right panel in Figure 3.9 shows the IR

color adjusted correlation, where the good agreement between the KINGFISH and the GOALS samples with Equation (4.5) across nearly 5 orders of magnitude in $\Sigma_{[\text{C II}]}$ and Σ_{SFR} is evident. On the other hand, the linear [C II]-based calibration – even after applying the IR color adjustment – continue to underestimate the reference Σ_{SFR} value.

Next, we do the comparison in luminosity space. In addition to the galaxies from the GOALS sample, we include in the analysis galaxies used by Boselli et al. (2002), De Looze et al. (2011) and Sargsyan et al. (2012) to derive their [C II]-based SFR calibrations. We also include non-AGN, non-merger LIRGs from Weiner et al. (in prep.). The general properties of these additional samples of galaxies are described in Appendix A.5. In order to compare our KINGFISH results to the other samples, we re-derive their published SFRs and TIR luminosities, so we can ensure uniformity and comparability to our work.

The results of the comparison between the KINGFISH galaxies and the samples described above are shown in Fig. 3.10. The two panels show the ratio of the [C II]-based SFR calibration (Equation 3.3) to the SFR measured using standard tracers as a function of TIR luminosity. Each black point corresponds to the mean SFR of a KINGFISH galaxy, and the vertical bars represent the $1\text{-}\sigma$ standard deviation around the mean value. The TIR luminosity of the KINGFISH galaxies was measured over the area covered by the [C II] observations and not the entire system. The left panel shows the galaxies before applying the IR color adjustment. We see that the largest deviations occur at both TIR luminosity ends. At $L_{\text{TIR}} \lesssim 10^9 L_{\odot}$, 6 out of the 8 systems that show deviations larger than a factor of ~ 3 have metallicities below $12 + \log_{10}(\text{O}/\text{H}) \lesssim 8.2$: Holmberg II and IC 2574 from the KINGFISH sample; NGC 625, NGC 1569 and NGC 1156 from De Looze et al. (2011) sample; IC 4662 from Boselli et al. (2002) sample. The remaining two galaxies, NGC 4698

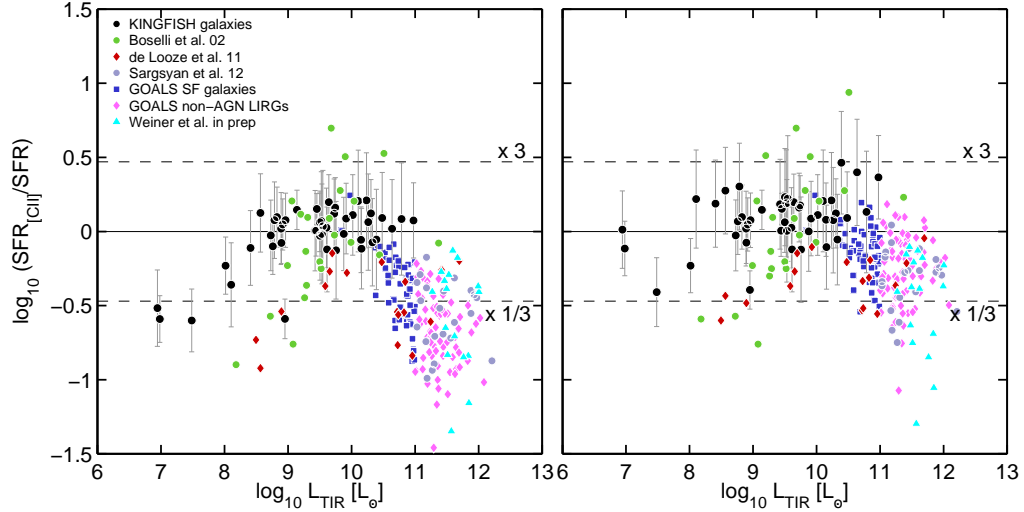


Figure 3.10: Ratio of the SFR measured using this work [C II] calibration (Eq. 3.3) to the SFR measured based on tracers other than [C II]. We treat each KINGFISH galaxy as an individual point (black circle) by taking the median value of the SFR and the sum of the TIR luminosity of all the regions in the galaxy that were observed in [C II]. The vertical bar represents the $1\text{-}\sigma$ standard deviation around the SFR median. The other galaxy global measurements correspond to Boselli et al. 2002 (green circles), De Looze et al. 2011 (red diamonds), Sargsyan et al. 2012 (purple circles), Díaz-Santos et al. (2013) (blue squares and magenta diamonds) and Weiner et al. in prep (cyan circles). The left and right panels show the data before and after applying the IR color adjustment.

and NGC 4429 from Boselli et al. (2002) sample, do not have metallicity measurements available. At the high TIR luminosity end, the SFR measured using the [C II]–SFR calibration underestimates the SFR(TIR) value for almost all the LIRGs. The non-AGN LIRGs show deviations that can be as high as a factor of ~ 10 . If we fit these systems using the slope from Equation 3.3, we find that the fit normalization is, on average, a factor of 4.4 ± 1.9 higher. Similarly, De Looze et al. (2014) find that in the $L_{[\text{CII}]} - \text{SFR}$ plane, ULIRGs tend to be offset from starburst and AGNs by a factor between 3 and ~ 10 . These deviations are a direct consequence of the significant scatter in the [C II] to TIR ratio observed in U/LIRGs (Brauhar et al. 2008; Díaz-Santos et al. 2013; Malhotra et al. 1997, 2001). It is important to mention, however, that monochromatic IR-based SFR tracers (e.g., $24 \mu\text{m}$) agree much

better with the SFR inferred from [C II] through our calibration; but integrated indicators such as TIR are usually considered better measures of the SFR in U/LIRGs.

The right panel shows the result of applying the IR color adjustment derived in our study. As shown in §4.1, the IR color adjustment helps to reduce the discrepancy for the low-metallicity KINGFISH galaxies; this is also true for the low metallicity systems from the other samples. For the LIRGs, the IR color adjustment proves to have an important effect by reducing the difference between the SFR([C II]) and SFR(TIR) values to less than a factor of two for more than half of the systems. The IR color adjustment is especially effective with the $L_{\text{IR}} < 10^{11} L_{\odot}$ pure starbursts from the GOALS sample. The LIRGs of the Sargsyan et al. (2012) sample, however, are not corrected enough to bring them into good agreement with the calibration. It is possible that the IR color of these galaxies is redder than the color of the regions from which most of the [C II] arises, or maybe the color adjustment – although adequate for the KINGFISH sample – is too mild for many of these systems. If we fit all the LIRGs using the same slope as equation 3.3, we find that the fit normalization is a factor of 1.9 higher. That is, the LIRGs can be placed on a relation approximately parallel to our calibration for normal galaxies, but displaced toward higher SFR per [C II] emission. Note, however, that there is a large scatter of the U/LIRGs around this offset.

In summary, for samples of normal, star-forming galaxies and non-AGN LIRGs, the SFR measured using our [C II]–SFR calibration – after applying IR color adjustment – agrees within a factor of ~ 3 with the SFR from standard SFR tracers ($\text{H}\alpha$, FUV, $24 \mu\text{m}$ and FIR) for at least $\sim 80\%$ of the systems. The remaining galaxies can exhibit deviations as high as factor of ~ 10 , showing the limitations of using the [C II] luminosities to measure SFRs in IR luminous and ultra-luminous systems. This is not the case for the $\Sigma_{[\text{CII}]} - \Sigma_{\text{SFR}}$ correlation, where the KINGFISH regions

and the GOALS starbursts agree within a factor of ~ 2 with the calibration (Equation 4.5) over 5 orders of magnitude in $\Sigma_{[\text{C II}]}$. This calibration is more physically motivated than the luminosity one, because surface densities are connected to the radiation field strength, which has a strong influence on the drivers of the [C II] emission process. In the luminosity case, the same [C II] luminosity can be attained by a combination of high/low [C II] surface brightness over a small/large emitting area. The physical conditions in these two scenarios are significantly different, resulting in large deviations from the calibration for a given fixed [C II] luminosity.

3.5.2 Comparison with Models: Starburst99

In regions where the cooling is dominated by [C II] emission, we expect the FUV heating and the [C II] cooling to be closely related through the photoelectric effect in PAHs and small dust grains. In this section we explore this connection using a simple model based on the *Starburst99* code (Leitherer et al. 1999).

The first step in our calculation is to use *Starburst99* to model the luminosity of a stellar population for a constant SFR over 100 Myr. For the calculations we adopt the default evolutionary tracks, and assume a stellar population with solar metallicity. For the stellar initial mass function (IMF), we adopt the *starburst99* default. The output of the model is the spectrum of a stellar population as a function of the duration of the star formation episode (t_d). From this spectrum, we measure the FUV luminosity by integrating over the FUV range of energy which dominates the grain photoelectric heating, i.e. $6 < E_\gamma < 13.6$ eV. Then, we scale the FUV luminosity by assuming a heating efficiency, ϵ_h , to estimate the amount of heating of the gas. ϵ_h is the product of two factors: (1) the photoelectric heating efficiency of the dust (ϵ_{ph}), that is mainly set by the ratio of the photoionization rate over the recombination rate of electrons with neutral grains/PAHs (Hollenbach & Tielens

1999; Weingartner & Draine 2001). Typical values for ϵ_{ph} are in the 0.1 – 3% range and, (2) the fraction of the FUV photons in the $6 < E_\gamma < 13.6$ eV range that interact with dust and result in gas heating of the neutral and molecular ISM. We assume that the cooling of the gas is dominated by the [C II] transition, so for a given SFR, we connect the [C II] and FUV luminosities via $L_{[\text{C II}]} \sim \epsilon_h \times L_{\text{FUV}}(t_d)$ (as we show in Fig. 3.6, this is a valid assumption for metal-rich regions).

Figure 3.11 shows the model results plotted on top of the $\Sigma_{[\text{C II}]} - \Sigma_{\text{SFR}}$ correlation. Each line represents a model output for a combination of t_d and ϵ_h . Dashed lines correspond to a population with a constant star formation rate and $t_d = 2$ Myr; the solid lines correspond to $t_d \geq 20$ Myr (because we are assuming a constant star formation rate scenario, the variation of the FUV luminosity in the 20 – 100 Myr range is less than $\sim 25\%$). As expected, for a given t_d and Σ_{SFR} , as ϵ_h increases, so does the predicted $\Sigma_{[\text{C II}]}$. Note that there is a degeneracy in the model between t_d and ϵ_h . For instance, the model output for the combination of input parameters $t_d = 2$ Myr and $\epsilon_h = 3\%$ is very similar to the model output when assuming $t_d \geq 20$ Myr and $\epsilon_h = 1\%$.

Figure 3.11 also shows individual star-forming regions (no IR color adjustment applied) selected from 46 KINGFISH galaxies. The data density contours represent the ensemble of all these regions. The bulk of the data can be explained as arising from regions that have been actively star-forming for $t_d > 20$ Myr, with ϵ_h in the 1–3% range. This suggests that the scatter is mainly driven by changes in ϵ_h . On the other hand, to describe the bulk of the data assuming $t_d = 2$ Myr requires an unusually high heating efficiency of $\epsilon_h > 3\%$.

The model suggests two possible explanations to describe the regions that deviate the most from the main trend and tend to lie in the upper side of the scatter cloud: (1) an early stage of the star formation episode ($t_d = 2$ Myr) and ϵ_h in the 1–3%

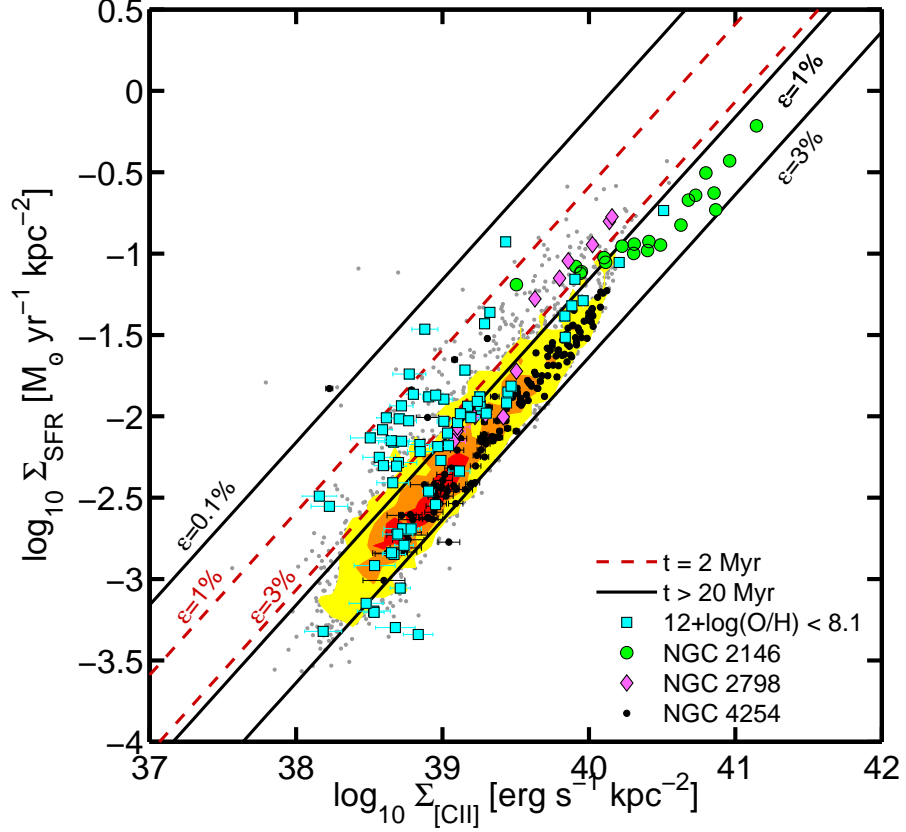


Figure 3.11: Star formation rate surface density versus [C II] surface density (no IR color adjustment applied). The gray points and the corresponding data density contours show the star-forming regions selected from 48 galaxies of the KINGFISH sample. We also highlight individual galaxy cases: NGC 2146 (green circles), NGC 2798 (magenta diamonds), NGC 4254 (black circles) and regions from low metallicity galaxies with $12+\log(\text{O}/\text{H}) \lesssim 8.1$ (cyan squares). The diagonal lines represent the model output. We use *Starburst99* to model the FUV luminosity of a stellar population for a given SFR value and a constant star formation scenario. We then convert the FUV emission into a [C II] surface brightness by assuming a heating efficiency of, ϵ_h . Thus, each diagonal line is the combination of a t_d Myr old population with constant star formation rate and ϵ_h . Dashed lines correspond to $t_d = 2$ Myr; the solid line correspond to $t_d \geq 20$ Myr.

range, or (2) standard star formation duration of $t_d \geq 20$ Myr and low ϵ_h ($\lesssim 1\%$). The second scenario is widely applicable because it does not require fine tuning of the ages, and we know that at high UV fields small grains become positively charged or are destroyed, thus reducing ϵ_h .

Finally, Figure 3.11 highlights four individual cases. One of them, NGC 4254, is a spiral galaxy chosen to illustrate a system that follows the main trend. The other three are:

NGC 2146: this system has the highest total IR luminosity in our sample, $L_{\text{TIR}} = 10^{11} L_{\odot}$ and can be classified as a LIRG. The regions from NGC 2146 have [C II] luminosity surface densities in the range $10^{40} \lesssim \Sigma_{[\text{CII}]} \lesssim 10^{41.3}$ [$\text{erg s}^{-1} \text{kpc}^{-2}$]. The majority of them follow the main trend and can be described by heating efficiencies in the 1 – 3% range and $t_d \geq 20$ Myr.

NGC 2798: about half of the regions of this galaxy show a higher ratio of Σ_{SFR} to $\Sigma_{[\text{CII}]}$ compared to the rest of the data. NGC 2798 is a barred spiral that is part of an interacting pair with NGC 2799. There is evidence from UV spectra for a recent burst of star formation (Joseph et al. 1986). This agrees well with the calculations for a duration of the star formation of about $t_d = 2$ Myr and ϵ_h in the range 1–3%.

Galaxies with $12 + \log(\text{O}/\text{H}) < 8.1$: here we select regions from four low metallicity galaxies that have oxygen abundances $12 + \log(\text{O}/\text{H}) < 8.1$. These systems are: Holmberg II, IC 2574, NGC 2915, and NGC 5408 (Moustakas et al. 2010). As shown in Fig. 3.5, about half of the low metallicity regions deviate from the fit showing higher $\Sigma_{\text{SFR}}/\Sigma_{[\text{CII}]}$ ratios than the rest of the points. In these systems two scenarios are possible: (1) the regions are young and have been forming stars at a continuous rate for only $t_d = 2$ Myr, and the heating efficiency is in the $\epsilon_h \simeq 1 - 3\%$ range; (2) the regions have been forming stars at a continuous rate for $t_d \geq 20$ Myr and the heating efficiency of the medium is lower than $\epsilon_h \sim 1\%$. As we concluded in

§4.2.2, the deviations observed in low metallicity regions are most likely described by the latter scenario, where a reduction in the heating efficiency is expected due to reduced trapping of FUV photons by the dust.

3.6 Summary and Conclusions

We study the [C II] 158 μm line emission and its potential to be used as a star formation rate tracer using a set of nearby galaxies drawn from the *Herschel* KINGFISH sample. The [C II] surface brightness, $\Sigma_{[\text{CII}]}$, can be used as a robust Σ_{SFR} tracer in normal, star-forming galaxies in the absence of strong AGNs. In this work we present a calibration for that relation (Equation 4.5) that is based on 3,486 regions selected from 46 nearby galaxies. The uncertainty associated with the calibration is ± 0.21 dex. One of the main sources of scatter are regions with warm IR colors. We derive a set of adjustments based on the IR color factor Ψ (Equation 3.4 and Table 3.2) that helps to reduce the scatter among the warmer regions. Therefore, if the size of the object and two of the 70, 100 and 160 μm fluxes are available, we recommend to measure the SFR surface density using the IR color adjusted version of Equation 4.5:

$$\Sigma_{\text{SFR}} (\text{M}_{\odot} \text{ yr}^{-1} \text{ kpc}^{-2}) = 3.79 \times 10^{-47} \times (\Sigma_{[\text{CII}]} [\text{erg s}^{-1} \text{ kpc}^{-2}] \times \Psi)^{1.13}. \quad (3.6)$$

where Ψ is the color adjustment derived from Equation 3.4 and the values in Table 3.2.

Compared to pure starburst systems from the GOALS sample, this color-adjusted $\Sigma_{[\text{CII}]} - \Sigma_{\text{SFR}}$ correlation is valid over almost 5 orders of magnitude. We caution, however, that blind application of this calibration to systems that may host an AGN or where enough information to determine or bracket the color adjustment Ψ is not

available, risks a significant underestimate of the SFR.

For cases where no information on the size of the emitting object is available, we derive a SFR calibration (Equation 3.3) based on the [C II] luminosity, $L_{[\text{C II}]}$. The dispersion in this correlation is similar to that of the $\Sigma_{[\text{C II}]} - \Sigma_{\text{SFR}}$ correlation. However, when compared to samples of galaxies with $L_{\text{TIR}} > 10^{11} L_{\odot}$, our $L_{[\text{C II}]}$ -based calibration – even after applying the IR color adjustment – can underestimate the SFRs by more than a factor of ~ 3 . We suspect that the reason why the surface brightness calibration has better systematics is because it is more closely related to the local FUV field, most likely the main parameter controlling the photoelectric heating efficiency.

We highlight the following points:

1. We find a tight correlation between the surface brightness of [C II] and $24 \mu\text{m}$ dust emission in normal galaxies. Regions located in the central ~ 1 kpc of galaxies that show AGN activity tend to show an excess of $24 \mu\text{m}$ emission compared to [C II]. After excluding these points, the best linear fit yields a slope of 1.20 ± 0.01 (which is close to the slope measured by Calzetti et al. 2007, for the correlation between $24 \mu\text{m}$ and SFR). The scatter of the correlation is ± 0.23 dex.
2. For each individual region in our galaxy sample, we estimate the contribution from old stars to the $24 \mu\text{m}$ dust emission using the procedure described in Leroy et al. (2012). We refer to this emission as cirrus. We assume that the radiation field produced by these older populations is $U_{\text{cirrus}} = 0.5 \times U_{\text{min}}$, where U_{min} corresponds to the least interstellar radiation field heating the diffuse ISM in the Draine & Li (2007) model. We find that the median $24 \mu\text{m}$ cirrus contribution across the sample is 18%. In order to obtain a more accurate

measure of the SFR based on the 24 μm emission, we subtract from it our estimate of the cirrus contribution.

3. We estimate the SFR and Σ_{SFR} values for each region using a combination of obscured (24 μm and TIR) and unobscured SFR tracers ($\text{H}\alpha$ and FUV). We then derive calibrations for the Σ_{SFR} and SFR based on $L_{[\text{C II}]}$ and $\Sigma_{[\text{C II}]}$, respectively. The calibration coefficients can be found in Table 3.3. We find that, for $\nu f_\nu(70)/\nu f_\nu(160) \gtrsim 1.2$ or $\nu f_\nu(70)/\nu f_\nu(100) \gtrsim 0.8$, the fit residuals systematically increase with increasing IR color (dust temperature), radiation field strength, fraction of the luminosity coming from regions with $U > 100$ and decreasing q_{PAH} . At a slightly higher IR color threshold, $\nu f_\nu(70)/\nu f_\nu(100) \gtrsim 0.95$, Croxall et al. (2012) find a drop in the [C II] to FIR ratio for regions in NGC 4559 and NGC 1097. We parametrize the deviations we find for our warm regions as a function of IR color by a linear fit and derive a set of adjustments that reduces the residuals significantly. The list of IR color adjustments is given in Table 3.2.
4. For regions with oxygen abundances $12 + \log(\text{O}/\text{H}) \lesssim 8.1$, we find that our [C II]-based SFR calibration is not reliable. Regions from the low metallicity galaxies Holmberg II, IC 2574 and NGC 5408 show [C II]-based SFRs that are a factor of ~ 4 smaller than their SFR measured as a combination of 24 μm and FUV emission for the first two systems, and 24 μm for NGC 5408. These regions not only have the highest dust temperatures in the sample, but they also show significantly higher FUV to TIR ratios than their metal-rich counterparts. This suggests that a larger fraction of FUV photons escapes without interacting with the dust. If the [C II] emission is mainly produced by grain photoelectric emission – which requires FUV absorption by dust –

then the reduced trapping of FUV photons would explain the low [C II]-based SFRs observed in low metallicity regions. In addition to this, we find that in NGC 5408 the [O I] $63\mu\text{m}$ to [C II] line ratio can be as high as ~ 1 , thus the cooling can be equally split between these two FIR transitions. For this particular galaxy, a SFR estimated from [C II] alone will underpredict the total SFR by a factor of two. The line ratios and upper limits in Holmberg II and IC 2574 do not rule out a similar scenario for these objects.

5. We find that an IR color adjusted $\Sigma_{[\text{C II}]}$ can provide a good estimation of Σ_{SFR} using Equation (4.5), valid for starburst galaxies over almost 5 orders of magnitude in surface brightness. Without applying the IR color adjustment, KINGFISH regions and starbursts systems with $L_{\text{FIR}} \leq 10^{11} L_{\odot}$ agree within a factor of ~ 2 with Equation 4.5. Starbursts with $L_{\text{FIR}} \geq 10^{11} L_{\odot}$ tend to follow the same trend, but with Σ_{SFR} values that are, on average, a factor of ~ 3 higher for a given $\Sigma_{[\text{C II}]}$.
6. In the luminosity regime, the SFR calibration defined by Equation 3.3 works well for samples of normal, star-forming galaxies (Boselli et al. 2002; De Looze et al. 2011), but underestimates the SFR derived from the TIR value by a factor greater than ~ 3 for more than half of the GOALS galaxies and non-AGN LIRGs (Sargsyan et al. 2012; Weiner et al. in prep.). The IR color adjustment helps to reduce the discrepancy – especially for the GOALS sample – but even after applying the adjustment there are LIRGs that show deviations as high as a factor ~ 10 . This demonstrates the limitations of using the [C II] luminosity as a SFR measure in warm or compact IR luminous and ultra luminous galaxies, for which low [C II] to TIR ratios – or the so called “[C II]-deficit” – have been extensively reported in the literature. One additional

factor behind these deviations is the different tracers we are using to measure the SFR of LIRGs (TIR) and the KINGFISH regions ($24 \mu\text{m}$ combined with $\text{H}\alpha$ or FUV). Interestingly, we find that if we measure the SFR of LIRGs using monochromatic IR-based SFR tracers (e.g., $24 \mu\text{m}$), the agreement with the SFR inferred from [C II] through our calibration is considerably better.

7. We use the *Starburst99* code to connect the FUV luminosity of modeled stellar populations to the [C II] emission via the heating efficiency, ϵ_h . We find that the [C II] emission from most of the galaxies can be attributed to regions that have been forming stars continuously for more than 20 Myr in combination with a heating efficiency in the range $\epsilon_h \sim 1 - 3\%$. It appears likely that the variation in the latter drives much of the scatter in the [C II]-SFR correlation.

Chapter 4

The Ionized Gas in Nearby Galaxies as Traced by the [N II] 122 and 205 μm Transitions

4.1 Introduction

Infrared transitions are a powerful tool for investigating the neutral and ionized gas in the interstellar medium (ISM). At wavelengths greater than 100 μm , the brightest lines in star-forming galaxies are the [C II] 158 μm and [N II] 122 and 205 μm fine structure transitions (Bennett et al. 1994; Brauher et al. 2008; Malhotra et al. 2001; Wright et al. 1991; Zhao et al. 2013). Unlike Carbon—which requires 11.3 eV to be ionized, and thus exists in both neutral and ionized gas—the 14.5 eV ionization potential of Nitrogen is higher than the 13.6 eV required to ionize Hydrogen, resulting in the N^+ ions residing predominantly in the ionized ISM. This enables the use of the far-infrared [N II] transitions to explore, in all but the most extreme cases free of dust extinction, properties of the ionized gas such as its density and the rate

of ionizing photons (which is directly related to recent star formation activity).

The pair of infrared [N II] lines is the result of the splitting of the ground-state of N^+ into three fine-structure levels. These levels are excited primarily by electron collisions, and the critical densities (n_{crit}) for the resulting [N II] 121.89 μm ($^3P_2 \rightarrow ^3P_1$) and [N II] 205.19 μm ($^3P_1 \rightarrow ^3P_0$) transitions are 290 cm^{-3} and 44 cm^{-3} (assuming $T \approx 8,000 \text{ K}$), respectively (Hudson & Bell 2004). These excitation conditions imply that most of the [N II] emission arises from H II regions, and that the infrared [N II] 205 μm power per N II scales linearly with electron density (n_e) up to $\sim 10 \text{ cm}^{-3}$, growing increasingly more slowly with n_e until leveling off at $n_e \sim 60 - 70 \text{ cm}^{-3}$ (e.g., see Figure 8 in Langer et al. 2015). From this point, the [N II] 122 to 205 μm line ratio starts to increase from its base value of ~ 0.7 (Rubin et al. 1994) as a function of n_e , and it will continue growing until n_e approaches the critical density of the [N II] 122 μm line. Beyond this density threshold, the [N II] 122 μm power per N II levels off, and the [N II] line ratio is no longer sensitive to n_e . Using this method, n_e measurements of the photoionized gas have been made for a handful of sources: the Milky Way ($\lesssim 10 \text{ cm}^{-3}$, Bennett et al. 1994), M 82 ($\sim 180 \text{ cm}^{-3}$, Petuchowski et al. 1994), Carina nebula ($\sim 28 \text{ cm}^{-3}$, Oberst et al. 2011, 2006), the central region of NGC 1097 ($\sim 160 \text{ cm}^{-3}$, Beirão et al. 2012), M 51 ($\sim 8 \text{ cm}^{-3}$, Parkin et al. 2013), NGC 891 ($\sim 10\text{-}100 \text{ cm}^{-3}$, Hughes et al. 2014) and the central region of IC 342 ($\sim 110 \text{ cm}^{-3}$, Rigopoulou et al. 2013).

Another interesting application of the [N II] far-infrared lines is to use them as tracers of star formation activity. This use is motivated by the fact that the [N II] lines arise from gas ionized by O and early-B type stars, thus providing a direct measurement of the ionizing photon rate, which is directly related to the star formation rate (Bennett et al. 1994; McKee & Williams 1997). The other advantage is

that the [N II] far-infrared line emission can be observed in high-redshift galaxies by ground-based observatories like the Atacama Large Millimeter Array (Combes et al. 2012; Decarli et al. 2012; Ferkinhoff et al. 2011, 2015; Nagao et al. 2012). Empirical calibrations of the star formation rate (SFR) based on [N II] 122 and 205 μm luminosities have been derived using samples of star-forming and luminous infrared galaxies (LIRGs) by Farrah et al. (2013) and Zhao et al. (2013). These calibrations provide SFR estimates with an uncertainty of a factor of ~ 3 for star-forming galaxies with infrared luminosities below $\sim 10^{11.5} L_{\odot}$; for more luminous galaxies, these calibrations tend to underestimate the amount of star formation by factors that can be as high as ~ 10 . A decrease of the [N II] to FIR luminosity ratio (also known as the “[N II]-deficit”) is also observed in some local and high redshift galaxies (Decarli et al. 2012; Farrah et al. 2013; Fischer et al. 2010; Graciá-Carpio et al. 2011; Zhao et al. 2013). The origin of the “[N II]-deficit” could be related to dusty H II regions whose ionizing photons are intercepted by dust (Graciá-Carpio et al. 2011; Luhman et al. 2003), although it is likely that additional factors also play a significant role (Croxall et al. 2012; Farrah et al. 2013). Certainly, the “[N II]-deficit” is one of the most important limitations for using the [N II] emission as a star formation tracer. The other important limitation that we explore in this work is the role of collisional quenching of the [N II] lines when the electron density of the source exceeds the critical density.

Based on a sample of [N II] 122 and 205 μm resolved observations of 21 nearby galaxies by *Herschel*, the goal of this paper is twofold. First, to measure the electron density of the diffuse ionized gas and explore any potential dependence with the environment (metallicity, radiation field strength, etc). Second, to derive [N II]-based star formation rate calibrations and study their reliability. This paper is organized as follows. In Section 2 we describe the observations and the sample

under investigation. In Section 3 we use the [N II] 122 to 205 μm line ratio to measure electron densities, and explore the properties of the diffuse ionized gas; we also investigate the connection between [N II] emission, star formation activity and electron density. Finally, in Section 4 we summarize our main conclusions.

4.2 Main Sample Description

Our study focuses on 21 spiral galaxies drawn from the “*Beyond the Peak*” (BtP; P.I. J. D. Smith) and “Key Insights on Nearby Galaxies: A Far-Infrared Survey with *Herschel*” (KINGFISH; Kennicutt et al. 2011) samples. Combined, these surveys provide deep photometric and spectroscopic measurements of 20 centrally pointed regions and one extra-nuclear region (NGC 5457). According to their optical spectral properties, 12 of these 21 galaxies show signatures of active galactic nuclei (AGN) emission (Ho et al. 1997; Moustakas et al. 2010); however, by design of the sample, the luminosity of the AGN is only a small contribution to the total luminosity of the galaxy. Our galaxies cover a distance range of 3.5 – 30.6 Mpc, a total infrared luminosity range of $L_{\text{TIR}} \sim 10^{8.9} - 10^{10.7} L_{\odot}$ (Dale et al. 2012) and a global metallicity range of $12 + \log(\text{O}/\text{H}) \sim 8.1 - 8.9$ for the Pilyugin & Thuan (2005) calibration (PT05) and $12 + \log(\text{O}/\text{H}) \sim 8.7 - 9.2$ for the Kobulnicky & Kewley (2004) calibration (KK04) (Moustakas et al. 2010).

4.2.1 Spectroscopic Data

Observations of the [N II] 122 μm transition were carried out with the *Herschel* Photodetector Array Camera & Spectrometer (PACS, Poglitsch et al. 2010) on board *Herschel* as part of the KINGFISH survey. The spectral observations were reduced using the *Herschel* Interactive Processing Environment (HIPE) version 11.0. The

reduced cubes were then processed to obtain zero, first and second moment maps. The calibration uncertainty on the PACS red grating order is on the order of 20% (Croxall et al. 2013). The PACS beam size at $122 \mu\text{m}$ is $\approx 10''$ ¹. For a detailed description on the reduction and processing of the KINGFISH FIR spectral maps we refer to Croxall et al. (2013).

The [N II] $205 \mu\text{m}$ transition was observed with the *Herschel* Fourier Transform Spectrometer (SPIRE-FTS, Griffin et al. 2010) as part of the BtP survey. For a detailed description on the reduction and processing of the spectral maps we refer to Pellegrini et al. (2013) and Pellegrini et al. 2015 (in prep.). The SPIRE-FTS beam size at $205 \mu\text{m}$ is $16.6''$ (Makiwa et al. 2013). Hereafter, we will refer to the area covered by a single SPIRE-FTS beam as an “individual region”. The SPIRE-FTS instrumental spectral resolution is not sufficient to resolve line profiles in BtP. Profile fitting was done with a fixed-width sinc function, where we fit for the line position and peak. Thus the dominant uncertainty in any line flux measurement is in uncertainty of the peak above the continuum. To estimate the uncertainty in the continuum under the line we measure the $1 - \sigma$ standard deviation in the residual of the fit and take this to be the uncertainty in 1-spectral element. Because the noise pattern in the continuum is correlated (fringe pattern) we scale the uncertainty in a single spectral pixel by the number of pixels under an unresolved line to estimate the uncertainty in our fluxes.

The SPIRE-FTS spectra depend on the intrinsic source structure, i.e., the reduction and calibration routines are optimized for a source that, compared to the beam size, is either completely resolved or fully extended. This implies that sources that are semi-extended compared to the beam size may need additional corrections that can be as high as factor of ~ 2 (e.g., see Figure 4 in Wu et al. 2013). This is

¹http://herschel.esac.esa.int/Docs/PACS/pdf/pacs_om.pdf

the case for our data, which was first reduced assuming a point-source distribution, although there is a potential contribution to the emission by extended sources. To account for the change in the gain for an extended component at 205 μm emission, we assume that: (1) the flux measured at 250 μm from the SPIRE-FTS spectrum and the SPIRE continuum should be the same, and (2), any scaling factor applied to the SPIRE-FTS spectrum in order to fulfill condition (1), can also be applied to the 205 μm data. Based on these two main assumptions, we scale the surface brightness at 205 μm of each bolometer by the ratio between the synthetic and imaging photometry at 250 μm . The mean value of this correction is 1.13, with a 1- σ dispersion of ± 0.5 .

4.2.2 Supplementary Data

The supplementary data available includes: (1) near and mid-infrared (24 μm) data from the *Spitzer* Infrared Nearby Galaxy Survey (SINGS; Kennicutt et al. 2003); (2) FIR maps observed with *Herschel* PACS (70, 100 and 160 μm) and SPIRE (250, 350 and 500 μm) drawn from the photometric KINGFISH sample (Dale et al. 2012); (3) $\text{H}\alpha$ images corrected for Galactic extinction, with foreground stars masked and the optical [N II] contribution subtracted (Leroy et al. 2012). These are drawn mainly from the SINGS (Kennicutt et al. 2003) and Local Volume Legacy survey (LVL, Dale et al. 2009a).

As an example of the data used in this study, Figure 4.1 shows the [N II] 122 μm surface brightness map of the spiral galaxy NGC 4254. The blue contours show the 24 μm dust continuum emission and the grey circles show the spatial distribution of the 68 SPIRE-FTS bolometers used to observe the [N II] 205 μm line emission. For this particular galaxy, the fraction of 205 μm bolometers that overlap with [N II] 122 μm data is 45%. For the entire sample, this fraction is 23%. On the other

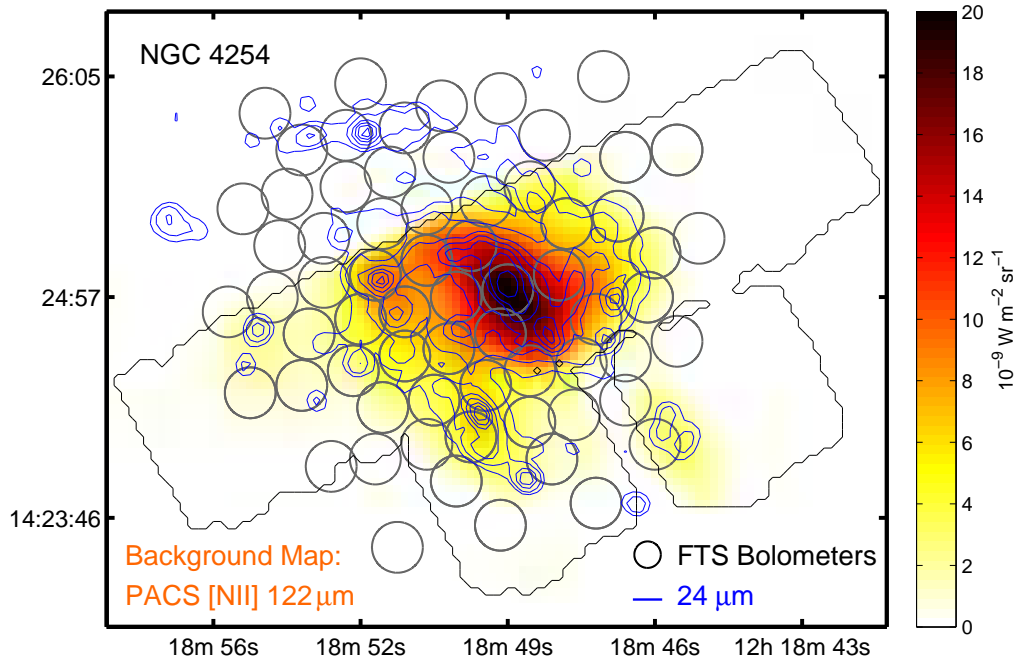


Figure 4.1: PACS [N II] $122 \mu\text{m}$ image of NGC 4254. The color scale shows the [N II] $122 \mu\text{m}$ surface brightness in units of $10^{-9} \text{ W m}^{-2} \text{ sr}^{-1}$. The black contours delineate the areas which have [N II] $122 \mu\text{m}$ data and the blue contours show the $24 \mu\text{m}$ dust continuum emission. The grey circles show the distribution of the $17''$ SPIRE-FTS bolometers used to detect the [N II] $205 \mu\text{m}$ line. The axes show the RA(J2000) and DEC(J2000) position coordinates.

hand, the overlap between the [N II] spectroscopic data and the complementary photometric data available (e.g. $24 \mu\text{m}$, $H\alpha$, etc) is nearly total.

In Section 4 we compare the BtP and KINGFISH data to a sample of local luminous infrared galaxies. This sample consist of 25 LIRGs observed in [N II] $122 \mu\text{m}$ emission by Farrah et al. (2013) and 44 LIRGs observed in [N II] $205 \mu\text{m}$ emission by Zhao et al. (2013) as part of the Great Observatories All-sky LIRG Survey (GOALS; Armus et al. 2009). For these samples of LIRGs we measure SFRs based on the total infrared luminosity (TIR; $L(8 - 1000 \mu\text{m})$) and the calibration by Murphy et al. (2011).

4.2.3 Models

Draine & Li dust model

For each BtP galaxy we have maps of dust properties based on the Draine & Li dust model (DL07; Draine & Li 2007). In brief, the DL07 model considers that dust consists of a combination of carbonaceous and amorphous silicate grains whose grain size distribution and normalization is chosen to match the abundance and average extinction in the Milky Way (Weingartner & Draine 2001). In the model, the dust is heated by a range of radiation fields U , including: (1) a diffuse component that is heated by a single radiation field, U_{\min} ; (2) a more intense component, $U_{\min} < U < U_{\max}$, that heats dust located near luminous stars (e.g., dust in photodissociation regions heated by OB stars). For reference, $U = 1$ is the local interstellar radiation field in the Milky Way, normalized to the MMP field (Mathis et al. 1983). The dust maps we use in this work are similar to the ones presented in Aniano et al. (2012), and were processed by G. Aniano (private communication) by fitting the DL07 model to the infrared spectral energy distribution in the $3.6 - 250 \mu\text{m}$ wavelength range. The output of the fit includes the dust mass, the dust-weighted mean starlight intensity, $\langle U \rangle$, and the fraction of the dust luminosity produced by photodissociation regions with $U > 100$ (f_{PDR}).

MAPPINGS-III photoionization code

In Section 4 we investigate the relationship between [N II] emission, electron density and star formation activity based on the predictions by the shock and photoionization code MAPPINGS-III (Binette 1985; Groves et al. 2004; Kewley et al. 2001). This code takes synthetic FUV spectra generated by the *Starburst99* code (Leitherer et al. 1999) and produces model HII region spectra integrated over the

full ionized volume. The code incorporates a sophisticated treatment of the dust that includes absorption, charging and photoelectric heating (Groves et al. 2004). The final spectra consist of a set of emission lines that include the [N II] 122 and 205 μm transitions. In this work we use the pre-computed grids of MAPPINGS-III generated by Levesque et al. (2010). These grids adopt a wide range of parameters, including: (1) star formation history (continuous or instantaneous burst), (2) age ($0 \leq t_{\text{age}} \leq 5$ Myr), (3) metallicity ($0.05 \leq Z/Z_{\odot} \leq 2$), (4) ionization parameter q , which is the ratio between the incident ionizing photon flux and the gas density ($10^7 \leq q \leq 4 \times 10^8 \text{ cm s}^{-1}$), and (4) electron density ($n_e = 10$ or 100 cm^{-3}). We use a set of grids that adopt a characteristic ionization parameter for star-forming galaxies of $q = 2 \times 10^7 \text{ cm s}^{-1}$ (Kewley & Dopita 2002), and for a fixed electron density of $n_e = 10$ or 100 cm^{-3} , allow the metallicity to vary between $Z = Z_{\odot}$ and $Z = 2Z_{\odot}$. We also adopt a continuous star formation history model at 5 Myr, which correspond to the age in the *Starburst99* model at which there is a balance between the number of O stars being born and dying (Kewley et al. 2001). The SFR calibrations used in this work (Calzetti et al. 2007; Murphy et al. 2011) are also based on *Starburst99* calculations that assume a continuous star formation history model.

4.2.4 Methods

In order to assure proper comparison between the supplementary data and the [N II] 205 μm observations, we convolved all of our maps to match the SPIRE-FTS resolution at 205 μm ($\approx 17''$) using convolution kernels constructed using the methodology of Aniano et al. (2011). We then use the 70, 100 and 160 μm convolved data to measure the total infrared (TIR) luminosity based on the calibration by Galametz et al. (2013). Finally, we measure star formation rate surface densities (Σ_{SFR}) and SFRs based on a combination of the convolved 24 μm and H α

data following the calibration by Calzetti et al. (2007). This calibration adopts a truncated Salpeter IMF with slope -1.3 in the range $0.1 - 0.5 M_{\odot}$ and slope -2.3 in the range $0.5 - 120 M_{\odot}$. This choice of IMF produce SFRs that, for the same number of ionizing photons, are $\sim 14\%$ higher than if we change the upper-mass cutoff to $100 M_{\odot}$, and a factor 1.59 lower if we assume a Salpeter IMF in the range $0.1 - 100 M_{\odot}$. For the global metallicities of 17 of the 21 galaxies, we use the average between the KK04 and PT05 “characteristic” metallicities listed in Table 9 of Moustakas et al. (2010). For the four remaining galaxies with metallicity measurements not available in Moustakas et al. (2010), we use oxygen abundances derived from the Luminosity-Metallicity relation listed in Kennicutt et al. (2011). Finally, we correct all the surface brightness and SFR surface density values for inclination by a factor of $\cos(i)$. We remove NGC 4631 from the analysis due to its high inclination ($i \approx 86^{\circ}$; Muñoz-Mateos et al. 2009a).

4.3 Results and Discussion

4.3.1 Estimating ionized gas densities from the [N II] fine-structure transitions

In this section we discuss how the electron density can be derived from the ratio between the [N II] $122 \mu\text{m}$ and [N II] $205 \mu\text{m}$ transitions (from now on [N II] 122/205 line ratio). Let $f_j(n_e)$ be the fraction of N II in level i , where $i = 0$ is the ground state. The power radiated in fine structure lines is

$$L_\lambda = \int n(\text{N}^+) P_\lambda(n_e) dV \quad (4.1)$$

$$= \left[\frac{\text{N}^+}{\text{H}^+} \right] \int n_e P_\lambda(n_e) dV \quad (4.2)$$

$$P_{205\mu\text{m}}(n_e) = f_1(n_e) A_{10} h\nu_{10} \quad (4.3)$$

$$P_{122\mu\text{m}}(n_e) = f_2(n_e) A_{21} h\nu_{21} \quad (4.4)$$

where A_{10} and A_{21} are the Einstein coefficients for the $1 \rightarrow 0$ (205 μm) and $2 \rightarrow 1$ (122 μm) transitions of N II, respectively. We have calculated $f_i(n_e)$ for N II levels $i = 0, \dots, 4$, using electron collision strengths from Tayal (2011), and radiative decay rates from Galavis et al. (1997) and Storey & Zeippen (2000), for an assumed electron temperature $T = 8,000$ K, and a range of n_e . The left panel of Figure 4.2 shows the variation of the [N II] 122/205 ratio with electron density, n_e . It can be seen that the line ratio is sensitive to the density of the singly-ionized gas in the $n_e \sim 10 - 1,000 \text{ cm}^{-3}$ range.

The right panel of Figure 4.2 shows P/n_e , where P is the power radiated per ion, for each individual [N II] transition and for their sum, as a function of the [N II] 122/205 line ratio. This figure illustrates the effect of collisional quenching on the [N II] transitions once the electron density of the gas exceeds the critical density of the line. For example, as the electron density exceeds the critical density of the [N II] 122 μm line –which happens around a line ratio [N II] 122/205 ≈ 5 ($n_e \approx 250 \text{ cm}^{-3}$)–, the power radiated per ion by the [N II] 122 μm line starts to decrease at a rate comparable to that of the [N II] 205 μm line.

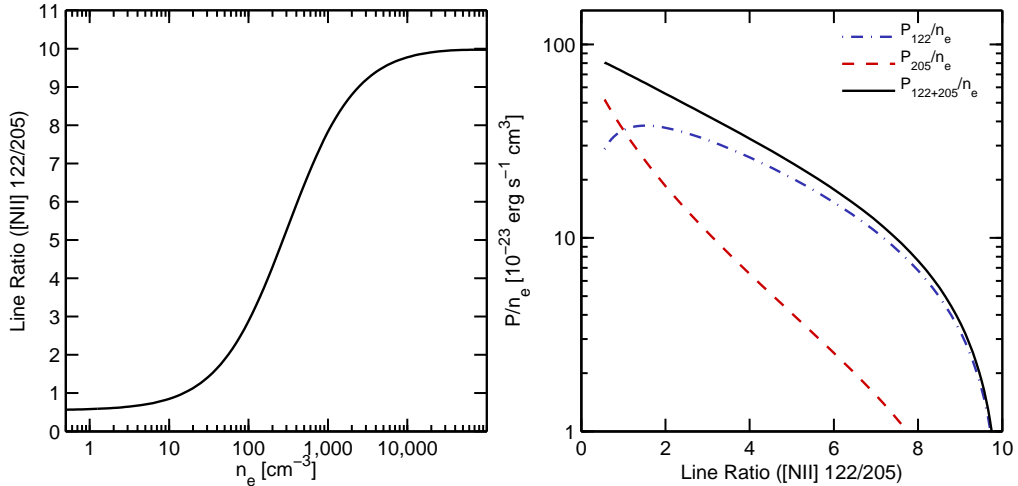


Figure 4.2: (*Left*) Ratio between the [N II] 122 μm and [N II] 205 μm transitions as a function of electron density n_e . The theoretical curve shows how the [N II] 122/205 line ratio can be used as a probe of the electron density of the singly-ionized, warm ionized gas in the $\sim 10 - 1,000 \text{ cm}^{-3}$ range. We have assumed an electron temperature of $T = 8000 \text{ K}$. (*Right*) Power radiated per N^+ ion, P/n_e , in the [N II] 122 μm transition (blue), the [N II] 205 μm transition (red) and the sum of both [N II] transitions (black), as a function of the [N II] 122/205 line ratio. At [N II] 122/205 line ratios greater than ~ 1 , the total power radiated per ion starts to be dominated by the [N II] 122 μm transition.

4.3.2 Distribution of [N II] 122/205 line ratios and electron densities in the Beyond the Peak sample

For 140 individual regions (defined by the area covered by a single SPIRE-FTS beam at 205 μm) for which we have observations of both [N II] transitions with $S/N \geq 3$, Figure 4.3 shows the histogram of the observed [N II] 122/205 line ratios (left panel) and the fraction of the total emitted [N II] 122 μm power per [N II] 122/205 bin (right panel). The two [N II] 122/205 line ratio distributions show the data calibrated as a point-source (grey) and after applying the extended emission correction (blue). Both distributions are roughly similar, but the corrected version of the data tend to show higher line ratios. This is the direct result of applying the extended emission correction, which accounts for the overestimation of the [N II] 205 μm intensity when

extracted as a point source (see Section 2.1 for details). From this point of the paper, we base all of the results on the extended emission corrected version of the data. The red dashed line shows the line ratio limit of $[\text{N II}] 122/205 \approx 0.55$ expected for regions with $n_e \ll n_{\text{crit}}$ assuming Tayal (2011) electron collision strengths (this ratio limit is 0.66 if we assume Hudson & Bell (2005) electron collision strengths instead). Below this limit, the $[\text{N II}] 122/205$ line ratio is no longer sensitive to n_e . In our sample, there is only one region with a $[\text{N II}] 122/205$ line ratio lower than 0.55. This region is located in NGC 4254 and has a $[\text{N II}] 122/205$ line ratio of 0.38 ± 0.15 . As a cautionary note, this region is one of the few where the extended emission correction increases the $[\text{N II}] 205 \mu\text{m}$ intensity by a factor of ~ 2 . Therefore, it may be the case that the origin of this low $[\text{N II}]$ line ratio is not physical. Regarding the fraction of the emitted $[\text{N II}] 122 \mu\text{m}$ power per $[\text{N II}] 122/205$ line ratio bin, about 40% of the total $[\text{N II}] 122 \mu\text{m}$ power arises from regions with $[\text{N II}] 122/205 \gtrsim 2$, or equivalently, electron densities higher than the critical density of the $[\text{N II}] 205 \mu\text{m}$ line.

The left panel of Figure 4.4 shows the theoretical dependence of the electron density on the $[\text{N II}] 122/205$ line ratio calculated in Section 3.1. The blue vertical lines on top of the curve correspond to the ratios measured in 140 regions selected from the BtP sample. The observed $[\text{N II}] 122/205$ line ratios range between ~ 0.6 and 5, which corresponds to electron densities in the ~ 3 to 230 cm^{-3} range. Typical uncertainties in the electron density measurements are in the order of 20%. Figure 4.4 also includes $[\text{N II}] 122/205$ line ratios observed in the Milky Way with the Cosmic Background Explorer (Bennett et al. 1994), M 82 with the Kuiper Airborne Observatory (Petuchowski et al. 1994), the young open cluster Trumpler 14 and the H II region Carina I in the Carina nebula observed with the South Pole Imaging Fabry-Perot Interferometer at the Antarctic Submillimeter Telescope and Remote

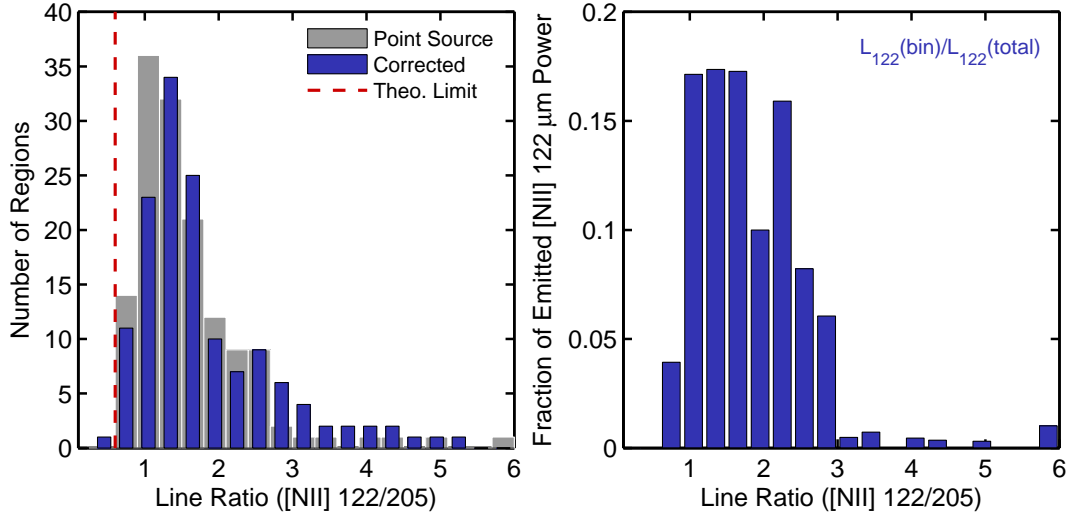


Figure 4.3: (Left) Histograms of the [N II] 122/205 line ratio for the 140 regions in our sample when reduced as a point-source (grey) and after applying the extended emission correction (blue). Both distributions are roughly similar, with the main effect of the extended emission correction being a small overall increase of the line ratios. The red dashed line shows the theoretical line ratio of ≈ 0.55 expected for regions of low electron density ($n_e \ll n_{\text{crit}}$); in this regime the [N II] 122/205 line ratio is insensitive to the ionized gas density. Most of our regions have line ratios above this limit, which means that their line ratios can be used to measure the electron density of the diffuse, singly-ionized gas. (Right) Fraction of the emitted [N II] 122 μm power per [N II] 122/205 line ratio bin. About 40% of the total [N II] 122 μm power arises from regions with [N II] 122/205 $\gtrsim 2$ ($n_e \gtrsim 50 \text{ cm}^{-3}$).

Observatory and the Infrared Space Observatory (Oberst et al. 2011), M 51 central and arm regions observed with *Herschel* PACS (Parkin et al. 2013) and the central region of IC 342 observed with *Herschel* PACS and SPIRE (Rigopoulou et al. 2013). We measure a mean electron density in the BtP sample of $n_e \approx 30 \text{ cm}^{-3}$, which is similar to the electron density in the young open cluster Trumpler 14 and the Carina I H II region.

The right panel of Figure 4.4 shows the resulting distribution of electron densities for the Beyond the Peak regions. We also plot the literature measurements included in the left panel and we add the distributions of electron densities measured in 20 regions of the edge-on galaxy NGC 891 (Hughes et al. 2014), and 27 regions in

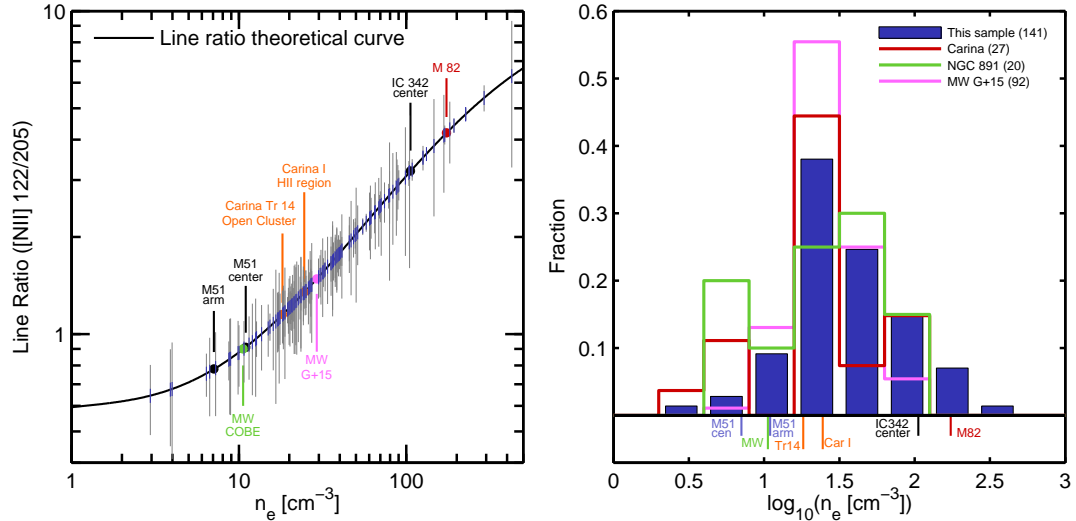


Figure 4.4: (Left) $[\text{N II}] 122/205$ line ratio as a function of electron density (n_e). The blue vertical lines show the observed ratios, and corresponding n_e measurements, for 141 regions selected from 21 galaxies in the Beyond the Peak Sample. The grey vertical lines show the line ratio error. We measure electron densities in the range $n_e \sim 1 - 300 \text{ cm}^{-3}$. We also include $[\text{N II}] 122/205$ line ratio measurements from M 51 central region and spiral arm (Parkin et al. 2013), the Milky Way (Bennett et al. 1994; Goldsmith et al. 2015), the young open cluster Trumpler 14 and the H II region Carina I in the Carina nebula (Oberst et al. 2011), IC 342 central region (Rigopoulou et al. 2013) and M 82 (Petuchowski et al. 1994). The median electron density in our sample is $n_e \approx 30 \text{ cm}^{-3}$, similar to the ionized gas density of the Carina I H II region. (Right) Distribution of electron densities for the Beyond the Peak sample (blue bars), 22 regions in the Carina nebula (red, Oberst et al. 2011), 92 regions in the Milky Way (G+15; Goldsmith et al. 2015), and 20 regions in the edge-on galaxy NGC 891 (Hughes et al. 2014). On the bottom of the plot we also show the individual measurements displayed in the left panel.

the Carina nebula (Oberst et al. 2011). In the latter, the highest density regions are associated with the outskirts of the H II regions Carina I and II, and the lowest density regions correspond to an extended component detectable all over the ~ 30 pc map (Oberst et al. 2011, 2006). The comparison between the BtP data and the external samples reveal the wide range of environments and physical conditions that are represented in our sample. On one hand, we are sensitive to a more extended, low-density ionized gas component, like the one that fills the medium in between

H II regions in the Carina nebula. On the other hand, we have regions with high electron densities (measured in the central regions of NGC 1097, NGC 4536 and NGC 6946) that are comparable to the ones measured in very active star-forming galaxies, like M 82 and the central region of IC 342.

4.3.3 Electron density variations within individual galaxies

The photoionized gas traced by the [N II] transitions in our sample spans two orders of magnitude in electron density. In this section we explore the dependence between the electron density and a number of ISM properties that might be playing a role in these variations, such as metallicity, radiation field strength and star formation activity.

How much does the electron density vary within the area sampled in each galaxy? To answer this, Figure 4.5 shows the electron density of our 140 regions grouped by galaxy. The names of the galaxies are listed in the bottom of the panel, and their characteristic metallicities are listed in the top part of the plot. Galaxies are sorted from left to right in order of increasing metallicity. We use color to include information about the local radiation field strength, derived using the dust-weighted mean starlight intensity U from the Draine & Li (2007) model. Finally, we mark using open circles regions with deprojected distances to the center of the galaxy less than the median physical radius of the SPIRE-FTS bolometer in our sample, i.e. ≈ 400 pc. We measure the distance to the center by calculating the angular separation between the position of the center of the galaxy (taken from the NASA Extragalactic Database) and the position of the SPIRE-FTS bolometers. We then convert the angular separation into a deprojected distance using distances to galaxies and inclinations drawn from the compiled lists in Kennicutt et al. (2011) and Hunt et al. (2014). From Figure 4.5 we notice that the highest electron density

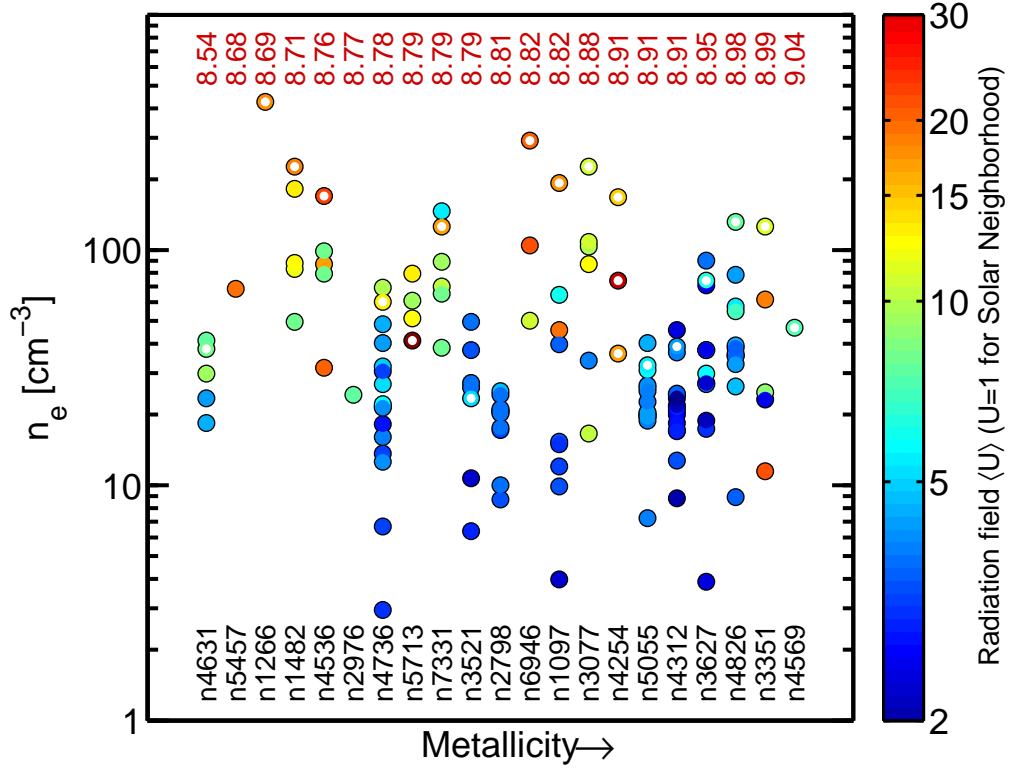


Figure 4.5: Electron density as a function of metallicity for all regions in our sample sorted by galaxy. The name of the galaxy is listed in the bottom part of the plot and the characteristic global value of the Oxygen abundance $12 + \log(\text{O}/\text{H})$ –measured by Moustakas et al. (2010)– is listed on the top part of the plot in red. Metallicity increases to the right. The color scale corresponds to the dust-weighted mean starlight intensity U derived from the Draine & Li (2007) model. The open circles show the regions where the position of the bolometer is located within a deprojected distance of 400 pc to the center of the galaxy. Within galaxies, and despite the limited spatial coverage of the disk, we observe variations in electron density greater than a factor of ~ 10 (e.g., NGC 3627, NGC 4826, NGC 7331). For most galaxies, the highest electron density measurements are found in the central regions. Finally, the color scale reveals a clear trend of increasing electron density with radiation field strength.

measurements within a galaxy tend to be found in its central region; the three exceptions are NGC 3627, NGC 4736 and NGC 7331. In these cases the highest ionized gas density is found in regions located in circumnuclear rings of molecular gas and star formation.

Figure 4.5 also shows that we are able to detect variations in the electron den-

sity within individual galaxies as high as a factor of ~ 20 . One good example is NGC 3627, a Leo Triplet interacting spiral galaxy with a strong inner molecular gas ring and bar (Regan et al. 2002). The highest gas density in the system, $n_e = 71 \text{ cm}^{-3}$, is measured in the section of the ring that coincides with one of the ends of the bar. This region is characterized by strong star formation activity and high average radiation field strength ($\langle U \rangle \approx 10$). The second highest ionized gas density measurement comes from the central region of the galaxy ($n_e = 40 \text{ cm}^{-3}$, $\langle U \rangle \approx 13$), and the lowest ionized gas density ($n_e = 4 \text{ cm}^{-3}$) is measured in a more quiescent region ($\langle U \rangle \approx 3$) located in between the circumnuclear ring and the center of the galaxy. This trend of increasing electron density with radiation field strength is not exclusive of NGC 3627. In fact, Figure 4.5 reveals a similar trend for the rest of the sample: while regions with $n_e \lesssim 20 \text{ cm}^{-3}$ tend to have radiation field strengths of only a few times the radiation field in the solar neighborhood, regions with $n_e \gtrsim 100 \text{ cm}^{-3}$ tend to have $\langle U \rangle \gtrsim 15$.

There is not a clear trend of varying electron density with oxygen abundance. However, low metallicity galaxies in our sample tend to have, on average, higher radiation fields and electron densities than the rest of the sample. This, however, could be an observational bias as the spatial coverage of the [N II] line emission in these low metallicity environments –especially in the case of the [N II] $122 \mu\text{m}$ transition– is mostly limited to bright, star-forming regions.

4.3.4 Relationship between electron density and the ISM environment

One of our main goals is to understand the variations in the ionized gas density as a function of the ISM environment. This is possible thanks to the spatial coverage of our target galaxies provided by SPIRE-FTS and the rich characterization of the ISM

properties derived from the ancillary data. We start our analysis by studying how the electron gas density changes with radial distance. The first panel in Figure 4.6 shows the electron density of the 140 regions in our sample as a function of the deprojected distance to the center of the galaxy. The resulting 19 regions with deprojected distances to the center less than 400 pc are shown as red open squares. As we already discussed for Figure 4.5, central regions in galaxies tend to have higher electron densities (median $n_e \approx 77 \text{ cm}^{-3}$) than those located in the disk (median $n_e \approx 25 \text{ cm}^{-3}$).

The second panel shows the ionized gas density as a function of the infrared color $\nu f_\nu(70 \mu\text{m})/\nu f_\nu(100 \mu\text{m})$ measured using the PACS 70 and 100 μm data. There is a good correlation of increasing gas density with increasing infrared color (Spearman correlation coefficient $r = 0.7$). The best linear fit to the data in the log-log space, shown as a solid line in the second panel, yields:

$$\log_{10}(n_e/\text{cm}^{-3}) = 3.41 \times \log_{10}(\nu f_\nu(70)/\nu f_\nu(100)) + 1.68. \quad (4.5)$$

The standard deviation around the fit, shown as dashed grey lines, is 0.42 dex. This parametrization could be useful for studies that require an electron density in order to predict the [N II] 205 μm flux based on the [N II] 122 μm flux (or viceversa) (e.g., Zhao et al. 2013).

The third and fourth panel in Figure 4.6 show the electron density as a function of the dust-weighted mean starlight intensity, $\langle U \rangle$, and the fraction of the dust luminosity produced by photodissociation regions with $U > 100$, f_{PDR} (both parameters derived from the Draine & Li 2007 model). The correlation of electron density with starlight intensity is as good as the correlation with infrared color, which is expected given the good correspondence between infrared color and $\langle U \rangle$ (e.g., see Figure 19 in Muñoz-Mateos et al. 2009a). On the other hand, there is no strong dependence

between electron density and f_{PDR} , although regions with $f_{\text{PDR}} \gtrsim 10\%$ tend to have, on average, higher electron densities than the rest of the regions.

Finally, the last two panels show the correlation between electron density and total infrared luminosity surface density, Σ_{TIR} , and star formation surface density, Σ_{SFR} . Similar to what is found for the dependences with infrared color or radiation field strength, there is a clear trend of increasing electron density with increasing infrared surface brightness and star formation activity (Spearman correlation coefficient $r \approx 0.7$).

The observed relationship between electron density and star formation activity, or radiation field strength, could have at least two origins. The first one is related to the first stages of the evolution of H II regions. For recent episodes of star formation activity, we expect massive stars to produce very intense radiation fields. The corresponding young H II regions created around this newly-formed stars are more compact than evolved H II regions, characterized by electron densities higher than $n_e \approx 10^3 \text{ cm}^{-3}$, and located in the high-pressure, inner regions of molecular clouds (Franco et al. 2000). Although our sensitivity to high electron densities is limited by the critical density of the [N II] 122 μm line, we believe that regions in our sample that exhibit high radiation fields and high electron densities could be related to young, compact H II regions. The second possible explanation is based on a thermal pressure argument. Once a young, compact H II region has expanded and reaches pressure equilibrium with its surrounding medium, a high electron density implies a high neutral density of the cold ISM gas in which the H II region is embedded. This high density molecular gas environment provides the conditions for further star formation to occur, establishing a link between the high density of the ionized gas and more intense star formation activity.

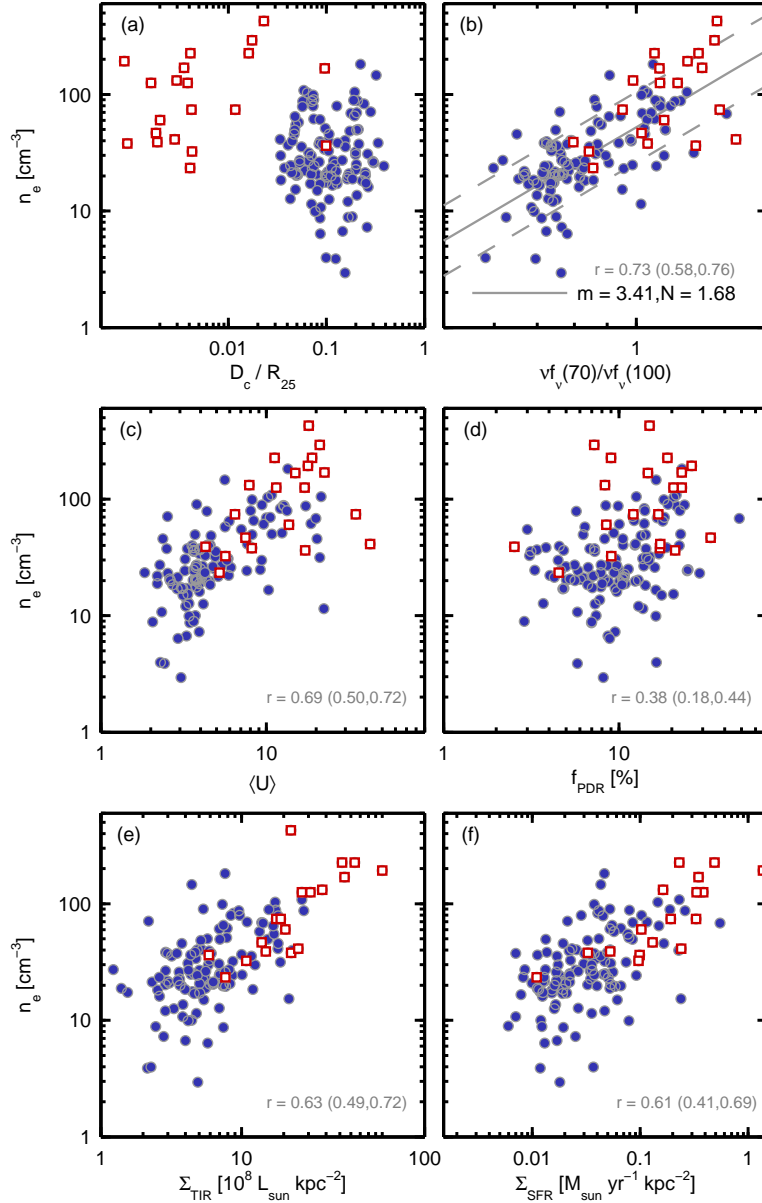


Figure 4.6: Electron density (n_e) as a function of six parameters. (First panel) galactocentric distance. Central regions with deprojected distances less than 400 pc are shown as open red squares. These regions have an average electron density a factor of ~ 3 higher than the rest of the regions. (Second panel) infrared color ($\nu f_\nu(70 \mu\text{m})/\nu f_\nu(100 \mu\text{m})$). The solid and dashed grey lines show the best linear fit to the data (in the log-log space) and the $\pm 1\sigma$ standard deviation around the fit, respectively. The slope (m) and normalization of the fit (N) are listed in the bottom-right corner and in Equation 1. (Third panel) dust-weighted mean starlight intensity ($\langle U \rangle$) derived from the Draine & Li (2007) model. (Fourth panel) fraction of the dust luminosity produced by photodissociation regions with $U > 100$ (f_{PDR}) also derived from the Draine & Li (2007) model. (Fifth panel) total infrared luminosity surface density, Σ_{TIR} . (Sixth panel) star formation rate surface density (Σ_{SFR}).

4.3.5 Estimating star formation rates from the [N II] fine-structure transitions

Another interesting application of the [N II] transitions is to use them as tracers of the star formation activity (e.g., McKee & Williams 1997; Zhao et al. 2013). One of the advantages of the [N II] infrared transitions is that, unlike H α or other optical tracers, they are insensitive to dust extinction and can provide a robust estimate of the ionizing photon rate, Q_0 .

Low Density Limit

To understand how [N II] emission works as a measure of star formation we can assume that the excitation is dominated by collisions from the ground level and balanced by radiative de-excitation. This will be correct at low densities, where collisional de-excitation does not play a role. Thus, we can approximate the power radiated in the [N II] 122 or 205 μm lines in a given volume V as

$$L_\lambda \cong n_e n(\text{N}^+) q_\lambda h\nu V, \quad (4.6)$$

where we have assumed that most N^+ is in the ground level, $q_{122} = q_{02}$ and $q_{205} = q_{01} + q_{02}$, where q_{01} and q_{02} are the collisional excitation coefficients from the ground level to level 1 and 2, respectively, and V is the corresponding volume. For an ionization bounded H II region the ionization-recombination balance dictates that

$$Q_0 = n_e n(\text{H}^+) \alpha_B V, \quad (4.7)$$

where the total rate of H photoionizations, Q_0 , is equal to the rate of radiative recombinations determined by the case B recombination coefficient $\alpha_B = 3.04 \times 10^{-13} \text{ cm}^3 \text{ s}^{-1}$ at $T = 8000 \text{ K}$, and $n(\text{H}^+)$ is the number density of ionized hydrogen

atoms. Under these hypotheses, and combining Equations (4.6) and (4.7), the ionizing photon rate is proportional to the [N II] luminosity through (c.f., Eq. 15 in McKee & Williams 1997)

$$Q_0 \cong \frac{L_\lambda \alpha_B n(\text{H}^+)}{q_\lambda h \nu_\lambda n(\text{N}^+)}. \quad (4.8)$$

Given the similarities in the ionization potentials (13.6 eV vs. 14.5 eV), and assuming that the ionizing source is such that the fraction of N in N^{++} (which requires 29.6 eV) and higher ionizations states is negligible, the last factor is equal to the inverse of the gas-phase abundance of Nitrogen.

Assuming solar abundance $(\text{N}/\text{H})_\odot = 7.4 \times 10^{-5}$ (Asplund et al. 2009) and $q_{205} = q_{01} + q_{02} = 6.8 \times 10^{-8} \text{ cm}^3 \text{ s}^{-1}$ (Hudson & Bell 2005), we measure a median [N II] 205 μm -based global ionizing photon rate for the BtP galaxies of $Q_0 = 1.98 \times 10^{52} \text{ photons s}^{-1}$. Normalized to the covered area, this corresponds to $1.96 \times 10^{51} \text{ photons s}^{-1} \text{ kpc}^{-2}$. If we use the collisional excitation coefficients from Tayal (2011) instead, then $q_{01} + q_{02} = 5.1 \times 10^{-8} \text{ cm}^3 \text{ s}^{-1}$, which increases the ionizing photons rates by a factor of 1.3. The median ionizing photon rate surface density in our sample is about 3 times the ionizing photon rate measured by Bennett et al. (1994) inside the solar circle in our Galaxy. Using the [N II] 122 μm transition –in principle a better tracer than [N II] 205 μm due to its higher critical density– yields an average ionizing photon rate surface density a factor of ~ 4 higher than the one based on the [N II] 205 μm emission.

To relate the ionizing photon rate Q_0 to the SFR, we use the fact that for a standard IMF with an upper-mass cutoff of $120 M_\odot$, and steady star formation for 10^8 yr , the star formation rate and rate of production of photoionizing photons are related by

$$\frac{Q_0}{f_{\text{ion}}} = 1.60 \times 10^{53} \text{ s}^{-1} \frac{SFR}{M_{\odot} \text{ yr}^{-1}}, \quad (4.9)$$

where f_{ion} is the fraction of H ionizing photons emitted by stars that photoionize H or He; i.e., $(1 - f_{\text{ion}})$ is the fraction absorbed by dust. According to the discussion of dusty H II regions by Draine (2011a), we expect $f_{\text{ion}} \approx 1$. Also note that if we change the IMF upper-mass cutoff to $100 M_{\odot}$ (e.g., Murphy et al. 2011), the rate of ionizing photons per SFR decreases by a factor of $\sim 14\%$.

Combining Equations (4.8) and (4.9) we find that the SFR as a function of the [N II] luminosity in the low density limit is given by:

$$\frac{SFR}{M_{\odot} \text{ yr}^{-1}} = 1.49 \times 10^{-7} \left(\frac{6.79 \times 10^{-8} \text{ cm}^3 \text{ s}^{-1}}{q_{01} + q_{02}} \right) \times \left(\frac{(N/H)_{\odot}}{N^+/H^+} \right) \frac{L_{205}}{L_{\odot}}, \quad (4.10)$$

and

$$\frac{SFR}{M_{\odot} \text{ yr}^{-1}} = 2.35 \times 10^{-7} \left(\frac{2.57 \times 10^{-8} \text{ cm}^3 \text{ s}^{-1}}{q_{02} \text{ cm}^3} \right) \times \left(\frac{(N/H)_{\odot}}{N^+/H^+} \right) \frac{L_{122}}{L_{\odot}}. \quad (4.11)$$

We can see through this example that a measurement of SFR using the fine structure lines of [N II] is possible, but it will depend on the abundance of Nitrogen, its ionization state, and ultimately the density of the ionized region, as collisional de-excitation will be increasingly important at higher densities.

Effect of a Distribution of Densities

The photoionized gas in a galaxy will generally have a wide range of electron densities, from compact H II regions to diffuse photoionized gas. The balance between photoionization and radiative recombination can then be expressed as

$$Q_0 = \int \alpha_B n(\text{H}^+) n_e dV = \int \alpha_B n(\text{H}^+) n_e \frac{dV}{d \ln n_e} d \ln n_e. \quad (4.12)$$

In order to assess the effect on Q_0 of having a range of electron densities, we parametrize the distribution of electron densities using a log-normal distribution

$$\alpha_B n(\text{H}^+) n_e \frac{dV}{d \ln n_e} = \frac{Q_0}{\sqrt{2\pi\sigma^2}} \exp \left[-\frac{(\ln(n_e/n_{e0}))^2}{2\sigma^2} \right] \quad ; \quad (4.13)$$

n_{e0} is then a characteristic electron density for the recombining gas, while σ represents the width of the distribution of electron densities. The case $\sigma = 0$ correspond to uniform density. For $\sigma = 1$, for example, if the characteristic electron density is $n_{e0} = 100 \text{ cm}^{-3}$, then the $1\text{-}\sigma$ (68%) and $2\text{-}\sigma$ (95.5%) confidence intervals encompass the density ranges $n_e = 38.8 - 271.8 \text{ cm}^{-3}$ and $n_e = 13.5 - 738.9 \text{ cm}^{-3}$, respectively. Log-normal distributions have been used to characterize the electron density distribution of the warm ionized medium (Berkhuijsen & Fletcher 2008; Hill et al. 2008; Redfield & Falcon 2008).

Then, if we replace dV in Eq. (4.2) using Eq. (4.13) we can express the power radiated in a line as

$$L_\lambda = \frac{Q_0}{\alpha_B \sqrt{2\pi\sigma^2}} \left[\frac{\text{N}^+}{\text{H}^+} \right] \int \exp \left[-\frac{(\ln(n_e/n_{e0}))^2}{2\sigma^2} \right] \times \frac{P_\lambda(n_e)}{n_e} d \ln n_e. \quad (4.14)$$

The observed line ratio is then a function of both n_{e0} and σ

$$\frac{L_{122}}{L_{205}} = \frac{\int d \ln n_e \exp[-(\ln(n_e/n_{e0}))^2/2\sigma^2] P_{122}(n_e)/n_e}{\int d \ln n_e \exp[-(\ln(n_e/n_{e0}))^2/2\sigma^2] P_{205}(n_e)/n_e} \quad , \quad (4.15)$$

and the radiative recombination rate Q_0 can be expressed as

$$Q_0 = C \left(\frac{(\text{N}/\text{H})_\odot}{\text{N}^+/\text{H}^+} \right) [L_{205} + L_{122}] \quad , \quad (4.16)$$

where N^+/H^+ is the ionized gas phase abundance ratio and

$$C = \frac{\alpha_B}{(\text{N}/\text{H})_{\odot}} \frac{\sqrt{2\pi}\sigma}{\int d \ln n_e \exp[-(\ln(n_e/n_{e0}))^2/2\sigma^2]} \times \frac{1}{(P_{205}(n_e) + P_{122}(n_e))/n_e} . \quad (4.17)$$

Here we introduce the calibration coefficient C , which is the number of ionizing photons per erg of emitted energy in the [N II] lines. C is a function of n_{e0} and the distribution parameter σ , but it can also be regarded as a function of the observed line ratio L_{122}/L_{205} and σ , $C(L_{122}/L_{205}, \sigma)$. The calculations assume a solar abundance $(\text{N}/\text{H})_{\odot} = 7.4 \times 10^{-5}$ (Asplund et al. 2009).

Thus,

$$\frac{\text{SFR}}{\text{M}_{\odot} \text{ yr}^{-1}} = \frac{2.77 \times 10^{-7}}{f_{\text{ion}}} \left(\frac{C(L_{122}/L_{205}, \sigma)}{10^{13} \text{ erg}^{-1}} \right) \times \left(\frac{(\text{N}/\text{H})_{\odot}}{\text{N}^+/\text{H}^+} \right) \frac{L_{122} + L_{205}}{L_{\odot}} . \quad (4.18)$$

In summary, we expect that a [N II]-based SFR calibration will depend on the calibration coefficient C –which is a function of the [N II] 122/205 line ratio (or n_e) and the width of the distribution of electron densities–, and the nitrogen abundance. Note that in our sample the oxygen abundance varies between galaxies by a factor of ~ 3 (Figure 5), and in addition to that, there are radial variations of the metal abundances within individual galaxies.

Figure 4.7 shows the behavior of C as a function of the [N II] 122/205 line ratio and σ . The solid and dashed lines represent the predictions based on the Tayal (2011) and Hudson & Bell (2005) collision coefficients, respectively. The first thing we notice is that, for a fixed value of σ , C increases as a function of the [N II] 122/205 line ratio (or electron density). This is the direct effect of the collisional suppression of the [N II] emission at electron densities near and above the critical density of the transition. In this regime, [N II] collisional de-excitations compete with the radiative decays and the [N II] intensity starts to systematically underestimate the amount

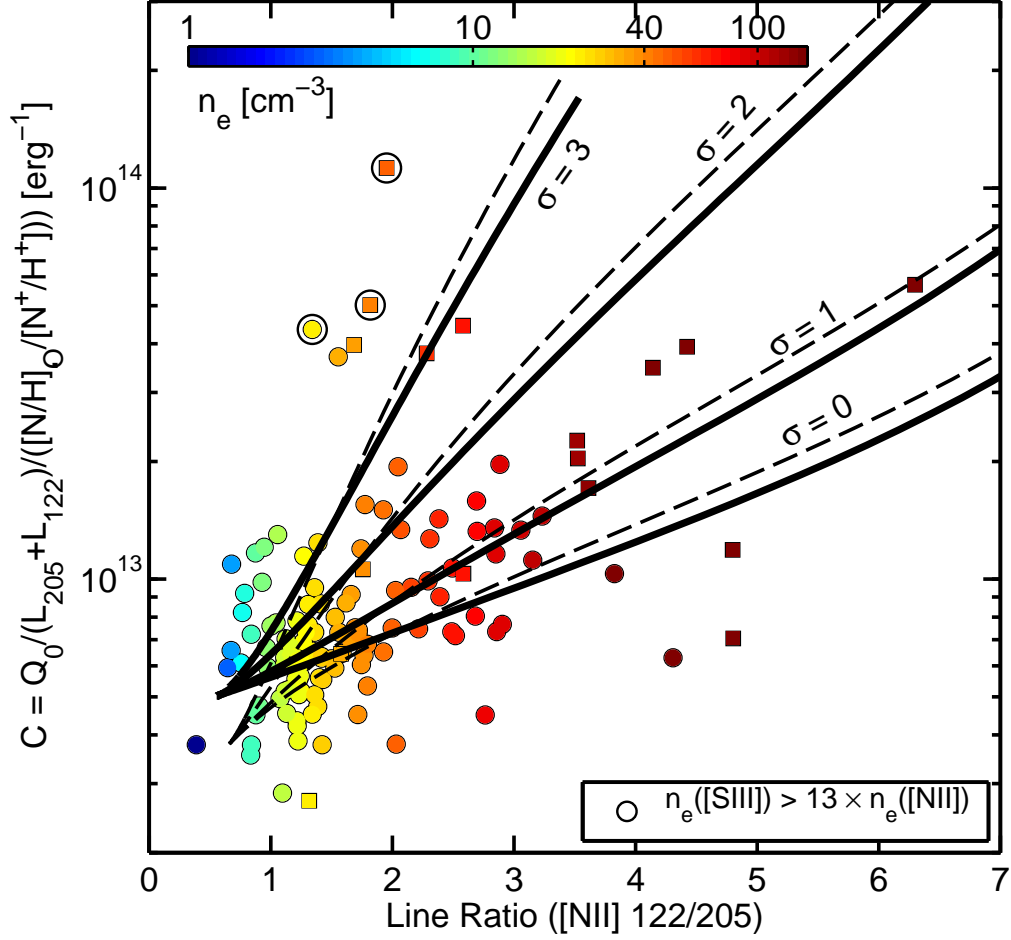


Figure 4.7: Number of ionizing photons per erg of emitted energy in the [NII] lines, C , as a function of the [N II] 122/205 line ratio, for four values of the electron density distribution parameter: $\sigma = 0$ (uniform density), 1, 2 and 3. The solid and dashed lines are based on the Tayal (2011) and Hudson & Bell (2005) collision coefficients, respectively. As the [N II] 122/205 line ratio increases, the parameter C becomes increasingly sensitive to the distribution of electron densities. This behavior has a direct effect on the accuracy of the determination of SFRs based on the [N II] lines, as $\text{SFR} \propto C \times L_{122+205}$ (see Equation 4.18). We also include the measured calibration coefficient C for 140 regions in our sample for which we have [N II] 122/205 line ratios available. For each region we use the characteristic oxygen abundance of its parent galaxy as a proxy for the nitrogen abundance. Finally, we use open circles to indicate three regions that show high C values and have [S III]-based electron density measurements that are a factor of ~ 13 or higher than those based on the [N II] lines. This could be an indication that these regions have wide electron density distributions.

of star formation activity. In practical terms, this means that two regions with the same SFR, similar electron density distribution, but different [N II] 122/205 line ratio, then the one with the higher line ratio (or higher n_e) will have a lower $L_{122+205}$ luminosity. This is especially true for cases when the electron density is higher than the critical density of the [N II] 205 μm line, $n_e \gtrsim 44 \text{ cm}^{-3}$ ([N II] 122/205 $\gtrsim 1.6$).

The second thing to note in Figure 4.7 is that the calibration coefficient C becomes increasingly sensitive to the distribution of electron densities σ . For example, for an observed line ratio [N II] 122/205 = 4, the value of C increases by a factor ~ 5 as σ varies from 0 to 2. This implies that in galaxies with $L_{122}/L_{205} \gtrsim 2$, the inferred SFR will be uncertain unless there is additional information available (e.g., from observations of [S III] line ratios) to constrain the actual distribution of electron densities.

Finally, Figure 4.7 also includes the calibration coefficient C measured in regions with [N II] 122/205 line ratios available obtained by inverting Equation (4.18). For the nitrogen abundance of the gas relative to the Sun, $(\text{N}^+/\text{H}^+)/(\text{N}/\text{H})_{\odot}$, we used as a proxy the oxygen abundance of its parent galaxy, and we assume that nitrogen and oxygen abundances scale linearly. This assumption is consistent with the observed scatter in the N/O – (O/H) correlation (e.g, Groves et al. 2004; Pérez-Montero & Contini 2009) in the metallicity range of the BtP galaxies ($12 + \log_{10}(\text{O}/\text{H}) \sim 8.6 - 9$). If we assume instead of the linear scaling an analytic function dependence of the nitrogen abundance with oxygen –like the one used in the MAPPINGS code–, then we observe an increase in the scatter of the observed C –[N II] 122/205 line ratio relation.

In general, the calibration coefficient C predictions are consistent with the observations, and as the [N II] 122/205 line ratio increases, the scatter in the observations can be explained by different assumptions on the width of the electron density dis-

tribution. A handful of exceptions are the group of 7 regions with [N II] 122/205 line ratios around $\sim 1.5 - 2.5$ that show significantly higher C values compared to the theoretical expectations, even for the $\sigma = 2$ case. To explore if the reason for the high calibration coefficients measured in these regions is associated to high σ values, we add the [S III] lines to our analysis. Since sulfur has a second ionization potential (23.3 eV) higher than that of N II, the sulfur forbidden lines [S III] 18.7 and 33.5 μm probe a higher ionization gas than the [N II] infrared lines, being sensitive to changes in the electron density in the $n_e \sim 100 - 10^4 \text{ cm}^{-3}$ range. For three of the seven regions we found [S III] 18.7 and 33.5 μm flux measurements obtained using The Infrared Spectrograph (IRS) on board *Spitzer* (Dale et al. 2009b). The size of the aperture used to measure the [S III] line fluxes is $23'' \times 15''$, roughly similar to the $\sim 17''$ SPIRE-FTS beam at 205 μm . We find that the [S III]-based electron densities of these regions are at least a factor of ~ 13 higher than those obtained using the [N II] lines. This suggests that these regions could have a wide distribution of electron densities, where a higher-ionization, higher-density gas component powered by massive stars coexists with the more diffuse gas traced by the [N II] lines. A complete analysis of the distribution of electron densities based on the combination of multiple tracers of ionized gas density (e.g., [N II], [S III], [O III]) will be presented in a future paper.

4.3.6 Correlations between the [N II] 122 and 205 μm transitions and the star formation activity

In this section we continue the study of the relationship between [N II] emission and star formation activity, but this time we also include the individual correlations with the [N II] 122 and 205 μm transitions, as for many sources only one of these two lines will be available.

The first panel in Figure 4.8 shows the correlation between $\Sigma_{\text{SFR}}(\text{H}\alpha + 24 \mu\text{m})$ and $\Sigma_{122+205}$ scaled by the nitrogen abundance factor $(\text{N}/\text{H})_{\odot}/(\text{N}/\text{H})$. The best linear fit through the data using a fixed slope of one yields:

$$\frac{\Sigma_{\text{SFR}}}{\text{M}_{\odot} \text{ yr}^{-1} \text{ kpc}^{-2}} = 3.31 \times 10^{-7} \left(\frac{(\text{N}/\text{H})_{\odot}}{\text{N}^{+}/\text{H}^{+}} \right) \frac{\Sigma_{122+205}}{L_{\odot} \text{ kpc}^{-2}}. \quad (4.19)$$

Based on this fit, the right panel shows the scatter as a function of IR color. We also plot the relation from Equation (4.18) for three cases: two uniform density cases ($\sigma = 0$) with electron densities of $n_e = 10$ and 100 cm^{-3} , and one case with a wider electron density distribution ($\sigma = 2$) and $n_{e0} = 100 \text{ cm}^{-3}$. For the nitrogen abundance term in Equation (4.18), we use as a proxy the median oxygen abundance of the sample ($12 + \log_{10}(\text{O}/\text{H}) \approx 8.83$). We find that the best linear fit to the data lies between the expectations from the $n_e = 10$ and $n_e = 100 \text{ cm}^{-3}$, single density ($\sigma = 0$) models (long-dashed and dot-dashed lines). We also observe that the $\Sigma_{\text{SFR}}/\Sigma_{122+205}$ ratio tends to increase as a function of infrared color and electron density. As we discussed in Section 3.5, these deviations can be understood in terms of the electron density of the gas relative to the critical density of the [N II] transitions, and the density distribution parameter σ . For example, from Equation (4.18) we expect regions with a density distribution parameter $\sigma = 2$ and $n_{e0} = 100 \text{ cm}^{-3}$ (short-dashed line) to have $\Sigma_{\text{SFR}}/\Sigma_{122+205}$ ratios a factor of ~ 5 higher than the ratio found by the best linear fit. In our sample, there are two galaxy central regions with densities around $n_e \approx 100 \text{ cm}^{-3}$ that have $\Sigma_{\text{SFR}}/\Sigma_{122+205}$ ratios that are consistent with the $\sigma = 2$, $n_{e0} = 100 \text{ cm}^{-3}$ model.

In the case of the [N II] 205 μm emission, we include in our analysis 366 additional regions that lie outside the KINGFISH/PACS coverage (thus, they lack [N II] 122 μm observations). The best fit through the $\Sigma_{205} - \Sigma_{\text{SFR}}$ correlation using a fixed slope of one yields:

$$\frac{\Sigma_{\text{SFR}}}{M_{\odot} \text{ yr}^{-1} \text{ kpc}^{-2}} = 4.51 \times 10^{-7} \left(\frac{(N/H)_{\odot}}{N^{+}/H^{+}} \right) \frac{\Sigma_{205}}{L_{\odot} \text{ kpc}^{-2}}. \quad (4.20)$$

The scatter around this fit is higher than the scatter in the $\Sigma_{122+205} - \Sigma_{\text{SFR}}$ correlation. We also observe a larger spread in the results from Equation (4.18) for the same set of assumptions on n_e and σ than in the case of the combined $\Sigma_{122+205}$ emission. For regions with infrared colors cooler than $\nu f_{\nu}(70 \mu\text{m})/\nu f_{\nu}(100 \mu\text{m}) \approx 0.9$ the scatter cloud around the linear fit is roughly symmetric, with a standard deviation of 0.25 dex. At about the same infrared color threshold, Herrera-Camus et al. (2015) find a systematic increase of the fit residuals from the $\Sigma_{[\text{CII}]} - \Sigma_{\text{SFR}}$ correlation, and Croxall et al. (2012) find a drop in the [C II] to FIR ratio for regions in NGC 4559 and NGC 1097 (although they do not find any signs of a “[N II]-deficit”). For IR colors warmer than $\nu f_{\nu}(70 \mu\text{m})/\nu f_{\nu}(100 \mu\text{m}) \approx 0.9$ –which according to Equation (4.5) corresponds to an electron density of $n_e \approx 33 \text{ cm}^{-3}$, close to the critical density of the line– we observe a strong increase in the $\Sigma_{\text{SFR}}/\Sigma_{205}$ ratio as a function of infrared color and electron density. These deviations are mainly driven by the collisional quenching of the [N II] 205 μm line due to its relatively low critical density.

Finally, in the case of the $\Sigma_{122} - \Sigma_{\text{SFR}}$ correlation, shown in the bottom two panels of Figure 4.8, the best fit through the data using a fixed slope of one yields:

$$\frac{\Sigma_{\text{SFR}}}{M_{\odot} \text{ yr}^{-1} \text{ kpc}^{-2}} = 3.33 \times 10^{-7} \left(\frac{(N/H)_{\odot}}{N^{+}/H^{+}} \right) \frac{\Sigma_{122}}{L_{\odot} \text{ kpc}^{-2}}. \quad (4.21)$$

This linear fit is similar to the relation from Equation (4.18) for both single density, $n_e = 10$ and 100 cm^{-3} models. The scatter around the fit is 0.26 dex, slightly better than the 0.28 dex we measure in the $\Sigma_{122+205} - \Sigma_{\text{SFR}}$ correlation. Compared to the [N II] 205 μm case, regions start to deviate from the best linear fit at higher IR colors, and there seems to be a smaller dependence between the amplitude of these

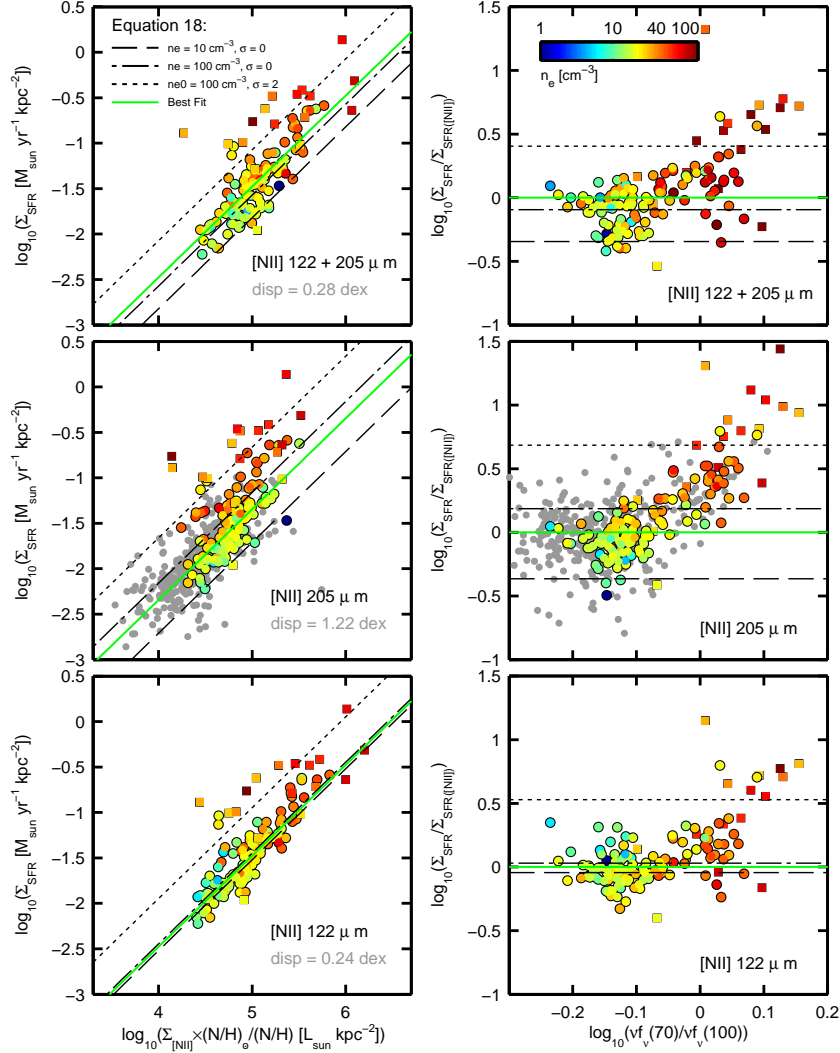


Figure 4.8: (Left panels) Star formation rate surface density ($\Sigma_{\text{SFR}}(\text{H}\alpha + 24 \mu\text{m})$) versus the combined ($\Sigma_{122+205}$) and individual (Σ_{122} and Σ_{205}) [N II] line surface brightness scaled by the nitrogen abundance factor $(N/H)_{\odot}/(N/H)$. Each point represents a $17''$ region selected from the 21 BtP galaxies. For regions with [N II] 122/205 line ratios available, the color represents the electron density. In the case of the [N II] 205 μm line, the gray points correspond to 366 additional regions that lie outside the KINGFISH/PACS coverage and therefore lack [N II] 122 μm observations. We also show regions with deprojected distances to the center smaller than 400 pc as squares. The green solid line corresponds to the best fit through the data for a fixed slope of one. The rest of the line correspond to results from Equation (4.18) for different assumptions on the electron density distribution parameters n_e and σ . (Right panels) Ratio between Σ_{SFR} measured using H α +24 μm and the [N II] lines (based on the best linear fit) as a function of infrared color and electron density. We also include the predictions from Equation (4.18) shown in the left panels. We observe a systematic increase of the $\Sigma_{\text{SFR}}/\Sigma_{\text{SFR}}([\text{N II}])$ ratio as a function of infrared color and electron density.

deviations and the electron density of the region. This could be explained by the fact that the critical density of the [N II] 122 μm transition is about six times higher than that of the [N II] 205 μm line, which makes the former line a more reliable tracer of the star formation activity in case the electron density of the source is unknown.

4.3.7 Comparison with models and other extragalactic [N II] samples

In this section we continue the study of the relation between [N II] emission, star formation activity and electron density by complementing our sample of nearby spirals with local LIRGs, and comparing these observations to predictions from Equation (4.18) and the photoionization code MAPPINGS-III (Levesque et al. 2010). A brief description of the LIRG sample and the code MAPPINGS-III can be found in Section 2.

The first panel in Figure 4.9 shows the $L_{205} - \text{SFR}$ correlation for the BtP galaxies and local LIRGs drawn from the GOALS (Zhao et al. 2013) sample. The luminosities and SFRs for the BtP galaxies are the result of the sum of the individual regions shown in Figure 4.8; the color of the circles indicate the average electron density of the galaxy. The only exception is NGC 1266 for which we only have an upper limit of the electron density due to a non-detection in [N II] 122 μm emission. We observe that the average electron density of BtP galaxies range between $n_e = 15$ and 100 cm^{-3} , and those systems with electron densities higher than the critical density of the line tend to have higher SFR/L_{205} ratios. This result is similar to what we find in the analysis of the spatially resolved $\Sigma_{205} - \Sigma_{\text{SFR}}$ correlation.

In addition to the observations, Figure 4.9 includes results from Equation (4.18) and the MAPPINGS-III code. For the latter, the shaded color areas represent the

model results for different assumptions on the electron density (blue for $n_e = 10 \text{ cm}^{-3}$ and red for $n_e = 100 \text{ cm}^{-3}$) and metallicity of the gas (lower and upper boundaries for $Z = 2Z_\odot$ and $Z = Z_\odot$, respectively). The MAPPINGS-III code predicts that, for a fixed metallicity, H II regions with electron densities of $n_e = 100 \text{ cm}^{-3}$ will have SFR/L_{205} ratios a factor of ~ 4 higher than those with $n_e = 10 \text{ cm}^{-3}$. These results are consistent with the observed $L_{205} - \text{SFR}$ relationship for the BtP galaxies. As we discussed in Section 3.5, one of the reasons for this behavior is the collisional quenching of the [N II] 205 μm line when $n_e \gtrsim n_{\text{crit}}$. Regarding the GOALS galaxies, about half of them have SFR/L_{205} ratios consistent with the MAPPINGS-III results for H II regions with $n_e = 100 \text{ cm}^{-3}$. The other half have SFR/L_{205} ratios too high to be interpreted by the MAPPINGS-III model outputs. For these cases, one possibility is that the ionized gas is denser than $n_e = 100 \text{ cm}^{-3}$. We explore this scenario using Equation (4.18) and we found that, under the assumption of isodensity gas ($\sigma = 0$), an electron density of 800 cm^{-3} is required to reproduce the high SFR/L_{205} ratios (dot-dashed line). Another possibility is to drop the assumption of a single density gas. In that case, we can increase the density distribution parameter from $\sigma = 0$ to $\sigma = 2$, which will only require a characteristic electron density of $n_{e0} = 100 \text{ cm}^{-3}$ to reproduce the high SFR/L_{205} ratios observed in some of the GOALS galaxies. This analysis reinforces our previous conclusion about the limitations on using the [N II] 205 μm line as a star formation tracer when the properties of the ionized gas of the source (in particular n_e and σ) are not constrained.

Compared to the [N II] 205 μm case, the observed correlations for the BtP galaxies that involve the [N II] 122 μm line are tighter, resulting from a weaker dependence of the [N II] 122 μm line emission with electron density. This result is consistent with the predictions from the MAPPINGS-III code, where, for example, the SFR/L_{122} ratios for the $n_e = 10$ and 100 cm^{-3} cases only differ by a factor of 1.5.

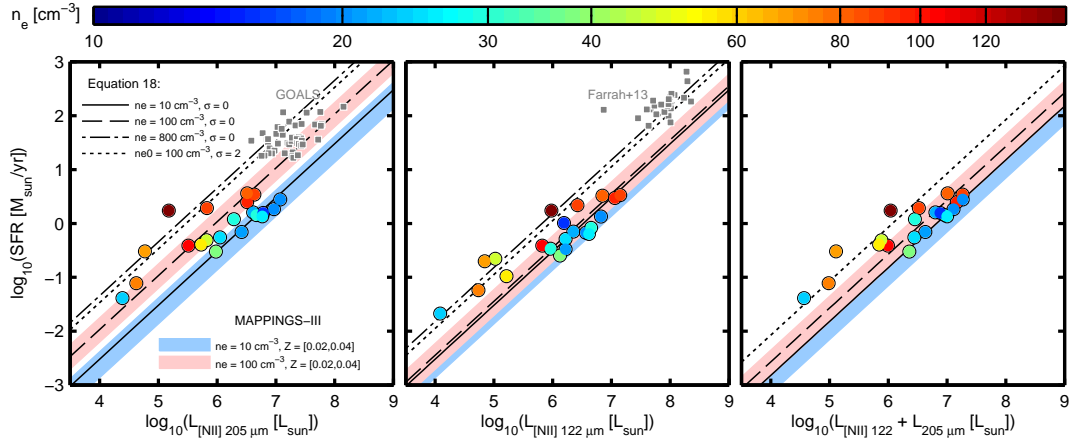


Figure 4.9: $[\text{N II}]$ 122 and 205 μm luminosities versus SFR compared to the results from the MAPPINGS-III code and Equation (4.18). BtP galaxies are shown as circles, where the color represents the electron density. In general, we find a good agreement between the observed correlations and the model predictions, where the scatter of the correlation can be understood in terms of variations in properties of the ionized gas (n_e and σ) and metallicity. The galaxy NGC 1266 is shown as a white circle because we do not have a measurement of the electron density due to a non-detection in $[\text{N II}]$ 122 μm emission. The SFRs were measured using a combination of 24 μm and $\text{H}\alpha$ emission based on the calibration by (Calzetti et al. 2007). For comparison with our sample of star-forming galaxies we include LIRGs from the GOALS (Zhao et al. 2013) and Farrah et al. (2013) samples, both used to derive SFR calibrations based on the $[\text{N II}]$ lines. The MAPPINGS-III results are based on assuming H II regions with electron densities of $n_e = 10$ and 100 cm^{-3} and gas metallicities in the $Z = Z_\odot - 2Z_\odot$ range. Finally, the results from Equation (4.18) are based on the following set of conditions: $\sigma = 0$ and $n_e = 10 \text{ cm}^{-3}$ (solid line), $\sigma = 0$ and $n_e = 100 \text{ cm}^{-3}$ (dashed line), $\sigma = 0$ and $n_e = 800 \text{ cm}^{-3}$ (dot-dashed line), and $\sigma = 2$ and $n_{e0} = 100 \text{ cm}^{-3}$ (short-dashed line).

Similarly, the results from Equation (4.18) for $\sigma = 0$ and $n_e = 10$ and 100 cm^{-3} differ only by a factor of 1.2. Regarding the LIRGs drawn from the Farrah et al. (2013) sample, they tend to have SFR/L_{122} ratios that are a factor of ~ 3 higher than those of the BtP galaxies. According to the results from Equation (4.18), this difference between the BtP galaxies and the LIRGs suggest that the ionized gas in the latter is dominated by dissimilar conditions, e.g., an homogeneous ionized medium with a high electron density ($n_e = 800 \text{ cm}^{-3}$), or ionized gas with $n_{e0} = 100 \text{ cm}^{-3}$ but characterized by a wide electron density distribution ($\sigma = 2$).

In summary, the [N II] 122 and 205 μm lines can be used for measurements of the SFR in galaxies. Note however that the [N II]-based SFR calibration (Equation 4.18) depends, among other things, on the electron density of the gas and the shape of the electron density distribution. Additional constraints on the properties of the ionized gas, provided for example by the combination of the [N II] and [S III] lines, are required to avoid uncertainties in the SFR determinations larger than a factor of ~ 2 . Without prior knowledge on these variables, the [N II] 122 μm transition is in principle a better tracer than the [N II] 205 μm line due to its approximately six times higher critical density.

4.4 Summary and Conclusions

In this paper we use the [N II] 122 and 205 μm far-infrared transitions to study the properties of the low-excitation H II gas in 21 galaxies observed by *Herschel* as part of the “Beyond the Peak” and KINGFISH projects. In particular, we use the [N II] 122/205 line ratio to measure the electron density of the singly-ionized gas. We then study the dependence between the electron density and properties of the ISM such as radiation field strength, infrared color, metallicity, among others. The [N II] 122 and 205 μm far-infrared lines also have potential as star formation tracers, and in this work we study the correlations between the [N II] 122 and 205 μm emission and the star formation activity. In particular, we explore the dependence of these correlations with properties of the ionized gas such as its density and metallicity.

We highlight the following points:

1. For 140 regions selected from 21 galaxies we measure [N II] 122/205 line ratios in the range $\sim 0.6 - 5$, which correspond to electron densities of the singly-

ionized gas in the range $n_e \sim 3 - 230 \text{ cm}^{-3}$. This assumes that the distribution of gas within each region is homogeneous. If we consider instead a distribution of electron densities that follows a log-normal distribution characterized by a width σ , and a characteristic electron density n_{e0} (Equation 4.13), then the relationship between the [N II] 122/205 line ratio and n_{e0} is given by Equation 4.15. We find that only one region has a [N II] 122/205 line ratio below the theoretical limit of ~ 0.6 , which corresponds to gas with $n_e \ll n_{\text{crit}}$. The median ionized gas density in the sample is $n_e \approx 30 \text{ cm}^{-3}$, comparable to the median electron density measured in the Carina nebula (Oberst et al. 2011, 2006). Within individual galaxies we measure variations in the ionized gas density as high as a factor of ~ 20 . In general, the central $\sim 400 \text{ pc}$ regions exhibit the highest electron densities in the galaxy.

2. We find a good correlation between electron density and infrared color, dust-weighted mean starlight intensity ($\langle U \rangle$), TIR surface density (Σ_{TIR}) and SFR surface density (Σ_{SFR}). The origin of these good correlations could be associated with: (1) the evolutionary stage of the H II region, as young, compact H II regions will produce very intense radiation fields, or (2) the fact that dense H II regions in pressure equilibrium with the surrounding neutral gas implies a high density molecular gas environment that may lead to further star formation activity.

These relationships can also be useful when, in order to predict the [N II] 205 μm intensity from the [N II] 122 μm intensity (or vice versa), an electron density needs to be assumed. In particular, we provide an equation (Equation 5) to estimate the electron density from the $\nu f_\nu(70 \mu\text{m})/\nu f_\nu(100 \mu\text{m})$ infrared color.

3. We use the [N II] far-infrared transitions to measure the ionizing photon rate

Q_0 . In the low-density limit (Equation 4.8) we find a median global ionizing photon rate among the BtP galaxies of $Q_0 = 1.98 \times 10^{52} \text{ s}^{-1}$. Normalized by the covered area, the median ionizing photon rate surface density is $1.96 \times 10^{51} \text{ s}^{-1} \text{ kpc}^{-2}$, which is ~ 3 times the ionizing photon rate measured inside the solar circle ($\sim 8.5 \text{ kpc}$) in the Milky Way (Bennett et al. 1994).

4. We derive relations between the [N II] line emission and star formation rate in the low density limit (Equations 4.10 and 4.11), and for a range of electron densities (Equation 4.18). The latter assumes a log-normal distribution of electron densities characterized by the width of the distribution σ ($\sigma = 0$ corresponds to uniform density), and the characteristic electron density of the ionized gas n_{e0} . We then relate the SFR and the [N II] luminosity via the the calibration coefficient C (Equation 4.17), which is the number of ionizing photons per erg of emitted energy in the [N II] lines. C is a function of the [N II] 122/205 line ratio (or electron density) and σ . We find that C increases as a function of both the [N II] 122/205 line ratio and the density distribution parameter σ . The differences between the values of C for different ionized gas conditions can be significant, and imply that not only the [N II] 122/205 line ratio, but additional constraints on the electron density distribution are important to accurately measure SFRs based on the [N II] transitions.
5. In general, we find good correlations between the surface brightness of the [N II] line emission and the star formation rate surface density. However, and as we show in Equation (4.18), these correlations depend on the nitrogen abundance, the characteristic electron gas density and the density distribution parameter σ . The lack of constraints on any of these parameters can result in large uncertainties in the SFR determination based on the [N II] lines. The

best linear fit to the observed correlations of Σ_{SFR} with Σ_{205} , Σ_{122} and $\Sigma_{122+205}$ for the BtP regions are:

$$\begin{aligned} \frac{\Sigma_{\text{SFR}}}{M_{\odot} \text{ yr}^{-1} \text{ kpc}^{-2}} &= 4.51 \times 10^{-7} \left(\frac{(\text{N}/\text{H})_{\odot}}{\text{N}^{+}/\text{H}^{+}} \right) \frac{\Sigma_{205}}{L_{\odot} \text{ kpc}^{-2}}, \\ &= 3.33 \times 10^{-7} \left(\frac{(\text{N}/\text{H})_{\odot}}{\text{N}^{+}/\text{H}^{+}} \right) \frac{\Sigma_{122}}{L_{\odot} \text{ kpc}^{-2}}, \\ &= 3.31 \times 10^{-7} \left(\frac{(\text{N}/\text{H})_{\odot}}{\text{N}^{+}/\text{H}^{+}} \right) \frac{\Sigma_{122+205}}{L_{\odot} \text{ kpc}^{-2}}. \end{aligned}$$

For all three correlations we find that regions with warm infrared colors tend to show deviations from the best linear fit in the sense that a [N II]-based SFR calibration will underestimate the reference amount of star formation activity (measured as a combination of 24 μm and $\text{H}\alpha$ emission). For the [N II] 205 μm line, these deviations starts at an IR color threshold of $\nu f_{\nu}(70 \mu\text{m})/\nu f_{\nu}(100 \mu\text{m}) \approx 0.9$, and they increase as a function of infrared color and electron density until reaching deviations of ~ 1 dex at $\nu f_{\nu}(70 \mu\text{m})/\nu f_{\nu}(100 \mu\text{m}) \approx 1.2$. This is likely a density effect, given that in regions with gas densities closer or greater than n_{crit} , the [N II] 205 μm collisional de-excitations compete with the radiative decays and the [N II] 205 μm intensity stops tracing any increment in the star formation activity.

For the two correlations that involve the [N II] 122 μm line we also observe deviations from the best linear fit growing with IR color, but at a higher IR color threshold than in the [N II] 205 μm case ($\nu f_{\nu}(70 \mu\text{m})/\nu f_{\nu}(100 \mu\text{m}) \approx 1.1$). This is probably because the critical density of the [N II] 122 μm transition is ~ 6 times higher than that of [N II] 205 μm , which makes the [N II] 122 μm transition a better star formation tracer than the [N II] 205 μm emission.

6. We compare the $L_{[\text{NII}]} - \text{SFR}$ correlations for the BtP galaxies to a sample

of local LIRGs (Farrah et al. 2013; Zhao et al. 2013) and predictions from the MAPPINGS-III photoionization code and Equation (4.18) for different assumptions on the ionized gas properties. In general, we find a good agreement between the $L_{[\text{NII}]} - \text{SFR}$ correlations and the model results, where the observed trends and scatter can be understood in terms of variations of the electron density of the gas and the width of the electron density distribution. Both theory and observations reveal the importance of having prior knowledge of the ionized gas properties of the source (e.g., metallicity, $[\text{N II}]$ and $[\text{S III}]$ based electron density measurements) in order to avoid underestimating the star formation activity. In case there are no constraints on the ionized gas, the $[\text{N II}] 122 \mu\text{m}$ emission proves to be a more reliable tracer than $[\text{N II}] 205 \mu\text{m}$ due to its higher critical density.

Chapter 5

Thermal Pressure in the Neutral Gas of Nearby Galaxies

5.1 Introduction

In our current model of the multiphase interstellar medium (ISM), the neutral atomic gas resides in two distinct phases commonly referred as the cold neutral medium (CNM; $T \lesssim 300$ K), and the warm neutral medium (WNM; peak temperature around $T \approx 8,000$ K) (Cox 2005; Field et al. 1969; Heiles & Troland 2003). These two phases coexist in pressure equilibrium, regulated by the thermal balance between heating and radiative cooling (Draine 1978; Wolfire et al. 1995, 2003), and the vertical pressure exerted by the weight of the interstellar medium (Badhwar & Stephens 1977; Ostriker et al. 2010). These equilibrium conditions define a thermal pressure (P_{th}) curve that is a function of the neutral gas density (n), and set the minimum (P_{min}) and maximum (P_{max}) pressures for which the WNM and CNM phases can coexist.

In the Galactic plane, different observational techniques have been employed

to characterize the distribution of thermal pressures of the diffuse, neutral gas. Jenkins & Tripp (2011) use ultraviolet spectra of local stars to identify absorption features created by neutral carbon (C I). These features can be used to determine the population ratios between the three fine-structure ground state levels of C I, revealing the excitation conditions and thermal pressure of the diffuse gas along the line of sight. Jenkins & Tripp (2011) find a distribution of thermal pressures that can be well represented by a log-normal distribution that extends from $P_{\text{th}}/k \sim 10^3$ to 10^4 K cm^{-3} , with a mean value of $P_{\text{th}}/k \approx 3,800 \text{ K cm}^{-3}$. An additional method to probe the diffuse gas along a particular line of sight is to use [C II] $158 \mu\text{m}$ velocity-resolved observations towards bright infrared continuum sources. This allows, based on the absorption and emission features in the spectra, to measure the line opacity and the line peak temperature, which in turn can be used to derive the density and thermal pressure of the neutral gas. Using this technique, Gerin et al. (2015) find a median thermal pressure of $P_{\text{th}}/k \approx 5,900 \text{ K cm}^{-3}$ in 13 line of sights in the Galactic plane.

On the modeling side, Wolfire et al. (2003) use a comprehensive approach that considers the different sources of heating and cooling of the gas in order to estimate P_{min} , P_{max} and the average thermal pressure in the Galaxy as a function of radius. They conclude that most of the neutral gas in the ISM of the Galaxy out to $\sim 18 \text{ kpc}$ have thermal pressures that lie between P_{min} and P_{max} . Inside the solar circle, they calculate a mean thermal pressure of $P_{\text{th}}/k \approx 3,000 \text{ K cm}^{-3}$, which is consistent with the observational results.

The characteristics of the thermal pressure curve depend directly on the gas heating rate, which in turn is a function of the metallicity, the ionization rate of atomic hydrogen and the FUV radiation field (e.g., Wolfire et al. 1995, 2003). The latter is directly proportional to the star formation activity and illustrate the strong

connection between pressure and star formation in the ISM. Blitz & Rosolowsky (2006) find that the hydrostatic pressure (of which the thermal pressure is about $\sim 10\text{--}25\%$) determines the fraction of the neutral gas that is molecular and therefore available to form stars. Ostriker et al. (2010) also explore the connection between thermal pressure and star formation on $\sim\text{kpc}$ scales in the context of a model where the gas in the disk evolves into a dynamical, thermal, and star formation equilibrium. This implies that if the midplane pressure is higher than P_{max} or lower than P_{min} , then the fraction of the cold gas and the star formation activity evolve in order to bring the midplane pressure close to the average value defined by the two-phase thermal pressure curve.

In a multi-phase ISM in pressure equilibrium it is of great interest to obtain a direct measurement of the thermal pressure. In this paper we use a method that combines the [C II] 158 μm and HI 21 cm line to measure the [C II]-cooling rate, the density of atomic hydrogen and, for a given temperature of the CNM, the thermal pressure in the ISM of nearby galaxies. This paper is organized as follows. In Section 2 we describe the sample of galaxies and the data. In Section 3 we discuss our method to derive thermal pressures using the [C II] and HI data. In Section 4 we describe how we select our sample of atomic-dominated regions. We also analyze the thermal pressure distribution we derive for the sample of atomic-dominated regions and a sub-sample of regions that resemble the conditions in the solar neighborhood. Finally, we study the relationship between thermal pressure and radiation field strength and star formation activity, including a comparison to the results from the Wolfire et al. (2003) model.

5.2 Main Sample Description

Our sample consist of 31 galaxies drawn from the KINGFISH sample (“Key Insights on Nearby Galaxies: A Far-Infrared Survey with Herschel”; Kennicutt et al. 2011) that have CO and HI observations available from the THINGS (“The HI Nearby Galaxy Survey”; Walter et al. 2008) and HERACLES (“The HERA CO Line Extragalactic Survey”; Leroy et al. 2009) surveys. With the exception of NGC 3077, that is classified as I0pec, all the other galaxies in our sample are late-type spirals. They span a range in distance of $D \sim 2.8 - 26.5$ Mpc, and in total infrared (TIR) luminosity of $L_{\text{TIR}} \sim 10^{8.3} - 10^{10.7} L_{\odot}$ (Dale et al. 2012). Their metallicity, taken from Moustakas et al. (2010) and measured as the average between the characteristic oxygen abundances from the Pilyugin & Thuan (2005) (PT05) and Kobulnicky & Kewley (2004) (KK04) calibrations, are in the $12 + \log(\text{O}/\text{H}) \sim 8.1 - 9.0$ range.

5.2.1 KINGFISH [C II]

In this work we use [C II] $158 \mu\text{m}$ observations drawn from the *Herschel* key program KINGFISH (Kennicutt et al. 2011). These were carried out with the Photodetector Array Camera & Spectrometer (PACS) on board *Herschel*, and were reduced using the Herschel Interactive Processing Environment (HIPE) version 11.0. For more details on the data reduction process we refer to Croxall et al. (2013) and Croxall et al. (in prep). The angular resolution of the PACS spectrometer at $158 \mu\text{m}$ is about $\sim 12''$. More than half of the [C II] maps consist of a strip that covers the central region of the galaxy and part of the disk. In addition, there are cases where we have coverage of extra-nuclear regions located in the outskirts of the disk (e.g. M 101, NGC 6946).

5.2.2 THINGS HI

We draw HI maps from the Very Large Array THINGS survey (Walter et al. 2008). These have angular resolutions in the $6'' - 25''$ range. For more details on the data reduction and map properties we refer to Walter et al. (2008). We convert the 21 cm intensities into HI surface densities via

$$\Sigma_{\text{HI}} [M_{\odot} \text{ pc}^{-2}] = 0.02 I_{\text{HI}} \times \cos i [\text{K km s}^{-1}]. \quad (5.1)$$

This equation assumes optically thin emission, includes the contribution from heavy elements and is projected to face-on orientation using inclinations (i) drawn from the compiled list in Kennicutt et al. (2011) and Hunt et al. (2014).

5.2.3 HERACLES CO

We trace the molecular gas using CO($J = 2 - 1$) observations taken with the Heterodyne Receiver Array (HERA) on the IRAM 30 m telescope obtained as part of the HERACLES survey (Leroy et al. 2009). The angular resolution of the HERACLES data is about $\sim 13''$, similar to the resolution of the *Herschel*/PACS [C II] observations. We convert the CO($2-1$) intensities into H₂ surface densities following

$$\Sigma_{\text{H}_2} [M_{\odot} \text{ pc}^{-2}] = 6.25 I_{\text{CO}} \times \cos i [\text{K km s}^{-1}], \quad (5.2)$$

where we have assumed a CO line ratio of $I_{\text{CO}}(2-1)/I_{\text{CO}}(1-0) = 0.7$ and a standard Milky Way CO($1-0$)-to-H₂ conversion factor $X_{\text{CO}} = 2.0 \times 10^{20} \text{ cm}^{-2} (\text{K km s}^{-1})^{-1}$. Similar to the HI case, we correct the mass surface density for inclination. HERACLES is sensitive to molecular gas mass surface densities down to $\Sigma_{\text{H}_2} \sim 3 M_{\odot} \text{ pc}^{-2}$.

5.2.4 Additional Data

In order to trace the un-obscured and obscured components of the star formation activity in our galaxies we use 24 μm and $\text{H}\alpha$ maps, respectively. The 24 μm maps were drawn from the Spitzer Infrared Nearby Galaxy Survey (SINGS; Kennicutt et al. 2003). The $\text{H}\alpha$ images were assembled by (Leroy et al. 2012) and come mainly from the SINGS and Local Volume Legacy (Dale et al. 2009a) surveys. The $\text{H}\alpha$ data were corrected for Galactic extinction, foreground stars were masked and the [N II] contribution was removed. Finally, we also use *Herschel*/PACS 70 and 160 μm maps drawn from the photometric KINGFISH sample (Dale et al. 2012).

5.2.5 Methods

We convolve all of our maps to have the same angular resolution. The final angular resolution varies from galaxy to galaxy, as the HI map beam size can be higher or lower than the angular resolution of the [C II], CO and PACS 160 μm maps ($\approx 13''$). The $\text{H}\alpha$, 24 μm and PACS 70 μm maps have all higher resolution than the [C II] and CO data. The typical size of the regions in our sample is about ~ 1 kpc.

We measure star formation rate surface densities (Σ_{SFR}) using a combination of the $\text{H}\alpha$ and 24 μm emission following the calibration by Calzetti et al. (2007). We also estimate the dust-weighted mean starlight intensity, $\langle U \rangle$, using the 70 to 160 μm ratio and the empirical fit to the Draine & Li (2007) model derived by Muñoz-Mateos et al. (2009a) (Equation A5). As a reference, $U = 1$ is the local interstellar radiation field in the Milky Way, normalized to the MMP field (Mathis et al. 1983).

5.3 [C II] 158 μm emission and the thermal pressure in the diffuse ISM

The [C II] 158 μm emission is the result of the radiative de-excitation of carbon ions (C^+) collisionally excited by electrons (e^-), hydrogen atoms (H) and/or hydrogen molecules (H_2). Which of these collisional partners dominate the excitation of C^+ depend on the properties of the gas where the [C II] emission originates. Due to the low ionization potential of neutral carbon (11.3 eV), the predominant sources of [C II] emission are the CNM, dense PDRs, and the WIM.

In the optically thin limit, the [C II] integrated line intensity $I_{[\text{CII}]}$ is given by (e.g., Crawford et al. 1985; Goldsmith et al. 2012)

$$I_{[\text{CII}]} = 2.3 \times 10^{-21} \left(\frac{2e^{-91.2/T}}{1 + 2e^{-91.2/T} + n_{\text{crit}}/n} \right) N_{\text{C}^+}, \quad (5.3)$$

where $I_{[\text{CII}]}$ is in units of $\text{erg s}^{-1} \text{cm}^{-2} \text{sr}^{-1}$, T is the kinetic temperature in K, n is the volume density of the collisional partner (H , H_2 or e^-) in cm^{-3} , N_{C^+} is the column density of C^+ in cm^{-2} and n_{crit} is the critical density for collisions with a given partner in cm^{-3} .

When the excitation of C^+ ions is dominated by collisions with hydrogen atoms from the diffuse, atomic gas (i.e., $n \approx n_{\text{HI}}$), we can write the [C II] cooling per hydrogen atom as

$$\Lambda_{[\text{CII}]} [\text{erg s}^{-1} \text{atom}^{-1}] = \frac{4\pi I_{[\text{CII}]}}{f_{\text{CNM}} N_{\text{HI}}}, \quad (5.4)$$

where N_{HI} corresponds to the HI column density in cm^{-2} and f_{CNM} to the fraction of the neutral atomic gas that is in the CNM. Considering f_{CNM} is important because the contribution to the [C II] emission per hydrogen atom from the CNM is about

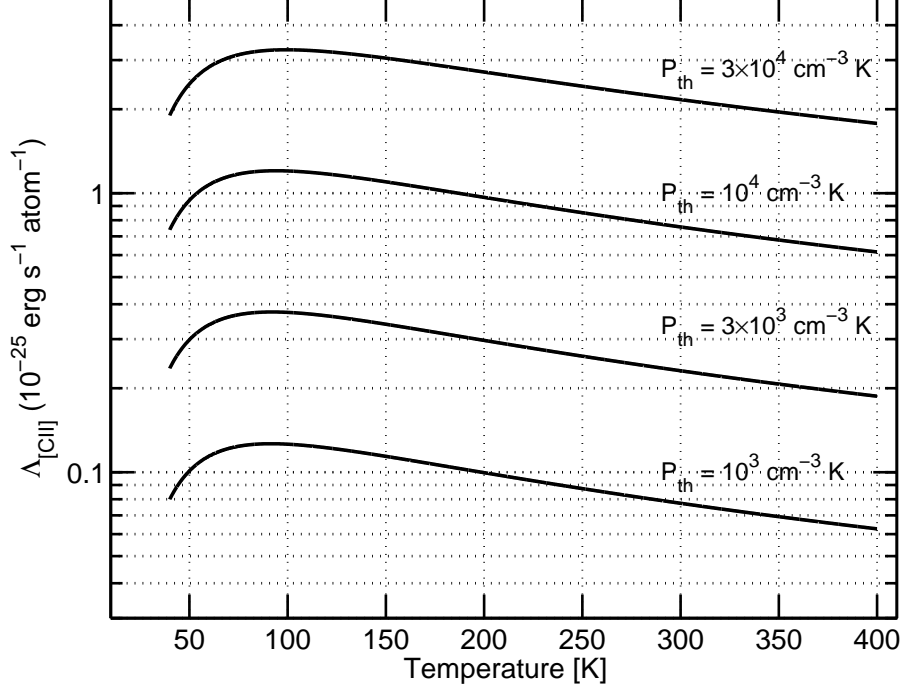


Figure 5.1: [C II] cooling rate per H atom ($\Lambda_{[CII]}$) as a function of temperature for four different values of the thermal pressure of the gas (P_{th}). We assume a carbon abundance of $[C/H] = 1.4 \times 10^{-4}$. For a given P_{th} , the [C II] cooling rate varies less than a factor of ~ 2 in the temperature range $40 \gtrsim T \gtrsim 400$ K. For reference, the typical CNM temperature is ~ 80 K.

~ 20 higher compared to that of the WNM (Wolfire et al. 2010).

We combine Equations (5.3) and (5.4) to link the [C II] cooling rate to the density of atomic hydrogen

$$\Lambda_{[CII]} = 2.9 \times 10^{-20} \left[\frac{C}{H} \right] \left(\frac{2e^{-91.2/T}}{1 + 2e^{-91.2/T} + 3 \times 10^3/n_{HI}} \right). \quad (5.5)$$

Here we have assumed that the critical density for collisions with H atoms for a typical CNM temperature of $T \approx 100$ K (e.g., Heiles & Troland 2003) is $n_{crit} \approx 3,000 \text{ cm}^{-3}$ (Goldsmith et al. 2012). We also assume that all carbon is in a singly ionized state, thus $N_{C^+}/N_{HI} = [C/H]$. The advantage of Equation 5.5 is that, for assumptions on the temperature of the CNM gas and the carbon abundance ($[C/H]$), we can estimate n_{HI} based on the observed [C II] cooling rate. Finally, we can

measure the thermal pressure of the diffuse, atomic gas following

$$P_{th}/k \text{ [K cm}^{-3}] = 1.1n_{\text{HI}}T. \quad (5.6)$$

How sensitive is this $\Lambda_{[\text{C II}]}$ -based determination of the thermal pressure to changes in the assumption of the temperature of the gas? Figure 5.1 shows an estimate of $\Lambda_{[\text{C II}]}$ as a function of temperature for four different values of P_{th} (see also Figure 3.1 in Kulkarni & Heiles 1987) and assuming $[\text{C}/\text{H}] = 1.4 \times 10^{-4}$ (Sofia et al. 2004). We see that the $[\text{C II}]$ cooling rate per hydrogen atom varies less than a factor of ~ 1.3 in the $60 \gtrsim T \gtrsim 120$ K range, and less than a factor ~ 2 in the $40 \gtrsim T \gtrsim 400$ K range. This illustrates the great potential of the $[\text{C II}]$ line as an estimator of the thermal pressure in the diffuse, atomic ISM.

5.4 Results and Discussion

5.4.1 Criteria for selection of atomic dominated regions

If we want to use the $[\text{C II}]$ line as a tracer of the thermal pressure of the neutral atomic gas, then we need to select regions in our sample where the collisional excitation of C^+ is dominated by H atoms. We do that by comparing the mass surface densities of molecular and atomic gas. Figure 5.2 shows the $[\text{C II}]$ cooling rate as a function the $\Sigma_{\text{H}_2}/\Sigma_{\text{HI}}$ ratio for 2,093 regions for which we have $[\text{C II}]$ and HI detections with $S/N \geq 3$. Triangles represent regions for which we only have $3\text{-}\sigma$ upper limits on Σ_{H_2} driven by a non-detection in CO. $\Lambda_{[\text{C II}]}$ is calculated using Equation (5.4) assuming $f_{\text{CNM}} = 0.5$, i.e., half of the atomic gas is in the CNM phase (Heiles & Troland 2003; Pineda et al. 2013). The color scale indicates the star formation rate surface density. We find that the $[\text{C II}]$ cooling rate increases as a function of the $\Sigma_{\text{H}_2}/\Sigma_{\text{HI}}$ ratio, and that for a given $\Sigma_{\text{H}_2}/\Sigma_{\text{HI}}$ ratio, regions

with higher Σ_{SFR} have higher [C II] cooling rates. This is expected as in thermal equilibrium, the heating of the gas powered by the star formation activity is balanced by the cooling, of which the [C II] emission is one of the main channels (e.g., Herrera-Camus et al. 2015).

We consider as atomic dominated regions those where $\Sigma_{\text{HI}} \geq \Sigma_{\text{H}_2}$. A total of 534 regions fulfill this criteria, 345 of them with upper limits on Σ_{H_2} . Lowering the cut-off level to $\Sigma_{\text{H}_2}/\Sigma_{\text{HI}} \leq 0.5$ reduce the number of selected regions to 145, but it does not have a significant effect on the distribution of [C II] cooling rates. In the next two sections we use this sub-sample of atomic dominated regions to characterize the distribution of thermal pressures in the diffuse, atomic gas and to explore the connection between the thermal pressure and the star formation activity.

As we discussed in Section 3, in order to measure the thermal pressure using the [C II] emission we need to consider the gas carbon abundance, the temperature of the CNM and the contribution to the [C II] emission from the ionized gas.

[C II] emission from ionized gas: There is a fraction of the observed [C II] emission that is not associated with collisional excitation by hydrogen atoms, but with collisions with electrons. We refer to this fraction as f_{WIM} . One method to account for f_{WIM} is to use the [N II] 205 μm transition, which arise exclusively from the ionized gas and has a critical density similar to that of the [C II] line in the ionized medium. This way, the [C II] to [N II] 205 μm ratio yields the fraction of [C II] emission that arise from the ionized gas. Based on [N II] 205 μm observations from the ‘‘Beyond the Peak’’ survey, which include multiple regions selected from 21 of the galaxies in our sample, the contribution from the ionized gas to the [C II] emission is $f_{\text{WIM}} \sim 20 - 40\%$ for regions with infrared colors $\nu f_\nu(70)/\nu f_\nu(160) \lesssim 1.5$, and $\sim 10 - 15\%$ for regions between $1.5 \gtrsim \nu f_\nu(70)/\nu f_\nu(160) \lesssim 2.5$ (Croxall et al. in prep.). In our sample of atomic-dominated regions, 92% have $\nu f_\nu(70)/\nu f_\nu(160) \lesssim 1.5$, and thus

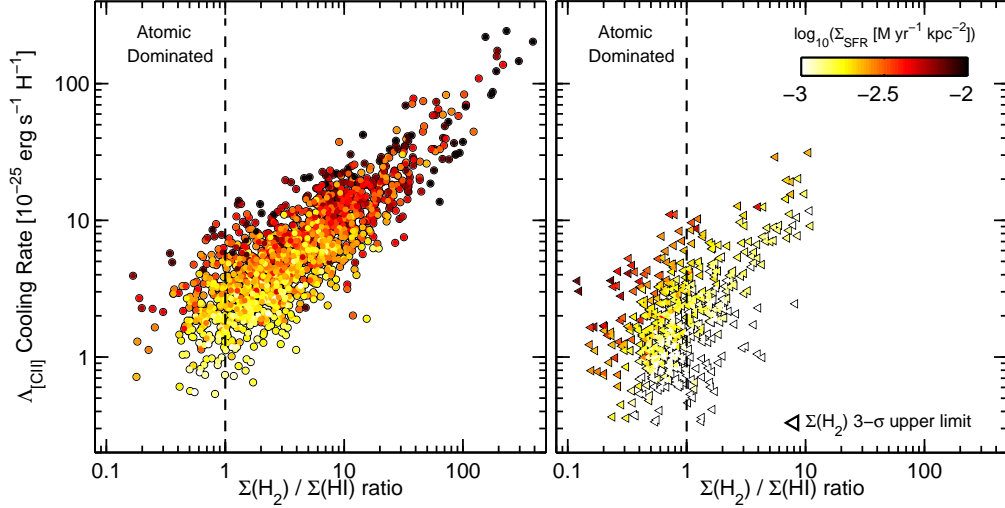


Figure 5.2: [C II] cooling rate per H atom (Λ_{C^+}) as a function of the ratio between the surface density of molecular (Σ_{H_2}) and atomic (Σ_{HI}) gas. The left panel shows the regions for which we have detections of [CII], CO and HI emission with $S/N > 3$. The right panel, on the other hand, shows the regions for which we only have upper limits driven by non-detections in CO emission. We consider as atomic dominated regions those with $\Sigma_{\text{H}_2}/\Sigma_{\text{HI}}$ ratios (or $3\text{-}\sigma$ upper limits) lower than 1 (dashed line). In these regions, we expect the C^+ collisional excitations to be dominated by collisions with H atoms. The color scale represent the star formation rate surface density (Σ_{SFR}) of the regions measured as a combination of $24\ \mu\text{m}$ and $\text{H}\alpha$ emission. Regions with lower [C II] cooling rates tend to show lower Σ_{SFR} values. This is expected given that in thermal equilibrium, the heating –proportional to Σ_{SFR} – and the cooling –dominated by the [C II] emission– are in balance.

we choose $f_{\text{WIM}} = 0.2$. Thus, the [C II] cooling rate associated with the atomic medium is $\Lambda_{\text{[CII]}}^{\text{CNM}} = \Lambda_{\text{[CII]}} \times (1 - f_{\text{WIM}})$.

Carbon abundance: To determine the carbon abundance of a particular region, we use as a proxy the oxygen abundance of its parent galaxy. The oxygen abundances were measured by Moustakas et al. (2010) and correspond to the average between the KK04 and PT05 methods. We convert the oxygen abundances into carbon abundances using the analytic function from the latest version of the MAPPINGS photoionization code (Dopita et al. 2013), i.e.,

$$[\text{C}/\text{H}] = [\text{O}/\text{H}] \times (10^{-0.8} + 10^{2.72+[\text{O}/\text{H}]}). \quad (5.7)$$

The analytic function in Equation (5.7) is normalized to the abundances in the solar neighborhood (Nieva & Przybilla 2012).

CNM temperature: For the CNM temperature we assume $T = 100$ K (Gerin et al. 2015). We note that the temperature in the Large and Small Magellanic Clouds diffuse gas as measured by the low rotational states of H_2 are quite similar to the Galactic case, even though their metallicities are lower by $\sim 1/2$ and $\sim 1/5$, respectively (Tumlinson et al. 2002). Finally, remember that a change in the temperature assumption of a factor of ~ 2 around $T = 100$ K will only have a small effect ($\lesssim 30\%$) on the determination of P_{th} (see Figure 5.1).

Based on the assumptions discussed above, we use Equation (5.5) to estimate the volume density of atomic hydrogen, n_{H^0} , and then Equation (5.6) to calculate the thermal pressure. The characteristics of the thermal pressures are summarized in Figure 5.3. The upper panels show the dependence of P_{th} on the radiation field strength (U) and the star formation activity (Σ_{SFR}). The regions that are classified as atomic-dominated are marked blue. We find correlations of increasing P_{th} with increasing U and Σ_{SFR} . These trends are expected given that the main source of heating of the gas—the photoelectric effect on small dust grains and PAHs—is proportional to the FUV intensity, which is also proportional to the star formation activity (we discuss more about the $P_{\text{th}}\text{-}\Sigma_{\text{SFR}}$ connection in Section 4.3). The distribution of thermal pressures for all regions (grey histogram) and the atomic-dominated regions (blue histogram) are shown in the lower panels. The median thermal pressure for the atomic-dominated regions is $P_{\text{th}}/k \approx 1.1 \times 10^4$ K cm $^{-3}$ and the distribution extends from $P_{\text{th}}/k \sim 10^3$ to $\sim 10^5$ K cm $^{-3}$.

Now, in order to compare the distribution of pressures in our sample to those

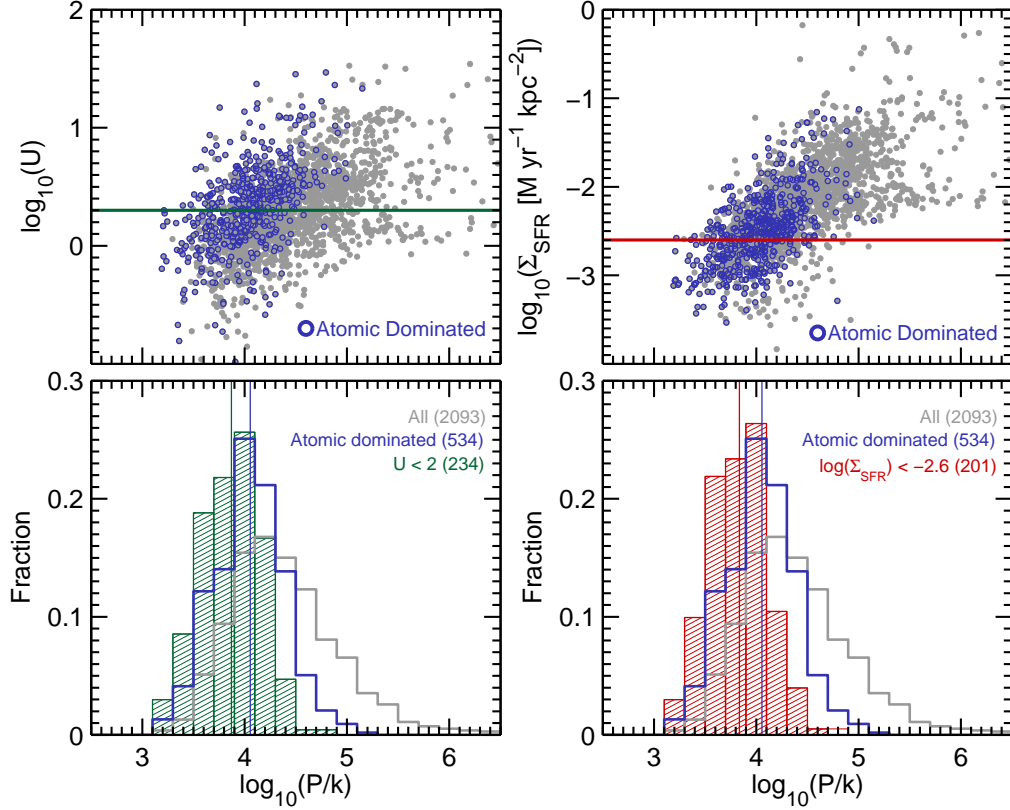


Figure 5.3: (*Upper panels*) Correlations between thermal pressure and radiation field strength U (left) and Σ_{SFR} (right) for all the regions in our sample (grey dots), and the subsample of atomic dominated regions (grey dots with blue border). In order to compare our thermal pressures with those measured in the diffuse gas of the solar neighborhood, we apply selection cuts in U and Σ_{SFR} with the aim of selecting region that resemble the conditions in this environment. The cutoff levels we chose are: $U = 2$ (green line) and $\Sigma_{\text{SFR}} = 2.5 \times 10^{-3} M_{\odot} \text{ yr}^{-1} \text{ kpc}^{-2}$ (blue line). (*Bottom panels*) Distribution of thermal pressures for all the regions in our sample (grey histogram), the subsample of atomic-dominated regions (blue histogram), and the atomic-dominated regions selected based on U (green histogram) and Σ_{SFR} (red histogram). The total number of regions in each subsample is shown in parentheses.

observed in the diffuse gas of the solar neighborhood and the Galactic plane, we need to select regions that resemble the conditions in these environments, i.e., $U \approx 1$ and $\Sigma_{\text{SFR}} \lesssim 2.5 \times 10^{-3} \text{ M}_{\odot} \text{ yr}^{-1} \text{ kpc}^{-2}$ (Bertelli & Nasi 2001; Fuchs et al. 2009). We attempt to do this by applying independent selection cuts to our atomic-dominated regions based on the radiation field strength, $U \leq 2$, and the star formation activity, $\Sigma_{\text{SFR}} \leq 2.5 \times 10^{-3} \text{ M}_{\odot} \text{ yr}^{-1} \text{ kpc}^{-2}$. The resulting thermal pressure distributions are shown in the lower panels of Figure 5.3. In both cases the resulting distributions are shifted to lower thermal pressures, with a median that is a factor ~ 1.4 lower than the one from its parent sample.

Figure 5.4 shows the distribution of thermal pressures of our atomic-dominated, Σ_{SFR} selected regions (red histogram). The distribution can be well represented by a log-normal distribution given by

$$f(P_{\text{th}}/k) = 0.27 \exp\left(-\frac{(\log_{10}(P_{\text{th}}/k) - 3.73)^2}{2(0.30)^2}\right). \quad (5.8)$$

We find a mean thermal pressure of $P_{\text{th}}/k \approx 5,500 \text{ K cm}^{-3}$, similar to the median thermal pressure measured by Gerin et al. (2015) in the plane of the Galaxy (dashed line histogram). This value is also $\sim 40\%$ higher than the mean thermal pressure found by Jenkins & Tripp (2011) (solid line histogram), and the rms dispersion in our sample is a factor ~ 1.3 higher, which might reflect the greater diversity in the gas properties of our sample such as metallicity, which varies by a factor of ~ 3 among our atomic-dominated regions.

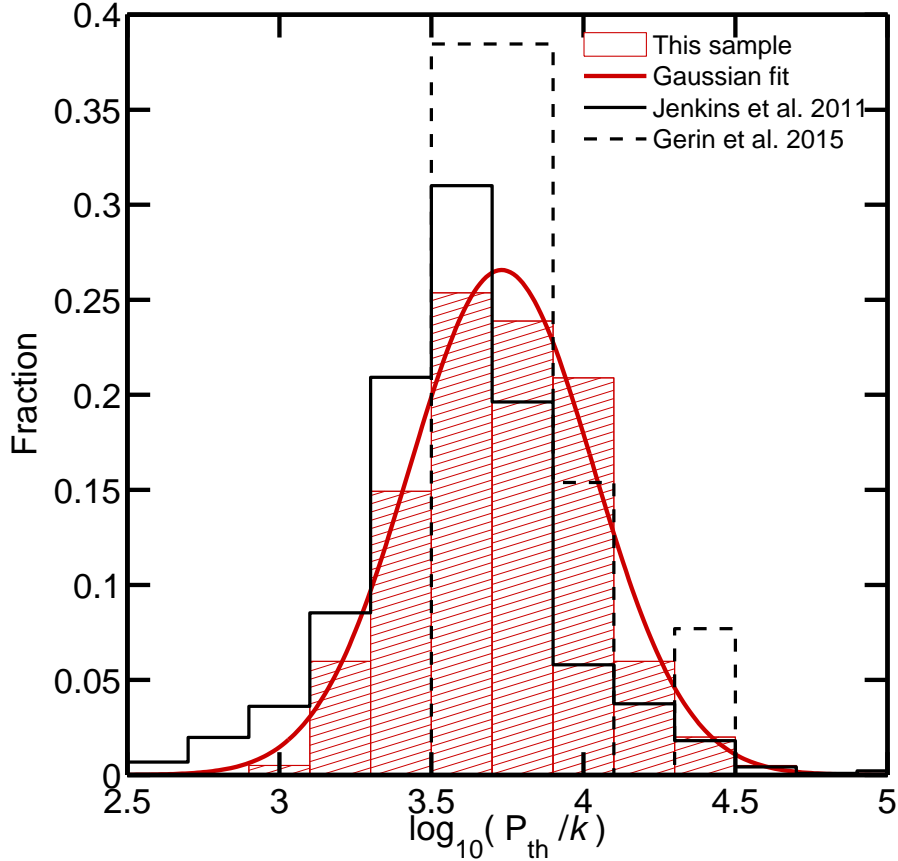


Figure 5.4: Comparison between the P_{th} distributions from quiescent, atomic dominated regions in the KINGFISH sample (red dashed histogram) and regions in the Galactic plane based on [C I] observations (Jenkins & Tripp 2011, 2,380 regions, black solid line) and [C II] measurements (Gerin et al. 2015, 13 regions, dashed solid line). The KINGFISH distribution of P_{th} can be well represented by a log-normal distribution with a mean $P_{\text{th}} \approx 5,500$ K and distribution width of $\sigma \approx 0.30$ dex. The KINGFISH mean P_{th} is similar to the one found by Gerin et al. (2015), and $\sim 40\%$ higher than that measured by Jenkins & Tripp (2011).

5.4.2 Thermal pressure and star formation activity

In the two-phase model for the ISM, the CNM and WNM phases can coexist in pressure equilibrium when the thermal pressure lies within a range set by P_{min} and P_{max} . We define the two-phase pressure as the geometric mean between these two, i.e., $P_{\text{two-phase}} = (P_{\text{min}}P_{\text{max}})^{1/2}$. Hydrodynamical models find the thermal pressure of the multiphase medium to be close to the $P_{\text{two-phase}}$ pressure (Kim et al. 2011).

Based on the definition of $P_{\text{two-phase}}$ and using the expression for P_{min} derived by Wolfire et al. (2003), we can express $P_{\text{two-phase}}$ as

$$\frac{P_{\text{two-phase}}}{k} \simeq 8,500 \left(\frac{P_{\text{max}}}{P_{\text{min}}} \right)^{1/2} \frac{G'_0 Z'_d / Z'_g}{1 + 3.1 (G'_0 Z'_d / \zeta'_t)^{0.365}}. \quad (5.9)$$

Here, the units of $P_{\text{two-phase}}$ are K cm^{-3} , G'_0 corresponds to the FUV intensity relative to the value measured locally ($I_{\text{FUV},0} = 2.1 \times 10^{-4} \text{ erg cm}^{-2} \text{ s}^{-1} \text{ sr}^{-1}$; Draine 1978), Z'_d and Z'_g are the dust and gas abundances relative to the solar neighborhood values and ζ'_t corresponds to the total cosmic ray/EUV/X-ray ionization rate relative to the value 10^{-16} s^{-1} . The ratio between P_{min} and P_{max} depends on various properties of the gas, including metallicity and the shielding of ionizing radiation. According to Wolfire et al. (1995, 2003), we expect $P_{\text{max}}/P_{\text{min}}$ to be in the $\sim 2 - 5$ range. If we assume $P_{\text{max}}/P_{\text{min}} = 2$ we recover the expression for $P_{\text{two-phase}}$ used by Ostriker et al. (2010).

Following a similar procedure to that of Ostriker et al. (2010), we can elaborate more on Equation (5.9) and derive an expression for $P_{\text{two-phase}}$ that is a function of the star formation rate surface density, Σ_{SFR} , and the total surface density of the gas, Σ , for a disk. First, we assume that the high-energy ionization rate ζ'_t is proportional to Σ_{SFR} and inversely proportional to Σ . This way, $G'_0/\zeta'_t = \Sigma/\Sigma_0$, where Σ_0 is the surface gas density in the solar neighborhood. Second, we rewrite the expression for $G'_0 = I_{\text{FUV}}/I_{\text{FUV},0}$ by expressing I_{FUV} in terms of Σ_{SFR} using the FUV-based SFR calibration derived by Salim et al. (2007). Finally, if we assume that the dust-to-gas ratio follow the metallicity, $Z'_d/Z'_g \approx 1$, the new expression for $P_{\text{two-phase}}$ is

$$\frac{P_{\text{two-phase}}}{k} \simeq 9.8 \times 10^6 \left(\frac{P_{\text{max}}}{P_{\text{min}}} \right)^{1/2} \frac{\Sigma_{\text{SFR}}}{1 + 3.1 (Z'_d \Sigma / \Sigma_0)^{0.365}}. \quad (5.10)$$

The units of $P_{\text{two-phase}}$ are K cm^{-3} and the units of Σ_{SFR} are $\text{M}_\odot \text{ yr}^{-1} \text{ kpc}^{-2}$.

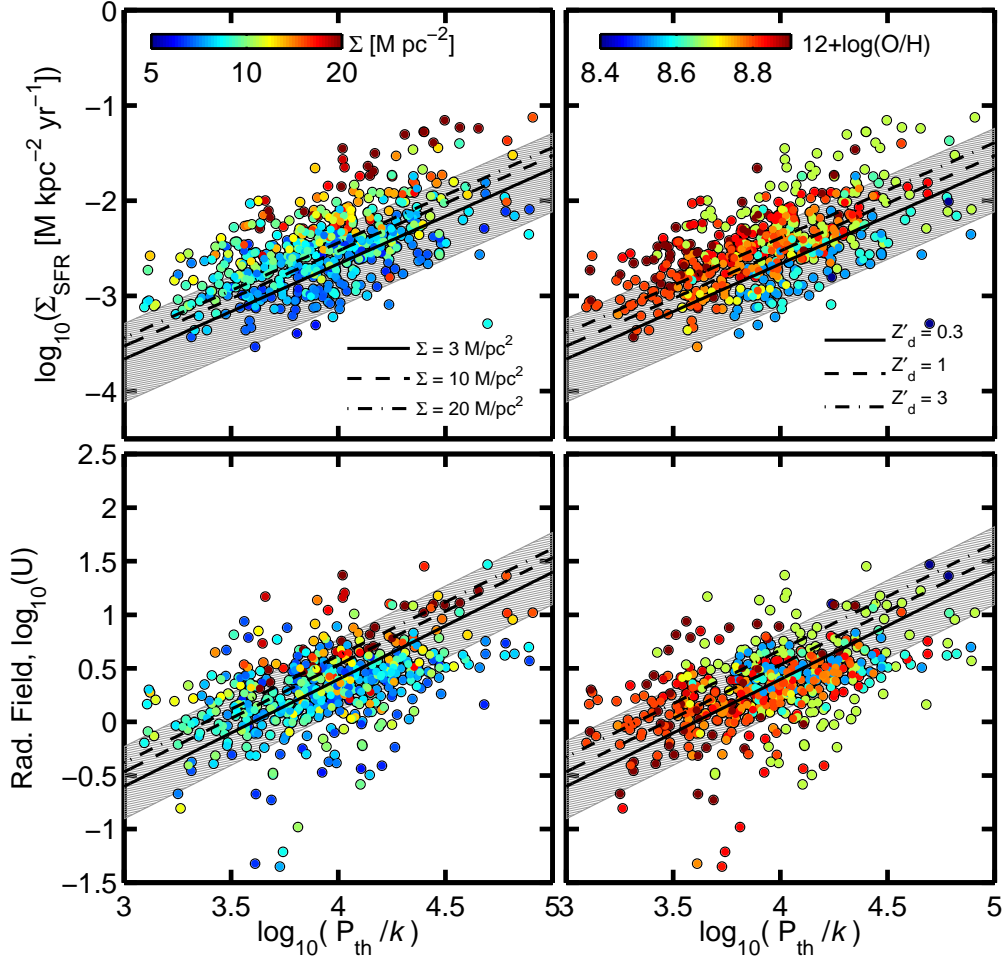


Figure 5.5: Thermal pressure versus star formation surface density (upper panels) and radiation field strength (lower panels) for atomic-dominated regions in the KINGFISH sample. (*Left panels*) The color scale represents the gas surface density $\Sigma = \Sigma_{\text{HI}} + \Sigma_{\text{H}_2}$. The results from the Wolfire et al. (2003) model (Equation 5.9 and Equation 5.10) when assuming $P_{\text{max}}/P_{\text{min}} = 2$, $Z'_d = 1$ and $\Sigma = 3, 10$ and $20 M_{\odot} \text{ pc}^{-2}$ are shown as a solid, dashed and dot-dashed lines. The hatched grey region represents the area where $P_{\text{min}} \lesssim P_{\text{th}} \lesssim P_{\text{max}}$ is satisfied when assuming $P_{\text{max}}/P_{\text{min}} = 5$. (*Right panels*) Similar to the left panel, but this time the color scale represents the oxygen abundance taken from Moustakas et al. (2010). The model predictions from the Wolfire et al. (2003) model (Equation 5.9 and Equation 5.10) when assuming $P_{\text{max}}/P_{\text{min}} = 2$, $\Sigma = 10 M_{\odot} \text{ pc}^{-2}$ and $Z'_d = 0.3, 1, 3$ are shown using solid, dashed and dot-dashed lines. The hatched grey region represents the area where $P_{\text{min}} \lesssim P_{\text{th}} \lesssim P_{\text{max}}$ is satisfied when assuming $P_{\text{max}}/P_{\text{min}} = 5$.

In a two-phase ISM model in equilibrium we expect $P_{\min} \lesssim P_{\text{th}} \lesssim P_{\max}$, with P_{th} close to the value of $P_{\text{two-phase}}$. In Figure 5.5 we explore these model expectations by comparing the thermal pressures measured in our sample of atomic-dominated regions to the predictions from the Wolfire et al. (2003) model. In the left panels we show the correlation between P_{th} and Σ_{SFR} (upper panel), and P_{th} and $\langle U \rangle$ (lower panel). In both cases we use color to indicate the value of the total gas surface density Σ . We include the model results from Equation (5.9) for the $P_{\text{th}} - \Sigma_{\text{SFR}}$ case, and Equation (5.10) for the $P_{\text{th}} - \langle U \rangle$ correlation. In both cases we assume that $P_{\max}/P_{\min} = 2$, $Z'_d = 1$ and three different values for the gas surface density, $\Sigma = 3$ (solid line), 5 (dashed line) and $20 \text{ M}_{\odot} \text{ pc}^{-2}$ (dot-dashed line). The grey hatched region represents the range of thermal pressures where $P_{\min} \lesssim P_{\text{th}} \lesssim P_{\max}$ if we assume that $P_{\max}/P_{\min} = 5$. We also assume that the dust-weighted mean starlight intensity $\langle U \rangle$ –that we measure using the 70 to 160 μm ratio and the empirical fit to the Draine & Li (2007) model by Muñoz-Mateos et al. (2009a)– is approximately equal to G_0 . As predicted by the model, we observe a correlation of increasing P_{th} with increasing $\langle U \rangle$ and increasing Σ_{SFR} . This is expected due to the increase of the photoelectric heating as G_0 ($\approx \langle U \rangle$ and $\propto \Sigma_{\text{SFR}}$) rises. In addition, the model also predicts that for a fixed SFR, the thermal pressure decreases as a function of Σ . Recall that $\zeta'_t \propto (\Sigma)^{-1}$, so if Σ drops, the electron abundance in the gas rises, which helps to neutralize the charge of the dust grains and thus increase the grain photoelectric heating. Our data are also consistent with this prediction, as we observe that for a fixed Σ_{SFR} , regions with higher values of Σ tend to have lower thermal pressures. Finally, it is worth noting that the dispersion in our data (~ 0.35 dex) is larger than that expected from the model, even if we assume the more extreme case where $P_{\max}/P_{\min} = 5$ (grey hatched area). This could be an indication that the gas properties of some regions are still evolving towards an overall

equilibrium, e.g., simultaneous dynamical, thermal and star formation equilibrium as discussed by Ostriker et al. (2010). However, it is likely that an important part of the observed scatter is driven by observational uncertainties. In particular, Σ_{SFR} measurements below the $\sim 10^{-3} \text{ M}_{\odot} \text{ yr}^{-1} \text{ kpc}^{-2}$ level can be unreliable due to large uncertainties in the $\text{H}\alpha$ data and a growing contribution to the $24 \mu\text{m}$ emission from old stars (e.g., Draine et al. 2014; Groves et al. 2012; Leroy et al. 2012).

Similar to the left panels in Figure 5.5, the right panels show the $P_{\text{th}} - \Sigma_{\text{SFR}}$ (upper panel) and $P_{\text{th}} - \langle U \rangle$ (lower panel) correlations. This time, however, we color code the regions according to the characteristic oxygen abundance of its parent galaxy. For the model comparison, we include results from Equations (5.9) and (5.10) assuming $P_{\text{max}}/P_{\text{min}} = 2$, $\Sigma = 10 \text{ M}_{\odot} \text{ pc}^{-2}$ and three different values for the dust abundance relative to the solar neighborhood, $Z'_d = 0.3$ (solid line), 1 (dashed line) and 3 (dot-dashed line). Once again, the grey hatched region represents the range of thermal pressures where $P_{\text{min}} \lesssim P_{\text{th}} \lesssim P_{\text{max}}$ if we assume that $P_{\text{max}}/P_{\text{min}} = 5$. The model predicts that for a fixed amount of Σ_{SFR} , the thermal pressure increases with decreasing dust abundance Z'_d . Now, in principle, we should expect the opposite, i.e., if the dust abundance drops, so does the photoelectric heating, causing the thermal pressure to decrease. What happens is that in the model calculations we assume that the dust and gas phase abundances are proportional to each other, so Z'_d and Z'_g decrease at the same rate. In this scenario, the photoelectric heating and the cooling decrease, however, the X-ray heating remains constant and starts to dominate the heating, causing the thermal pressure to increase (Wolfire et al. 1995). In our sample, we find that for regions with similar $\langle U \rangle$ or Σ_{SFR} , those with lower metallicities tend to have higher thermal pressures. This is expected as a drop in the abundance of the main coolant elements, carbon and oxygen, implies an increase in the equilibrium gas temperature, and, in consequence,

an increase in the thermal pressure.

5.5 Summary and Conclusions

We study the distribution of thermal pressures in extragalactic regions selected from nearby galaxies that are part of the KINGFISH, HERACLES and THINGS samples. The method we use to measure the thermal pressure relies on [C II] 158 μm emission that arise from regions where the excitation of the C^+ ions is dominated by collisions with hydrogen atoms. In these atomic-dominated environments, the [C II] and HI 21 cm line emission can be used to measure cooling rate per hydrogen atom $\Lambda_{[\text{CII}]}$ (Equation 5.4), and then, by assuming a typical temperature for the cold neutral medium T_{CNM} , to obtain the thermal pressure P_{th} (Equations 5.5 and 5.6). One advantage of this method is that is very robust against changes in the assumption of T_{CNM} (Kulkarni & Heiles 1987).

We highlight the following points:

1. From a sample of 2,093 extragalactic regions that have [C II] and HI observations with $S/N \geq 3$, we classify as atomic-dominated regions those with $\Sigma_{\text{H}_2}/\Sigma_{\text{HI}}$ ratios (or 3- σ upper limits) lower than one. The resulting number of atomic-dominated regions is 534. The distribution of thermal pressures for these regions extends from $P_{\text{th}}/k \sim 10^3$ to $\sim 10^5 \text{ K cm}^{-3}$, with a median value of $P_{\text{th}}/k \approx 1.1 \times 10^4 \text{ K cm}^{-3}$.
2. In order to compare the distribution of thermal pressures in our sample to those measured in the Galactic plane, we select a sub-sample of regions that approximately resembles the conditions found in the solar neighborhood. We find that the distribution of thermal pressures in this sub-sample of regions can be well represented by a log-normal distribution with median thermal pressure

$P_{\text{th}}/k \approx 5,500 \text{ K cm}^{-3}$ and distribution width $\sigma \approx 0.30$ dex. These results are consistent with those from studies in the Galactic plane using other methods (Gerin et al. 2015; Jenkins & Tripp 2011).

3. We find that the trends observed in the relations between P_{th} and Σ_{SFR} , and P_{th} and $\langle U \rangle$, as a function of G_0 , Σ and metallicity are consistent with the results from the Wolfire et al. (1995, 2003) and Ostriker et al. (2010) models. In general, the thermal pressures of our atomic-dominated regions are consistent with the expectations from a two-phase model in pressure equilibrium.

Chapter 6

Summary and Future Work

6.1 Summary and Conclusions

The goal of my Ph. D. thesis was to study the complex interplay between physical processes that play a crucial role in galaxy formation and evolution, in particular star formation and the thermal balance in the neutral, molecular and ionized interstellar medium. This work was based on infrared observations performed by *Spitzer* and *Herschel* space telescopes, including the largest ever sample of spatially resolved, infrared spectroscopic observations of nearby galaxies. This sample was assembled from the combination of the KINGFISH (Kennicutt et al. 2011) and “Beyond the Peak” (Smith et al. in prep.) surveys. The infrared data was supplemented by observations of the atomic gas (via 21 cm line emission), molecular gas (via CO line emission), and star formation activity (based on ground based H α and GALEX FUV observations).

The main questions that motivated my thesis work, and a summary of the corresponding findings, are the following:

- (1) *Is the fraction of metals incorporated into dust the same in high and low-*

metallicity environments? In other words, is the relationship between dust-to-gas ratio (DGR) and metallicity in galaxies always linear?

In Chapter 2 we studied the dust and gas properties of the blue compact dwarf galaxy I Zw 18. Due to its extremely low-metallicity ($Z \approx 1/30 Z_{\odot}$), this galaxy represents a key datum for understanding the relationship between DGR and metallicity. Based on the most sensitive infrared maps to date of the study, we constrained the dust mass of the galaxy to be $M_{\text{dust}} < 1.1 \times 10^4 M_{\odot}$, and the DGR to be $M_{\text{dust}}/M_{\text{gas}} < 8.1 \times 10^{-5}$. While normal, star-forming galaxies follow a linear relationship between DGR and metallicity (e.g., Draine et al. 2007), the DGR of I Zw 18 falls below this linear relationship by at least a factor of ~ 5 (Figure 2.4). This result was later confirmed with deeper *Herschel* observations that allowed us to detect for the first time I Zw 18 at 100 and 160 μm (Fisher et al. 2014, a study of which I was a co-author). The SED fitting of the updated IR SED using the Draine & Li (2007) model yielded a DGR in the range $3.2 - 13 \times 10^{-6}$, which is at least a factor of ~ 6 lower than our previous DGR estimate. We conclude that the DGR of I Zw 18 is inconsistent with the hypothesis that the fraction of heavy elements incorporated into dust is the same in high-metallicity galaxies (such as the Milky Way) and in extremely low-metallicity galaxies (such as I Zw 18). This result is consistent with the trends observed in a much larger sample of low- and high-metallicity galaxies assembled by Rémy-Ruyer et al. (2014). They found that the DGR-metallicity relation cannot be represented by a simple linear scaling over the whole metallicity range, as for galaxies with metallicities lower than $12 + \log_{10}(\text{O}/\text{H}) \lesssim 8$ the observed trend is steeper.

(2) *The [C II] 158 μm line is the major coolant of the neutral ISM, and the [N II] 122 and 205 μm lines predominately arise from the gas ionized and heated by young, massive stars. How reliable are these fine-structure transitions as tracers of*

star formation activity?

Let us start by reviewing the results for the [C II] 158 μm line discussed in Chapter 3. Using a sample of 3,486 regions selected from 46 KINGFISH galaxies, we find that the [C II] surface brightness, $\Sigma_{[\text{CII}]}$, can be used as a robust tracer of star formation activity in normal, star forming galaxies in the absence of strong AGNs (Figure 3.3). Regarding the scatter of the $\Sigma_{[\text{CII}]} - \Sigma_{\text{SFR}}$ correlation, we find that regions with warm IR colors systematically deviate from the best linear fit to the data as a function of IR color (Figure 3.4), with a median deviation from the fit as high as a factor of ~ 3 for the warmest regions (i.e., warm dust regions are underluminous in [C II] emission). One of the possible reasons for these deviations is that at high UV fields small grains become positively charged or are destroyed, thus decreasing the photoelectric heating efficiency of the gas. In order to improve the accuracy of the [C II]-based SFR calibration, we provide an adjustment to the calibration based on IR color (Equation 3.4 and Table 3.2). We find that an IR-color-adjusted $\Sigma_{[\text{CII}]}$ can provide a good estimation of $\Sigma_{[\text{CII}]} - \Sigma_{\text{SFR}}$ using Equation (3.2), valid for starburst galaxies over almost five orders of magnitude in surface brightness (Figure 3.7). Using [C II] luminosity instead of surface brightness to estimate SFR suffers from worse systematics, frequently underpredicting SFR in luminous infrared galaxies even after IR color adjustment (Figure 3.9). This demonstrates the limitations of using the [C II] luminosity as an SFR measure in warm or compact sources, such as (U)LIRGs.

Regarding the use of the [N II] 122 and 205 μm fine-structure lines as star formation tracers, in Chapter 4 we derive relations between the [N II] emission and SFR in the low density limit, and separately, assuming a log-normal distribution of electron densities. In the latter case, the [N II] line luminosity and SFR are related by a calibration coefficient C , which is the number of ionizing photons per erg of

emitted energy in the [N II] lines, and is a function of the [N II] 122/205 line ratio (or electron density) and the density distribution parameter σ (Equation 4.17). For a sample of regions selected from 21 “Beyond the Peak” galaxies, we find a good correlation between the [N II] surface brightness and Σ_{SFR} with a scatter that can be understood in terms of variations in the calibration coefficient C (Figure 4.8). For regions with electron densities closer to or higher than the [N II] line critical density, the [N II]-based SFR calibration systematically underestimates the reference SFR coming from the combination of 24 μm and $\text{H}\alpha$ emission. At those densities, the [N II] collisional de-excitation competes with the radiative decay and the [N II] emission is collisionally quenched, thus underestimating the star formation activity. We conclude that both theory and observations reveal the importance of having prior knowledge of the ionized gas properties of the source in order to avoid underestimating the star formation activity. In case there are no constraints on the ionized gas, the [N II] 122 μm emission proves to be a more reliable tracer than [N II] 205 μm due to its higher critical density.

(3) *What are the properties of the low-excitation, ionized gas of nearby galaxies on $\sim\text{kpc}$ scales? how is the ionized gas density connected to other ISM properties such as metallicity, star formation activity and radiation field strength?*

In Chapter 4 we used the combination of the [N II] 122 μm and [N II] 205 μm fine structure lines to probe the singly-ionized gas of nearby galaxies (e.g., Oberst et al. 2006). For 140 regions selected from 21 galaxies for which we have [N II] 122 and 205 μm observations with $S/N > 3$ available, we measured [N II] 122/205 line ratios in the range $\sim 0.6 - 5$, which correspond to electron densities of the singly-ionized gas in the range $n_e \sim 3 - 230 \text{ cm}^{-3}$ (This assuming that the distribution of gas within each region is homogeneous). The distribution of electron densities in our sample is consistent with those found for the Carina nebula (Oberst et al. 2011) and NGC 891

(Hughes et al. 2014). The median ionized gas density in our sample is $n_e \approx 30 \text{ cm}^{-3}$, comparable to the median electron density measured in the Carina I H II region in the Carina nebula (Oberst et al. 2011, 2006).

We found a good correlation of increasing n_e with infrared color, dust-weighted mean starlight intensity, total infrared surface density, and star formation rate surface density (Figure 4.8). The origin of these good correlations could be associated with: (1) the evolutionary stage of the H II region, as young, compact H II regions will produce very intense radiation fields, or (2) the fact that dense H II regions in pressure equilibrium with the surrounding neutral gas implies a high density molecular gas environment that may lead to further star formation activity.

(4) *What is the distribution of thermal pressures in the neutral gas of nearby galaxies? What is the relation between thermal pressure and other properties of the ISM that set the heating and cooling functions of the gas (e.g. metallicity, neutral gas surface density, star formation activity, radiation field strength)?*

In Chapter 5 we studied the thermal pressure in the neutral gas of 31 nearby galaxies. The method we used relies on the [C II] and HI 21 cm line emission arising from atomic-dominated regions, which we select based on their $\Sigma_{\text{H}_2}/\Sigma_{\text{HI}}$ ratio. For a total of 543 regions that we classified as atomic dominated, we found a distribution of thermal pressures in the $P_{\text{th}}/k \sim 10^3$ to $\sim 10^5 \text{ K cm}^{-3}$ range, with a median value of $P_{\text{th}}/k \approx 1.1 \times 10^4 \text{ K cm}^{-3}$. When we select from this sample regions that resemble the conditions of the solar neighborhood, we find a distribution of thermal pressures that follow a log-normal distribution with median thermal pressure $P_{\text{th}}/k \approx 5,500 \text{ K cm}^{-3}$. This value is consistent with the P_{th} measured in the Galactic plane using other methods (Gerin et al. 2015; Jenkins & Tripp 2011). Finally, we observed that the P_{th} increases as a function of increasing SFR and radiation field intensity, and that for a given SFR, P_{th} decreases as a function of

metallicity and the surface density of the gas. All these trends are consistent with the results from the Wolfire et al. (1995, 2003) and Ostriker et al. (2010) models.

6.2 Future Work

The results obtained in this thesis on the ISM properties of nearby-galaxies are crucial for connecting the local, detailed Galactic observations with those of distant galaxies observable with ALMA.

For high-redshift galaxies, the far-IR cooling lines are one of the primary tracers of their ISM. In Chapter 3 and 4 we show how the [C II] and [N II] transitions can be used to trace the star formation activity. One group of galaxies that would be interesting to study in the future are those that hosted a gamma-ray burst (GRB) events. Our current knowledge of the GRB hosts at high- z is very limited, and more observations are needed to understand how GRB host galaxies compare to the whole galaxy population. ALMA [C II] observations of these systems can provide the first measurements of the star formation activity and kinematics of GRB host at $z \gtrsim 4$. The second group of galaxies that would be interesting to study with ALMA are the so-called main-sequence star-forming galaxies. These galaxies follow a tight correlation between SFR and stellar mass as shown by deep extragalactic surveys over the past decade (Daddi et al. 2007, Genzel et al. 2014). ALMA observations of the dust continuum and [C II] emission can provide key information on the obscured part of the star formation activity and the thermodynamics of the gas in this systems.

In this thesis we also showed how the combination of the main far-infrared fine-structure lines can be used to study the properties of the multiple phases of the ISM. This opens the possibility to address one of the open questions in the field of nearby

galaxies, which is how much each phase of the ISM contributes to the emission of the infrared cooling lines. One approach to address this question would be to first identify the emitting ISM phases, and then measure the fraction of the total emission arising from that particular phase, f_{line} . This could be done for hundreds of nearby galaxies that are available in the *Herschel* archive. In the case of the [C II] line, we know that the emitting sources are the ionized gas, neutral atomic gas and dense PDRs. For the ionized gas, the ratio between the [C II] and [N II] 122 μm far-infrared lines can be used to measure $f_{\text{[CII]}}$. In the case of the neutral atomic gas and dense PDRs, the discrimination between phases can be done based on a combination of at least two diagnostics: (1) the HI/CO ratio (PDRs have HI/CO \ll 1), and (2) the radiation field strength from the modeling of the dust (e.g., using the Draine & Li 2007). For the regions that we will identify as diffuse, neutral atomic gas we can measure $f_{\text{[CII]}}$ using the direct proportionality between the [C II] emission and the HI column density (Crawford et al. 1985; Goldsmith et al. 2012). Finally, for the PDR component, we can measure $f_{\text{[CII]}}$ after we subtract the contribution to the [C II] emission from the ionized gas (most likely coming from H II regions in this case).

Together with the analysis of the [C II] line, the case of the [O I] 63 μm emission is also very interesting. Dense PDRs are thought to be the main source of [O I] 63 μm emission. However, as we show in Figure 3.6, [O I] 63 μm emission can also be produced in more diffuse, less active regions. One possibility is that high columns densities of atomic gas in the warm neutral medium are responsible for this [O I] 63 μm emission. If this is the case, this project will provide the first measurement of the fraction of [O I] 63 μm emission that arise from non-PDR phases.

The analysis based on the infrared observations can be complemented by per-

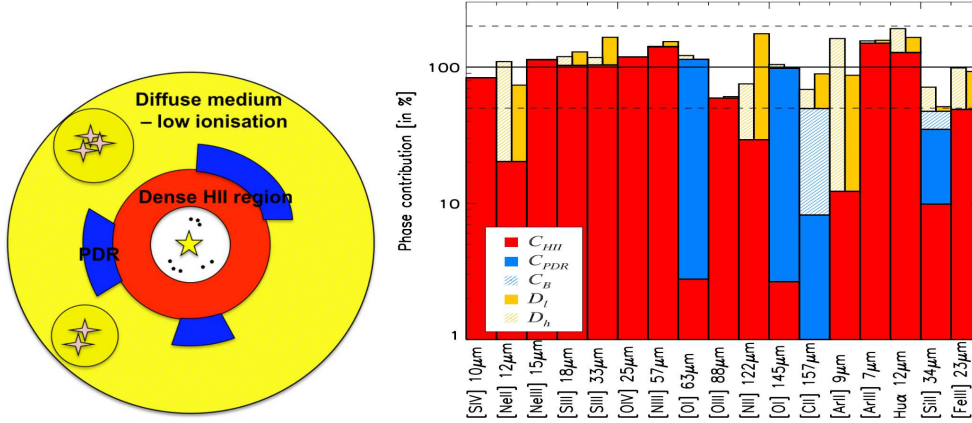


Figure 6.1: (Left) Multi-phase model assumed for Haro 11 composed of a compact H II region, dense PDRs, a diffuse medium of low-ionization and warm dust in the inner region. (Right) Diagram of the contribution of each individual ISM phase to the global emission of the mid- and far-infrared lines (Cormier et al. 2012).

forming a multi-phase modeling of the infrared emission using one of the various codes available (e.g., PDR Toolbox, MAPPINGS, Cloudy). One example of this type of analysis is the modeling using the code CLOUDY of the emission from 17 mid- and far-infrared spectral lines in the galaxy Haro 11 (Cormier et al. 2012). Figure 5 shows the multi-phase model assumed for Haro 11 that consist of PDRs, H II regions, dust and diffuse gas. Next to the model, Figure 6.1 shows the contribution from each phase to the infrared line emission. In the case of [C II], the PDR component only accounts for 10% of the emission, and a diffuse, low-ionization gas is needed to explain the total observed [C II] line intensity.

Appendix A

Appendix

A.1 KINGFISH galaxies not included in Chapter 3 analysis

Among the 54 galaxies in the KINGFISH sample with PACS spectroscopic data available, we decided not to include eight of them: NGC 1266, NGC 1316, NGC 1097, NGC 1377, NGC 1404, NGC 4594, NGC 4631 and NGC 4559. We excluded the two elliptical galaxies NGC 1266 and NGC 1316 (also known as Fornax A) because they both have AGNs (Ekers et al. 1983; Moustakas et al. 2010; Nyland et al. 2013) that may contaminate the infrared emission used to measure SFRs. Unfortunately, masking the AGN emission at the center of these galaxies is not an option because it removes a significant fraction of the [C II] map. NGC 1377 is a peculiar system that shows a $24 \mu\text{m} - [\text{C II}]$ ratio nearly two orders of magnitude higher than the rest of the points at a given [C II] surface brightness. The strong infrared excess in this system is produced either by a nascent starburst (Roussel et al. 2006) or a buried AGN (Imanishi et al. 2009). Given that the central source that dominates the emission of NGC 1377 is debated, we remove this system from the analysis. We also do not

include NGC 1404 and NGC 4594 because the quality of the spectroscopic data is poor. We remove NGC 4631 from the sample because of its high inclination of 86° (Muñoz-Mateos et al. 2009a). Finally, we do not include NGC 1097 and NGC 4559 because these two galaxies were observed in the Science Demonstration Phase using a different observing mode (i.e. Chop-Nod and Wavelength Switching) than the one used to observe the rest of the sample (Unchopped Grating Scan). Note, however, that these two systems agree well with the correlations presented in this work.

A.2 Supplementary data in Chapter 3

SINGS & KINGFISH IR: For all galaxies in our sample we have images that cover the entire IR continuum from $3.6 \mu\text{m}$ to $500 \mu\text{m}$. Near and mid-infrared (8 and $24 \mu\text{m}$) images were drawn from the *Spitzer* Infrared Nearby Galaxy Survey (Kennicutt et al. 2003, SINGS). Far-infrared maps observed with *Herschel* PACS (70 , 100 and $160 \mu\text{m}$) and SPIRE (250 , 350 and $500 \mu\text{m}$) instruments are drawn from the photometric KINGFISH sample (Dale et al. 2012). We also add [O I] $63 \mu\text{m}$ data reduced and calibrated in the same way as the [C II] data.

H α : We have H α images for 27 galaxies. The assembly of these images and the methods to correct for Galactic extinction, mask foreground stars and remove the [NII] contribution are described in detail in Leroy et al. (2012). The source of these images are (in order of importance): SINGS (Kennicutt et al. 2003), Local Volume Legacy survey (LVL, Dale et al. 2009a), GOLDMine (Gavazzi et al. 2003), Palomar Las Campanas Atlas, Boselli & Gavazzi (2002), Knapen et al. (2004) and Hoopes et al. (2001).

FUV: We have GALEX FUV images for 33 of the galaxies in our sample. The assembly of these images and the additional processing that includes background subtraction and masking of foreground stars via their UV color, by-eye inspection, and the color-based masks of Muñoz-Mateos et al. (2009b) is described in Leroy et al. (2012). The source of these images are (in order of importance): Nearby Galaxy Survey (NGS, Gil de Paz et al. 2007), Medium Imaging Survey (MIS) and All-sky Imaging Survey (AIS, Martin et al. 2005).

Draine & Li Dust Model Maps: We use maps of dust properties, like the ones presented in Aniano et al. (2012), based on the Draine & Li dust model (Draine & Li 2007) (DL07). The DL07 model treats the dust as a combination of carbonaceous and amorphous silicate grains, with the smallest carbonaceous grains having the physical properties of PAH particles. The PAH mass fraction, q_{PAH} , is defined as the percentage of the total grain mass contributed by PAHs containing fewer than 10^3 C atoms (see Draine et al. 2007, eq. 4). The grain size distribution and normalization is chosen to match the abundance and average extinction in the Milky Way. The DL07 model considers that dust is exposed to a range of radiation fields: a “diffuse ISM” component – that contains most of the dust – which is heated by a single (δ function) radiation field, $U = U_{\text{min}}$; and a “PDR component” that is heated by a power-law distribution of intensities U over a wide range, $U_{\text{min}} < U < U_{\text{max}}$, where ($U_{\text{max}} \gg U_{\text{min}}$). For the “PDR component”, the DL07 model estimate the fraction of the dust luminosity radiated from regions where $U > 100$ (see Draine et al. 2007, eq. 18). Finally, the DL07 model also yields a dust mass (M_{dust}) and a dust mass surface density (Σ_{dust}) for each line of sight. In this paper we use the version of the dust maps generated by fitting the IR SED composed of the MIPS 24 μm and PACS 70, 100 and 160 μm fluxes. We use this version of the dust maps, as opposed

to the version that include SPIRE fluxes, to have dust maps with similar spatial resolution to the [C II] 158 μm maps.

A.3 Cirrus emission

Following the procedure described in Leroy et al. (2012), the 24 μm cirrus intensity (I_{24}^{cirrus}) can be computed as the product of the dust surface density (Σ_{dust}), and the emission per unit dust mass of dust heated by non star-forming sources ($\epsilon_{24}^{\text{cirrus}}$):

$$I_{24}^{\text{cirrus}} = \epsilon_{24}^{\text{cirrus}}(U_{\text{cirrus}}, q_{\text{PAH}}) \times \Sigma_{\text{dust}}. \quad (\text{A.1})$$

In the Draine & Li (2007) model, ϵ_{24} depends linearly on the incident radiation field, U ($U = 1$ is the local interstellar radiation field in the Milky Way, normalized to the MMP field (Mathis et al. 1983)) and weakly on the PAH abundance index, q_{PAH} (Fig. 4, Leroy et al. 2012). For instance, for a radiation field $U = 1$, the emission per unit dust mass ϵ_{24} increases only by a factor of ~ 1.75 in the $q_{\text{PAH}} = 0.47 - 4.58\%$ range (Draine & Li 2007, Table 4). Therefore, the challenge here is to find the incident radiation field produced by non star-forming sources, i.e., U_{cirrus} . Leroy et al. (2012) test different values of U_{cirrus} with the goal of producing 24 μm cirrus emission such that its subtraction removes the 24 μm faint emission, but not oversubtract emission associated with star formation. For a sample of 30 disk galaxies (20 of them part of the KINGFISH sample), they find that this optimal cirrus radiation field is $U_{\text{cirrus}} \approx 0.5 U_{\text{min}}$, where U_{min} corresponds - in the Draine & Li (2007) model - to the least interstellar radiation field heating the diffuse ISM. There is a factor of ~ 2 scatter associated with this value (Leroy et al. 2012, Appendix A).

We explore the effects of the cirrus subtraction estimating U_{cirrus} as a scaled

version of U_{min} , i.e., $U_{\text{cirrus}} = \xi \times U_{\text{min}}$ for $\xi = 0.5, 0.75$ and 1 . We also explore adopting a constant U_{cirrus} across the galaxy. Given that we measure a median value of U_{min} in our sample of 1.15 , we adopt a constant $U_{\text{cirrus}} = \xi \times 1.15 = 0.6, 0.8$ and 1.1 . Choosing a high cirrus radiation field, such as $U_{\text{cirrus}} = U_{\text{min}}$ or $U_{\text{cirrus}} = 1.1$, will likely overestimate the cirrus emission. As Leroy et al. (2012) point out, the OB associations present within 1 kpc of the Sun would substantially contribute to the local interstellar radiation field; so non star-forming sources - like old stars - cannot by themselves account on their own to the local measured value of $U = 1$.

Table 3.1 summarizes the effect of the cirrus correction on the $\Sigma_{24\mu\text{m}}-\Sigma_{[\text{CII}]}$ correlation and the fraction of the $24 \mu\text{m}$ emission associated with cirrus (f_{cir}). When cirrus is estimated using $U_{\text{cirrus}} = 0.5 U_{\text{min}}$, the shape and scatter of the corrected correlation remains essentially the same, but the normalization scales down about 18% (as expected since $f_{\text{cir}} \sim 18\%$ for this case). For the cirrus removal based on $U_{\text{cirrus}} = 0.6$, the cirrus subtraction is higher at lower luminosities of $24 \mu\text{m}$, thus we observe an increase in the slope from 1.20 to 1.30 ; the scatter of the correlation remains the same. For these two sets of assumptions on U_{cirrus} , the median f_{cir} is similar to the $f_{\text{cir}} \sim 19\%$ found by Leroy et al. (2012) (the overlap between our samples is 23 galaxies) and larger than the $f_{\text{cir}} \sim 7\%$ found by Law et al. (2011) in their analysis of integrated SEDs for LVL and SINGS galaxies. For the $U_{\text{cirrus}} = 1.1$ case, the changes in the correlation after the cirrus removal are more dramatic: the slope changes from 1.20 to 1.60 ; as a result, the subtracted $24 \mu\text{m}$ emission in the low $[\text{C II}]$ luminosity regions ($\Sigma_{[\text{CII}]} < 10^{39} [\text{erg s}^{-1} \text{ kpc}^{-2}]$) can be a factor of ~ 2 smaller compared to the uncorrected correlation.

A.4 Dust attenuation

Another physical variable of interest in the analysis of the local variations is the dust attenuation. For 33 galaxies for which we have FUV images available, we measure the fraction of FUV and optical emission absorbed and reprocessed by dust versus the escaping FUV emission as the ratio of the 24 μm to the FUV intensity, $I_{24\mu\text{m}}/I_{\text{FUV}}$. Figure A.1 shows the residuals of the correlation between the [C II]-based Σ_{SFR} and $\Sigma_{\text{SFR}}(\text{FUV} + 24 \mu\text{m})$. The top panel shows the fit residuals for all the 12'' regions from the 33 galaxies for which we have FUV maps available. Around the $I_{24\mu\text{m}}/I_{\text{FUV}}$ ratio of ~ 10 , we observe a systematic increase of the fit residuals as a function of decreasing extinction. The bottom panel of Figure A.1 shows that the regions that deviate are mainly coming from two galaxies: NGC 6946 and NGC 7793. Visual inspection of the [C II] and dust attenuation maps reveals that the regions with low $I_{24\mu\text{m}}/I_{\text{FUV}}$ ratios are located preferentially in regions of low surface brightness in the “extranuclear” pointings. The rest of the regions that show high fit residuals at low $I_{24\mu\text{m}}$ to I_{FUV} ratios are from the low metallicity systems ($12+\log_{10}(\text{O}/\text{H}) < 8.1$) Holmberg II and IC 2574.

A.5 Additional samples of galaxies included in Chapter 3

Díaz-Santos et al. (2013): From the 241 systems comprising the GOALS sample, we only select a subset of 116 systems that are classified as pure starburst following the criteria described in Díaz-Santos et al. (2013), i.e., that have 6.2 μm PAH equivalent widths that are greater than 0.5. The sample covers a distance range of $\sim 16 - 350$ Mpc. We compiled PACS [C II] flux densities, [C II] to FIR ratios

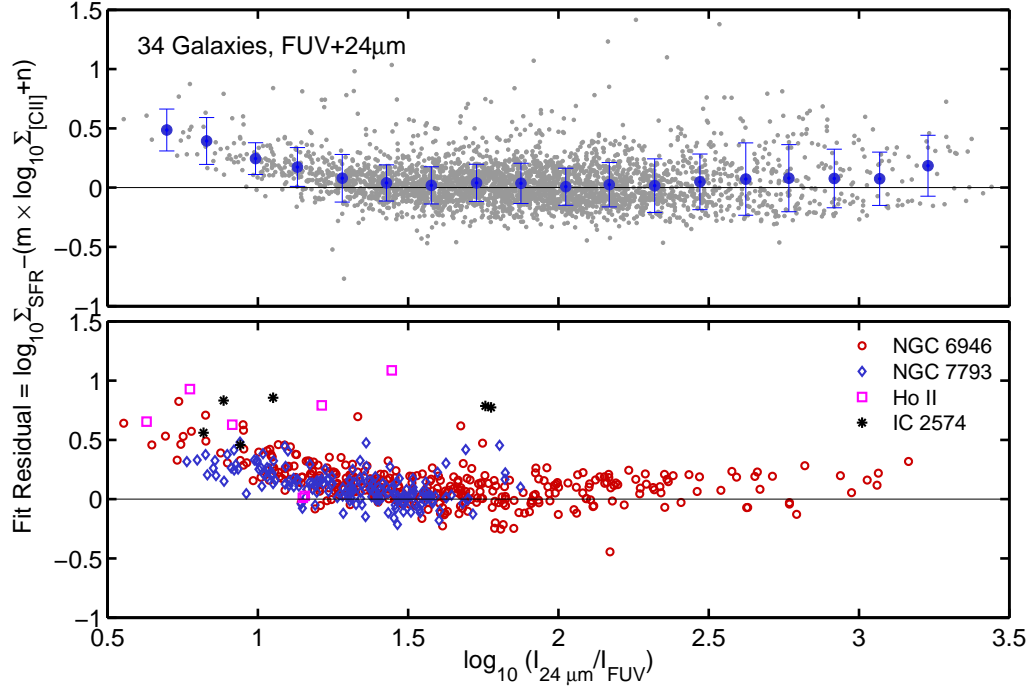


Figure A.1: Fit residual of the $\Sigma_{[\text{CII}]} - \Sigma_{\text{SFR}}$ correlation as a function of the fraction of FUV absorbed and reprocessed by dust versus the escaping FUV emission ($I_{24\mu\text{m}}/I_{\text{FUV}}$). Each point represent a $12''$ size region. Blue dots and the corresponding vertical bars correspond to the median and the 1σ standard deviation of the binned distribution of points. (*Top panel*) For 33 galaxies for which we have FUV maps available, we measure Σ_{SFR} as a linear combination of $24\mu\text{m}$ and FUV emission (Leroy et al. 2008) and the dust attenuation as the ratio of the $24\mu\text{m}$ intensity, $I_{24\mu\text{m}}$ [MJy sr^{-1}], and the FUV intensity, I_{FUV} [MJy sr^{-1}]. (*Bottom panel*) Four individual galaxy cases: two galaxies with global average low metallicity (Holmberg II and IC 2574) and two galaxies that are the main source of the low extinction regions that deviate from the fit (NGC 6946 and NGC 7793).

and PACS continuum flux densities at 63 and $158\mu\text{m}$ under the $[\text{O I}]$ and $[\text{C II}]$ lines, respectively, from Díaz-Santos et al. (2013). The areas of the infrared emitting nuclear regions of the GOALS sample were provided by T. Diaz-Santos (priv. comm.).

The FIR luminosities in Díaz-Santos et al. (2013) were measured based on the 60 and $100\mu\text{m}$ IRAS bands using Helou et al. (1988) calibration. In order to use the SFR calibration by Murphy et al. (2011) (or Kennicutt (1998), which yields

a SFR value ~ 1.3 times higher), we need to convert these FIR($60 - 100 \mu\text{m}$) luminosities into TIR($8 - 1000 \mu\text{m}$) luminosities. The ideal would be to measure the TIR luminosity of the GOALS galaxies by integrating their SED from 8 to $1000 \mu\text{m}$. This can be done for 64 U/LIRGs from the GOALS sample, for which U et al. (2012) compiled aperture photometry from radio through X-ray wavelengths. Based on these SEDs, U et al. (2012) use different dust models and a modified blackbody fit to measure the TIR luminosity from 8 to $1000 \mu\text{m}$. They find that these integrated TIR($8 - 1000 \mu\text{m}$) luminosities are about 0.02 dex lower than the FIR($12 - 100 \mu\text{m}$) luminosities measured using the calibration by Sanders & Mirabel (1996). Compared to the FIR($60 - 100 \mu\text{m}$) luminosities based on the Helou et al. (1988) calibration, the TIR($8 - 1000 \mu\text{m}$) luminosities are higher by a factor of 1.74. We adopt this factor to convert the FIR luminosities listed in Díaz-Santos et al. (2013) into TIR($8 - 1000 \mu\text{m}$) luminosities, and then we measure the SFR based on TIR($8 - 1000 \mu\text{m}$) using the calibration by Murphy et al. (2011).

Boselli et al. (2002): This work encompasses 23 galaxies detected in [C II] line emission by ISO. The sample include 18 spiral systems from the Virgo cluster ($D = 17 \text{ Mpc}$). The [C II], $\text{H}\alpha$ and FIR luminosities were taken from the paper. Additional IRAS 60 and $100 \mu\text{m}$ fluxes were added from Leech et al. (1999) and Smith & Madden (1997). We measure the SFR from the $\text{H}\alpha$ luminosities using the Calzetti et al. (2007) calibration. In order to derive individual IR color adjustments, we interpolate the value of the $70 \mu\text{m}$ flux based in the 60 and $100 \mu\text{m}$ fluxes, and then we measure the $70/100 \mu\text{m}$ ratio for each galaxy.

De Looze et al. (2011): This work encompasses 17 star-forming and starburst galaxies observed by ISO and located within 60 Mpc, with the exception of one system that is 139 Mpc away. The [C II], $24 \mu\text{m}$, FUV and FIR luminosities were taken from the paper. We measure the SFR as a combination of $24 \mu\text{m}$ and FUV

emission using the Leroy et al. (2008) calibration. For the IR color adjustment, we compile 60 and 100 μm fluxes from Brauher et al. (2008). Based on interpolated values of the 70 μm flux, we measure the 70/100 μm ratio for each galaxy in the sample.

Sargsyan et al. (2012): This work includes 23 starbursting LIRGs observed by *Herschel* and located in the distance range from ~ 66 to 505 Mpc. We compiled [C II] and FIR(12 – 100 μm) luminosities from their paper. As we mentioned in §4.2, the FIR(12 – 100 μm) luminosities measured using Sanders & Mirabel (1996) calibration are similar to the integrated TIR(8 – 1000 μm) luminosities in U/LIRGs (U et al. 2012). Therefore, we use the FIR(12 – 100 μm) luminosities to measure the SFR based on Murphy et al. (2011) calibration.

Weiner et al. in prep.: This work includes 16 disk non-mergers, non-AGN, LIRGs located at $z \sim 0.1$. The [C II] 158 μm , 60 and 100 μm IRAS fluxes were provided by B. Weiner (priv. comm.). We measure the FIR luminosities using the 60 and 100 μm fluxes. We then measure the TIR luminosities, SFRs and 70/100 μm IR colors using the same procedure applied to the Díaz-Santos et al. (2013) sample.

A.6 $\Sigma_{[\text{CII}]} - \Sigma_{24 \mu\text{m}}$ Correlation for the KINGFISH Galaxies

In Figures A.2 and A.3, we present individual correlations between the [C II] and 24 μm luminosity surface densities for each of the galaxies in our sample. For the systems that host an AGN, the diamonds mark the regions selected from the central $\sim 0.5\text{kpc}$ radius aperture. Next to each correlation, we also list the global metallicity, mean IR color, and mean starlight intensity of the galaxy.

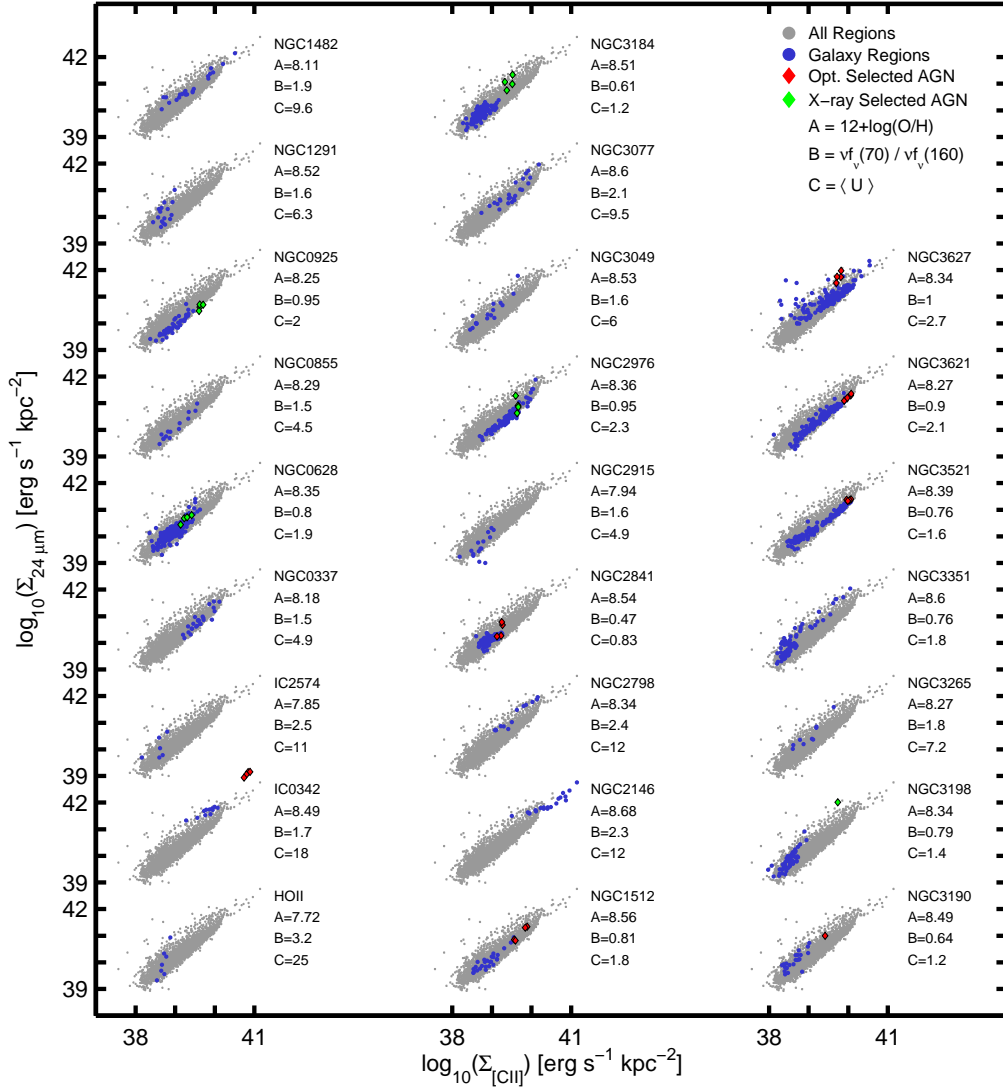


Figure A.2: [C II] luminosity surface density versus 24 μm surface density for each of the KINGFISH galaxies in our sample. The grey dots correspond to all the regions from the 46 KINGFISH galaxies in our sample. The blue dots correspond to the regions of the galaxy whose name is on the top right of the correlation. We also list the metallicity (A), mean IR color (B) and mean starlight intensity of the galaxy. If the galaxy host an AGN, the regions from the central ~ 0.5 kpc radius are show as diamonds: red for optically selected AGN (Moustakas et al. 2010) and green for X-ray selected AGN (Grier et al. 2011; Tajer et al. 2005).

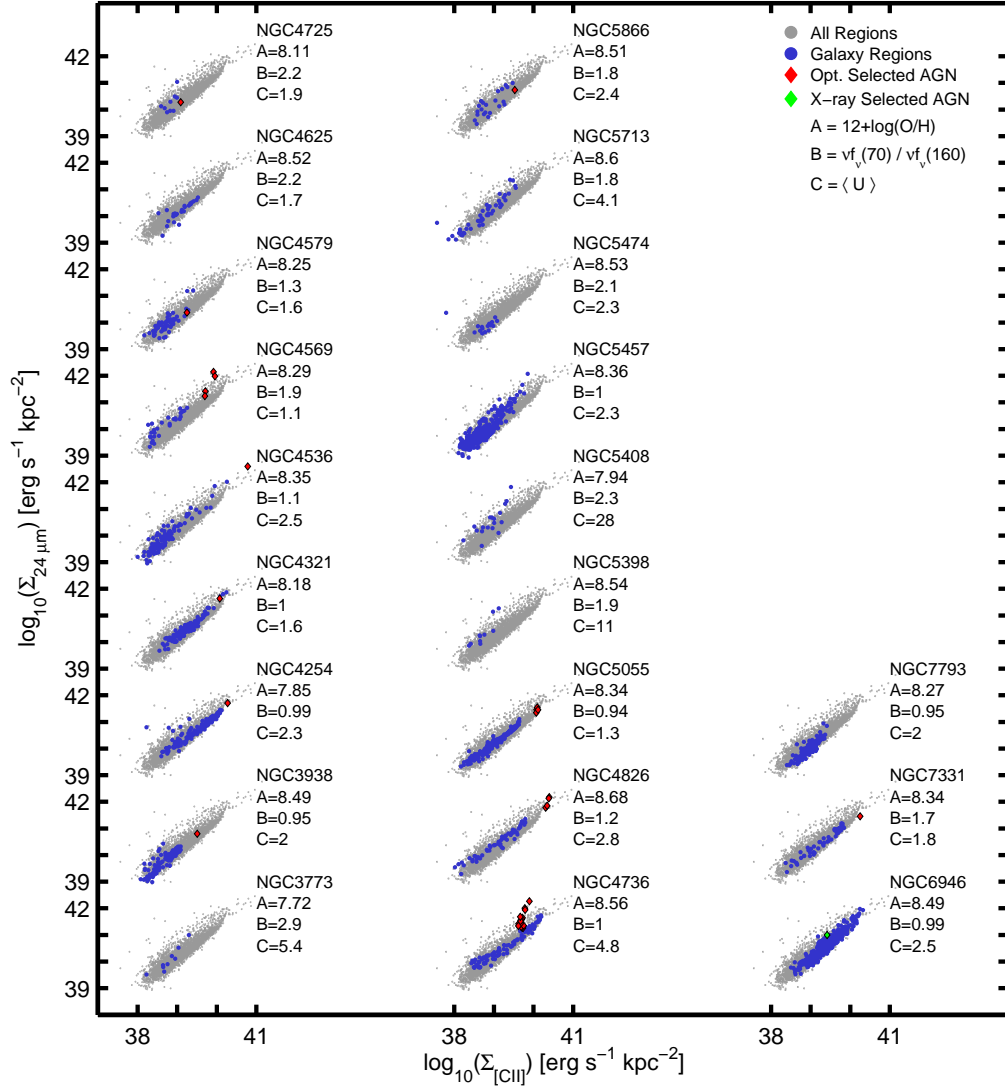


Figure A.3: As Figure A.2.

Bibliography

- Aloisi, A., Clementini, G., Tosi, M., Annibali, F., Contreras, R., Fiorentino, G., Mack, J., Marconi, M., Musella, I., Saha, A., Sirianni, M., & van der Marel, R. P. 2007, *ApJ*, 667, L151
- Alton, P. B., Xilouris, E. M., Misiriotis, A., Dasyra, K. M., & Dumke, M. 2004, *A&A*, 425, 109
- Aniano, G., Draine, B. T., Calzetti, D., Dale, D. A., Engelbracht, C. W., Gordon, K. D., Hunt, L. K., Kennicutt, R. C., Krause, O., Leroy, A. K., Rix, H.-W., Roussel, H., Sandstrom, K., Sauvage, M., Walter, F., Armus, L., Bolatto, A. D., Crocker, A., Donovan Meyer, J., Galametz, M., Helou, G., Hinz, J., Johnson, B. D., Koda, J., Montiel, E., Murphy, E. J., Skibba, R., Smith, J.-D. T., & Wolfire, M. G. 2012, *ApJ*, 756, 138
- Aniano, G., Draine, B. T., Gordon, K. D., & Sandstrom, K. 2011, *PASP*, 123, 1218
- Armus, L., Mazzarella, J. M., Evans, A. S., Surace, J. A., Sanders, D. B., Iwasawa, K., Frayer, D. T., Howell, J. H., Chan, B., Petric, A., Vavilkin, T., Kim, D. C., Haan, S., Inami, H., Murphy, E. J., Appleton, P. N., Barnes, J. E., Bothun, G., Bridge, C. R., Charmandaris, V., Jensen, J. B., Kewley, L. J., Lord, S., Madore, B. F., Marshall, J. A., Melbourne, J. E., Rich, J., Satyapal, S., Schulz, B., Spoon, H. W. W., Sturm, E., U, V., Veilleux, S., & Xu, K. 2009, *PASP*, 121, 559
- Asplund, M., Grevesse, N., Sauval, A. J., & Scott, P. 2009, *ARA&A*, 47, 481

- Badhwar, G. D. & Stephens, S. A. 1977, *ApJ*, 212, 494
- Baumgartner, W. H. & Mushotzky, R. F. 2006, *ApJ*, 639, 929
- Beirão, P., Armus, L., Helou, G., Appleton, P. N., Smith, J.-D. T., Croxall, K. V.,
Murphy, E. J., Dale, D. A., Draine, B. T., Wolfire, M. G., Sandstrom, K. M.,
Aniano, G., Bolatto, A. D., Groves, B., Brandl, B. R., Schinnerer, E., Crocker,
A. F., Hinz, J. L., Rix, H.-W., Kennicutt, R. C., Calzetti, D., Gil de Paz, A.,
Dumas, G., Galametz, M., Gordon, K. D., Hao, C.-N., Johnson, B., Koda, J.,
Krause, O., van der Laan, T., Leroy, A. K., Li, Y., Meidt, S. E., Meyer, J. D.,
Rahman, N., Roussel, H., Sauvage, M., Srinivasan, S., Vigroux, L., Walter, F., &
Warren, B. E. 2012, *ApJ*, 751, 144
- Bennett, C. L., Fixsen, D. J., Hinshaw, G., Mather, J. C., Moseley, S. H., Wright,
E. L., Eplee, Jr., R. E., Gales, J., Hewagama, T., Isaacman, R. B., Shafer, R. A.,
& Turpie, K. 1994, *ApJ*, 434, 587
- Berkhuijsen, E. M. & Fletcher, A. 2008, *MNRAS*, 390, L19
- Bertelli, G. & Nasi, E. 2001, *AJ*, 121, 1013
- Bigiel, F., Leroy, A. K., Walter, F., Brinks, E., de Blok, W. J. G., Kramer, C., Rix,
H. W., Schrubba, A., Schuster, K.-F., Usero, A., & Wiesemeyer, H. W. 2011, *ApJ*,
730, L13
- Binette, L. 1985, *A&A*, 143, 334
- Blitz, L., Fukui, Y., Kawamura, A., Leroy, A., Mizuno, N., & Rosolowsky, E. 2007,
Protostars and Planets V, 81
- Blitz, L. & Rosolowsky, E. 2006, *ApJ*, 650, 933
- Bolatto, A. D., Leroy, A. K., Jameson, K., Ostriker, E., Gordon, K., Lawton, B.,
Stanimirović, S., Israel, F. P., Madden, S. C., Hony, S., Sandstrom, K. M., Bot,
C., Rubio, M., Winkler, P. F., Roman-Duval, J., van Loon, J. T., Oliveira, J. M.,
& Indebetouw, R. 2011, *ApJ*, 741, 12

- Boselli, A. & Gavazzi, G. 2002, *A&A*, 386, 124
- Boselli, A., Gavazzi, G., Lequeux, J., & Pierini, D. 2002, *A&A*, 385, 454
- Bot, C., Ysard, N., Paradis, D., Bernard, J. P., Lagache, G., Israel, F. P., & Wall, W. F. 2010, *A&A*, 523, A20
- Boulanger, F., Abergel, A., Bernard, J.-P., Burton, W. B., Desert, F.-X., Hartmann, D., Lagache, G., & Puget, J.-L. 1996, *A&A*, 312, 256
- Brauher, J. R., Dale, D. A., & Helou, G. 2008, *ApJS*, 178, 280
- Calzetti, D., Kennicutt, R. C., Engelbracht, C. W., Leitherer, C., Draine, B. T., Kewley, L., Moustakas, J., Sosey, M., Dale, D. A., Gordon, K. D., Helou, G. X., Hollenbach, D. J., Armus, L., Bendo, G., Bot, C., Buckalew, B., Jarrett, T., Li, A., Meyer, M., Murphy, E. J., Prescott, M., Regan, M. W., Rieke, G. H., Roussel, H., Sheth, K., Smith, J. D. T., Thornley, M. D., & Walter, F. 2007, *ApJ*, 666, 870
- Cannon, J. M., Skillman, E. D., Garnett, D. R., & Dufour, R. J. 2002, *ApJ*, 565, 931
- Clark, B. G. 1965, *ApJ*, 142, 1398
- Combes, F., Rex, M., Rawle, T. D., Egami, E., Boone, F., Smail, I., Richard, J., Ivison, R. J., Gurwell, M., Casey, C. M., Omont, A., Berciano Alba, A., Dessauges-Zavadsky, M., Edge, A. C., Fazio, G. G., Kneib, J.-P., Okabe, N., Pelló, R., Pérez-González, P. G., Schaerer, D., Smith, G. P., Swinbank, A. M., & van der Werf, P. 2012, *A&A*, 538, L4
- Cormier, D., Lebouteiller, V., Madden, S. C., Abel, N., Hony, S., Galliano, F., Baes, M., Barlow, M. J., Cooray, A., De Looze, I., Galametz, M., Karczewski, O. L., Parkin, T. J., Rémy, A., Sauvage, M., Spinoglio, L., Wilson, C. D., & Wu, R. 2012, *A&A*, 548, A20
- Cormier, D., Madden, S. C., Hony, S., Contursi, A., Poglitsch, A., Galliano, F.,

- Sturm, E., Doublier, V., Feuchtgruber, H., Galametz, M., Geis, N., de Jong, J., Okumura, K., Panuzzo, P., & Sauvage, M. 2010, *A&A*, 518, L57
- Cox, D. P. 2005, *ARA&A*, 43, 337
- Crawford, M. K., Genzel, R., Townes, C. H., & Watson, D. M. 1985, *ApJ*, 291, 755
- Croxall, K. V., Smith, J. D., Brandl, B. R., Groves, B. A., Kennicutt, R. C., Kreckel, K., Johnson, B. D., Pellegrini, E., Sandstrom, K. M., Walter, F., Armus, L., Beirão, P., Calzetti, D., Dale, D. A., Galametz, M., Hinz, J. L., Hunt, L. K., Koda, J., & Schinnerer, E. 2013, *ApJ*, 777, 96
- Croxall, K. V., Smith, J. D., Wolfire, M. G., Roussel, H., Sandstrom, K. M., Draine, B. T., Aniano, G., Dale, D. A., Armus, L., Beirão, P., Helou, G., Bolatto, A. D., Appleton, P. N., Brandl, B. R., Calzetti, D., Crocker, A. F., Galametz, M., Groves, B. A., Hao, C.-N., Hunt, L. K., Johnson, B. D., Kennicutt, R. C., Koda, J., Krause, O., Li, Y., Meidt, S. E., Murphy, E. J., Rahman, N., Rix, H.-W., Sauvage, M., Schinnerer, E., Walter, F., & Wilson, C. D. 2012, *ApJ*, 747, 81
- Dale, D. A., Aniano, G., Engelbracht, C. W., Hinz, J. L., Krause, O., Montiel, E. J., Roussel, H., Appleton, P. N., Armus, L., Beirão, P., Bolatto, A. D., Brandl, B. R., Calzetti, D., Crocker, A. F., Croxall, K. V., Draine, B. T., Galametz, M., Gordon, K. D., Groves, B. A., Hao, C.-N., Helou, G., Hunt, L. K., Johnson, B. D., Kennicutt, R. C., Koda, J., Leroy, A. K., Li, Y., Meidt, S. E., Miller, A. E., Murphy, E. J., Rahman, N., Rix, H.-W., Sandstrom, K. M., Sauvage, M., Schinnerer, E., Skibba, R. A., Smith, J.-D. T., Tabatabaei, F. S., Walter, F., Wilson, C. D., Wolfire, M. G., & Zibetti, S. 2012, *ApJ*, 745, 95
- Dale, D. A., Cohen, S. A., Johnson, L. C., Schuster, M. D., Calzetti, D., Engelbracht, C. W., Gil de Paz, A., Kennicutt, R. C., Lee, J. C., Begum, A., Block, M., Dalcanton, J. J., Funes, J. G., Gordon, K. D., Johnson, B. D., Marble, A. R., Sakai, S., Skillman, E. D., van Zee, L., Walter, F., Weisz, D. R., Williams, B.,

- Wu, S.-Y., & Wu, Y. 2009a, *ApJ*, 703, 517
- Dale, D. A., Gil de Paz, A., Gordon, K. D., Hanson, H. M., Armus, L., Bendo, G. J., Bianchi, L., Block, M., Boissier, S., Boselli, A., Buckalew, B. A., Buat, V., Burgarella, D., Calzetti, D., Cannon, J. M., Engelbracht, C. W., Helou, G., Hollenbach, D. J., Jarrett, T. H., Kennicutt, R. C., Leitherer, C., Li, A., Madore, B. F., Martin, D. C., Meyer, M. J., Murphy, E. J., Regan, M. W., Roussel, H., Smith, J. D. T., Sosey, M. L., Thilker, D. A., & Walter, F. 2007, *ApJ*, 655, 863
- Dale, D. A., Smith, J. D. T., Armus, L., Buckalew, B. A., Helou, G., Kennicutt, Jr., R. C., Moustakas, J., Roussel, H., Sheth, K., Bendo, G. J., Calzetti, D., Draine, B. T., Engelbracht, C. W., Gordon, K. D., Hollenbach, D. J., Jarrett, T. H., Kewley, L. J., Leitherer, C., Li, A., Malhotra, S., Murphy, E. J., & Walter, F. 2006, *ApJ*, 646, 161
- Dale, D. A., Smith, J. D. T., Schlawin, E. A., Armus, L., Buckalew, B. A., Cohen, S. A., Helou, G., Jarrett, T. H., Johnson, L. C., Moustakas, J., Murphy, E. J., Roussel, H., Sheth, K., Staudaher, S., Bot, C., Calzetti, D., Engelbracht, C. W., Gordon, K. D., Hollenbach, D. J., Kennicutt, R. C., & Malhotra, S. 2009b, *ApJ*, 693, 1821
- de Graauw, T., Whyborn, N., Caux, E., Phillips, T., Stutzki, J., Tielens, A., Güsten, R., Helmich, F., Luinge, W., Martin-Pintado, J., Pearson, J., Planesas, P., Roelfsema, P., Saraceno, P., Schieder, R., Wildeman, K., & Wafelbakker, K. 2009, in *EAS Publications Series*, Vol. 34, *EAS Publications Series*, ed. L. Pagani & M. Gerin, 3–20
- De Looze, I., Baes, M., Bendo, G. J., Cortese, L., & Fritz, J. 2011, *MNRAS*, 416, 2712
- De Looze, I., Cormier, D., Lebouteiller, V., Madden, S., Baes, M., Bendo, G. J., Boquien, M., Boselli, A., Clements, D. L., Cortese, L., Cooray, A., Galametz,

- M., Galliano, F., Graciá-Carpio, J., Isaak, K., Karczewski, O. L., Parkin, T. J., Pellegrini, E. W., Rémy-Ruyer, A., Spinoglio, L., Smith, M. W. L., & Sturm, E. 2014, *A&A*, 568, A62
- Decarli, R., Walter, F., Neri, R., Bertoldi, F., Carilli, C., Cox, P., Kneib, J. P., Lestrade, J. F., Maiolino, R., Omont, A., Richard, J., Riechers, D., Thanjavur, K., & Weiss, A. 2012, *ApJ*, 752, 2
- Deo, R. P., Richards, G. T., Crenshaw, D. M., & Kraemer, S. B. 2009, *ApJ*, 705, 14
- Díaz-Santos, T., Armus, L., Charmandaris, V., Stierwalt, S., Murphy, E. J., Haan, S., Inami, H., Malhotra, S., Meijerink, R., Stacey, G., Petric, A. O., Evans, A. S., Veilleux, S., van der Werf, P. P., Lord, S., Lu, N., Howell, J. H., Appleton, P., Mazzarella, J. M., Surace, J. A., Xu, C. K., Schulz, B., Sanders, D. B., Bridge, C., Chan, B. H. P., Frayer, D. T., Iwasawa, K., Melbourne, J., & Sturm, E. 2013, *ApJ*, 774, 68
- Dole, H., Rieke, G. H., Lagache, G., Puget, J., Alonso-Herrero, A., Bai, L., Blaylock, M., Egami, E., Engelbracht, C. W., Gordon, K. D., Hines, D. C., Kelly, D. M., Le Floc'h, E., Misselt, K. A., Morrison, J. E., Muzerolle, J., Papovich, C., Pérez-González, P. G., Rieke, M. J., Rigby, J. R., Neugebauer, G., Stansberry, J. A., Su, K. Y. L., Young, E. T., Beichman, C. A., & Richards, P. L. 2004, *ApJS*, 154, 93
- Dopita, M. A., Sutherland, R. S., Nicholls, D. C., Kewley, L. J., & Vogt, F. P. A. 2013, *VizieR Online Data Catalog*, 220, 80010
- Draine, B. T. 1978, *ApJS*, 36, 595
- . 2011a, *ApJ*, 732, 100
- . 2011b, *Princeton Series in Astrophysics*, 36
- Draine, B. T., Aniano, G., Krause, O., Groves, B., Sandstrom, K., Braun, R., Leroy, A., Klaas, U., Linz, H., Rix, H.-W., Schinnerer, E., Schmiedeke, A., & Walter, F.

- 2014, ApJ, 780, 172
- Draine, B. T., Dale, D. A., Bendo, G., Gordon, K. D., Smith, J. D. T., Armus, L., Engelbracht, C. W., Helou, G., Kennicutt, Jr., R. C., Li, A., Roussel, H., Walter, F., Calzetti, D., Moustakas, J., Murphy, E. J., Rieke, G. H., Bot, C., Hollenbach, D. J., Sheth, K., & Teplitz, H. I. 2007, ApJ, 663, 866
- Draine, B. T. & Li, A. 2007, ApJ, 657, 810
- Edmunds, M. G. 2001, MNRAS, 328, 223
- Ekers, R. D., Goss, W. M., Wellington, K. J., Bosma, A., Smith, R. M., & Schweizer, F. 1983, A&A, 127, 361
- Engelbracht, C. W., Rieke, G. H., Gordon, K. D., Smith, J., Werner, M. W., Moustakas, J., Willmer, C. N. A., & Vanzi, L. 2008, ApJ, 678, 804
- Farrah, D., Lebouteiller, V., Spoon, H. W. W., Bernard-Salas, J., Pearson, C., Rigopoulou, D., Smith, H. A., González-Alfonso, E., Clements, D. L., Efstathiou, A., Cormier, D., Afonso, J., Petty, S. M., Harris, K., Hurley, P., Borys, C., Verma, A., Cooray, A., & Salvatelli, V. 2013, ApJ, 776, 38
- Ferkinhoff, C., Brisbin, D., Nikola, T., Parshley, S. C., Stacey, G. J., Phillips, T. G., Falgarone, E., Benford, D. J., Staguhn, J. G., & Tucker, C. E. 2011, ApJ, 740, L29
- Ferkinhoff, C., Brisbin, D., Nikola, T., Stacey, G. J., Sheth, K., Hailey-Dunsheath, S., & Falgarone, E. 2015, ArXiv e-prints
- Field, G. B., Goldsmith, D. W., & Habing, H. J. 1969, ApJ, 155, L149
- Fischer, J., Sturm, E., González-Alfonso, E., Graciá-Carpio, J., Hailey-Dunsheath, S., Poglitsch, A., Contursi, A., Lutz, D., Genzel, R., Sternberg, A., Verma, A., & Tacconi, L. 2010, A&A, 518, L41
- Fisher, D. B., Bolatto, A. D., Herrera-Camus, R., Draine, B. T., Donaldson, J., Walter, F., Sandstrom, K. M., Leroy, A. K., Cannon, J., & Gordon, K. 2014,

- Nature, 505, 186
- Franco, J., Kurtz, S. E., García-Segura, G., & Hofner, P. 2000, *Ap&SS*, 272, 169
- Fuchs, B., Jahreiß, H., & Flynn, C. 2009, *AJ*, 137, 266
- Galametz, M., Kennicutt, R. C., Calzetti, D., Aniano, G., Draine, B. T., Boquien, M., Brandl, B., Croxall, K. V., Dale, D. A., Engelbracht, C. W., Gordon, K. D., Groves, B., Hao, C.-N., Helou, G., Hinz, J. L., Hunt, L. K., Johnson, B. D., Li, Y., Murphy, E., Roussel, H., Sandstrom, K., Skibba, R. A., & Tabatabaei, F. S. 2013, *MNRAS*, 431, 1956
- Galametz, M., Madden, S. C., Galliano, F., Hony, S., Bendo, G. J., & Sauvage, M. 2011, *A&A*, 532, A56+
- Galavis, M. E., Mendoza, C., & Zeppen, C. J. 1997, *A&AS*, 123, 159
- Galliano, F., Dwek, E., & Chaniel, P. 2008, *ApJ*, 672, 214
- Galliano, F., Hony, S., Bernard, J.-P., Bot, C., Madden, S. C., Roman-Duval, J., Galametz, M., Li, A., Meixner, M., Engelbracht, C. W., Lebouteiller, V., Misselt, K., Montiel, E., Panuzzo, P., Reach, W. T., & Skibba, R. 2011, *A&A*, 536, A88
- Garnett, D. R., Shields, G. A., Peimbert, M., Torres-Peimbert, S., Skillman, E. D., Dufour, R. J., Terlevich, E., & Terlevich, R. J. 1999, *ApJ*, 513, 168
- Gavazzi, G., Boselli, A., Donati, A., Franzetti, P., & Scodreggio, M. 2003, *A&A*, 400, 451
- Genzel, R., Tacconi, L. J., Combes, F., Bolatto, A., Neri, R., Sternberg, A., Cooper, M. C., Bouché, N., Bournaud, F., Burkert, A., Comerford, J., Cox, P., Davis, M., Förster Schreiber, N. M., Garcia-Burillo, S., Gracia-Carpio, J., Lutz, D., Naab, T., Newman, S., Saintonge, A., Shapiro, K., Shapley, A., & Weiner, B. 2012, *ApJ*, 746, 69
- Gerin, M., Ruaud, M., Goicoechea, J. R., Gusdorf, A., Godard, B., de Luca, M., Falgarone, E., Goldsmith, P., Lis, D. C., Menten, K. M., Neufeld, D., Phillips,

- T. G., & Liszt, H. 2015, *A&A*, 573, A30
- Gil de Paz, A., Boissier, S., Madore, B. F., Seibert, M., Joe, Y. H., Boselli, A., Wyder, T. K., Thilker, D., Bianchi, L., Rey, S.-C., Rich, R. M., Barlow, T. A., Conrow, T., Forster, K., Friedman, P. G., Martin, D. C., Morrissey, P., Neff, S. G., Schiminovich, D., Small, T., Donas, J., Heckman, T. M., Lee, Y.-W., Milliard, B., Szalay, A. S., & Yi, S. 2007, *ApJS*, 173, 185
- Goldsmith, P. F., Langer, W. D., Pineda, J. L., & Velusamy, T. 2012, *ApJS*, 203, 13
- Goldsmith, P. F., Yıldız, U. A., Langer, W. D., & Pineda, J. L. 2015, *ArXiv e-prints*
- Gordon, K. D., Engelbracht, C. W., Fadda, D., Stansberry, J., Wachter, S., Frayer, D. T., Rieke, G., Noriega-Crespo, A., Latter, W. B., Young, E., Neugebauer, G., Balog, Z., Beeman, J. W., Dole, H., Egami, E., Haller, E. E., Hines, D., Kelly, D., Marleau, F., Misselt, K., Morrison, J., Pérez-González, P., Rho, J., & Wheaton, W. A. 2007, *PASP*, 119, 1019
- Graciá-Carpio, J., Sturm, E., Hailey-Dunsheath, S., Fischer, J., Contursi, A., Poglitsch, A., Genzel, R., González-Alfonso, E., Sternberg, A., Verma, A., Christopher, N., Davies, R., Feuchtgruber, H., de Jong, J. A., Lutz, D., & Tacconi, L. J. 2011, *ApJ*, 728, L7
- Grier, C. J., Mathur, S., Ghosh, H., & Ferrarese, L. 2011, *ApJ*, 731, 60
- Griffin, M. J., Abergel, A., Abreu, A., Ade, P. A. R., André, P., Augeres, J.-L., Babbedge, T., Bae, Y., Baillie, T., Baluteau, J.-P., Barlow, M. J., Bendo, G., Benielli, D., Bock, J. J., Bonhomme, P., Brisbin, D., Brockley-Blatt, C., Caldwell, M., Cara, C., Castro-Rodriguez, N., Cerulli, R., Chaniel, P., Chen, S., Clark, E., Clements, D. L., Clerc, L., Coker, J., Communal, D., Conversi, L., Cox, P., Crumb, D., Cunningham, C., Daly, F., Davis, G. R., de Antoni, P., Delderfield, J., Devin, N., di Giorgio, A., Didschuns, I., Dohlen, K., Donati, M., Dowell,

A., Dowell, C. D., Duband, L., Dumaye, L., Emery, R. J., Ferlet, M., Ferrand, D., Fontignie, J., Fox, M., Franceschini, A., Frerking, M., Fulton, T., Garcia, J., Gastaud, R., Gear, W. K., Glenn, J., Goizel, A., Griffin, D. K., Grundy, T., Guest, S., Guillemet, L., Hargrave, P. C., Harwit, M., Hastings, P., Hatziminaoglou, E., Herman, M., Hinde, B., Hristov, V., Huang, M., Imhof, P., Isaak, K. J., Israelsson, U., Ivison, R. J., Jennings, D., Kiernan, B., King, K. J., Lange, A. E., Latter, W., Laurent, G., Laurent, P., Leeks, S. J., Lellouch, E., Levenson, L., Li, B., Li, J., Lilienthal, J., Lim, T., Liu, S. J., Lu, N., Madden, S., Mainetti, G., Marliani, P., McKay, D., Mercier, K., Molinari, S., Morris, H., Moseley, H., Mulder, J., Mur, M., Naylor, D. A., Nguyen, H., O'Halloran, B., Oliver, S., Olofsson, G., Olofsson, H.-G., Orfei, R., Page, M. J., Pain, I., Panuzzo, P., Papageorgiou, A., Parks, G., Parr-Burman, P., Pearce, A., Pearson, C., Pérez-Fournon, I., Pinsard, F., Pisano, G., Podosek, J., Pohlen, M., Polehampton, E. T., Pouliquen, D., Rigopoulou, D., Rizzo, D., Roseboom, I. G., Roussel, H., Rowan-Robinson, M., Rownd, B., Saraceno, P., Sauvage, M., Savage, R., Savini, G., Sawyer, E., Scharmberg, C., Schmitt, D., Schneider, N., Schulz, B., Schwartz, A., Shafer, R., Shupe, D. L., Sibthorpe, B., Sidher, S., Smith, A., Smith, A. J., Smith, D., Spencer, L., Stobie, B., Sudiwala, R., Sukhatme, K., Surace, C., Stevens, J. A., Swinyard, B. M., Trichas, M., Tourette, T., Triou, H., Tseng, S., Tucker, C., Turner, A., Vaccari, M., Valtchanov, I., Vigroux, L., Virique, E., Voellmer, G., Walker, H., Ward, R., Waskett, T., Weilert, M., Wesson, R., White, G. J., Whitehouse, N., Wilson, C. D., Winter, B., Woodcraft, A. L., Wright, G. S., Xu, C. K., Zavagno, A., Zemcov, M., Zhang, L., & Zonca, E. 2010, *A&A*, 518, L3

Groves, B., Krause, O., Sandstrom, K., Schmiedeke, A., Leroy, A., Linz, H., Kapala, M., Rix, H.-W., Schinnerer, E., Tabatabaei, F., Walter, F., & da Cunha, E. 2012, *MNRAS*, 426, 892

- Groves, B. A., Dopita, M. A., & Sutherland, R. S. 2004, *ApJS*, 153, 9
- Haffner, L. M., Dettmar, R.-J., Beckman, J. E., Wood, K., Slavin, J. D., Giannamanco, C., Madsen, G. J., Zurita, A., & Reynolds, R. J. 2009, *Reviews of Modern Physics*, 81, 969
- Haffner, L. M., Reynolds, R. J., & Tufte, S. L. 1999, *ApJ*, 523, 223
- Hagen, J. P., Lilley, A. E., & McClain, E. F. 1955, *ApJ*, 122, 361
- Heiles, C. 1994, *ApJ*, 436, 720
- Heiles, C. & Troland, T. H. 2003, *ApJ*, 586, 1067
- Helou, G., Khan, I. R., Malek, L., & Boehmer, L. 1988, *ApJS*, 68, 151
- Helou, G., Malhotra, S., Hollenbach, D. J., Dale, D. A., & Contursi, A. 2001, *ApJ*, 548, L73
- Herrera-Camus, R., Bolatto, A. D., Wolfire, M. G., Smith, J. D., Croxall, K. V., Kennicutt, R. C., Calzetti, D., Helou, G., Walter, F., Leroy, A. K., Draine, B., Brandl, B. R., Armus, L., Sandstrom, K. M., Dale, D. A., Aniano, G., Meidt, S. E., Boquien, M., Hunt, L. K., Galametz, M., Tabatabaei, F. S., Murphy, E. J., Appleton, P., Roussel, H., Engelbracht, C., & Beirao, P. 2015, *ApJ*, 800, 1
- Hildebrand, R. H. 1983, *QJRAS*, 24, 267
- Hill, A. S., Benjamin, R. A., Kowal, G., Reynolds, R. J., Haffner, L. M., & Lazarian, A. 2008, *ApJ*, 686, 363
- Hirashita, H., Tajiri, Y. Y., & Kamaya, H. 2002, *A&A*, 388, 439
- Ho, L. C., Filippenko, A. V., & Sargent, W. L. W. 1997, *ApJS*, 112, 315
- Hollenbach, D. J. & Tielens, A. G. G. M. 1999, *Reviews of Modern Physics*, 71, 173
- Hoopes, C. G., Walterbos, R. A. M., & Bothun, G. D. 2001, *ApJ*, 559, 878
- Hudson, C. E. & Bell, K. L. 2004, *VizieR Online Data Catalog*, 343, 725
- . 2005, *A&A*, 436, 1131
- Hughes, T. M., Foyle, K., Schirm, M. R. P., Parkin, T. J., De Looze, I., Wilson,

- C. D., Bendo, G. J., Baes, M., Fritz, J., Boselli, A., Cooray, A., Cormier, D., Karczewski, O. L., Lebouteiller, V., Lu, N., Madden, S. C., Spinoglio, L., & Viaene, S. 2014, ArXiv e-prints
- Hunt, L., Bianchi, S., & Maiolino, R. 2005, *A&A*, 434, 849
- Hunt, L. K., Draine, B. T., Bianchi, S., Gordon, K. D., Aniano, G., Calzetti, D., Dale, D. A., Helou, G., Hinz, J. L., Kennicutt, R. C., Roussel, H., Wilson, C. D., Bolatto, A., Boquien, M., Croxall, K. V., Galametz, M., Gil de Paz, A., Koda, J., Munoz-Mateos, J. C., Sandstrom, K. M., Sauvage, M., Vigroux, L., & Zibetti, S. 2014, ArXiv e-prints
- Hunter, D. A., Kaufman, M., Hollenbach, D. J., Rubin, R. H., Malhotra, S., Dale, D. A., Brauher, J. R., Silbermann, N. A., Helou, G., Contursi, A., & Lord, S. D. 2001, *ApJ*, 553, 121
- Imanishi, M., Nakanishi, K., Tamura, Y., & Peng, C.-H. 2009, *AJ*, 137, 3581
- Isobe, T., Feigelson, E. D., Akritas, M. G., & Babu, G. J. 1990, *ApJ*, 364, 104
- Israel, F. P. & Maloney, P. R. 2011, *A&A*, 531, A19
- Israel, F. P., Wall, W. F., Raban, D., Reach, W. T., Bot, C., Oonk, J. B. R., Ysard, N., & Bernard, J. P. 2010, *A&A*, 519, A67
- James, A., Dunne, L., Eales, S., & Edmunds, M. G. 2002, *MNRAS*, 335, 753
- Jenkins, E. B. & Tripp, T. M. 2011, *ApJ*, 734, 65
- Joseph, R. D., Wright, G. S., & Prestwich, A. H. 1986, in *ESA Special Publication*, Vol. 263, *New Insights in Astrophysics. Eight Years of UV Astronomy with IUE*, ed. E. J. Rolfe, 597–600
- Kennicutt, R. C., Bendo, G., Engelbracht, C., Gordon, K., Li, A., Rieke, G. H., Rieke, M. J., Smith, J. D., Armus, L., Helou, G., Jarrett, T. H., Roussel, H., Calzetti, D., Leitherer, C., Malhotra, S., Meyer, M., Regan, M. W., Dale, D. A., Draine, B., Grauer, A. D., Hollenbach, D. J., Kewley, L. J., Murphy, E., Thornley,

- M. D., & Walter, F. 2003, in *Bulletin of the American Astronomical Society*, Vol. 35, American Astronomical Society Meeting Abstracts, 1351
- Kennicutt, R. C., Calzetti, D., Aniano, G., Appleton, P., Armus, L., Beirão, P., Bolatto, A. D., Brandl, B., Crocker, A., Croxall, K., Dale, D. A., Meyer, J. D., Draine, B. T., Engelbracht, C. W., Galametz, M., Gordon, K. D., Groves, B., Hao, C.-N., Helou, G., Hinz, J., Hunt, L. K., Johnson, B., Koda, J., Krause, O., Leroy, A. K., Li, Y., Meidt, S., Montiel, E., Murphy, E. J., Rahman, N., Rix, H.-W., Roussel, H., Sandstrom, K., Sauvage, M., Schinnerer, E., Skibba, R., Smith, J. D. T., Srinivasan, S., Vigroux, L., Walter, F., Wilson, C. D., Wolfire, M., & Zibetti, S. 2011, *PASP*, 123, 1347
- Kennicutt, R. C. & Evans, N. J. 2012, *ARA&A*, 50, 531
- Kennicutt, Jr., R. C. 1983, *ApJ*, 272, 54
- . 1984, *ApJ*, 287, 116
- . 1998, *ApJ*, 498, 541
- Kennicutt, Jr., R. C., Hao, C.-N., Calzetti, D., Moustakas, J., Dale, D. A., Bendo, G., Engelbracht, C. W., Johnson, B. D., & Lee, J. C. 2009, *ApJ*, 703, 1672
- Kewley, L. J. & Dopita, M. A. 2002, *ApJS*, 142, 35
- Kewley, L. J., Dopita, M. A., Sutherland, R. S., Heisler, C. A., & Trevena, J. 2001, *ApJ*, 556, 121
- Kim, C.-G., Kim, W.-T., & Ostriker, E. C. 2011, *ApJ*, 743, 25
- Knapen, J. H., Stedman, S., Bramich, D. M., Folkes, S. L., & Bradley, T. R. 2004, *A&A*, 426, 1135
- Kobulnicky, H. A. & Kewley, L. J. 2004, *ApJ*, 617, 240
- Krumholz, M. R., Leroy, A. K., & McKee, C. F. 2011, *ApJ*, 731, 25
- Kulkarni, S. R. & Heiles, C. 1987, in *Astrophysics and Space Science Library*, Vol. 134, *Interstellar Processes*, ed. D. J. Hollenbach & H. A. Thronson, Jr., 87–122

- Langer, W. D., Goldsmith, P. F., Pineda, J. L., Velusamy, T., Requena-Torres, M. A., & Wiesemeyer, H. 2015, ArXiv e-prints
- Law, K.-H., Gordon, K. D., & Misselt, K. A. 2011, ApJ, 738, 124
- Leech, K. J., Völk, H. J., Heinrichsen, I., Hippelein, H., Metcalfe, L., Pierini, D., Popescu, C. C., Tuffs, R. J., & Xu, C. 1999, MNRAS, 310, 317
- Leitherer, C., Schaerer, D., Goldader, J. D., González Delgado, R. M., Robert, C., Kune, D. F., de Mello, D. F., Devost, D., & Heckman, T. M. 1999, ApJS, 123, 3
- Leroy, A., Bolatto, A., Stanimirovic, S., Mizuno, N., Israel, F., & Bot, C. 2007a, ApJ, 658, 1027
- Leroy, A., Cannon, J., Walter, F., Bolatto, A., & Weiss, A. 2007b, ApJ, 663, 990
- Leroy, A. K., Bigiel, F., de Blok, W. J. G., Boissier, S., Bolatto, A., Brinks, E., Madore, B., Muñoz-Mateos, J.-C., Murphy, E., Sandstrom, K., Schrubba, A., & Walter, F. 2012, AJ, 144, 3
- Leroy, A. K., Bolatto, A., Gordon, K., Sandstrom, K., Gratier, P., Rosolowsky, E., Engelbracht, C. W., Mizuno, N., Corbelli, E., Fukui, Y., & Kawamura, A. 2011, ApJ, 737, 12
- Leroy, A. K., Walter, F., Bigiel, F., Usero, A., Weiss, A., Brinks, E., de Blok, W. J. G., Kennicutt, R. C., Schuster, K.-F., Kramer, C., Wiesemeyer, H. W., & Roussel, H. 2009, AJ, 137, 4670
- Leroy, A. K., Walter, F., Brinks, E., Bigiel, F., de Blok, W. J. G., Madore, B., & Thornley, M. D. 2008, AJ, 136, 2782
- Levesque, E. M., Kewley, L. J., & Larson, K. L. 2010, AJ, 139, 712
- Lisenfeld, U. & Ferrara, A. 1998, ApJ, 496, 145
- Luhman, M. L., Satyapal, S., Fischer, J., Wolfire, M. G., Cox, P., Lord, S. D., Smith, H. A., Stacey, G. J., & Unger, S. J. 1998, ApJ, 504, L11
- Luhman, M. L., Satyapal, S., Fischer, J., Wolfire, M. G., Sturm, E., Dudley, C. C.,

- Lutz, D., & Genzel, R. 2003, *ApJ*, 594, 758
- Madau, P. & Dickinson, M. 2014, *ARA&A*, 52, 415
- Madden, S. C., Geis, N., Genzel, R., Herrmann, F., Jackson, J., Poglitsch, A., Stacey, G. J., & Townes, C. H. 1993, *ApJ*, 407, 579
- Madden, S. C., Poglitsch, A., Geis, N., Stacey, G. J., & Townes, C. H. 1997, *ApJ*, 483, 200
- Madden, S. C., Rémy-Ruyer, A., Galametz, M., Cormier, D., Lebouteiller, V., Galiano, F., Hony, S., Bendo, G. J., Smith, M. W. L., Pohlen, M., Roussel, H., Sauvage, M., Wu, R., Sturm, E., Poglitsch, A., Contursi, A., Doublier, V., Baes, M., Barlow, M. J., Boselli, A., Boquien, M., Carlson, L. R., Ciesla, L., Cooray, A., Cortese, L., de Looze, I., Irwin, J. A., Isaak, K., Kamenetzky, J., Karczewski, O. L., Lu, N., MacHattie, J. A., O'Halloran, B., Parkin, T. J., Rangwala, N., Schirm, M. R. P., Schulz, B., Spinoglio, L., Vaccari, M., Wilson, C. D., & Wozniak, H. 2013, *PASP*, 125, 600
- Magdis, G. E., Rigopoulou, D., Hopwood, R., Huang, J.-S., Farrah, D., Pearson, C., Alonso-Herrero, A., Bock, J. J., Clements, D., Cooray, A., Griffin, M. J., Oliver, S., Perez Fournon, I., Riechers, D., Swinyard, B. M., Scott, D., Thatte, N., Valtchanov, I., & Vaccari, M. 2014, *ApJ*, 796, 63
- Magrini, L., Bianchi, S., Corbelli, E., Cortese, L., Hunt, L., Smith, M., Vlahakis, C., Davies, J., Bendo, G. J., Baes, M., Boselli, A., Clemens, M., Casasola, V., De Looze, I., Fritz, J., Giovanardi, C., Grossi, M., Hughes, T., Madden, S., Pappalardo, C., Pohlen, M., di Serego Alighieri, S., & Verstappen, J. 2011, *A&A*, 535, A13
- Makiwa, G., Naylor, D. A., Ferlet, M., Salji, C., Swinyard, B., Polehampton, E., & van der Wiel, M. H. D. 2013, *Appl. Opt.*, 52, 3864
- Malhotra, S., Helou, G., Stacey, G., Hollenbach, D., Lord, S., Beichman, C. A.,

- Dinerstein, H., Hunter, D. A., Lo, K. Y., Lu, N. Y., Rubin, R. H., Silbermann, N., Thronson, Jr., H. A., & Werner, M. W. 1997, *ApJ*, 491, L27
- Malhotra, S., Kaufman, M. J., Hollenbach, D., Helou, G., Rubin, R. H., Brauher, J., Dale, D., Lu, N. Y., Lord, S., Stacey, G., Contursi, A., Hunter, D. A., & Dinerstein, H. 2001, *ApJ*, 561, 766
- Maloney, P. R., Hollenbach, D. J., & Tielens, A. G. G. M. 1996, *ApJ*, 466, 561
- Martin, D. C., Fanson, J., Schiminovich, D., Morrissey, P., Friedman, P. G., Barlow, T. A., Conrow, T., Grange, R., Jelinsky, P. N., Milliard, B., Siegmund, O. H. W., Bianchi, L., Byun, Y.-I., Donas, J., Forster, K., Heckman, T. M., Lee, Y.-W., Madore, B. F., Malina, R. F., Neff, S. G., Rich, R. M., Small, T., Surber, F., Szalay, A. S., Welsh, B., & Wyder, T. K. 2005, *ApJ*, 619, L1
- Mathis, J. S., Mezger, P. G., & Panagia, N. 1983, *A&A*, 128, 212
- McKee, C. F. & Ostriker, J. P. 1977, *ApJ*, 218, 148
- McKee, C. F. & Williams, J. P. 1997, *ApJ*, 476, 144
- Mookerjea, B., Kramer, C., Buchbender, C., Boquien, M., Verley, S., Relaño, M., Quintana-Lacaci, G., Aalto, S., Braine, J., Calzetti, D., Combes, F., Garcia-Burillo, S., Gratier, P., Henkel, C., Israel, F., Lord, S., Nikola, T., Röllig, M., Stacey, G., Tabatabaei, F. S., van der Tak, F., & van der Werf, P. 2011, *A&A*, 532, A152
- Moustakas, J., Kennicutt, Jr., R. C., Tremonti, C. A., Dale, D. A., Smith, J., & Calzetti, D. 2010, *ApJS*, 190, 233
- Muñoz-Mateos, J. C., Gil de Paz, A., Boissier, S., Zamorano, J., Dale, D. A., Pérez-González, P. G., Gallego, J., Madore, B. F., Bendo, G., Thornley, M. D., Draine, B. T., Boselli, A., Buat, V., Calzetti, D., Moustakas, J., & Kennicutt, R. C. 2009a, *ApJ*, 701, 1965
- Muñoz-Mateos, J. C., Gil de Paz, A., Zamorano, J., Boissier, S., Dale, D. A., Pérez-

- González, P. G., Gallego, J., Madore, B. F., Bendo, G., Boselli, A., Buat, V., Calzetti, D., Moustakas, J., & Kennicutt, Jr., R. C. 2009b, *ApJ*, 703, 1569
- Murphy, E. J., Condon, J. J., Schinnerer, E., Kennicutt, R. C., Calzetti, D., Armus, L., Helou, G., Turner, J. L., Aniano, G., Beirão, P., Bolatto, A. D., Brandl, B. R., Croxall, K. V., Dale, D. A., Donovan Meyer, J. L., Draine, B. T., Engelbracht, C., Hunt, L. K., Hao, C.-N., Koda, J., Roussel, H., Skibba, R., & Smith, J.-D. T. 2011, *ApJ*, 737, 67
- Nagao, T., Maiolino, R., De Breuck, C., Caselli, P., Hatsukade, B., & Saigo, K. 2012, *A&A*, 542, L34
- Nieva, M.-F. & Przybilla, N. 2012, *A&A*, 539, A143
- Nyland, K., Alatalo, K., Wrobel, J. M., Young, L. M., Morganti, R., Davis, T. A., de Zeeuw, P. T., Deustua, S., & Bureau, M. 2013, *ApJ*, 779, 173
- Oberst, T. E., Parshley, S. C., Nikola, T., Stacey, G. J., Löhr, A., Lane, A. P., Stark, A. A., & Kamenetzky, J. 2011, *ApJ*, 739, 100
- Oberst, T. E., Parshley, S. C., Stacey, G. J., Nikola, T., Löhr, A., Harnett, J. I., Tothill, N. F. H., Lane, A. P., Stark, A. A., & Tucker, C. E. 2006, *ApJ*, 652, L125
- Ostriker, E. C., McKee, C. F., & Leroy, A. K. 2010, *ApJ*, 721, 975
- Parkin, T. J., Wilson, C. D., Schirm, M. R. P., Baes, M., Boquien, M., Boselli, A., Cooray, A., Cormier, D., Foyle, K., Karczewski, O. L., Lebouteiller, V., de Looze, I., Madden, S. C., Roussel, H., Sauvage, M., & Spinoglio, L. 2013, *ApJ*, 776, 65
- Pellegrini, E. W., Smith, J. D., Wolfire, M. G., Draine, B. T., Crocker, A. F., Croxall, K. V., van der Werf, P., Dale, D. A., Rigopoulou, D., Wilson, C. D., Schinnerer, E., Groves, B. A., Kreckel, K., Sandstrom, K. M., Armus, L., Calzetti, D., Murphy, E. J., Walter, F., Koda, J., Bayet, E., Beirao, P., Bolatto, A. D., Bradford, M., Brinks, E., Hunt, L., Kennicutt, R., Knapen, J. H., Leroy, A. K., Rosolowsky, E., Vigroux, L., & Hopwood, R. H. B. 2013, *ApJ*, 779, L19

- Pérez-Montero, E. & Contini, T. 2009, MNRAS, 398, 949
- Petuchowski, S. J., Bennett, C. L., Haas, M. R., Erickson, E. F., Lord, S. D., Rubin, R. H., Colgan, S. W. J., & Hollenbach, D. J. 1994, ApJ, 427, L17
- Pilbratt, G. L., Riedinger, J. R., Passvogel, T., Crone, G., Doyle, D., Gageur, U., Heras, A. M., Jewell, C., Metcalfe, L., Ott, S., & Schmidt, M. 2010, A&A, 518, L1
- Pilyugin, L. S. & Thuan, T. X. 2005, ApJ, 631, 231
- Pineda, J. L., Langer, W. D., & Goldsmith, P. F. 2014, ArXiv e-prints
- Pineda, J. L., Langer, W. D., Velusamy, T., & Goldsmith, P. F. 2013, A&A, 554, A103
- Poglitsch, A., Krabbe, A., Madden, S. C., Nikola, T., Geis, N., Johansson, L. E. B., Stacey, G. J., & Sternberg, A. 1995, ApJ, 454, 293
- Poglitsch, A., Waelkens, C., Geis, N., Feuchtgruber, H., Vandenbussche, B., Rodriguez, L., Krause, O., Renotte, E., van Hoof, C., Saraceno, P., Cepa, J., Kerschbaum, F., Agnèse, P., Ali, B., Altieri, B., Andreani, P., Augueres, J.-L., Balog, Z., Barl, L., Bauer, O. H., Belbachir, N., Benedettini, M., Billot, N., Boulade, O., Bischof, H., Blommaert, J., Callut, E., Cara, C., Cerulli, R., Cesarsky, D., Contursi, A., Creten, Y., De Meester, W., Doublier, V., Doumayrou, E., Duband, L., Exter, K., Genzel, R., Gillis, J.-M., Grözinger, U., Henning, T., Herreros, J., Huygen, R., Inguscio, M., Jakob, G., Jamar, C., Jean, C., de Jong, J., Katterloher, R., Kiss, C., Klaas, U., Lemke, D., Lutz, D., Madden, S., Marquet, B., Martignac, J., Mazy, A., Merken, P., Montfort, F., Morbidelli, L., Müller, T., Nielbock, M., Okumura, K., Orfei, R., Ottensamer, R., Pezzuto, S., Popesso, P., Putzeys, J., Regibo, S., Reveret, V., Royer, P., Sauvage, M., Schreiber, J., Stegmaier, J., Schmitt, D., Schubert, J., Sturm, E., Thiel, M., Tofani, G., Vavrek, R., Wetzstein, M., Wieprecht, E., & Wiezorrek, E. 2010, A&A, 518, L2+

- Povich, M. S., Stone, J. M., Churchwell, E., Zweibel, E. G., Wolfire, M. G., Babler, B. L., Indebetouw, R., Meade, M. R., & Whitney, B. A. 2007, *ApJ*, 660, 346
- Redfield, S. & Falcon, R. E. 2008, *ApJ*, 683, 207
- Regan, M. W., Sheth, K., Teuben, P. J., & Vogel, S. N. 2002, *ApJ*, 574, 126
- Rémy-Ruyer, A., Madden, S. C., Galliano, F., Galametz, M., Takeuchi, T. T., Asano, R. S., Zhukovska, S., Lebouteiller, V., Cormier, D., Jones, A., Bocchio, M., Baes, M., Bendo, G. J., Boquien, M., Boselli, A., DeLooze, I., Doublier-Pritchard, V., Hughes, T., Karczewski, O. L., & Spinoglio, L. 2014, *A&A*, 563, A31
- Rieke, G. H., Alonso-Herrero, A., Weiner, B. J., Pérez-González, P. G., Blaylock, M., Donley, J. L., & Marcillac, D. 2009, *ApJ*, 692, 556
- Rieke, G. H., Young, E. T., Engelbracht, C. W., Kelly, D. M., Low, F. J., Haller, E. E., Beeman, J. W., Gordon, K. D., Stansberry, J. A., Misselt, K. A., Cadien, J., Morrison, J. E., Rivlis, G., Latter, W. B., Noriega-Crespo, A., Padgett, D. L., Stapelfeldt, K. R., Hines, D. C., Egami, E., Muzerolle, J., Alonso-Herrero, A., Blaylock, M., Dole, H., Hinz, J. L., Le Flo'c'h, E., Papovich, C., Pérez-González, P. G., Smith, P. S., Su, K. Y. L., Bennett, L., Frayer, D. T., Henderson, D., Lu, N., Masci, F., Pesenson, M., Rebull, L., Rho, J., Keene, J., Stolovy, S., Wachter, S., Wheaton, W., Werner, M. W., & Richards, P. L. 2004, *ApJS*, 154, 25
- Rigopoulou, D., Hurley, P. D., Swinyard, B. M., Virdee, J., Croxall, K. V., Hopwood, R. H. B., Lim, T., Magdis, G. E., Pearson, C. P., Pellegrini, E., Polehampton, E., & Smith, J.-D. 2013, *MNRAS*, 434, 2051
- Roussel, H. 2012, in prep.
- Roussel, H., Helou, G., Smith, J. D., Draine, B. T., Hollenbach, D. J., Moustakas, J., Spoon, H. W., Kennicutt, R. C., Rieke, G. H., Walter, F., Armus, L., Dale, D. A., Sheth, K., Bendo, G. J., Engelbracht, C. W., Gordon, K. D., Meyer, M. J.,

- Regan, M. W., & Murphy, E. J. 2006, *ApJ*, 646, 841
- Rubin, D., Hony, S., Madden, S. C., Tielens, A. G. G. M., Meixner, M., Indebetouw, R., Reach, W., Ginsburg, A., Kim, S., Mochizuki, K., Babler, B., Block, M., Bracker, S. B., Engelbracht, C. W., For, B.-Q., Gordon, K., Hora, J. L., Leitherer, C., Meade, M., Misselt, K., Sewilo, M., Vijh, U., & Whitney, B. 2009, *A&A*, 494, 647
- Rubin, R. H., Simpson, J. P., Lord, S. D., Colgan, S. W. J., Erickson, E. F., & Haas, M. R. 1994, *ApJ*, 420, 772
- Salim, S., Rich, R. M., Charlot, S., Brinchmann, J., Johnson, B. D., Schiminovich, D., Seibert, M., Mallery, R., Heckman, T. M., Forster, K., Friedman, P. G., Martin, D. C., Morrissey, P., Neff, S. G., Small, T., Wyder, T. K., Bianchi, L., Donas, J., Lee, Y.-W., Madore, B. F., Milliard, B., Szalay, A. S., Welsh, B. Y., & Yi, S. K. 2007, *ApJS*, 173, 267
- Sanders, D. B. & Mirabel, I. F. 1996, *ARA&A*, 34, 749
- Sargsyan, L., Lebouteiller, V., Weedman, D., Spoon, H., Bernard-Salas, J., Engels, D., Stacey, G., Houck, J., Barry, D., Miles, J., & Samsonyan, A. 2012, *ApJ*, 755, 171
- Savage, B. D. & Sembach, K. R. 1996, *ARA&A*, 34, 279
- Schruba, A., Leroy, A. K., Walter, F., Bigiel, F., Brinks, E., de Blok, W. J. G., Dumas, G., Kramer, C., Rosolowsky, E., Sandstrom, K., Schuster, K., Usero, A., Weiss, A., & Wiese Meyer, H. 2011, *AJ*, 142, 37
- Shibai, H., Okuda, H., Nakagawa, T., Matsuhara, H., Maihara, T., Mizutani, K., Kobayashi, Y., Hiromoto, N., Nishimura, T., & Low, F. J. 1991, *ApJ*, 374, 522
- Skillman, E. D. & Kennicutt, Jr., R. C. 1993, *ApJ*, 411, 655
- Smith, B. J. & Madden, S. C. 1997, *AJ*, 114, 138
- Sofia, U. J., Lauroesch, J. T., Meyer, D. M., & Cartledge, S. I. B. 2004, *ApJ*, 605,

- Stacey, G. J., Geis, N., Genzel, R., Lugten, J. B., Poglitsch, A., Sternberg, A., & Townes, C. H. 1991, *ApJ*, 373, 423
- Stacey, G. J., Hailey-Dunsheath, S., Ferkinhoff, C., Nikola, T., Parshley, S. C., Benford, D. J., Staguhn, J. G., & Fiolet, N. 2010, *ApJ*, 724, 957
- Stacey, G. J., Viscuso, P. J., Fuller, C. E., & Kurtz, N. T. 1985, *ApJ*, 289, 803
- Stansberry, J. A., Gordon, K. D., Bhattacharya, B., Engelbracht, C. W., Rieke, G. H., Marleau, F. R., Fadda, D., Frayer, D. T., Noriega-Crespo, A., Wachter, S., Young, E. T., Müller, T. G., Kelly, D. M., Blaylock, M., Henderson, D., Neugebauer, G., Beeman, J. W., & Haller, E. E. 2007, *PASP*, 119, 1038
- Stewart, S. G. & Walter, F. 2000, *AJ*, 120, 1794
- Storey, P. J. & Zeppen, C. J. 2000, *MNRAS*, 312, 813
- Tajer, M., Trinchieri, G., Wolter, A., Campana, S., Moretti, A., & Tagliaferri, G. 2005, *A&A*, 435, 799
- Tayal, S. S. 2011, *ApJS*, 195, 12
- Tumlinson, J., Shull, J. M., Rachford, B. L., Browning, M. K., Snow, T. P., Fullerton, A. W., Jenkins, E. B., Savage, B. D., Crowther, P. A., Moos, H. W., Sembach, K. R., Sonneborn, G., & York, D. G. 2002, *ApJ*, 566, 857
- U, V., Sanders, D. B., Mazzarella, J. M., Evans, A. S., Howell, J. H., Surace, J. A., Armus, L., Iwasawa, K., Kim, D.-C., Casey, C. M., Vavilkin, T., Dufault, M., Larson, K. L., Barnes, J. E., Chan, B. H. P., Frayer, D. T., Haan, S., Inami, H., Ishida, C. M., Kartaltepe, J. S., Melbourne, J. L., & Petric, A. O. 2012, *ApJS*, 203, 9
- van Zee, L., Westpfahl, D., Haynes, M. P., & Salzer, J. J. 1998, *AJ*, 115, 1000
- Velusamy, T., Langer, W. D., Pineda, J. L., & Goldsmith, P. F. 2012, *A&A*, 541, L10

- Walter, F., Brinks, E., de Blok, W. J. G., Bigiel, F., Kennicutt, Jr., R. C., Thornley, M. D., & Leroy, A. 2008, *AJ*, 136, 2563
- Walter, F., Cannon, J. M., Roussel, H., Bendo, G. J., Calzetti, D., Dale, D. A., Draine, B. T., Helou, G., Kennicutt, Jr., R. C., Moustakas, J., Rieke, G. H., Armus, L., Engelbracht, C. W., Gordon, K., Hollenbach, D. J., Lee, J., Li, A., Meyer, M. J., Murphy, E. J., Regan, M. W., Smith, J.-D. T., Brinks, E., de Blok, W. J. G., Bigiel, F., & Thornley, M. D. 2007, *ApJ*, 661, 102
- Walter, F., Kerp, J., Duric, N., Brinks, E., & Klein, U. 1998, *ApJ*, 502, L143
- Watson, W. D. 1972, *ApJ*, 176, 103
- Weingartner, J. C. & Draine, B. T. 2001, *ApJS*, 134, 263
- Wolfire, M. G., Hollenbach, D., & McKee, C. F. 2010, *ApJ*, 716, 1191
- Wolfire, M. G., Hollenbach, D., McKee, C. F., Tielens, A. G. G. M., & Bakes, E. L. O. 1995, *ApJ*, 443, 152
- Wolfire, M. G., McKee, C. F., Hollenbach, D., & Tielens, A. G. G. M. 2003, *ApJ*, 587, 278
- Wright, E. L., Mather, J. C., Bennett, C. L., Cheng, E. S., Shafer, R. A., Fixsen, D. J., Eplee, Jr., R. E., Isaacman, R. B., Read, S. M., Boggess, N. W., Gulkis, S., Hauser, M. G., Janssen, M., Kelsall, T., Lubin, P. M., Meyer, S. S., Moseley, Jr., S. H., Murdock, T. L., Silverberg, R. F., Smoot, G. F., Weiss, R., & Wilkinson, D. T. 1991, *ApJ*, 381, 200
- Wu, R., Polehampton, E. T., Etxaluze, M., Makiwa, G., Naylor, D. A., Salji, C., Swinyard, B. M., Ferlet, M., van der Wiel, M. H. D., Smith, A. J., Fulton, T., Griffin, M. J., Baluteau, J.-P., Benielli, D., Glenn, J., Hopwood, R., Imhof, P., Lim, T., Lu, N., Panuzzo, P., Pearson, C., Sidher, S., & Valtchanov, I. 2013, *A&A*, 556, A116
- Wu, Y., Charmandaris, V., Hunt, L. K., Bernard-Salas, J., Brandl, B. R., Marshall,

- J. A., Leboutteiller, V., Hao, L., & Houck, J. R. 2007, ApJ, 662, 952
- Zhao, Y., Lu, N., Xu, C. K., Gao, Y., Lord, S., Howell, J., Isaak, K. G., Charmandaris, V., Diaz-Santos, T., Appleton, P., Evans, A., Iwasawa, K., Leech, J., Mazzarella, J., Petric, A. O., Sanders, D. B., Schulz, B., Surace, J., & van der Werf, P. P. 2013, ApJ, 765, L13
- Zubko, V., Dwek, E., & Arendt, R. G. 2004, ApJS, 152, 211